Impact of diversity in syngas/producer gas composition on stable and unstable laminar diffusion flames

Tananop Piemsinlapakunchon

Submitted in fulfilment of the requirements for the Degree of Doctor of Philosophy (PhD)

James Watt School of Engineering

College of Science and Engineer

University of Glasgow

August 2019

Abstract

Renewable and sustainable energy are developed to address global energy demand which has increased dramatically. Among them, syngas/producer gas, defined as a gas fuel consisting of hydrogen (H_2), carbon-monoxide (CO), carbon dioxide (CO_2), water vapour (H_2O), nitrogen (N_2), and methane (CH_4) as a major species, is one of the interesting options. The lower CO_2 emission than fossil fuel and flexibility in the production process and feedstock are its advantages. However, these benefits have a side effect because of the diversity in fuel composition which affects the combustion characteristics directly [1]. The utilisation of syngas in the conventional gas fuel combustion systems would, therefore, require an in-depth investigation and microscopic understanding of the impact of each species of hybrid gas composition on combustion. This information is an essential step in the development of efficient combustion technologies.

The research work presented in this thesis addresses some of these challenges with the identification of the knowledge gap in syngas combustion. The study focused on the numerical investigation of the impacts of syngas composition on the combustion and flame characteristics, with a particular focus on the role of syngas composition in heat generation capability, emission, and flame instability. The study firstly investigates the impact of the content of H_2 in fuel stream on the diffusion flame characteristics including flame temperature, flame dimension, heat generation and emission. The studied fuel is H_2/N_2 mixed, and the first modelling on a stable co-flow diffusion flame is performed based on an axisymmetric burner presented in Toro et al. [2]. The content or volume of H_2 in the fuel stream is controlled by the fuel rate as well as the concentration of H_2 in fuel composition (X_{H_2}). The results generally show that an increase in the H_2 content supplied into combustion escalate the flame size and heat generation. In particular, the flame width and flame temperature are dominated by X_{H_2} while the flame length is affected strongly by the fuel rate. The thermal nitrogen oxide (NO_x) formation mechanism also plays a significant role since the flame with a higher flame temperature formulates NO_x at a higher rate. Also, the heat generation from flame is affected strongly by the flame size and temperature, which compensate each other.

Secondly, the impact of diversity in syngas/producer gas composition on the heat generation capability and emission are examined. The study reports that the total heat generation

capability of the diffusion flame (Q_{total}) depends strongly on the combustion heat release property of fuel (Q_{max}) and flame dimension. These parameters also compensate for the role of each other; for example, the higher value of Q_{total} is obtained from a larger flame of fuel with a lower value of Q_{max}. CH_4 encourages heat generation capability but decreases the consumption and emission per unit of heat generated. CO promotes heat generation and decreases fuel consumption at a weaker level than CH_4. However, a higher production rate of CO_2 emission per unit of heat generated is a side impact of a higher concentration of CO. H_2 plays a significant role in the flame temperature but encourages heat generation at the weaker level than CO. Non-combustible species reduces the heat generation capability, and the weaker impact of CO_2 causes it is more desirable than N_2. Additionally, it is noticed that CO_2 assists the radiative heat transfer property of the flame.

Thirdly, an occurrence of oscillation in syngas laminar co-flow diffusion flame is studied. The phenomena occur due to the impact of Kelvin-Helmholtz instability on the mix of fuel and air at the flame front. Two types of flame oscillation 'flickering and tip-cutting' are found when the fuel and oxidiser are supplied into combustion at an improper ratio. The simulation model is formulated based on the burner geometry of Darabkhani et al. [3]. The oscillating flame is created without co-flow air to stabilise. The flame is stable at a low fuel rate then transforms into a flickering/tip-cutting flame at a higher fuel rate. The syngas with a lower H_2:CO promotes a higher magnitude of flame oscillation. However, the value does not increase further when H_2:CO < 1; i.e. the syngas flame with H_2:CO = 1 has a comparable impact of flame oscillation when considering H_2:CO < 1. Diluting CH_4 in syngas composition significantly increases the magnitude of oscillation at a significantly stronger level than CO. Adding CO_2 or N_2 to syngas composition results in the opposite direction. Also, the flame oscillation directly affects the fluctuation in heat generation capability.

Finally, further study is processed with an aim to minimise/eliminate the flame oscillation. The fuel rate is kept constant while the air rate supplied is escalated for this part of the study. The magnitude of oscillation of the flame reduces, then the flame becomes stable at a higher air rate since the vortices of the K-H instability are pushed outside the visible flame. Further, the impact of fuel composition on this phenomenon is analysed in order to derive a relation between the reduction of the magnitude of oscillation and air rate. Syngas with a relatively low ratio of H_2:CO demands a less air rate to eliminate the instability. On the other hand, diluting CH_4 to syngas composition significantly increases this demand, and the opposite result is observed when syngas is mixed with CO_2 and N_2.

Table of contents

List of Tables

List of Figures

Acknowledgement

This work is dedicated to my wife and my parents who have been supported in all aspects.

I am heartily thankful to my supervisor, Dr Manosh C Paul, whose encouragement, guidance and support from the initial to the final stage, enabled me to develop an understanding of the subject.

I must acknowledge the Royal Thai Navy for their funding and supports during my postgraduate research.

Lastly, I offer my regards and blessings to all the members of academic staff who supported in any respects during the completion of the project.

Author’s Declaration

I am aware of and understand the policy of the University of Glasgow regarding plagiarism and I certify that the work in this thesis is my own, except where indicated by referencing, and is in accordance with University and School guidance on good academic conduct.

……..

Tananop Piemsinlapakunchon

August 2019

Publications from this work

Journal Articles

No.	Description
1	Piemsinlapakunchon, T., and Paul, M. C., **Effects of content of hydrogen on the characteristics of co-flow laminar diffusion flame of hydrogen/nitrogen mixture in various flow conditions.** (International Journal of Hydrogen Energy, Volume 43, 2018, pp. 3015-3033)
2	Piemsinlapakunchon, T., and Paul, M. C., **Effects of fuel compositions on the heat generation and emission of syngas/producer gas laminar diffusion flame.** (International Journal of Hydrogen Energy, Volume 44 (33), 2019, pp. 18505-18516)

Proceeding

No.	Description
1	Piemsinlapakunchon, T., and Paul, M. C., **Characterization of Syngas Laminar Diffusion Flame with an Effect of its Varying Composition.** (Proceeding of World Congress on Engineering 2017 (WCE 2017), Vol II, Imperial College – London, UK, 5-7 July 2017, ISSN: 2078-0966).
2	Piemsinlapakunchon, T., and Paul, M. C., **Stability of buoyant laminar diffusion syngas flame: impacts of H2: CO.** (Digital Proceeding for 9th European Combustion Meeting 2019 (ECM 2019), Lisboa, Portugal, 14-17 April 2019)

Posters

No.	Description
1	Piemsinlapakunchon, T., and Paul, M. C., **Investigation of Laminar Diffusion Flame of Syngas.** (Poster Presentation on 29th edition of the Scottish Fluid Mechanics Meeting, Edinburgh, 20 May 2016)
2	Piemsinlapakunchon, T., and Paul, M. C., **Syngas Combustion Modelling.** (Poster was presented in All Energy Conference and Exhibition, Glasgow, 10-11 May 2017 and also in Innovation in Gasification and CHP Technology (IGATE), Glasgow, 23 May 2017)

Definitions/Abbreviations

Roman Symbol

A	Surface area of the control volume
A_f	Flame surface area
A_m	Pre-exponential factor
$C_{v,rot}$	Rotation contribution in thermal conductivity
$C_{v,tran}$	Translation contribution in thermal conductivity
$C_{v,vib}$	Vibration contribution in thermal conductivity
C_p	Specific heat at a constant pressure
d	Diameter of the fuel injector
D_i	Molecular diffusivity coefficient of species i
$D_{i,j}$	Binary diffusion coefficient between species i and j
$D_{i,t}$	Thermal diffusion coefficient for species i
E	Total energy
E_m	Activation energy
f	Mean reaction rate multiplier
g	Gravitational body force
H_f	Flame height
h	Enthalpy
$I_{b\lambda}$	Black body intensity
I_λ	Radiative intensity
$I_{pb\lambda}$	Particle black body intensity at particle temperature
J	Diffusive heat flux
k	Boltzmann constant ($1.3806503 \times 10^{-23}$ m^2-kg-s^{-2}-K^{-1})

$k_{a\lambda}$	Absorption coefficient
$k_{s\lambda}$	Scattering coefficient
$k_{pa\lambda}$	Particle absorption coefficient
$k_{ps\lambda}$	Particle scattering coefficient
L_f	Magnitude of oscillation
M	Molecular weight
$\dot{m}_f$	Mass flow rate
N	Number of species
p	Static pressure
Q	Total chemical heat release
Q	Thermal energy production rate
Q_f	Volume flow rate of fuel
$Q´$	Average heat flux
q	Energy flux
σ	Collision diameter
R	Production rate of species
R_{ef}	Reynolds number of fuel stream
r	Radial coordinate
S	Entropy, Stociometric ratio
S_b	Stefan-Boltzmann constant (5.67×10^{-8} W-m^{-2}K^4)
s_σ	distance in solid angle (σ) direction
T	Temperature
T_F	Temperature of fuel
T_f	Flame temperature
t	Time

u	Velocity
V	Cell volume
$\dot{v}$	Volume flow rate
v'	Stoichiometric coefficients of the reactants of chemical reaction
v''	Stoichiometric coefficients of the products of chemical reaction
X	Mole fraction
x	Axial coordinate
Y	Mass fraction
Y_s	Stoichiometry mixture fraction

Greek Symbol

β_m	Temperature exponent
ρ	Mixture density
μ	Dynamic viscosity
Ω	Collision integral
ε	Potential energy of attraction
λ_{con}	Thermal conductivity
α	Total absorptivity
∞	Ambient condition
$\emptyset$	Transport of a scalar property
σ	Solid angle
Γ	Diffusion coefficient
λ	Oscillation wavelength
φ	Under relaxation factor
ω	Angular velocity

ξ	Air/fuel density ratio

Subscript

ad	Adiabatic
avg	Average value
max	Maximum value
p	Constant pressure
x, r, i, j	Direction and species or phase
res	cell residence
$surr$	Surrounding
$total$	Total value
con	Conductivity
dil	Dilution

Superscript

c	Conduction
d	Diffusion

Abbreviations

BP	British Petroleum
CCN	Convective courant number
CFD	Computational fluid dynamics
CI	Compression ignition
DNS	Direct Numerical Simulation
DOM	Discrete Ordinate Method

ED	Eddy dissipation
EDC	Eddy dissipation concept
GT	Gas turbine
HHV	Higher heating value
IMF	International Monetary Fund
IEA	International Energy Agency
LES	Large Eddy Simulation
LFL	Lower flammability limit
LHV	Lower heating value
NO	Nitric oxide
ORC	Organic Rankine cycle
PM	Particulate matter
RANS	Reynolds-averaged Navier–Stokes
SI	Spark ignition
SLF	Steady laminar flamelets
SLPM	Standard litre per minute
TSG	Two stages gasifier
UFL	Upper flammability limit
UHC	Unburned hydrocarbons
WSGG	Weighted sum of gray gas model

Chapter 1 Introduction

Expansion of the global economy, which was assessed by the International Monetary Fund (IMF) as 3.7 % in 2017-2018 and predicted to be 3.5 % in 2018-2019, escalates the total global energy demand significantly [4]. According to the report of the International Energy Agency (IEA) [5], global energy consumption increased from 11,853 to 14,301 Mtoe between 2009 and 2018, as presented in Figure 1-1. This uptrend is expected to continue in the coming years according to the growth rate calculated each year. It is also noticed by the report of IEA that the energy demand during 2017-2018 was almost twice compared to the demand during 2009-2010.

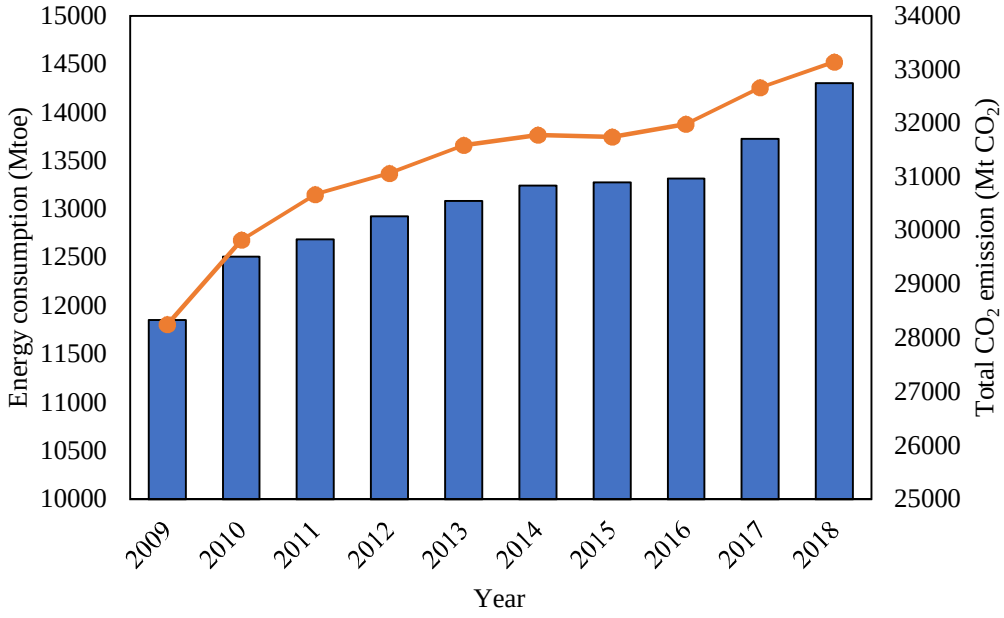

Figure 1-1 Global energy consumption and total CO_2 emission per year [5]

The demand for energy has been met by various sources (e.g. coal, oil, gas, nuclear, and renewable energy) at different portion, as shown in Figure 1-2 [5]. The percentage of contribution of energy source in 2010 is compared with one in 2018 in this figure. As seen, the primary global energy source is oil, followed by coal and natural gas. The contribution percentage of these sources is various in different years. However, it was evident that conventional fossil fuel is still a primary global energy source of the world. The total percentage of contribution of oil, coal and natural gas is approximately 80% of the global energy demand. Though the demand for oil reduced slightly from 36% in 2010 to 31% in 2018, the contribution of coal and natural gas rises by 3% and 2%, respectively. The report

of IEA [5] additionally pointed to the role of fossil fuel, which will remain the major energy source in the near future.

In contrast, fossil fuel is non-renewable, and the extensive use of this fuel causes concern in the sustainability of the global energy resource. According to the prediction based on the reserves-to-product (R/P) ratio of British Petroleum (BP) [6], the reserve amount of these fossil fuels show the sign of limitation which has the opposite trend compared to the global energy demand discussed above. It is expected that the reserve amount of oil, natural gas, and coal is capable of supporting the demand for approximately 51, 53, and 114 years, respectively.

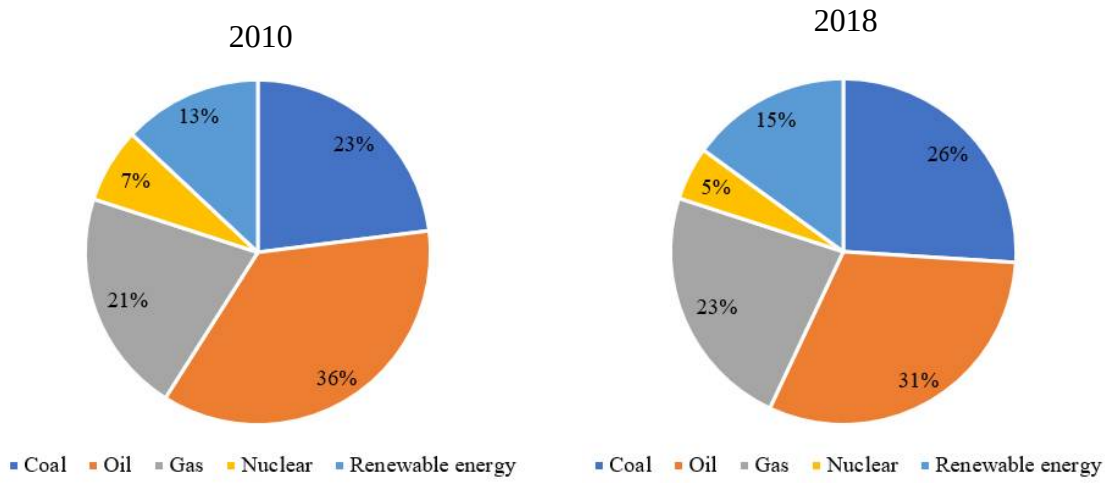

Figure 1-2 Energy demand by sources in 2010 and 2018 [5]

Furthermore, the scarcity is not only a concern for the utilisation of fossil fuel. Pollution and climate change are also other major global issues. The primary energy extraction process of fossil fuel is combustion which an inevitable side effect is pollutants such as soot, sulphur oxides (SO_x), nitrogen oxides (NO_x), unburned hydrocarbons (UHC), carbon dioxide (CO_2) and carbon monoxide (CO) [7]. The production rate and species of pollutant depend strongly on the type of fuel supplied into combustion. For instance, coal is the primary source of SO_x, while, generally, carbon fuel is the major source of CO_2. Research attention, therefore, has been paid on the reduction of CO_2 emission as it is an important heat-trapping (greenhouse) gas that plays a significant role in the climate change or global warming [8]. The emission of CO_2 has increased significantly in the last decade, as shown in Figure 1-1. This uptrend is in the same direction as the global energy consumption. Therefore, the fossil fuel (coal, oil and natural gas) has a massive contribution to the global CO_2 emission.

According to the analysis of the cause and impact of climate change, the phenomenon creates the never ended cycle that significantly raises the energy demand as well as the CO_2 emission. The change in the pattern of climate around the globe increases the utilisation of heating and cooling systems which provide human comfort [5]. A larger energy generation capacity is required to support this increasing demand. A higher emission rate of CO_2 is released from the energy generation process, especially one that relates to the combustion reaction. The situation in climate change is hence more severe, as reported in the data of IEA [5]. This report also expressed that the energy generation from coal combustion is the main cause of an increase in global temperature. It is responsible for over 0.3℃ of the 1℃ of global temperature escalation.

There are two significant challenges projected which are (i) finding of alternative and sustainable energy sources, and (ii) finding the method of reducing the pollution. An attempt to address these issues could be seen from the research and development of various renewable energy sources which produce less pollution and more sustainable. Typically, renewable energy is defined as an energy source apart from fossil fuel such as wind, solar, hydro, marine, geothermal energy and biomass or bioenergy. An overview of renewable energy sources is presented in Figure 1-3 [9]. The contribution of renewable energy to the total global energy demand rises slightly from 13 % in 2010 to 15 % in 2018, as presented in Figure 1-2. Majority of the renewable energy sources are used for generating the electricity [9]. The report of the international energy agency (IEA) reveals the growth rate in electricity generation for each type of renewable energy. The promising growth rate was found from solar photovoltaic, wind, and biomass, which respectively generated 31.2 %, 12.2 % and 7.4 % higher in 2018 than their production capability in 2017 [5].

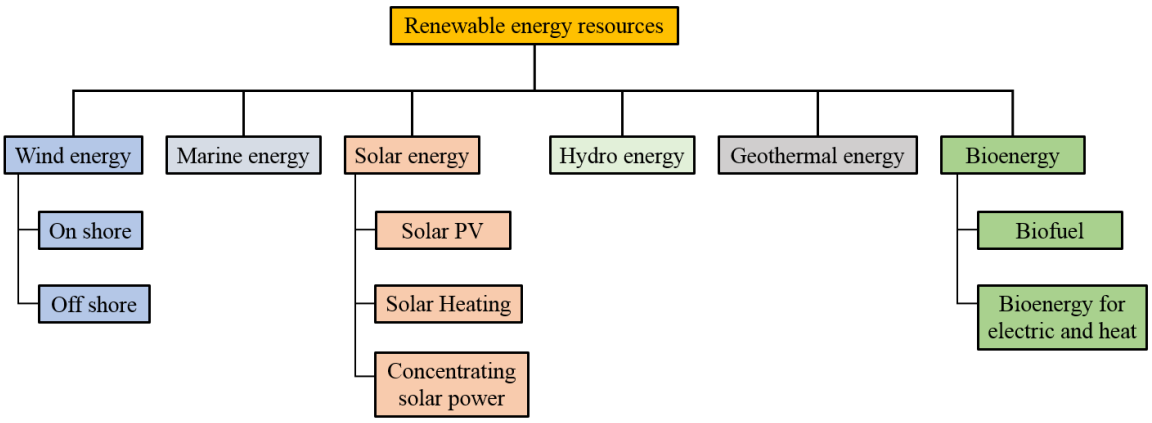

Figure 1-3 Overview of renewable energy sources [9]

However, it could be seen that the growth rate of the contribution of renewable energy is still insufficient to drive itself to be the primary global energy source. Geographical limitation and high upfront cost are major barriers for most types of renewable energy [9]. Different areas have different geography and natural resources (e.g. wind, solar, and tidal), and this causes constraint in the selection and utilisation of renewable energy. Further, natural resources are unpredictable; hence, the intermittency in energy production is another issue. Combining these drawbacks with the high upfront cost for the equipment and the energy storage system, the use of renewable energy might not be economically efficient and suitable for every part of the globe.

Unlike the other sources of renewable energy, the energy extraction from biomass does not have the geographical limitation and intermittency issue in the operation [9]. Combustion of biomass was the oldest and the first on-demand method of energy extraction with the purpose to make fire, cook, and produce heat. At present, this method stills the primary energy source in a variety of application for the production of heat and power. Biomass was the global primary energy source before the era of fossil fuel began in the mid-1800s and played a significant role in the reduction of oil consumption during the first oil crisis in 1970s. The resource of biomass is abundant and inexpensive. Additionally, organic and municipal solid wastes are also considered as an energy resource since the same method used for converting biomass to energy is also capable of transforming these wastes into energy [10]. The global waste is expected to rise from 2 billion tons in 2016 to 3.4 billion tons by 2050, according to the report of the World Bank [11]. Therefore, utilising biomass as an energy resource addresses not only the demand for energy but also the global waste issue. These benefits attract several researchers to develop energy conversion technology for biomass and waste.

On the other hand, the utilisation of biomass has two major drawbacks, which are air pollution and cost-effectiveness. Burning biomass produces air pollutants similar to those from fossil fuels. Koppmann et al. [12], Reid et al. [13], and Reid et al. [14] reviewed the emission and from biomass combustion. In China and the USA, the contribution of biomass burning is ~11.2-13% on the atmospheric particulate matter that has a diameter of fewer than 2.5 micrometres (PM 2.5) [15], [16]. The lower energy density of biomass fuels is another issue. This information refers to the larger storage and higher cost of transportation. It also potentially demands the intensive use of inputs (e.g. land, water, and crops) which have an opportunity cost. As a result, the price paid per unit of electricity generated could be higher than the other fuel types [17].

The technology has researched and developed for addressing the mentioned drawbacks. The biomass is converted to the clean energy fuel before combustion rather than directly burnt. Various methods are introduced for transforming the biomass to different end products as presented in Figure 1-4 [9], [10], [18]. The processes are pyrolysis, gasification and anaerobic digestion. These technologies are also compatible with the conversion from organic waste to energy. Each process provides different end products, e.g. fuel gases, hot-gas, and syngas/producer gas. Various applications (e.g. furnace, and internal combustion) could be used for extracting the energy from these end products which is in liquid or gas phase. The end products, which is also called 'biofuel', are allowed the transportation and storage in the better form than the original biomass. The development causes the biofuels an on-demand fuel that has the potential to play a significant role in the future energy scenarios [19].

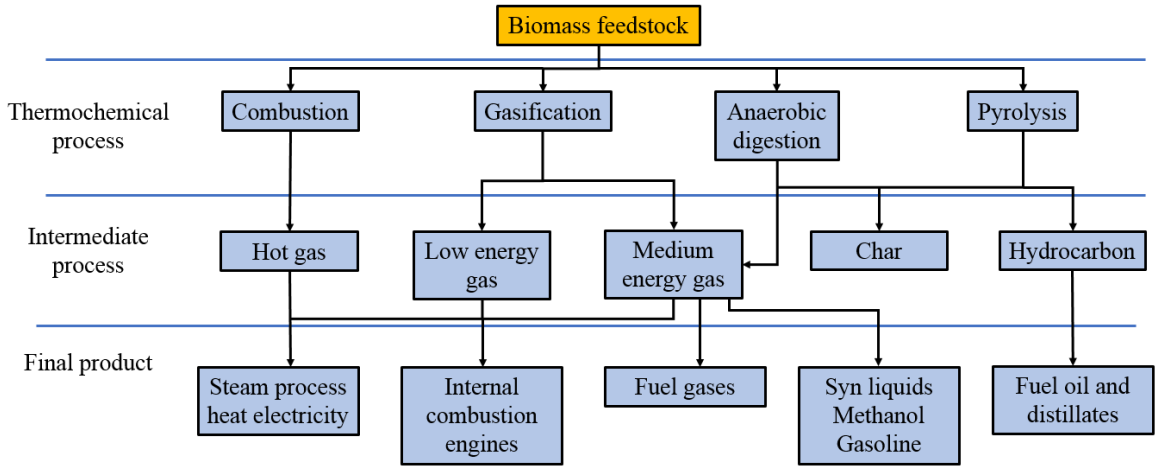

Figure 1-4 Biomass conversion process [9]

Syngas is one of the interesting options among the various biofuel end products. It is the fuel gas consisting of hydrogen (H_2), carbon monoxide (CO), methane (CH_4), carbon dioxide (CO_2), vapour (H_2O) and nitrogen (N_2) as primary species. The advantages of syngas are the flexibility in the production process and feedstocks. Gasification and pyrolysis are the main methods used for converting biomass to syngas [20]. Briefly, gasification is the thermochemical process that transforms various types of biomass feedstock in a low-level oxygen environment. The product of this process is syngas with various H_2:CO ratio. On the other hand, pyrolysis of biomass feedstocks undergoes thermal degradation under the oxygen-free environment [21].

As it is in the gas phase, syngas could be supplied to the combustion application (e.g. internal combustion engine, and furnace) similarly to the conventional gas fuel. However, the fuel composition of syngas contains not only single combustible species like conventional fuel. Based on Molino et al.[1], the syngas product from practical gasification and pyrolysis plants consist of H_2, CO, CH_4, CO_2 and N_2 as a primary component and H_2O, H_2S, NH_3, tar, and other traces species as a secondary component. The diversity in fuel composition of syngas causes the complex chemical reaction during the combustion [21], [22]. The higher number of species in fuel composition refers to the higher number of related chemical reactions. Also, the reaction pathways of each species in fuel composition could be different due to their various concentration percentages. The combustion characteristics and performance are hence strongly affected by the variety in fuel composition [23].

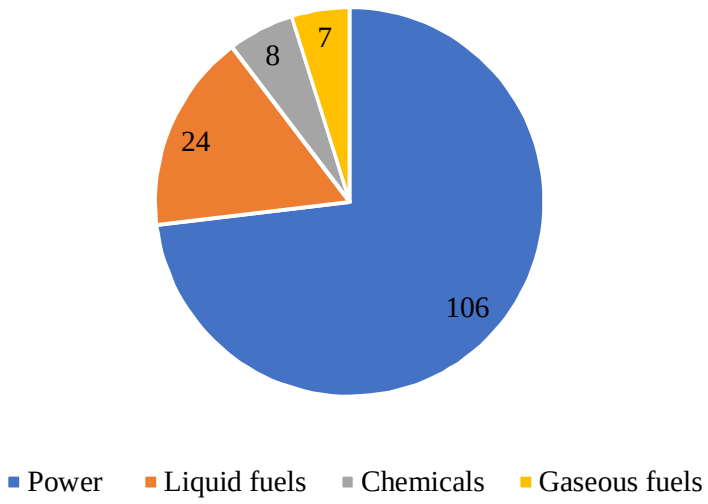

Figure 1-5 Number of biomass gasification plant by function [24]

An attempt to use syngas in the large scale for producing thermal power and electricity could be seen from the database of the International Energy Agency (IEA) Bioenergy Task 33E [24]. There are 141 biomass gasification plants, and 106 of them are used for power production which is capable of generating ~356 MW of electricity and ~185 MW of thermal power. The other plants produce liquid fuel (24 plants), gases fuel (7 plants), and chemical product (8 plants). The ratio of them is expressed through a pie chart in Figure 1-5. The analysis shows that the number of plants opened per year is high between 1985 and 2009, with the maximum number per year as 12 plants [24]. After that period, the number of plants opened per year is lower. The barriers preventing the selection of gasifier and pyrolysis as a power generation plant could be divided into economic and technical aspects. The capital

cost of the plant rose due to the recent termination of public funds, which were subsidised by the government for renewable energy production [1]. The complex combustion of syngas further leads to the complex operation of gasifier and pyrolysis plants [18]. Hence, the technology requires research and development to be mature and simple enough to attract a more substantial number of users.

As stated above, the development in syngas technology could be divided into two parts, which are the production process and the energy extraction of syngas. Both aspects require the microscopic understanding of the impact of each species in fuel composition on the combustion and flame characteristics. In detail, the essential topics which are beneficial for the development include flame temperature, dimension, heat generation, emission also the flame instability. This information points to the desirable and undesirable species. The desirable one is the species that encourages heat generation capability and produce a lower rate of pollution. Also, it provides with the guideline for improving the production technique of syngas and selecting the feedstocks which are capable of producing a higher concentration of a desirable species. On the other hand, the information is beneficial for the design of combustion application such as the size, geometry, and material of the combustion chamber and the fuel injector. Furthermore, it could be used for improving the operating condition; for instance, the effective combustion could be achieved by adjusting the proper fuel and oxidiser flow rate.

Consequently, this thesis focused on the impact of the diversity in syngas composition on combustion and flame characteristics. Computational fluid dynamics (CFD) is a selected method for simulating and studying the flame of syngas. This method takes into account the complex chemical reaction during the combustion of syngas. The capability of CFD in projecting the flow field as well as the flame appearance allows the analysis of syngas combustion and flame on the topics of the study mentioned previously in details.

1.1 Computational Fluid Dynamics (CFD)

Computational fluid dynamics (CFD) is the method of solving fluid dynamics and heat transfer complex problems. For combustion modelling, CFD predicts the reacting flow field by computing the numerical solution to the set of partial differential equations which govern the conservation of mass, momentum, and energy. The characteristics of the reacting flow are typically explained by the interaction of transport and chemical kinetics. The chemical

reactions describing the reaction pathway of species in fuel composition is required as well as the energy accounting for each exothermic and endothermic reactions. Also, each species has some finite characteristics times for their relevant reactions. The chemical kinetics is needed for defining the rate which the chemical reactions take place. As a result, the set of equations is highly coupled and non-linear. Finding the solution for the problem domain requires the discretisation process where the governing equations are transformed into a simpler algebraic form which could be numerically solved. The finite volume method plays a vital role in the discretisation of these equations that consequently provides the solution for the problem domain.

The combustion and flame modelling of syngas can be processed through CFD. The chemical kinetics mechanism prescribing the reaction pathway of each species in syngas composition is required for computing the reacting flow of this fuel. The flame of various types of burner and combustion chamber could be modelled based on their practical geometry and dimension. The sufficient level of mesh density and optimum time-step are necessary in order to obtain the converged solution from the simulation. The validation of the newly generated model is another important process. The generated CFD model should be able to initially formulate a similar result compared to the experiment result before using in a parametric study.

1.2 Purpose of the work

The objective of this thesis is the microscopic understanding of the impact of the diversity in fuel composition of syngas on the combustion and flame characteristics. The study focuses on the primary component in syngas composition, e.g. H_2, CO, CH_4, CO_2, and N_2. The investigation is processed under the following key objectives addressing.

1. Impact of the content of H_2 on flame characteristics
2. Analysis of heat generation and emission of various syngas composition
3. An occurrence and disappearance of the flame oscillation, and the side effect of this phenomenon

1.3 The importance of the research study

To encourage the utilisation of syngas, the development of the production process and the design of the combustion application are two major challenges. The detailed understanding of the role of each species on combustion and flame characteristics is necessary for addressing these challenges. The research works in this thesis will greatly provide the information in this area. This would potentially encourage the use of syngas and biomass, which are renewable and more sustainable than conventional fossil fuel.

1.4 Thesis outline

The structure of the thesis is presented below.

In Chapter 2, an overview of syngas composition and its variation as well as the research regarding the combustion characteristics of syngas are revised. The knowledge gap and the area of study requiring further research and development are pointed out.

In Chapter 3, the methodology of this thesis is presented. This includes the governing equation, the methods selected for defining the property of all components relating to the simulation of the reacting flow of syngas, and the solution procedure.

In Chapter 4, the role of species H_2, which is the primary species in syngas composition and also has a higher diffusive property than other species in syngas composition, is examined. The study specifically examines the impact of H_2 content ($\dot{v}_{H_2}$) defined as the volume flow rate of this species in the fuel stream. The aspects of flame characteristics considered in this study are the flame behaviour, flame characteristics, heat generation, and emission formation rate of NO_x. Also, the impact of the methods used for controlling the content of H_2 is examined. This includes an increase or decrease of velocity of fuel stream, and concentration percentage of H_2 (X_{H_2}) in fuel composition. As the study focuses only on species H_2, the fuel composition selected is the mixture of H_2 and N_2 at various ratio and 100% H_2. The CFD model is formulated based on the burner configuration of Toro et al. [2]. The validation process of this model is presented at an early stage of this chapter.

In Chapter 5, the stable flames of CH_4, H_2, and syngas having the variation in fuel composition are formulated by a modified CFD model created in Chapter 4. The dimension of the domain is extended to support the flame dimension of the studied fuel composition.

Comparing the simulation result obtained from flames formulated by different fuel compositions projects the impact of syngas primary component, e.g. H_2, CO, CH_4, CO_2, and N_2. The study investigates the role of these species individually on the generation and transfer of heat. The emission formation is also affected by the fuel composition. The analysis of this topic is carried out by perceiving that it is a price to pay for a certain amount of generated heat.

In Chapter 6, another CFD model based on the study of Darabkhani et al. [3] is generated to study the oscillating movement of syngas flame. The focus of the study here is the impact of syngas composition on the occurrence of flame oscillation (e.g. flickering and tip-cutting flames). A Kelvin-Helmholtz (K-H) type of instability is the main causes of this phenomenon. This type of instability is encouraged by an improper ratio between fuel and air rate supplied into combustion, and buoyancy force due to the gravity. An occurrence of flickering and tip-cutting flame would be affected directly by the diversity of syngas composition. This impact is studied by creating the K-H instability in syngas flame; for instance, increasing the fuel rate without enough support in air rate. The stable flame hence transforms into the unstable oscillating flame. The phenomenon occurred in the flames of different syngas compositions is observed. Then, the result is compared to project the impact of each species. The side effects of the flame oscillation, which are the fluctuation in heat generation and temperature of the flame, are also examined.

In Chapter 7, the CFD model and fuel composition of Chapter 6 are utilised; however, the topic of interest is altered to the disappearance of flame oscillation. Increasing the air rate reduces the impact of K-H instability. Thus, the magnitude of oscillation reduces, and the flame oscillation disappears once the flow rate of oxidiser is sufficient. The diversity in fuel composition affects this phenomenon, and this research topic is studied as well as the reduction of the fluctuation of heat generation of the flame.

In Chapter 8, the finding obtained from the study in the previous chapter is concluded. The recommendations based on the conclusion is given for future work.

Chapter 2 Literature review

An overview of the research works relating to the combustion and flame of syngas is presented in this chapter. The description of syngas and its varying composition is firstly presented, followed by the combustion application and the obstacles preventing the utilisation of syngas. Then, the recent studies relating to the impact of syngas composition on the combustion and flame characteristics are reviewed. The result of this process is the recent knowledge as well as the gap which demands further study to fulfil. The following sections are the related theory and the area of study and methods. Lastly, the discussion and conclusion are provided.

2.1 Syngas and its varying compositions

Syngas or producer gas defined as the fuel gas containing hydrogen (H_2) and carbon monoxide (CO) as the primary species is one of the promising options amid various types of alternative and renewable energy [25]. The strong point of this fuel is the flexibility in the production process and feedstock. Nevertheless, this advantage significantly affects the diversity in the fuel composition of product syngas/producer gas. Gasification and pyrolysis are two major production processes of syngas. The feedstocks of these processes are solid fuel, e.g. coal or biomass. The process which is incomplete combustion produces the mixture with approximately 40% combustible gases containing hydrogen (H_2), carbon monoxide (CO), and methane (CH_4). The remainder of the process is the non-combustible gases such as nitrogen (N_2), carbon dioxide (CO_2), water vapour (H_2O), ammonia (NH_3), Hydrogen sulphide (H_2S), tar, and other traces species. The species H_2, CO, CH_4, CO_2, and N_2 are the primary component of syngas/producer gas due to their concentration percentage. The property of syngas/producer gas is hence dominated by the concentration of these species [1].

The composition of syngas/producer gas produced from different gasification techniques (downdraft fixed-bed gasifier, fluidised bed gasifier, and two-stage gasifier) and feedstocks obtained from various sources are compared, as shown in Table 2-1. Analysing this information reveals the factors affecting the syngas composition which are feedstock, particle size, gas and feedstock supply rate, chemical reactor configurations, operating conditions, gasifying agent and catalyst, and gas residence time. According to the

concentration percentage of combustible species, H_2 (10.7-43.6%) and CO (6.32-33.2%) are the major fuel species in syngas, whereas CH_4 (2.7-13.4%) is the minor fuel species. The concentration ratio of H_2:CO ranges between 0.67 and 3. The non-combustible species could be the majority of syngas composition as seen from the total concentration of CO_2 and N_2. The range of percentage of N_2 is 2.3-56.87% while one of CO_2 is 5.15-32.35%. On the other hand, the analysis shows that the concentration percentage of combustible species could be higher if the proper production techniques and feedstocks are used. For instance, two stages gasifier (TSG) with air as an agent should be used for producing syngas from mixed plastic waste in the case that CH_4 is preferable.

Table 2-1 Composition of syngas from various types of biomass

Flame	**Gasifier type/agent**	**H_2 (%)**	**CO (%)**	**CH_4 (%)**	**CO_2 (%)**	**N_2 (%)**	**Heating value (MJ/Nm^3)**
Mixed plastic wastes [26]	TSG/Air	14.65	6.32	13.74	5.15	53.09	11.84
Corn straw [27]	DDG/ Air	10.7	16.2	2.7	18.1	54	4.3
Olive kernels [28]	FBG/ Air	23.98	14.26	3.75	19.42	38.59	6.54
Waste cooking oil [29]	FBG/ Air	14.75	17.58	3.55	8.65	53.95	5.9
Hazelnut shells [30]	DDG/ Air	13.51	14.62	1.95	12.38	56.87	4.32
Oil palm trunk [31]	DDG/Steam, O_2	35.52	26.82	7.85	23.24	4.72	10.04
Oil palm trunk [31]	DDG/Steam, air	19.53	13.99	3.5	18.36	43.3	5.13
Cotton stalk pellets [32]	TSG/O_2	36	38	2.8	21	2.3	9.62
Crushed almond shells [33]	FBG/Steam	43.6	33.2	11.5	11.7	-	13.02
Almond shells [34]	FBG/ Steam, O_2	33	32	11	27	5	11.7
Sewage sludge [35]	TSG/ Steam, O_2	28.02	19.3	8.5	32.35	6.66	11.71
Bamboo*	Air	19.7	21.0	-	11.9	45.9	5.22
Rubberwood*	Air	17.6	20.4	1.4	10.8	49.8	4.80
Wood pellets*	Air	21.7	20.8	2.2	12.6	42.7	5.79
Rice husk*	Air	19.8	22.6	2.0	13.1	42.5	5.57

*The fuel compositions of producer gas of bamboo, rubberwood, wood pellets, and rice husk are researched by [25], [36]–[39].

DDG = Downdraft fixed-bed gasifier.

FBG = Fluidized bed gasifier.

TSG = Two-stage gasifier

2.2 Compatible applications and the development challenges

The combustion applications, which could be fuelled by syngas/producer gas, are revised to project the progression and barrier in the utilisation of syngas as a primary fuel. Since syngas/producer gas is in the gas phase, it is expected to replace the role of natural gas in various combustion applications. The post-production process, e.g. cleaning and cooling, is recommended before supplying the product syngas to the combustion application. The cleaning process removes fine dust and particles, and tar while the cooling one raises the energy density of syngas. The details regarding the post-production process were reviewed in [7], [40]. It is noticed that the energy density of syngas/producer gas is significantly lower than that of natural gas. This could be explained by the high concentration percentage of non-combustible species in fuel composition, as discussed above [41].

Several pieces of research investigate the impact of utilising syngas in an internal combustion engine; both spark ignition (SI), and compression ignition (CI). Various aspects are focused such as engine's brake power, power de-rating, torque, efficiency, emissions, exhaust temperature and knock tendency [42]–[46]. The study of them also taken into account the impact of air/fuel, equivalence, and compression ratios. In the SI engine, the ignition timing is only part that is required an adjustment to be compatible with fuel property of syngas. The proper setup allows the engine to operate with syngas as a primary fuel. The result suggests that syngas is more suitable for the low-speed engine (1500-2500 rpm). On the other hand, fuelling CI engine with syngas demands the installation of several additional parts such as gas mixer, non-return valve, pressure regulator and gas carburettor. Moreover, the engine cannot be operated by combusting syngas/producer gas solely. A dual-fuel mode where syngas is the primary fuel and diesel is a secondary fuel is necessary. The reason is lower auto-ignition temperature of syngas than the temperature at the end of the compression stroke. The power de-rating of the engine fuelled with syngas is inevitable since syngas/producer gas has a lower energy density than the conventional gas fuel. SI engine has a higher power de-rating (40-50%) than CI engine (15-30%) even though the SI engine has less part to be modified [41].

The operation of a gas turbine (GT) engine requires the large exhaust gas flows to deliver the full power generation capacity and maintain combustion stability. The high-quality fuel is hence not necessary for the GT engine as long as the condition stated above is satisfied [47], [48]. Syngas/producer gas could be injected into the combustion chamber in either

single or dual mode. The high flow rate of exhaust gas, the stable combustion, and low combustion temperature are obtained from the utilisation of syngas/producer gas in GT engine, as reported in [49], [50]. Nonetheless, both injection mode (dual and single) cannot eliminate the power derating issue [51], [52]. As a result, Delattin et al. [53] suggested the redesign or the development of the GT engine combustion chamber, specifically for syngas/producer gas. The combustion condition should be designed to support the auto-ignition and flammability property of syngas/producer gas since the property of syngas is different from the conventional gas fuel. The proper configuration would consequently enhance the performance of syngas combustion. However, the concern is raised for the impact of diversity in the fuel composition of syngas, which could be a significant obstacle in the development [51].

Furnace and external combustion chamber, e.g. externally fired gas turbine [54], organic Rankine cycle (ORC) [55] are alternative options for the utilisation of syngas/producer gas. In this application, the consumption of syngas/producer gas is a major concern. The significantly lower energy density of syngas leads to a higher fuel consumption comparing to natural gas. To produce the same amount of thermal power, the volume of syngas supplied into the combustion could be seven times more than the consumption of natural gas [41]. However, the lower energy density of syngas has a benefit in terms of emission formation. The low-intensity thermal field causes a lower flame temperature and thermal NO_x formation rate. Also, the syngas composition contains the lower concentration of carbon and hydrocarbon fuel species (e.g. CO and CH_4) than the conventional fuel. Thus, the lower emission of carbon dioxide is another advantage.

As mentioned above, several issues are observed from an attempt to replace conventional gas fuel with syngas. Research and development are required for addressing these challenges and encouraging the use of syngas. The study is required in two main areas. The first one is the configuration of the combustion system, which needs the modification or redesign to support fuel and combustion property of syngas. The other area is the production and post-production process where the improvement of the fuel quality is the target.

According to the complex composition of syngas, analysing the property and performance of this gas fuel based only on the energy density might not be sufficient. The development in combustion system and production process requires the microscopic understanding of the impact of the diversity in syngas composition on combustion and flame characteristics. By

this information, the combustion and flame property of syngas can be predicted. The proper design of the combustion system for syngas is, hence, achievable. Also, the information is a guideline for improving the production process to provide a higher concentration of desirable species and a lower concentration of an undesirable species.

2.3 Diffusion flames of syngas

The gas turbine and external combustion chamber are an interesting option for extracting the energy from syngas since the high energy density fuel is not necessary. The combustion process in these applications frequently relates to the formulation of diffusion flame where the fuel and oxidiser are supplied to the combustion separately. The key literature and useful information benefiting the study of this flame type are presented as follows:

2.3.1 Property of combustible species

Table 2-2 The properties of hydrogen, carbon monoxide and methane at 300 K [7], [56]

Fuel Properties	**H_2**	**CO**	**CH_4**
Fuel LHV (MJ/Nm^{-3})	10.8	12.7	35.8
Air-Fuel Ratio	2.38	2.38	9.52
Flammability Limit φ (Lean/Rich)	0.01/74.2	0.34/6.8	0.54/1.69
Flame Speed at Stoichiometric combustion ($cm\text{-}s^{-1}$)	270	45	35
Adiabatic flame temperature (K)	2378	2384	2223
Density (kg/m^3)	0.0824	1.123	0.656
Dynamic viscosity (Pa-s)	0.89E-6	2.9E-5	1.88E-5
Thermal conductivity ($W\text{-}m^{-1}K^{-1}$)	0.191	0.023	0.030
Diffusion coefficient of gases in excess of air ($cm^2\text{-}s^{-1}$)	0.756	0.208	0.21
Specific heat ($kJ\text{-}kg^{-1}K^{-1}$)	14.31	1.040	2.226

Understanding the combustion property of combustible species H_2, CO, and CH_4 would be the first significant step. The property of these species was gathered by Pradhan et al. [7], as presented in Table 2-2. This information is a guideline for the analysis of syngas combustion and flame behaviour. CH_4 has the highest energy density as 35.8 MJ/Nm^3 of a lower heating value (LHV) followed by CO (12.7 MJ/Nm^3) and H_2 (10.8 MJ/Nm^3). The air-fuel ratio at the stoichiometric combustion condition is 2.38 for both H_2 and CO, which is lower than that of CH_4 (9.52). The flammability limit is the region of fuel-air ratio, where the flame is possible to propagate. This limit is affected by the direction of propagation, size and shape of the combustion chamber, temperature, pressure, and fuel property [57]. As a result, there are two types of the flammability limit, which are (i) lower flammability limit (LFL) and upper flammability limit (UFL). The value of LFL is the leanest fuel-limit while UFL is the richest fuel limit where the flame could propagate [58]–[60]. H_2 has the widest range between LFL and UFL (lowest LFL and highest UFL) as 0.01/74.2 followed by CO (0.34/6.80) and CH_4 (0.54/1.69). The flame speed is the rate that the flame propagates through unburned fuel-oxidant mixtures under laminar flow condition in the perpendicular direction to the expansion wave surfaces. The value of this parameter of H_2 (270 cm-s^{-1}) is the fastest one and is significantly higher than CO (45 cm-s^{-1}) and CH_4 (35 cm-s^{-1}), respectively. Lastly, the adiabatic flame temperature of CO (2384 K) is higher than H_2 (2378 K) and CH_4 (2223 K) [7].

The property of fluid such as density, viscosity, thermal conductivity, and diffusivity are obtained from Moran [61], presented in Table 2-2. H_2, CO and CH_4 have a lower density than air; thus, the buoyancy force due to the gravity affects the flow of these species at low velocity. The species H_2 has lower dynamic viscosity and thermal conductivity but more than two times higher in diffusivity than CO and CH_4. These properties affect the flow, chemical reaction, and energy generated directly. Also, H_2 has a significantly higher specific heat (more than 13 times than CO and 6 times than CH_4). This property affects the demand for heat to increase the temperature. Syngas which is the mixture of these combustible species (H_2, CO and CH_4) would have various fluid property depending on the concentration ratio between them. Nonetheless, the fluid property of non-combustible species e.g. CO_2 and N_2 are also significant since their concentration, in some case, dominates syngas composition, as presented in Table 2-1.

2.3.2 **Combustion property of syngas/producer gas**

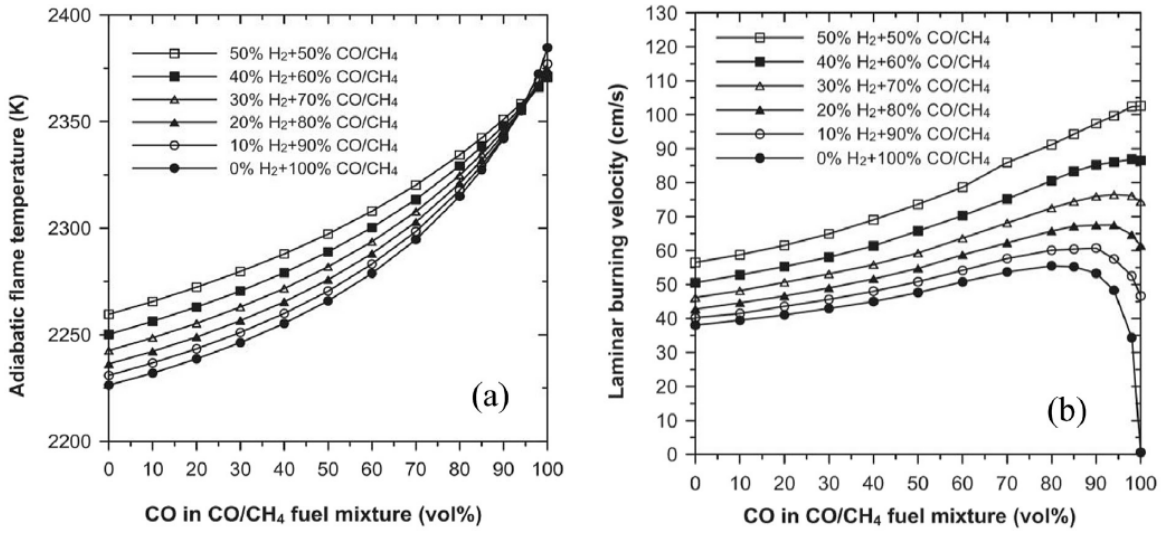

Figure 2-1 (a) Adiabatic flame temperature and (b) laminar burning velocity of H_2/CO/CH_4 flame at the stochiometric condition as a function of CO and H_2 condition [62]

The difference in property is observed from the comparison between H_2, CO, and CH_4. The property of syngas/producer gas, which is the mixture of these species, depends directly on the concentration of these species in fuel composition. The non-combustible species (CO_2 and N_2) in syngas composition would also play a significant role in the reduction of the combustion property of syngas. This could be seen from the lower heating value (LHV) of syngas from various sources presented in Table 2-1, which is between 5.9 and 13.02 MJ/Nm^3. The value of LHV is proportional to the concentration of H_2, CO, CH_4, CO_2 and N_2 in fuel composition. The other aspects of combustion property are also affected by the fuel composition of syngas/producer gas. The study of [7], [63] showed that the higher concentration of non-combustible species has an impact on the narrower range of flammability limit or less difference between UFL and LFL. In addition, the study of [62], [64]–[67] revealed the impact of the ratio between the combustible species on an increase of laminar flame speed and the adiabatic flame temperature which are two significant parameters of the combustion property, as shown in Figure 2-1. In addition, H_2, CO and CH_4 affect the adiabatic flame temperature at a different level. The stronger impact was found from the higher concentration of either CO or H_2 in syngas composition. The laminar burning velocity escalates at the higher concentration of H_2, whereas the opposite direction is obtained when the concentration of CO and CH_4 is higher; the impact of CO is stronger than CH_4 on this aspect.

2.3.3 **Impacts of fuel composition on diffusion flame**

The formation of diffusion flame relies on the burning rate, which is the result of diffusive mixing of fuel and oxidiser stream brought together in proper proportions for the reaction [68]. The high-temperature region is hence at the position where the fuel and oxidiser streams are encountered. The surface of the flame called 'flame-front' or 'stochiometric contour' is the boundary created by the number of positions on the high-temperature region where the stoichiometric combustion is achieved. The flame-front represents the appearance of the flame (shape and dimension). Thus, the appearance and dynamics of the flame rely strongly on the flow of fuel and oxidiser stream and their combustion reaction [69]. On the other hand, the temperature at each position of the flame relies on the heat from an exothermic chemical reaction, and fluid property (e.g. diffusivity, conductivity, and specific heat) according to the energy transport equation which will be presented in detail in the next chapter. The flow rate and composition of fuel and oxidizer injected into combustion are hence significant.

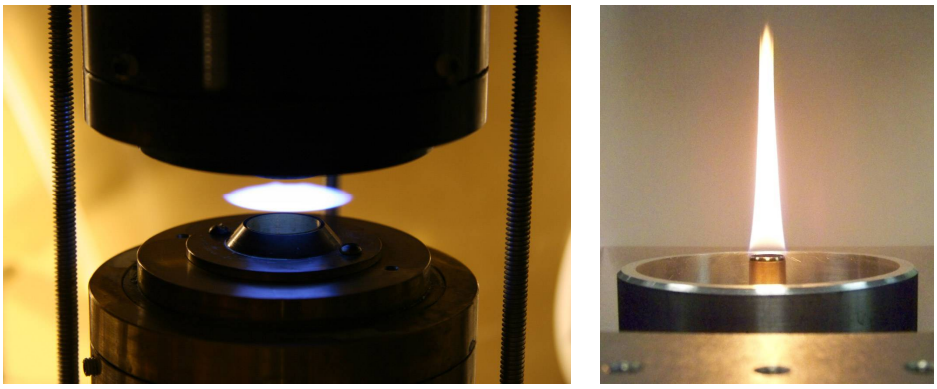

(a) (b)

Figure 2-2 the appearance of the burner of diffusion flame (a) Counter-flow burner [70], and (b) Co-flow burner [71]

Two types of burner configuration frequently selected in the study of diffusion flame are the counter-flow and co-flow burner. The former one refers to the burner which the fuel and oxidiser streams are injected to the combustion in the opposite direction, as shown in Figure 2-2a. The details and principal of the counter-flow diffusion flame were presented in Ref [72], [73]. This burner type is suitable for a fundamental study of laminar diffusion flame characteristics such as (i) the kinetic and characteristics of the high temperature flame, (ii) the reaction rates for the combination of fuel and oxidiser, (iii) dilution limits of diffusion flames, and (iv) the properties of a flame in an electric field [73], [74]. On the other hand,

the fuel and oxidiser are injected in parallel in the same direction to the combustion for the co-flow burner, as shown in Figure 2-2b. The typical configuration consists of the axis fuel injector that is surrounded by the oxidiser injector. The combustion could be triggered by the external ignitor or the heat of fuel or oxidiser stream. In some cases, the pilot injector is installed to provide a high-temperature stream of fuel or air [75] for the ignition. The co-flow burner is the conventional configuration which could be found in several practical combustion systems. The flow regime of air and fuel injected to the combustion can be laminar or turbulent. The benefit of utilising this burner in the study is the projection of flame shape, dimension, and structure.

The recent experimental and numerical results obtained from both co-flow and counter-flow burners are analysed for the impact of each species in syngas composition on combustion property and diffusion flame characteristics. The concentration of two major combustible species (H_2 and CO) plays a significant role in an increase in flame temperature or flame maximum temperature. The result obtained from the counter-flow burner shows that the effect of H_2 is stronger than CO on this aspect [74], [76], [77]. The effect of H_2 and CO on the temperature of laminar and turbulent co-flow flames are different. The impact of H_2 and CO are comparable and H_2:CO ratio has a minor impact on the flame temperature of turbulent diffusion co-flow flame [78]. The effect of H_2 is stronger than CO on an escalation of laminar diffusion flame temperature, and this result is in the same direction as the counter-flow flame [79]. The impact of H_2 and CO on the diffusion flame temperature of syngas/producer gas is not in the same direction as their impact on adiabatic flame temperature, where CO is expected to be slightly stronger than H_2.

CH_4 has a lower adiabatic flame temperature than the other two combustible species. Thus, the addition of CH_4 to fuel composition unsurprisingly results in the lower diffusion flame temperature [80]. Diluting syngas/producer gas with the non-combustible species (CO_2, N_2, and H_2O) reduces the concentration of combustible species, which consequently leads to the lower flame temperature [74], [80], [81]. The interesting finding is noticed as the level of impact of H_2O, CO_2, and N_2 are different. The strongest level among the non-combustible species is found from H_2O followed by CO_2, and N_2. These different levels of impact emphasise the effect of non-combustible species on the combustion and flame of syngas/producer gas, which could not be neglected. The results of Ref [74], [80], [81] were in the same direction, although the different burner configurations are utilised.

The utilisation of co-flow burner configuration allows the projection of the diffusion flame dimension. In laminar co-flow flame, increasing concentration of H_2 while reducing the concentration of N_2 in syngas composition results in the longer and wider flame dimension [79]. The impact of CH_4, CO_2, and N_2 on flame length are in the same direction as a higher dilution ratio of these species in syngas composition causes the longer flame. CH_4 plays a stronger role than CO_2 and N_2 in this case, and it also causes the wider flame at the higher dilution ratio [80]. Conversely, the narrower flame is observed from the addition of CO_2 and N_2. The flame dimension is found to be shorter when the concentration percentage of H_2O replaces N_2 in syngas composition. The opposite direction is obtained when the same action is processed with CO_2 rather than H_2O [81]. For turbulent co-flow flame, the higher H_2:CO ratio leads to the thicker flame [82]. At the same Reynolds number of fuel stream (R_{ef}), the flame of the same syngas composition is longer when the diameter of the fuel injector is larger [23].

The study of emission formation from syngas combustion typically focuses on the production rate of Nitric oxide (NO). Both types of burner configuration could be used for studying this topic. The results obtained from Ref [80], [83], [84] were in the same direction even though different types of the burner and flow regime of fuel stream were used in their works. A higher concentration of H_2 in fuel composition increases the flame temperature and encourage the thermal NO formation. Diluting CH_4 into syngas composition promotes NO emission rate while adding either CO_2, H_2O or N_2 to syngas composition decreases the production rate of NO since the flame temperature reduces. Additionally, the addition of H_2O to syngas composition is more effective for the reduction of NO formation than the other non-combustible species since the impact of H_2O on the reduction of flame temperature is stronger than the other diluted species.

Instability of syngas diffusion flame is another area that has been investigated in several research papers. The flammability and extinction limit were studied by [77], [85] with the counter-flow burner. Fuel composition, strain rate, and operation condition play a vital role in these aspects. The analysis of flammability and extinction limit might need to be processed case by case according to the role of these factors. Regarding the co-flow burner configuration, the lift-off and blowout phenomena of syngas diffusion flame were examined in Ref [86]. It is found that the phenomena occur when a sufficient concentration percentage of N_2 is diluted into syngas composition. This critical concentration of N_2 is specific for each H_2:CO concentration ratio. Nonetheless, the impact of H_2:CO on these phenomena is

insignificant when the concentration percentage of H_2 is higher than 30%. The effect of diluting H_2O, CO_2, and N_2 on syngas flame stability was studied by Mu et al. [87]. The flame of syngas mixed with H_2O is more stable than one added with N_2 and CO_2, respectively.

2.4 Knowledge gap

The literature survey provides the challenges in the development of syngas combustion system and production process as well as the recent understanding of syngas combustion and flame. The impact of species in syngas composition is studied extensively in several works. Nevertheless, there is still a knowledge gap identified in various aspects as follow:

The first one is the impact of H_2 content on syngas diffusion flame characteristics. The H_2 content, in this term, refers to the volume flow rate of H_2 supplied into combustion. Syngas is a mixture of several species, and the content of H_2 in fuel stream depends on fuel rate and concentration of H_2 in fuel composition. Increasing either of these parameters escalates the content of H_2 in the fuel stream. Research attention of [2], [78], [79] were paid on either the effect of fuel flow rate or the concentration of fuel species but not on the content of H_2. The study of the impact of H_2 content could be achieved by combining the study of the impact of fuel flow rate or concentration of fuel species presented in those papers together.

Secondly, the effect of a variety in syngas fuel composition on the generation and transfer of heat from diffusion flame remains unknown. The recent study of the impact of syngas composition mostly focuses on the other aspects, as presented in the previous section. The analysis of heat generation capability formulated from the flame of different fuel composition is necessary since it could reveal a desirable and undesirable species in syngas composition. The heat generation capability of the flame is also necessary for the analysis of the production rate of emission species (CO_2 and NO_x). Both aspects should be studied together to prevent any misunderstanding information about the role of each species in syngas composition. For instance, the species that encourages heat generation capability and promotes the production rate of emission might be categorised as an undesirable species if only the emission rate is considered. The alternative method of the analysis, which considers both the heat generation capability and emission formation together, is hence required. The emission formation of CO_2 and NO_x should be perceived as the price to pay for a certain amount of heat.

Thirdly, the instability of co-flow diffusion flame could occur in different schemes apart from lift-off and blowout phenomena. In a laminar co-flow diffusion flame, a flame intrinsic instability called flame oscillation is the area which has not been investigated for the flame of syngas/producer gas. The flickering and tip-cutting flames which are two types of oscillating flame are focused. These phenomena occur due to the interaction between the flame and the vortices both inside and surrounding the flame. They are triggered when the velocity difference across the interface between the two fluids is sufficient. The flame is non-lifted, and the flame length extends upward and downward for the flickering flame. The tip-cutting flame is also non-lifted, and its length expands upward until the tip cut at the flame body occurs causing the flame length reduces. The nature of these phenomena is typically periodic, regular and reproducible. This type of instability is also known as Kelvin–Helmholtz and could occur in both premixed and non-premixed flame. Two types of oscillating flame called 'flickering and tip-cutting flames' were studied in recent works by Ref [3], [88]–[91] where the fuel is methane (CH_4), propane (C_3H_8), or the mixture of both species (CH_4/C_8H_8). The major factors affecting these phenomena are the fuel and oxidiser rates, and combustion conditions, e.g. the gravitational force, and pressure. The diversity in the fuel composition of syngas is expected to play a significant role in the flame oscillation phenomenon. The study of the effect of syngas composition on an occurrence of these phenomena is investigated in this work.

Lastly, the impact of K-H instability could be reduced by increasing the co-flow air rate. This action will reduce the difference of velocity at the shear layer and push the vortices outside the visible flame. The magnitude of oscillation hence reduces and the flame oscillation disappears [88], [90]. The diversity in fuel composition plays a significant role in the magnitude of flame oscillation; therefore, it would affect the reduction of this parameter and the disappearance of flame oscillation when the co-flow air rate increases. This topic is lastly examined in this work.

2.5 Theory

Understanding the theory is the first step for fulfilling the knowledge gap. The related theory is reviewed in this section where the attention is paid on the characteristics of the laminar co-flow diffusion flame (e.g. flame temperature, flame length, and flame oscillation). The stable one has a clear shape and dimension, and the length could be estimated by several methods. The classical method was proposed by Burke and Schumann [92]. However, there

are several assumptions applied. Firstly, the velocity of fuel stream has single characteristics (only a vertical direction of the velocity is considered). Secondly, the impact of the buoyancy force is neglected. Lastly, the ratio between momentum and mass diffusivity or Schmidt number (Sc) is unity. This theory provides a reasonable agreement result with the circular pot burner. Roper [93] recognized that the buoyancy force could encourage the diffusion rate and narrows the flame. The theory of Burke and Schumann [92] was then developed by allowing the characteristics velocity to vary with the radial distance and taking into account the impact of buoyancy force. The analytical solution of this work was verified by the experiment in [94], [95]. For the circular pot burner, the length of the flame can be computed as

$$H_f = \frac{Q_f(T_\infty/T_F)}{4\pi D_\infty ln(1+1/S)}\left(\frac{T_\infty}{T_f}\right)^{0.67} \quad (1)$$

where D_∞ is mean diffusion coefficient evaluated at the oxidiser temperature, Q_f is volume flow rate of fuel stream, T_∞ is an oxidiser temperature, T_F is fuel temperature, T_f is flame temperature, and S is the molecular stoichiometric ratio which could be computed as follow:

$$S = \left(\frac{moles\ oxidiser\ fluid}{moles\ nozzle\ fuel}\right)_{stochiometric} \quad (2)$$

When the fuel gas is diluted with the inert gas, the flame length is reduced due to an influence of the molecular stochiometric (S). For the hydrocarbon fuel, the value of S when it is diluted by inert gas could be computed as

$$S = \frac{x + y/4}{\left(\frac{1}{1-X_{dil}}\right)X_{O_2}} \quad (3)$$

The formula presented above (equation (1)) assumes that the density is constant and suitable for the combustion that the oxidizer is excessive. A method for computing the flame length for the variable-density case was introduced by Fay [96]. The buoyancy force was again neglected to simplify the axial momentum equation. Also, the ratio between mass, momentum and thermal diffusivity is assumed to be unity. The solution of Fay [96] is presented below

$$H_{f-ave} = \frac{3}{8\pi}\frac{1}{Y_{f,sto}}\frac{\dot{m}_f}{\mu_{ref}}\frac{\rho_\infty}{\rho_{ref}}\frac{1}{I\left(\rho_\infty/\rho_{ref}\right)} \quad (4)$$

where $\dot{m}_f$ is mass flow rate of fuel stream, μ_{ref} is a dynamic viscosity at the reference temperature, ρ_∞ is a density of ambient air, and the numerical solution of term $I\left(\rho_\infty/\rho_{ref}\right)$ is provided in Fay [96].

When the flame is unstable and oscillates, the length is computed as the average flame length (H_{f-ave}). The dimensionless parameter can be used for calculating the average value as

$$\frac{H_f}{d} = 0.58Re^{0.667}Fr^{0.089} \quad (5)$$

where d is fuel nozzle diameter, Re is Reynolds number, and Fr is Froude number. The value of Re and Fr are defined below

$$Re = \frac{\rho u_f d}{\mu} \quad (6)$$

$$Fr = \frac{u_f}{\sqrt{gd}} \quad (7)$$

where ρ is fuel density, u_f is fuel velocity, g is gravity, and μ is dynamics viscosity.

The formula presented in equation (5) was presented by Sato et al. [91] and it is suitable for the buoyant dominated laminar diffusion flame with the range of Reynolds number between 5 and 570, ($5 \leq Re \leq 570$), and Froude number between 4.2E-4 and 5.3E3, ($4.2 \times 10^{-4} \leq Re \leq 5.3 \times 10^3$). However, the formular does not consider the combustion condition as the study focused on single fuel speceis. The diversity in fuel composition affects only the change of Re.

The temperature of the flame can be predicted through the chemical reaction at the stochiometric and adiabatic conditions. This flame temperature is called ‘adiabatic flame temperature’ which is the maximum temperature that can be achieved for given reactants. By utilising the first law of thermodynamics and balancing the energy in and out, the adiabatic flame temperature could be computed from

$$\sum H_{products}(T_i, p) = \sum n_i \left[\Delta H^0_{reactant,i} + C_{p,i}(T_{ad} - T_{ref})\right] \quad (8)$$

where H is enthalpy, n_i is a number of moles of reactant species i obtained from the chemical reaction, T_{ad} and T_{ref} are adiabatic and reference temperature, respectively, and C_p is the specific heat at constant pressure. Further, this method also provides the heat released from the combustion.

The flickering and tip-cutting flames are types of flame oscillating phenomenon. This phenomenon occurs due to the buoyancy force which causes the flame front regularly oscillates at the low frequency (10 – 20 Hz). According to ref [97]–[101], the result obtained from the numerical study shown that the shear layer of burnt gas had an inflexional profile of velocity resulting in the Kelvin-Helmholtz (K-H) type of instability. An occurrence of K-H instability can be assessed through Richardson number (Ri) where the layer is unstable at the value less than 0.25. This parameter is the ratio between the buoyancy term and shear flow term as presented below

$$R_i = \frac{Gr}{Re^2} \quad (9)$$

where Gr is the Grashof number which represents the ratio of the buoyancy to the viscous force acting on a fluid. The value of this parameter could be defined as

$$Gr = \frac{g\beta(T_s - T_{ref})d^3}{\nu^2} \quad (10)$$

where T_s is surface temperature, β is the coefficient of thermal expansion ($1/T_s$ for an ideal gas), and ν is kinematic viscosity.

As seen, the temperature, gravity, viscosity, velocity of the fluid, and fuel inlet diameter could encourage the occurrence of K-H instability. Once this phenomenon occurs, the mixing of fuel and oxidizer at the shear layer between both streams is directly affected resulting in the oscillating flame. The structure and the movement of this flame type were studied extensively in Ref [98], [99], [102]. The flickering motion of the flame is formed through the coupling of the fluttering with the movement of vortex rings. It is also found that the flickering frequency relies weakly on the type of fuel, fuel nozzle size, and velocity of fuel and co-flow air. Ambient pressure and gravity play a significant role in the flickering

frequency. The relationship between the frequency (F) and the gravity is $F \sim g^{2/3}$ while the relationship between F and ambient pressure is $F \sim P^{1/3}$ [103]. In other words, the weak gravity and pressure field reduce the velocity gradient on the shear layer of the jet resulting in the lower level of impact of K-H instability and magnitude of flame oscillation. The flickering frequency could also be defined through the dimensionless parameter such as Froude number (F_r) and Strouhal number (S_t). Sato et al. [91] and Arai et al. [104] expressed the relation between the frequency and these dimensionless parameters are presented as

$$S_t \propto F_r^{-0.57} \tag{11}$$

where

$$S_t = \frac{Fd}{u_f} \tag{12}$$

When the co-flow air is supplied into combustion, the difference of the velocity at the shear layer is lower, and the impact of K-H instability is lower. The flickering frequency is higher as the flame is more stable. In this case, the flickering frequency could be estimated by the formula introduced by Darabkhani et al. [88] as

$$F = 0.33a + 11 \tag{13}$$

where a is a co-flow air flow rate in the unit of 'standard litre per minute (SLPM).

According to equation (1) - (5), flame length depends on several variables such as fuel rate, density, viscosity, stoichiometric ratio, the concentration of the inert species, gravity, and diffusivity. Most of these variables are affected directly by the variety of syngas composition. Thus, the difference in flame length is expected from the diffusion flame of different compositions. For the fuel rate, the equations presented above clearly express the direct proportion relation between this parameter and flame length; the higher fuel rate supplied would result in the longer flame. However, this condition is valid when the fuel stream is in laminar flow regime. The higher velocity of fuel may push the flow regime of fuel to turbulent where the mentioned theory cannot be applied.

For syngas flame, the theory of flame height presented in equations (1) could be used for explaining the role of CH_4 on flame length mentioned in the previous section. The molecular

stochiometric ratio of CH_4 is more than 3 times higher than H_2 and CO, and this causes the significantly longer flame length when it is diluted into syngas. For the addition of CO_2, and N_2, the result obtained was not in the same direction as the theory (equation (1) - (3)) where the higher inert gas in fuel composition was expected to reduce the flame length.

As stated above, the adiabatic flame temperature only provides the upper limit of the flame temperature of the reactant. The actual combustion also depends on other factors e.g. diffusion, and incomplete combustion. Therefore, the flame temperature of the diffusion flame is expected to be lower than its adiabatic flame temperature. Further, the fluid interaction due to K-H instability can affect the mixing of fuel and oxidizer resulting in the lower flam temperature.

The flame oscillation phenomenon was extensively studied in various aspects as mentioned above. However, most works focused on the single or mixture of hydrocarbon fuel species. The diversity in fuel composition of syngas could affect the phenomenon differently. Firstly, the different density of various syngas composition leads to the different level of impact of buoyancy force. Secondly, a significantly higher diffusive property and burning velocity of H_2 which is a major species in syngas composition than fuel species may affect the shear layer of the burnt gas. As a result, the flickering frequency, average flame length and the movement of the oscillating flame obtained from the flame of different syngas compositions would be different.

2.6 Combustion modelling by CFD

CFD is one of the effective techniques for studying combustion and flame. It is capable of simulating the combustion and flame of the complex combustion system such as gas turbine, burner, and internal combustion engine [105]–[107]. Regarding the diffusion flame of syngas, this method was utilised in Ref [23], [78]–[83] for examining the turbulent and laminar co-flow diffusion flame. The CFD models generated in these papers are capable of formulating the flame with the similar result comparing to one obtained from the experiment. However, the proper selection of numerical methods for computing the fluid flow, chemical reaction, materials property, and heat transfer is needed as well as the validation of the newly generated model.

Combustion modelling by CFD is a proper method for fulfilling the knowledge gap mentioned above. Once the CFD model is validated, it could be used for formulating the flame of various syngas composition with a reliable result. The contour plot of temperature, velocity, and species allows the analysis of flame characteristics in detail. Furthermore, the methodology and result of the published papers relating to the combustion modelling of co-flow diffusion flame of gas fuel having H_2 as a primary fuel species could be used as a guideline and reference for model formulation and validation processes.

Regarding combustion modelling by CFD, various techniques are available for the modelling of combustion and flame. Direct Numerical Simulation (DNS), Large Eddy Simulation (LES), and Reynolds-averaged Navier–Stokes (RANS) were selected in Ref [23], [78], [82] for simulating the turbulent syngas co-flow flame. The combustion models such as the Eddy dissipation (ED) the Eddy dissipation concept (EDC) and steady laminar flamelets (SLF) model were compared in Ref [23]. The result obtained from the EDC model supplied with the detailed chemical reaction mechanism is closer to the experimental result; however, it is computationally costly. For the laminar co-flow flame, DNS is the standard approach, and the combustion is typically computed based on the chemical reaction mechanism supplied to the model, as seen in Ref [2], [79], [108]. Apart from the combustion model, the accuracy of the simulation results also relies on the method used for defining the species property, e.g. viscosity, thermal conductivity, diffusivity and specific heat. Also, the thermal radiation and diffusion could be considered in the model to provide more detail on the analysis of the flame.

The simulation of the reacting flow requires the reaction pathway for each species in fuel composition. The chemical reaction mechanism explaining syngas/producer gas combustion has been developed and introduced in several research works. The size of the mechanism depends on the number of species and chemical reactions related. A larger reaction mechanism provides a higher level of the details of the formation of species; however, it requires a more expensive computational cost. As several reaction mechanisms are available, selecting a proper chemical reaction mechanism is significant for combustion modelling. The proper one should contain the reaction pathway of all species in syngas composition and has a suitable size for the computational ability.

Various reaction mechanisms being capable of predicting syngas/producer gas combustion were compared by Fischer and Jiang [109] and Olm et al. [110] to find the most suitable one.

All compared reaction mechanisms predicted the ignition delay time and flame velocity in the same direction as the experimental data with a different level of accuracy. A similar approach can apply for finding the most suitable mechanism for the modelling of the syngas diffusion flame. This can be processed by supplying different reaction mechanisms to the CFD model, then comparing the result obtained from them based on the experimental result of the reference combustor.

Table 2-3 Selected chemical reaction mechanisms

Mechanisms	Consist of					NOx emission	Number of species/reactions
	H_2	CO	CH_4	CO_2	N_2		
GRI3.0 [111]	/	/	/	/	/	/	53/325
DRM22 [112]	/	/	/	/	/	-	22/104
Yetter et al. [113]	/	/	-	/	/	-	13/28
Davis et al. [114]	/	/	-	/	/	-	14/30
Lu and Law [115]	/	/	/	/	/	/	30/184
Sankaran et al. [116]	/	/	/	/	/	-	17/73

Consequently, chemical reaction mechanisms from various sources are revised, and six of them are selected for further analysis. These are GRI3.0 [111], DRM22 [112], Yetter et al [113], Davis et al [114], Lu and Law [115], and Sankaran et al [116]. The comparison in terms of the number of species and chemical reaction is presented in Table 2-3. The largest mechanism is GRI3.0 [111], which contains 53 species and 325 reactions, whereas the smallest one is Yetter et al. [113], which consists of 13 species and 28 reactions. Apart from Yetter et al. [113] and Davis et al. [114], the other mechanisms are capable of computing the reaction pathway of H_2, CO, CH_4, CO_2, and N_2. The reaction mechanisms of Yetter et al. [113] and Davis et al. [114] do not consist of the reaction pathway of CH_4. The GRI3.0 [111] mechanism was developed to provide a detailed step by step chemical reaction. The Lu and Law [115] mechanism (30 species/184 reactions) and Sankaran et al. [116] mechanism (17 species/73 reactions) were researched for studying methane/air combustion. DRM22 [112] (22 species/104 reactions) is the reduced reaction mechanism of GRI1.2 [117] to have the smallest number of variables but still a detailed mechanism. Lastly, Yetter et al. [113] and Davis et al. [114] mechanisms are different from the other selected mechanisms since both were designed specifically for the combustion of H_2 and CO. Among them, only GRI3.0

[111] and Lu and Law [115] consider the emission formation of NO_x (both thermal and prompt). All selected reaction mechanisms presented above are compatible with computational fluid dynamics (CFD). The reaction pathway of them can be supplied into the CFD model for simulating the reacting flow of syngas/producer gas, including diffusion flame. Comparing the flame formulated by CFD based on these mechanisms with the reference result obtained from the experiment would reveal the most suitable one.

2.7 Discussion

The development challenge needs to be addressed in order to encourage the utilisation of syngas/producer gas as a mainstream energy source. Fulfilling the knowledge gap is the pathway to this main objective. CFD is a proper technique for this purpose due to its advantages in various aspects. The classical co-flow laminar diffusion flame (Burke–Schumann flame [92]) is a better option than the turbulent one. The stable laminar flame has clear shape and dimension while the unstable one (e.g. oscillating flame) has the explicit pattern of movement. This allows the study of the impact of the variety in syngas composition on various aspects e.g. flame dimension, temperature, chemical heat release, emission formation, and flame oscillation. Also, less complexity in flow regime allows the computational power to be used for computing the chemical reactions rather than the complicated fluid interaction. Thus, the larger reaction mechanism with a higher number of related species and reactions could be supplied to the CFD model. This method also provides more in-depth detail in the reaction pathway, especially the heat released from each step of an exothermic reaction. The studies of [2], [3], [88], [108] are useful references and guideline for the simulation of stable and unstable oscillating laminar co-flow flame. These research works provide the burner geometry as well as an experimental and CFD result which could be used in the validation stage for assessing the reliability of the newly generated CFD model. The model is ready to be used for the formulation of syngas flame once the result obtained in the validation stage is satisfied.

2.8 Conclusion

An overview of the key literature is presented in this chapter. Understanding the impact of diversity in syngas composition on combustion and flame characteristics could guide the development of the syngas production process and its combustion application. The review points to the gap in the knowledge of syngas/producer gas diffusion flame. The areas which

are required research to fulfil are pointed out as (i) the effect of content of H_2 in fuel stream on flame characteristics, (ii) the analysis of heat generation capability of various syngas composition, (iii) the impact of syngas composition on an occurrence of unstable oscillating flame, and (iv) the the impact of syngas composition on the disappearance of flame oscillation. Finally, the modelling of stable and unstable laminar co-flow diffusion flame by CFD is purposed as a study technique.

Chapter 3 Methodology

The fuel composition of syngas/producer gas contains not only single species like a conventional fossil fuel but also multiple species (both combustible and non-combustible species) at the various possible concentration ratio. Computational fluid dynamic (CFD) is selected as a method for studying the stable and unstable laminar diffusion flames of this fuel. This method has flexibility in the parametric study of focused parameters (e.g. fuel and oxidiser flow rate and fuel composition) without the requirement of a practical installation and configuration of complex experimental apparatus. Thus, it is an effective tool for projecting the impact of fuel composition on various aspects of flame characteristics.

In this thesis, two simulation models are generated through CFD. The first one is used for the study of a stable flame, and the other one is for an investigation of the unstable oscillating flame. The burner configurations, utilised as a reference in the formulation of the stable and unstable flame CFD models, are taken from the studies of Toro et al. [2] and Darabkhani et al. [88], respectively. The governing equations, thermal radiation model, and chemical modelling technique of both models are almost the same. Only the methods used for defining the dynamic viscosity and molecular diffusivity are different. The details of the governing equations, numerical models and numerical procedure are presented in this chapter.

3.1 Governing equations

The generated CFD model considers that the properties of mass, momentum and energy are conserved, and the governing equations are derived by the control volume approach as explained in the sections below.

3.1.1 The Navier-Stokes (N-S) equations

The simulation model considers an axisymmetric domain based on the burner geometry of Toro et al. [2] and Darabkhani et al. [88]. The mass, axial momentum, and radial momentum conservation equations are therefore expressed in equations (14), (15), and (16) respectively as:

$$\frac{\partial \rho}{\partial t} + \frac{\partial (\rho u_x)}{\partial x} + \frac{\partial (\rho u_r)}{\partial r} + \frac{\rho u_r}{r} = 0, \quad (14)$$

$$\frac{\partial(\rho u_x)}{\partial t} + \frac{1}{r}\frac{\partial(r\rho u_x u_x)}{\partial x} + \frac{1}{r}\frac{\partial(r\rho u_r u_x)}{\partial r} = -\frac{\partial p}{\partial x} + \frac{1}{r}\frac{\partial}{\partial x}\left[r\mu\left(2\frac{\partial u_r}{\partial x} - \frac{2}{3}(\nabla\cdot\vec{u})\right)\right] + \frac{1}{r}\frac{\partial}{\partial r}\left[r\mu\left(\frac{\partial u_x}{\partial r} - \frac{\partial u_r}{\partial x}\right)\right] + \rho g_x, \quad (15)$$

$$\frac{\partial(\rho u_r)}{\partial t} + \frac{1}{r}\frac{\partial(r\rho u_x u_r)}{\partial x} + \frac{1}{r}\frac{\partial(r\rho u_r u_r)}{\partial r} = -\frac{\partial p}{\partial r} + \frac{1}{r}\frac{\partial}{\partial x}\left[r\mu\left(\frac{\partial u_r}{\partial x} - \frac{\partial u_x}{\partial r}\right)\right] + \frac{1}{r}\frac{\partial}{\partial r}\left[r\mu\left(2\frac{\partial u_r}{\partial r} - \frac{2}{3}(\nabla\cdot\vec{u})\right)\right] - 2\mu\frac{u_r}{r^2} + \frac{2}{3}\frac{\mu}{r}(\nabla\cdot\vec{u}) \quad (16)$$

where u is the velocity component (ms^{-1}), t is the time, ρ is the mixture density, x is the axial coordinate, r is the radial coordinate, the subscription x and r refers to the direction in the axial and radial coordinates respectively, μ is the dynamic viscosity, p is the static pressure, and ρg_x is the gravitational body force acting in the axial direction.

The term $\nabla\cdot\vec{u}$ is expressed as:

$$\nabla\cdot\vec{u} = \frac{\partial(\rho u_x)}{\partial x} + \frac{\partial(\rho u_r)}{\partial r} + \frac{\rho u_r}{r} \quad (17)$$

As the axisymmetric domain is utilised, the derivatives of flow variables (pressure, velocity etc.) in the circumferential direction are zero. In other words, the assumption is made by considering that the flow solution would not change in a circumferential direction. The axis of the simulation domain lies on the coordinate in which $r = 0$, the value of r is equal or more than zero to prevent the error. The mesh sweeps for an angle of 1 radian. Therefore, any volumetric or area quantities reported from the model are assumed to be for a 1-radian sector. The results that will be presented in the following chapters are multiplied by 2π for the value of a quantity for the full 360° revolution. The singularity of $\frac{u_r}{r}$ at $r = 0$ is avoided by replacing this term as $\frac{du_r}{dr}$. In this work, the flow regime of both fuel and oxidiser streams is laminar with the Reynolds number less than 600. Thus, the impact of turbulent on the mix of fuel and oxidiser is significantly weak.

The dynamic viscosity (μ) of the mixture is the combination of the same definition of each individual species. At the species level, the dynamic viscosity of species i (μ_i) is defined by either of the three different methods; (i) Chapman-Enskong method [118] shown in (18), (ii)

interpolation of the gas property data of Ref [119], and (iii) constant value based on temperature and pressure of the combustion condition. The stable flame CFD model utilises method (i) for defining the value of μ_i. Methods (ii) and (iii) are used in an unstable flame CFD model. The value μ_i of major reactant and product species, e.g. H_2, CO, CH_4, CO_2, N_2, O_2, and H_2O are computed by method (ii) whereas, one of the other species, it is provided by method (iii).

$$\mu_i = 2.6693 \times 10^{-6} \left(\frac{\sqrt{M_i T}}{\sigma_i^2 \Omega(T^*)} \right) \tag{18}$$

Here in this equation, μ_i is the viscosity of species i, M_i is the molecular weight of species i, T is temperature (in K), σ_i is the collision diameter or Lennard-Jones characteristics length of species i, $\Omega(T^*)$ is the collision integral term, T^* is reduced temperature (dimensionless) which is defined as:

$$T^* = \left(\frac{kT}{\varepsilon_i} \right) \tag{19}$$

where k is the Boltzmann constant ($1.3806503 \times 10^{-23}$ m^2-kg-s^{-2}-K^{-1}) and ε_i is the potential energy of attraction or Lennard-Jones energy of component i. Furthermore, the value of σ_i and ε_i of each individual species are provided by the database of STAR CCM+ software [120].

At the gas mixture level, the Mathur-Saxena averaging method [121] shown in (20) is used for combining μ_i computed from the method (i) in the stable flame CFD model. This method computes the dynamic viscosity of the mixture (μ) based on the mole fraction of species in the mixture. On the other hand, the Mass-weight mixture method in equation (21) is utilised for combining μ_i, which is obtained from either method (ii) or (iii). This combination method relies on the mass fraction of each species in the gas fuel mixture.

$$\mu = \frac{1}{2} \left(\sum_{i=1}^{n} X_i \emptyset_i + \left(\sum_{i=1}^{n} \frac{X_i}{\mu_i} \right)^{-1} \right), \tag{20}$$

$$\mu = \sum_{i=1}^{n} Y_i \mu_i \tag{21}$$

where Y_i is the mass fraction of species i, and X_i is the mole fraction of species i

3.1.2 **Species mass conservation equation**

The simulation of reacting flow relates to several species. The analysis of the species mass conservation is explained in the gas mixture level. In addition to the N-S equations, this equation is described as:

$$\frac{\partial}{\partial t}\rho Y_i + \nabla \cdot (\rho Y_i \vec{u} + J_i) = R_i \tag{22}$$

where R_i is the production rate of species i, and J_i is the diffusive heat flux which relates to the molecular diffusion and thermal diffusion. The expression of J_i is defined according to Fick's first law as:

$$J_i = \rho D_i (\nabla \cdot Y_i) \tag{23}$$

where D_i is the molecular diffusivity coefficient of species i in the gas mixture which is defined by the kinetic theory as:

$$D_i = \frac{1-X_i}{\sum_{i=1, i\neq j}^{N} \frac{X_j}{D_{i,m}}} \tag{24}$$

where X_j is the mole fraction of species j. The binary diffusion coefficient between species i and m ($D_{i,m}$) is computed according to the Chapman-Enskog method as:

$$D_{i,m} = \frac{2.66 \times 10^{-7} T^{1.5}}{p M_{i,j}^{0.5} \sigma_{i,j}^2 \Omega(T^*)} \tag{25}$$

where

$$M_{i,j} = \frac{2 M_i M_j}{M_i + M_j} \tag{26}$$

The parameter M_i in equation (26) is the molecular weight of species i, M_w is the molecular weight of the gas mixture, $\sigma_{i,j}$ is the collision diameter for the pair of component i and j which is computed from Lennard-Jones characteristics length of species i and j by the similar method as the calculation of $M_{i,j}$, and p is the (absolute) static pressure. The unstable flame CFD model utilised these set of equations for defining the diffusive flux. For the stable flame CFD model, the multicomponent diffusion and thermal diffusion (soret effect) are considered. Without the movement of the flame, the computational cost of the stable flame CFD model could be paid more on the impact of thermal and mass diffusion, especially one

of H_2, which has a significantly higher diffusivity than the other combustible species (the data is provided in Chapter 2). The diffusive heat flux (equation (23)) is hence modified as:

$$J_i = \rho \sum_{j=1}^{N} D_{i,j} (\nabla \cdot Y_i) + \rho \frac{D_{i,t}}{T} (\nabla \cdot T) \quad (27)$$

The first term in (27) refers to the multi-component diffusion where $D_{i,m}$ is computed using the Maxwell-Stefan equations [122], where N is the number of species. The implicitly of the diffusive flux is defined as a function of mole fraction gradients, which are given as:

$$\nabla X_i = \frac{M_w}{\rho} \sum_{j=1, j\neq i}^{N} \frac{X_i J_j}{M_j Ð_{i,j}} - \frac{X_j J_i}{M_i Ð_{i,j}} \quad (28)$$

where $Ð_{i,j}$ is the binary diffusion coefficient between species i and j. The equation could be written in the matrix form as:

$$[B]\nabla Y = [A]J \quad (29)$$

in which [B] is the mapping from mass fraction gradients to mole fraction gradients and [A] refers to the Maxwell-Stefan equations. The multi-component diffusion coefficient could be computed by inverting [A] and multiplying by the matrix [B] as:

$$D_{i,j} = \rho \sum_{k=1}^{N} A_{i,k}^{-1} B_{k,j} \quad (30)$$

In equation (27), $D_{i,t}$ is the thermal diffusion coefficient for species i, and the term $\rho \frac{D_{i,t}}{T} (\nabla \cdot T)$ refers to the soret effect or thermal diffusion model. Warnatz Model [123] is selected for computing the thermal diffusion coefficient ($D_{i,t}$). The method relies on the thermal diffusion ratio between species i and j as follows:

$$D_{i,t} = D_{i,eff} \frac{M_i}{M_w} \sum_{j=1}^{N} K_{T,ij} \quad (31)$$

where

$$K_{T,ij} = \frac{15}{2} \frac{(2A_{i,j}^* + 5)(6C_{i,j}^* - 5)}{(A_{i,j}^* (16A_{i,j}^* - 12B_{i,j}^* + 55)} \frac{M_i - M_j}{M_i + M_j} X_i X_j, \quad (32)$$

$$A_{i,j}^* = \frac{1}{2} \frac{\Omega_{i,j}^{(2,2)}}{\Omega_{i,j}^{(1,1)}}, \quad (33)$$

$$B_{i,j}^* = \frac{1}{3} \frac{5\Omega_{i,j}^{(1,2)} - \Omega_{i,j}^{(1,3)}}{\Omega_{i,j}^{(1,1)}}, \quad (34)$$

$$C_{i,j}^{*} = \frac{1}{3}\frac{\Omega_{i,j}^{(1,2)}}{\Omega_{i,j}^{(1,1)}} \tag{35}$$

For this set of equations, $\Omega_{i,j}$ represents the collision integrals term computed from the collision integrals of species i and j. The detail of this method is explained in Kee et al. [124]. The effective diffusion coefficient of species i ($D_{i,eff}$) in the gas mixture is given as:

$$D_{i,eff} = \frac{1 - X_i}{\sum_{i=1, i\neq j}^{N} \frac{X_j}{D_{i,j}}} \tag{36}$$

As seen, equation (25) and (36) are similar except the binary diffusion coefficient. $D_{i,m}$ is used in the previous equation (unstable flame CFD model), but $D_{i,j}$ is substituted in the latter one.

3.1.3 **Energy conservation equation**

The energy conservation equation is written as:

$$\frac{\partial}{\partial t}(\rho E) + \nabla \cdot (\vec{u}(\rho E + p) = -(\nabla \cdot q_j) + Q_r \tag{37}$$

where q_j is the energy flux, and Q_r is the thermal energy production rate. The total energy (E) is computed based on the enthalpy (h) of the mixture as:

$$h = E + \frac{p}{\rho} \tag{38}$$

The energy equation (37) is then re-written as:

$$\frac{\partial}{\partial t}(\rho h) + \nabla \cdot (\vec{u}\rho h) = \frac{\partial p}{\partial t} - (\nabla \cdot q_j) + Q_r \tag{39}$$

where the enthalpy (h) in this equation is computed by the combination of species enthalpy (h_i) and mass fraction as:

$$h = \sum_{i=1}^{N} Y_i h_i \tag{40}$$

The enthalpy of species i is a function of temperature which is calculated as follows:

$$h_i = h_i^{\circ} + \int_{T^{\circ}}^{T} C_{p,i} dT \tag{41}$$

where h_i° is the heat of formation of species i at the reference temperature (298.15 K). $C_{p,i}$ is the specific heat at a constant pressure of species i. The method utilised for estimating the value of $C_{p,i}$ is the 7 coefficient NASA thermodynamic polynomials method [125]. This method creates the polynomial curve profile of specific heat ($C_{p,i}$), enthalpy (h), and entropy (S) as a function of temperature based on 7 coefficients. For this work, these coefficients are provided for each individual species from the thermodynamics properties of GRI3.0 [111] chemical reaction mechanism.

As shown below in equation (42), the energy flux q_j is the contribution of the energy flux of conduction (q_j^c), diffusion (q_j^d), and energy flux (q_j^D) caused by concentration gradients (Dofour effect) [123]. The high diffusive property of H_2 is taken into account for the term q_j^D. The pilot case of hydrogen flame was run for estimating the value of this parameter, and it is found that the value of q_j^D is much smaller than q_j^c and q_j^d; thus, this term is neglected in this work.

$$q_j = q_j^c + q_j^d + q_j^D \tag{42}$$

Regarding the contribution of conduction (q_j^c), it could be expressed by Fourier's law as follows:

$$q_j^c = \lambda_{con} \frac{\partial T}{\partial x_j} \tag{43}$$

In equation (43), λ_{con} is the thermal conductivity of the gas mixture which is computed by combining the thermal conductivity of each individual species ($\lambda_{con,i}$). The kinetic theory is utilised for defining $\lambda_{con,i}$. This numerical model considers the translation contribution ($C_{v,tran}$), rotation contribution ($C_{v,rot}$) and vibration contribution ($C_{v,vib}$) as follows:

$$\lambda_{con,i} = \frac{\mu_i}{M_i}\left(f_{tran} C_{v,tran} + f_{rot} C_{v,rot} + f_{vib} C_{v,vib}\right) \tag{44}$$

where

$$f_{tran} = \frac{5}{2}\left[1 - \frac{4}{3\pi}\frac{A}{B}\right], \tag{45}$$

$$f_{rot} = \frac{\rho D_i}{\mu_i}\left[1 + \frac{2}{\pi}\frac{A}{B}\right], \quad (46)$$

$$f_{vib} = \frac{\rho D_i}{\mu_i}, \quad (47)$$

$$A = \frac{5}{2} - \frac{\rho D_i}{\mu_i}, \quad (48)$$

$$B = z_{rot} + \frac{2}{\pi}\left(\frac{5}{3}\frac{C_{v,rot}}{R_u} + \frac{\rho D_i}{\mu_i}\right), \quad (49)$$

$$C_{v,tran} = \frac{3}{2}R_u, \quad (50)$$

$$z_{rot} = z_{rot}(298)\frac{F(298)}{F(T)}, \quad (51)$$

$$F(T) = 1 + \frac{\pi^{3/2}}{2}\left(\frac{\varepsilon_i/k}{T}\right)^{1/2} + \left(\frac{\pi^2}{4} + 2\right)\frac{\varepsilon_i/k}{T} + \pi^{3/2}\left(\frac{\varepsilon_i/k}{T}\right)^{3/2}, \quad (52)$$

$$C_{v,vib} = C_v - \frac{5}{2}R_u \quad (53)$$

In these equations, R_u is the universal gas constant, $\lambda_{con,i}$ is the thermal conductivity of species i, and $z_{rot}(298)$ is the value of the rotation collision number at 298 K which is defined in the transport properties of the component. $C_{v,rot}$ presented in equation (49) is defined as equal as R_u, whereas C_v in equation (53) is the molar specific heat at constant volume of species i. D_i in equation (46) - (49) is replaced by $D_{i,eff}$ for the stable flame CFD model. The combination of $\lambda_{con,i}$ for λ_{con} is processed by the Mathur-Saxena averaging method which relies on the species mole fraction as follows:

$$\lambda_{con} = \frac{1}{2}\left(\sum_{i=1}^{n} X_i\lambda_i + \left(\sum_{i=1}^{n}\frac{X_i}{\lambda_i}\right)^{-1}\right) \quad (54)$$

Regarding the energy flux due to the diffusion (q_j^d) in equation (42), it is computed by the diffusion of species having different enthalpy as follows:

$$q_j^d = \sum_{i=1}^{n} h_i J_{i,j} \quad (55)$$

Therefore, the combination of equations (43) and (55) causing the energy flux presented in equation (42), becomes

$$q_j = \lambda_{con} \frac{\partial T}{\partial x_j} + \sum_{i=1}^{n} h_i J_{i,j} \quad (56)$$

3.1.4 The equation of state

The reactant and product of the combustion reaction are assumed to have the ideal gas behaviour. Therefore, the equation of state for ideal gas [126] is applied as presented in equation (57).

$$p = \rho R_u T \sum_{i}^{N} \frac{Y_i}{M_i} \quad (57)$$

where M_i is the molecular weight of species i.

3.1.5 Thermal radiation

The thermal radiation is considered as significant in the combustion process. The radiative energy transports from the higher temperature gas mixture to the surrounding lower temperature. This phenomenon results in the reduction of combustion temperature. The definition of the thermal radiative heat flux from the black body to the surrounding is expressed as:

$$Q_r = S_b(T^4 - T_{surr}^4) \quad (58)$$

where S_b is the Stefan-Boltzmann constant (5.67×10^{-8} W-m^{-2}K^4), and T_{surr} is the surrounding temperature.

As the radiative flux (Q_r) is proportional to T^4, it is significant compared to the heat transfer of conduction and convection. The high-temperature gas during combustion is the product of the chemical reaction, e.g. CO_2 and H_2O (water vapour). The radiation in the thermal spectrum is, hence, dominated by these participating medium gases. In opposite, the absorption of diatomic gases, e.g. N_2 and O_2, could be neglected as they have no significant absorption bands. Several numerical models were introduced to formulate the propagation of radiation e.g. P-1 [62] and [127], discrete transfer [128], discrete ordinates [129] and [130], and Rosseland [131] radiation models. In this work, the electromagnetic wave, which radiates through the gray gases (mainly CO_2 and H_2O), is modelled by the Discrete Ordinate Method (DOM), which is also called as 'Participating Media radiation'. A detailed

description of the method can be found in Modest [131]. Briefly, the model considers that the surface radiative property (e.g. emissivity, reflectivity, transmissivity, and radiation temperature) does not depend on direction but the wavelength of the medium which can also absorb, emit, or scatter radiation. Thus, the amount of radiation that each surface receives and emits depends on this effect as well as the optical properties of the surface controls.

The expression of the propagation of thermal radiation intensity (I) through the participating media in solid angle (Ω) direction is presented in the form of the radiative transport equation (RTE) as:

$$\frac{dI_\lambda}{ds_\sigma} = -\beta_\lambda I_\lambda + k_{a\lambda} I_{b\lambda} + \frac{k_{s\lambda}}{4\pi}\int_{4\pi}^{0} I_\lambda(\Omega) d(\Omega) + k_{pa\lambda} I_{pb\lambda} + \frac{k_{ps\lambda}}{4\pi}\int_{4\pi}^{0} I_\lambda(\Omega) d(\Omega) \qquad (59)$$

where

I_λ is the radiative intensity, $k_{a\lambda}$ is the absorption coefficient, $k_{s\lambda}$ is the scattering coefficient, $I_{b\lambda}$ is the black body intensity, Ω is the solid angle, $k_{pa\lambda}$ is the particle absorption coefficient, $k_{ps\lambda}$ is the particle scattering coefficient, $I_{pb\lambda}$ is the particle black body intensity at particle temperature, s_σ is the distance in the σ direction, and β_λ is defined as:

$$\beta_\lambda = k_{a\lambda} + k_{s\lambda} + k_{pa\lambda} + k_{ps\lambda} \qquad (60)$$

The black body intensity ($I_{b\lambda}$) is defined as:

$$I_{b\lambda} = \frac{2C_1}{\lambda^5 (e^{c_2/\lambda T} - 1)} \qquad (61)$$

where $C_1 = 0.595522 \times 10^{-16}$ Wm^2s^{-1} and $C_1 = 0.01439$ mK.

The process of DOM requires a specification of the number of solid angles or "ordinates", and the higher number usually increases the level of accuracy [132]–[134]. This model considers the surrounding volume as a sphere and solves the field equations for radiation intensity that is associated with a fixed direction S_i. This direction (S_i) is represented by a discrete solid angle in the surrounding hemisphere. It analyses the wavelength as a band rather than the specific value. The number of the ordinates is selected as eight in this work, and this results in the consideration of 80 directions of S_i. The ordinate equation of each wavelength band and is given as:

$$S_i \cdot \nabla I_{i\Delta\lambda} = -\beta_{\Delta\lambda} I_{i\Delta\lambda} + k_{a\Delta\lambda} I_{b\Delta\lambda} + \frac{k_{s\Delta\lambda}}{4\pi} \sum_{j=1}^{n} w_j I_{i\Delta\lambda} + k_{pa\Delta\lambda} I_{pb\Delta\lambda} + \frac{k_{ps\Delta\lambda}}{4\pi} \sum_{j=1}^{n} w_j I_{i\Delta\lambda} \quad (62)$$

where $\Delta\lambda$ represents a wavelength band from λ_m to λ_n, and w_j is the quadrature weight. The black body intensity in this equation is defined as:

$$I_{b\Delta\lambda} = \int_0^{\lambda_n} Ib_\lambda d_\lambda - \int_0^{\lambda_m} Ib_\lambda d_\lambda \quad (63)$$

The particle absorption and scattering coefficients as well as ω_j could be found in [131].

The Weighted Sum of Gray Gases Method (WSGGM) [135], which is widely used in the simulation of combustion of air-fuel is selected for computing the absorption coefficient ($k_{a\lambda}$) presented in equation (64). The model assumes that the property of the combustion product gases, e.g. CO_2 and H_2O, does not significantly scatter but strongly emit and absorb radiation.

$$k_{a\lambda} = -\frac{\ln(1-\epsilon)}{OPL} \quad (64)$$

where ϵ is the total emissivity over the optical pathlength (OPL). The value of ϵ is defined by considering all the gray gases (e.g. CO_2 and H_2O) as presented below.

$$\epsilon = \sum_{i=0}^{G} a_{\epsilon,i}\left(1 - e^{-K_i(OPL)}\right) \quad (65)$$

where $a_{\epsilon,i}$ is the emissivity weight factor for gray gas species i, G is number of gray gases, and K_i is the absorption coefficient of gray gas species i. The value of $a_{\epsilon,i}$ and K_i are obtained from Ref [135], [136]. The optical pathlength (OPL) is computed as:

$$OPL = 3.6(\text{volume/surface area}) \quad (66)$$

where the volume is the total volume of the gas, and the surface area is its total surface area. In this work, the value of OPL is computed and update every iteration, and the volume and surface area of the flame are utilised in equation (66).

To asses whether the impact of thermal radiation is significant or not, the pilot cases are run for both stable and unstable CFD flame models. The results of flames with and without the activation of thermal radiation are compared. It is found that the numerical result is closer to the experimental result when the thermal radiation model is activated. The result also shows that the consideration of thermal radiation causes a lower flame temperature. Thus, the absorption of combustion product gases e.g. H_2O and CO_2 are significant, and the CFD model should include the thermal radiation model.

3.2 Chemistry modelling

3.2.1 Chemical kinetics

The finite rate chemistry model where the production rate of each species is computed from the multi-steps chemical reaction mechanism is an effective method for modelling the laminar diffusion flame. The performance of this method could be found in Ref [2], [108], [137]. A good agreement result between the numerical result and the experimental result was found in these works. In this thesis, both stable and unstable flame CFD models utilised the finite rate chemistry model for modelling the reacting flow.

The term of the production rate of species i (R_i) in the species transport equation presented in (22) is computed based on the supplied chemical reaction mechanisms. The elementary forward and backward reaction can be expressed in a general form as:

$$v'_A\mathrm{A} + v'_B B + \cdots \xrightarrow{k_f} v'_C\mathrm{C} + v'_D D + \cdots \tag{67}$$

$$v'_A\mathrm{A} + v'_B B + \cdots \xleftarrow{k_b} v'_C\mathrm{C} + v'_D D + \cdots \tag{68}$$

where A and B are reactant species, C and D are product species, k_f is forward rate constant, k_b is backward rate constant, v'_i is the stoichiometric coefficients of the reactants of species i, and v''_i is the stoichiometric coefficients of the products of species i. For an elementary reaction the rate of reaction of species A can be expressed as:

$$\frac{d[A]}{dt} = v_A\left[k_f \cdot [A]^{v'_A}[B]^{v'_B} \ldots - k_b \cdot [C]^{v'_C}[D]^{v'_D} \ldots\right] \tag{69}$$

where

$$v_A = v''_A - v'_A$$

The blanket refers to the concentration of each species. As the chemical reaction mechanism consists of several species and reactions, the net rate of reaction of species A can be explained as:

$$\dot{\omega}_i = \sum_{j=1}^{N_j} v_{i,j} r_j \tag{70}$$

Where

$$r_j = \left(k_{f,j} \prod_i [A]^{v'_{j,i}} - k_{b,j} \prod_i [A]^{v''_{j,i}} \right) \tag{71}$$

The rate k_f and k_b are computed from the rate coefficient of reaction (k) which is expressed in the form of a modified Arrhenius equation as:

$$k = AT^{\beta} e^{-E/RT} \tag{72}$$

where $k = k_f$ for forward reaction, $k = k_b$ for backward reaction, A is the pre-exponential factor, β is the temperature exponent and E is the activation energy

Nevertheless, the unit of $\dot{\omega}_i$ in equation (70) is kmol-m^{-3}s^{-1} and requires the development to the preferred unit kg-m^{-3}s^{-1}. Thus, $\dot{\omega}_i$ is multiplied by the molecular weight of species i ($M_{w,i}$) as follows:

$$R_i = M_{w,i} \dot{\omega}_i \tag{73}$$

3.2.2 **Complex chemistry model**

The 'complex chemistry numerical model' in STAR CCM+ is selected. According to the diversity in syngas composition, the chemical reaction of combustible species (H_2, CH_4, and CO) occur at different chemical time scale. Also, the significantly higher diffusivity of H_2 causes the complex combustion of syngas flame; thus, the proper chemical reaction mechanism is required for modelling the combustion. The generated CFD model computes the chemical reaction and species transport based on the detailed reaction mechanism supplied. This model is capable of computing complex reaction systems with a wide range of reaction time scales [120]. It considers each computational cell as a constant pressure reactor and computes the chemical source term R_i (the production rate of species i in equation (22)) for each species. The detailed reaction mechanism containing the information about species, reactions, thermodynamics, and transport properties is required for the

complex chemistry model. This complex chemistry definition could be imported as Chemkin format to the model. The chemical reaction mechanisms revised in Section 2.5 are compatible with the complex chemistry model.

The 'operator splitting' algorithm is utilised for solving the species transport equation. This algorithm takes advantage of the difference in time scales involved for computing the flow field and the chemical reactions. The solving process consists of two steps. Firstly, in each time step, the chemical state is integrated into each cell from state $(Y_i, T, p)^n$ to $(Y_i, T, p)^*$, and this change accounts only for the chemical source term.

$$Y_i^* = Y_i + \int_0^\tau r_j(\boldsymbol{Y}, T, p)dt \tag{74}$$

Regarding equation (74), Y_i^* is the mass fraction at the end of time integration τ, $\boldsymbol{Y}$ is a mass fraction vector, T is temperature, and r_j is obtained from (71). The solution obtained in the first step is used in the second step where the species transport equation is solved with an explicit reaction rate R_i for the i'th species defined as follows:

$$R_i = \rho f \left(\frac{Y_i^* - Y_i}{t}\right) \tag{75}$$

where ρ is the density, and f is the mean reaction rate multiplier.

As the study focuses on the laminar flame, the value of f is set as 1, which means there is no consideration of the turbulent time scale and turbulent length scale. This setup is thus called 'Laminar flame concept' (LFC) model. The time integration t is specified through the time step in the unsteady simulation. On the other hand, the cell residence time (t_{res}) is used in the steady-state simulation. The value of t_{res} is defined as the time that a fluid element spends in the cell. It is calculated from the mass in the cell divided by the mass flux in the cell, as shown in equation (76).

$$t_{res} = \left(\frac{m}{\dot{m}}\right) \tag{76}$$

As this algorithm relates directly to the time step, the low convective courant number (CCN) is required for the unsteady simulation to ensure that the error is small. The definition of CCN is expressed as:

$$CCN = \frac{u\Delta t}{\Delta x} \tag{77}$$

where u is the magnitude of the velocity, Δt is the time step, Δx is the length interval.

3.3 Numerical method

3.3.1 Finite volume approach

The simulation of both the CFD models (stable and unstable flames) is conducted based on the finite volume method by which the governing differential equations presented in the previous sections are transformed into a system of algebraic equations [120]. An algebraic multigrid solver is then used for solving the resulting equations. The set of governing equations (mass, momentum, energy, and species) are discretised and expressed as a generalised transport equation. By integrating this equation over a control volume and applying the Gauss's divergence theorem, the generalised equations are expressed in the integral form as below:

$$\frac{d}{dt}\int_V \rho\emptyset dV + \int_A u_j\rho\emptyset \cdot da = \int_A (\Gamma(\nabla \cdot \emptyset))da + \int_V S_\emptyset dV \tag{78}$$

where $\emptyset$ is a scalar quantity of fluid property, V is denoted as control volume (cell volume), and A is the surface area of the control volume, da denotes the surface vector, Γ is the diffusion coefficient, and $S_\emptyset$ is the generation/destruction of fluid property $\emptyset$.

From left to right, the equation consists of four terms, which are the transient term, convective flux, diffusive flux, and source term. The details of each term could be found in Ref [136]. The source term is the external force that is linked to gravity. By giving the value of $\emptyset$ as 1, u_i, E, h or Y_i, and provides appropriate value for Γ and source term. The generalised equations become the partial differential equations for mass, momentum, energy, and species conservation. The diagram explaining the parameters in the generalised equations of two computational cells is presented below.

In the numerical method, the surface integral is approximated by quadrature approximations [136]. On the other hand, the volume integral is estimated by the product of the mean value of the source term. By applying the integration approximation, the semi-discrete transport equation is then rewritten by referring to the parameters presented in Figure 3-1 as:

$$\frac{d}{dt}(\rho \emptyset V) + \sum_f [\rho \emptyset u_j \cdot a]_f = \sum_f [(\Gamma(\nabla \cdot \emptyset)) \cdot a]_f + S_\emptyset dV \tag{79}$$

where a_f is the surface area vector of face f in the cell, and $\sum_f$ is the sum over all cell faces of the cell.

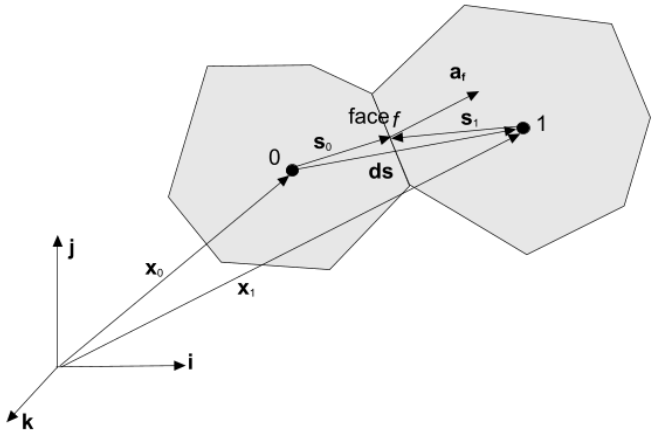

Figure 3-1 Discretization of the generalised equation [120]

In Figure 3-1, *f* is the cell face, a_f is the surface area vector of face f, s_0 and s_1 are the distance from the cell centroid to face centroid of cell 0 and cell 1, and ds is the distance between the centroid of cell 0 and cell 1.

For the unsteady simulation of an unstable flame CFD model, the analysis of the physical time interval is subdivided into an arbitrary number of sub-intervals called 'time-step'. The transient term (first term on the left of equation (79)) is activated, and the solution of the governing equations is computed at different time levels. In this work, the transient term is approximated based on the Euler implicit scheme [138]. The solution at time t requires the solutions obtained from the previous time-step for the computational process. A basic second-order temporal discretisation is selected; thus, the transient term uses the solution of the current time step as well as the solution of the previous two time-steps in a Backward Differentiation Formula [139] presented as follows:

$$\frac{d}{dt}(\rho \emptyset V) = \left(\frac{3}{2}(\rho \emptyset V)_{n+1} + 2(\rho \emptyset V)_n + \frac{1}{2}(\rho \emptyset V)_{n-1}\right)\frac{1}{\Delta t} \tag{80}$$

where $n + 1$ is the solution at the current time level, n and $n - 1$ are the solutions at the previous two-times levels, and Δt is the time-step.

However, a first-order temporal discretisation is used in the first time-step of the simulation since only two levels are available. The expression of the first-order temporal discretisation is presented as:

$$\frac{d}{dt}(\rho \emptyset V)_0 = \frac{(\rho \emptyset V)_0{}^{n+1} - (\rho \emptyset V)_0{}^{n}}{\Delta t} \tag{81}$$

The subscript 0 refers to the convective flux at the face f (the second term from the left of equation (79)) can be rearranged as follows:

$$(\emptyset \rho V \cdot a)_f = (\dot{m}\emptyset)_f = \dot{m}_f \emptyset_f \tag{82}$$

where $\dot{m}_f$ is the mass flow rate at face f while $\emptyset_f$ is a value of $\emptyset$ at face f in Figure 3-1.

The second-order upwind (SOU) scheme is selected for both the stable and unstable flame CFD models. The value of the term $\dot{m}_f \emptyset_f$ is given as:

$$(\dot{m}\emptyset)_f = \dot{m}_f \emptyset_{f,0} \text{ when } \dot{m}_f \geq 0, \text{ or } = \dot{m}_f \emptyset_{f,1} \text{ when } \dot{m}_f < 0 \tag{83}$$

In this scheme, $\emptyset_{f,0}$ and $\emptyset_{f,1}$ are computed using a multidimensional linear reconstruction approach [140]. In other words, the value of this parameter is obtained by interpolating linearly from the cell centre values on either side of the face f in Figure 3-1. The definition of them could also be expressed as:

$$\emptyset_{f,0} = \emptyset_0 + S_0 \cdot (\nabla \cdot \emptyset)_{r,0} \tag{84}$$

$$\emptyset_{f,1} = \emptyset_1 + S_1 \cdot (\nabla \cdot \emptyset)_{r,1} \tag{85}$$

where $S_0 = x_f - x_0$, $S_1 = x_f - x_1$, and $(\nabla\emptyset)_{r,0}$ and $(\nabla\emptyset)_{r,1}$ in equations (84) and (85) are the gradient of cell 0 and 1, respectively.

The second-order expression of diffusive flux (the first term on the right-hand side of equation (79)) is considered in both the CFD models created. The diffusive flux term is then rewritten as:

$$\Gamma_f(\nabla \cdot \emptyset_f) \cdot a = \Gamma_f\left[(\emptyset_1 - \emptyset_0)\vec{\alpha} \cdot a + \overline{\nabla \cdot \emptyset} \cdot a - \left(\overline{\nabla \cdot \emptyset} \cdot ds\right)\vec{\alpha} \cdot a\right] \quad (86)$$

where

$$\vec{\alpha} = \frac{a}{a \cdot ds}$$

$$ds = x_1 - x_0$$

$$\overline{\nabla \cdot \emptyset} = \frac{(\nabla \cdot \emptyset_0 - \nabla \cdot \emptyset_1)}{2}$$

The second and third terms represent the secondary gradient (or cross-diffusion), and they are essential for maintaining accuracy on non-orthogonal meshes. To simplify the equation, the analysis assumes that the centroids of cells 0 and 1 lie on opposing sides of the face. Their locations are also consistent with the convention that the face area vector points out of cell 0. According to this, the second and third term of equation (86) could be neglected. Thus, the diffusive flux is given as:

$$\Gamma_f(\nabla \cdot \emptyset_f) \cdot a \approx \Gamma_f[(\emptyset_1 - \emptyset_0)\vec{\alpha} \cdot a] \quad (87)$$

However, it is necessary to take into account that the angle between a and ds cannot be greater than 90 degrees. Also, the fine mesh pattern with a lower degree of skewness angle is needed.

As seen, the convective and diffusive flux relates to the cell gradient ($\nabla\emptyset$) which is computed in two steps. Firstly, the unlimited reconstruction gradient is computed by the Hybrid Gauss-Least Squares Method [141]. Secondly, the gradient limiter 'Venkatakrishnan [142]' is used for limiting the reconstruction gradient to the minimum and maximum bounds of the neighbouring cell values; i.e. the gradient is controlled and will not exceed the maximum and minimum value of the neighbour cell. The cell gradient obtained from this process is hence used in the convective and diffusive flux term.

The expression of convective and diffusive flux presented above are valid for all the interior cell faces and Neumann boundary conditions. For the Dirichlet boundary conditions, $\emptyset_f$ in the convective flux (equation (82)) is replaced by the boundary value ($\emptyset_b$). Also, the

diffusive flux in equation (86) is modified by replacing $\emptyset_1$ and $\overline{\nabla\emptyset}$ by $\emptyset_b$ and $\nabla\emptyset_0$, respectively.

Finally, the algebraic system for the transported variable $\emptyset$ is written as:

$$\frac{a_p}{\omega}\Delta\emptyset_p + \sum_n a_n\Delta\emptyset_n = r \tag{88}$$

where $\Delta\emptyset_p = \Delta\emptyset_p^{k+1} - \Delta\emptyset_p^k$, the parameter $\emptyset$ is a transported variable, the superscript $k+1$ refers to current iteration while k represents the previous iteration, and ω is an under relaxation factor. The equation explains the condition of the neighbours n of cell p. The residual (r) represents the discretized form of the original equation (88), and it becomes zero when the discretization is exactly satisfied.

3.3.2 **Solution procedures**

The segregated flow solver is selected in both CFD models. This solver solves the integral conservation equations of mass and momentum in a sequential manner. In other words, the governing equations are solved one after the other for the solution. The selected solver employs a pressure-velocity coupling algorithm called 'SIMPLE' which provides the linkage between the momentum and continuity equations. The pressure-velocity coupling could be derived from the continuity equation and presented in term of the mass flux correction $\dot{m}_f'$ as:

$$\sum_f \dot{m}_f = \sum_f \left(\dot{m}_f^* + \dot{m}_f'\right) = 0 \tag{89}$$

The algorithm demands the setup of boundary condition and also the initial condition which is provided based on the geometry and combustion condition of the reference co-flow burner (Toro et al. [2] and Darabkhani et al. [88]). The details of these aspects will be presented in the validation process of each CFD model in Chapters 4 and 6. The solving process begins by computing the reconstruction gradients and gradient of velocity and pressure. The discretised momentum equation (presented in the previous section) is latterly solved with a guessed pressure field (p^*), and this creates the intermediate velocity field (v^*). The uncorrected mass fluxes at interior faces ($\dot{m}_f^*$) is computed from the velocity field. However,

it does not satisfy the continuity and requires the mass flux correction $\dot{m}_f'$ to satisfy continuity. The pressure correction equation presented below (equation (90)) is solved, and this process produces the cell values as well as the pressure correction p'.

$$\dot{m}_f^* = \rho_f a \cdot \left(\frac{\mathsf{v}_0^* + \mathsf{v}_1^*}{2}\right) - Q_f\left(p_1 - p_0 - \overline{\nabla p_f^*} \cdot ds\right) \tag{90}$$

where

$$Q_f = \rho_f \left(\frac{V_0 + V_1}{\overline{a_0} + \overline{a_1}}\right) \vec{\alpha} \cdot a \tag{91}$$

In equation (90), and (91), v_0^* and v_1^* are the cell velocity obtained from the solution of the discrete momentum equation, V_0 and V_1 are the cell volumes for cell 0 and cell 1, $\overline{a_0}$ and $\overline{a_1}$ are the average of the momentum coefficients for all the components of momentum for cells 0 and 1, p_0 and p_1 are the pressure for cell 0 and cell 1, and $\overline{\nabla p_f^*}$ is the volume-weighted average of the cell gradients of pressure. The value of $\overline{\nabla p_f^*}$ is computed by volume-based interpolation between the gradient values of the two cells. Further, the cell variables in these equations are previously described in Figure 3-1.

Once the pressure correction p' is obtained, the pressure field and boundary condition are updated as:

$$p = p^* + \omega p' \tag{92}$$

The mass flux correction $\dot{m}_f'$ is latterly computed as:

$$\dot{m}_f' = Q_f(p_0' - p_1') + \frac{m_f^*}{\rho_f}\left(\frac{\partial \rho}{\partial p}\right)_T p' \tag{93}$$

where p' is equal to p_0' when $m_f^* > 0$, and it is equal to p_1' when $m_f^* < 0$.

The face mass flux and cell velocity are latterly corrected as

$$\dot{m}_f = \dot{m}_f^* + \dot{m}_f' \tag{94}$$

$$\mathrm{v} = \mathrm{v}^* - \frac{V\nabla_{p'}}{a_p'^{\mathrm{v}}} \tag{95}$$

where $\nabla_{p'}$ is the gradient of the pressure corrections, and $a_p'^{\mathrm{v}}$ is the vector of central coefficients for the discretised velocity equation.

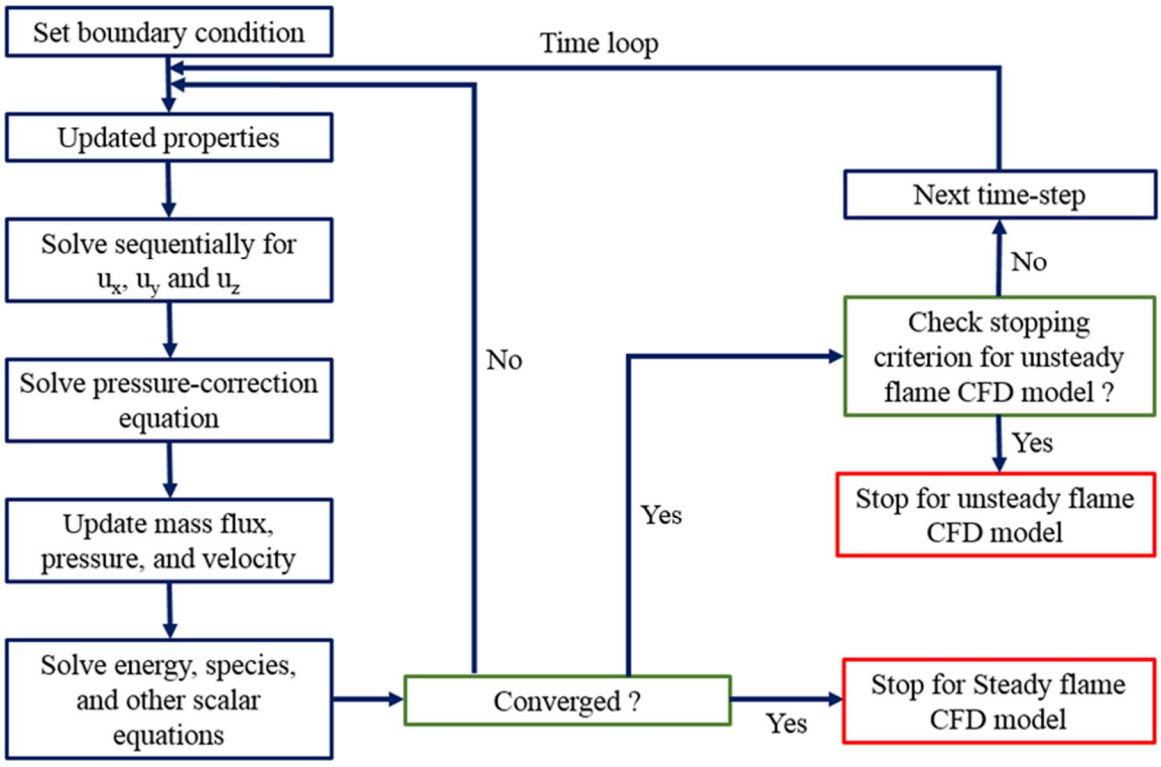

Figure 3-2 Solution procedure of the created CFD model

At the end of the sequent, fluid property, e.g. density, is updated according to the change of pressure and temperature. The other energy, species and other scalar transport equations are solved using the previously updated values of their variables. The residual is assessed by the convergence criterion, which is 10^{-6} for the residual of energy and radiation, and 10^{-4} for the other transport equations. The solving sequent continues until all the criterions are satisfied. According to the solving process, this solution procedure is also known as a predictor-corrector approach. The solution procedure diagram is presented in Figure 3-2.

3.4 Conclusion

CFD was selected as a method for formulating the laminar diffusion flame of syngas/producer gas. Two CFD models were created for simulating the stable and unstable laminar diffusion flame. The burner geometry, experimental condition, and methodology of

Toro et al. [2] and Darabkhani et al. [88] were utilised as a reference and a guideline for the creation of simulation model. The methodology used in this thesis was presented in this chapter. The details included the governing equations, numerical method, and solving procedure.

Chapter 4 Effects of hydrogen content on flame characteristics

Hydrogen (H_2) is a primary combustible species in syngas composition. The effect of content of this species in fuel stream on flame characteristics is studied in this chapter. The H_2 content, in this term, refers to the volume of this species in the fuel stream. It relates to two factors, such as the fuel velocity and the concentration of H_2 in fuel composition (X_{H_2}). Increasing either of these parameters results in the higher content of H_2 in fuel stream supplied into combustion. The generated CFD model (stable flame model) formulates the laminar diffusion flame of H_2/N_2 mixture fuel and pure hydrogen (H_2). The velocity of fuel and air stream (V_{avg}) and X_{H_2} are varied for projecting the effect of H_2 content. The study focuses on various aspects, such as the flame structure, flame dimension, flame temperature, species distribution, and NO_x emission formation.

4.1 Introduction

Unlike the conventional gas fuel which consists of only single combustible species, syngas is a mixture of combustible and non-combustible species at the various ratios. The content of combustible species supplied into the combustion hence relies not only on the flow rate of fuel but also on the concentration of combustible species in fuel composition. H_2 is one of the primary species in syngas composition; hence, understanding the role of this species on the flame characteristics is significant for the study of syngas combustion. Research attention has been paid on the impact of either fuel rate or the concentration of H_2 in fuel composition (X_{H_2}) on flame characteristics but not the combination of these factors together. The example could be seen from the study of Dinesh et al. [78] and Toro et al. [2] where the turbulent and laminar co-flow flame of H_2/N_2 were investigated numerically and experimentally. The result of these papers cannot be compared directly for the effect of H_2 content due to the different flame types and combustion conditions. However, the methodology of them can be used as a guideline for setting up the studied cases and model formulation.

As a result, the co-flow burner geometry of Toro et al. [2] is selected and modelled based on the methodology presented in Chapter 3. The experimental result presented in this paper is used as a reference in the validation process. The CFD model formulation, optimisation and

validation process are firstly presented in this chapter. Secondly, the study of the effect of H_2 content on the flame characteristic is presented. The discussion and conclusion are provided in the last stage.

4.2 Model formulation and validation

The CFD model is created according to the burner geometry and combustion condition of Ref [2]. The details regarding the formulation and validation of this model are presented as follows:

4.2.1 Burner geometry

The burner is co-flow in which the fuel injector is located at the centre of the axis, and it is surrounded by the co-flow air inlet. The inner diameter of the fuel and co-flow air inlets tube are 9 and 95 mm respectively. The fuel exit is 8 mm above the co-flow exit. The burner appearance is illustrated in Figure 4-1a.

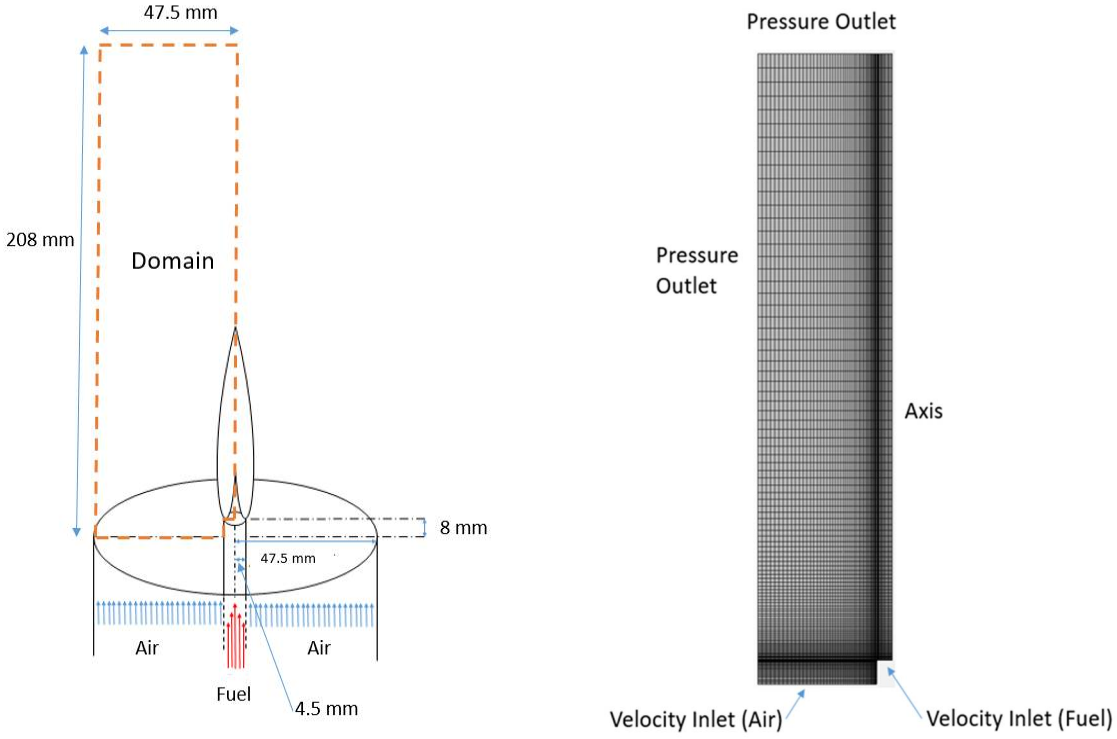

(a) (b)

Figure 4-1 (a) burner geometry and domain and (b) mesh generation and boundary condition

4.2.2 **Computational domain and boundary condition**

The numerical method requires the proper computational domain and grid refinement in order to obtain the converged and reliable solution. For the co-flow burner configuration, the flame is formulated above the fuel and co-flow air inlet. Thus, this location is the volume of interest which needs to be constructed by using a computational mesh. A two-dimensional (2D) axisymmetric domain representing this volume is considered. The mesh pattern is designed to project the reacting flow as well as the interaction between the fluid flow and burner geometry. More cells are concentrated close to the fuel and co-flow air exit. The higher density of cells at this location provides more accuracy for resolving the gradients by numerical method. The density of the cells slightly decreases at the higher vertical and horizontal distance from the fuel inlet. The number of cells and the distances between grids directly affect the reliability and accuracy of the result and the computational time. Thus, the mesh independency study and optimisation process are required for finding the proper mesh density for each simulation model. This process will be explained in Section 4.2.4.

The directed mesh procedure in the software, which allows the on-demand design of mesh construction is utilised. The width of the top plane of the domain is 47.5 mm which accounts from the centreline of the fuel tube to the outer line of the co-flow air tube horizontally. The width of the bottom plane is 4.2 cm and covers the distance from the outer of the co-flow air tube to the outer of the fuel inlet tube. The height of the domain from the top to the bottom planes is 208 mm. The thickness of the fuel tube is 1 mm, and the width of the fuel inlet is 4.5 mm. The axis of the domain is the centre line of the fuel inlet. The generated mesh is presented in Figure 4-1b.

The boundary condition of the simulation domain is illustrated in Figure 4-1b. Combustion occurs at the temperature and pressure of 298 K and 101325 Pa, respectively. The same temperature and pressure also apply on top and left boundaries, which are defined as pressure outlet. The species on these boundaries are air, which is defined as 79% N_2 and 21% O_2. The bottom boundary is a velocity inlet for both the fuel and co-flow air. The velocity profile is parabolic for fuel stream and bulk for the co-flow air stream. The fuel tube and its thickness are defined as a wall boundary with non-slip and non-adiabatic conditions.

4.2.3 **Numerical technique overview**

A segregated solver is utilised for solving the continuity, momentum, species transport, and energy equations. The methods used for calculating the dynamic viscosity and specific heat are Chapman-Enskong, and 7 coefficient NASA polynomials, respectively. The thermodynamic and transport property data are imported from the GRI3.0 mechanism [111] database. Molecular diffusivity and thermal conductivity are computed according to the kinetic theory. The generated CFD model considers multi-component diffusion, thermal diffusion also thermal radiation. The radiation transport equation is solved by the Discrete Ordinate Method (DOM) where the absorption coefficient is calculated based on the weighted sum of gray gas model (WSGG). The details of the mentioned methods were already presented in Chapter 3. The property of the gas fuel in this study at injected temperature (298K) is presented in Table 4-1

Table 4-1 Property gas fuel in this work at

	25%H_2+75%N_2	50%H_2+50%N_2	75%H_2+25%N_2	H_2
Density (kg/m^3)	0.88	0.614	0.348	0.0824
Dynamic viscosity (Pa-s)	1.515E-5	1.28E-5	1.08E-5	0.89E-6
Thermal conductivity (W-m^{-1}K^{-1})	0.051	0.078	0.112	0.191
Mass diffusion coefficient of gases in excess of air (cm^2-s^{-1})	H_2 = 0.756, O_2 = 0.176, H_2O = 0.242, and N_2 = 0.304			
Specific heat (kJ-kg^{-1}K^{-1})	1.35	1.93	3.39	14.31
Air-fuel ratio	0.60	1.19	1.79	2.38

The flame is ignited by setting the temperature of the cells close to the fuel and air exit at 1800 K for the first 20 iterations. The simulation was run until the convergence of the solution is obtained with a steady-state profile of the contour plots of the velocity, temperature and concentration of species H_2, N_2, O_2, N_2, H_2O, NO and NO_2. The residuals of the continuity, momentum, and energy equations are found between 10^{-4} and 10^{-6}. Thus, solution stability and steadiness are ensured.

4.2.4 **Mesh generation and optimisation**

A higher number of grids and cells on the computational domain provides greater detail of the solution; nevertheless, a higher computational cost is required. Three levels of mesh density (fine, medium, and coarse) are created by a hyperbolic function, and the results computed from them are compared to optimise the proper level of mesh resolution. A clustering mesh is stretched both vertically and horizontally from the outer edge of the fuel inlet tube to the pressure boundary (both top and left boundaries), axis, and co-flow air inlet. The mesh pattern is designed for computing the reacting flow field as well as the fluid interaction between the fuel inlet tube and the co-flow air stream. Different levels of mesh density have a different number of grids, cells and the smallest cell size. The detail of each mesh density level is presented in Table 4-2. The smallest cell size of the fine, medium and coarse mesh density model is 0.1, 0.2, and 0.5 mm, respectively. This setup results in the total number of cells of the fine, medium, and coarse mesh models as 26,000, 7800, and 2880 cells in order.

Table 4-2 Mesh density level

Resolution	Levels from outer of the fuel outlet tube to the axis	Levels from outer of the fuel outlet tube to the top plane	Levels from outer of fuel outlet tube to left plane	Levels from outer of the fuel outlet tube to the top plane	Total number of cells	Smallest cells size (mm)
Coarse	10	50	25	12	2880	0.5
Normal	16	100	50	24	7800	0.2
Fine	20	200	200	32	26000	0.1

The experimental data of Toro et al. [2] is used as a reference in this stage to assess the performance of the compared CFD models having different mesh resolution. The fuel gas has H_2:N_2 = 1 in terms of the mole fraction, and the flame is formulated at the velocity of both the fuel and air streams (V_{avg}) of 0.5 ms^{-1}. The simulation is, therefore, run at this condition of fuel and oxidiser streams for all the compared models. The chemical reaction mechanism supplied to these models is GRI3.0 [111]. The mesh resolution providing the result closer to the reference result has a higher reliability and accuracy level.

4.2.5 **Selection of chemical reaction mechanisms**

Several chemical reaction mechanisms being capable of computing the combustion of syngas/producer gas are selected and reviewed in Chapter 2 (Section 2.3.3). The most

suitable reaction mechanism for the generated CFD model can be obtained by comparing the results generated from different mechanisms with the reference result. One that provides a good agreement result will be selected. In this occasion, the comparison considers four different reaction mechanisms which are DRM22 [112], GRI3.0 [111], Yetter et al. [113], and Sankaran et al. [116]. The simulation is processed on the medium mesh density resolution which is found to be the most suitable mesh resolution according to the result obtained from the mesh dependency test. The result of the test will be presented together with the comparison of chemical reaction mechanism in the following section.

4.2.6 Validation of the simulation model

The simulation results obtained from the CFD models with the different mesh density levels and chemical mechanisms are compared. The axial and radial profiles of temperature and species are presented in Figure 4-2 - Figure 4-5. As seen, all the generated CFD models are able to predict the comparable result with those obtained by the experimental method. Only a slightly under-prediction/over-prediction is observed, and the details of which are discussed in the sections below.

4.2.6.1 Temperature and species distribution

The temperature and species axial profiles of flames formulated by all the compared CFD models are presented in Figure 4-2. All the models predict the good agreement temperature profile when it is compared with the experiment result at a distance lower than 20 mm except the CFD model with the Yetter et al. [113] mechanism, which underpredicts the temperature profile at this range. Above this level (20 mm), the temperature profile is over-predicted by all the CFD models. The CFD model with the coarse mesh predicts the significantly higher temperature profile than the other models. For the axial species profiles of (H_2, O_2, H_2O and N_2), good agreement between the experimental and numerical results for all the species is obtained from all the CFD models.

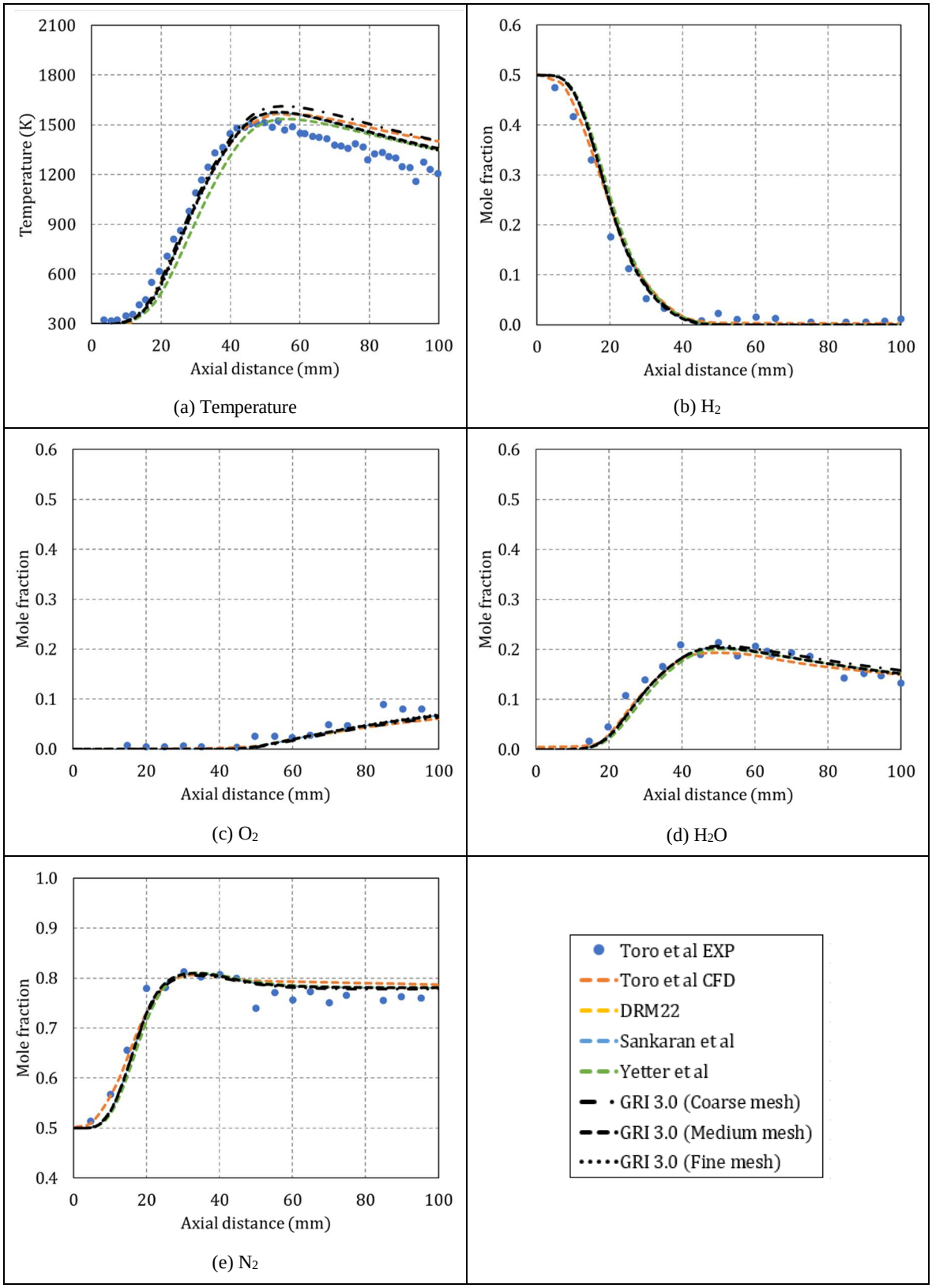

(a) Temperature

(b) H_2

(c) O_2

(d) H_2O

(e) N_2

Figure 4-2 Axial temperature and species profile comparison

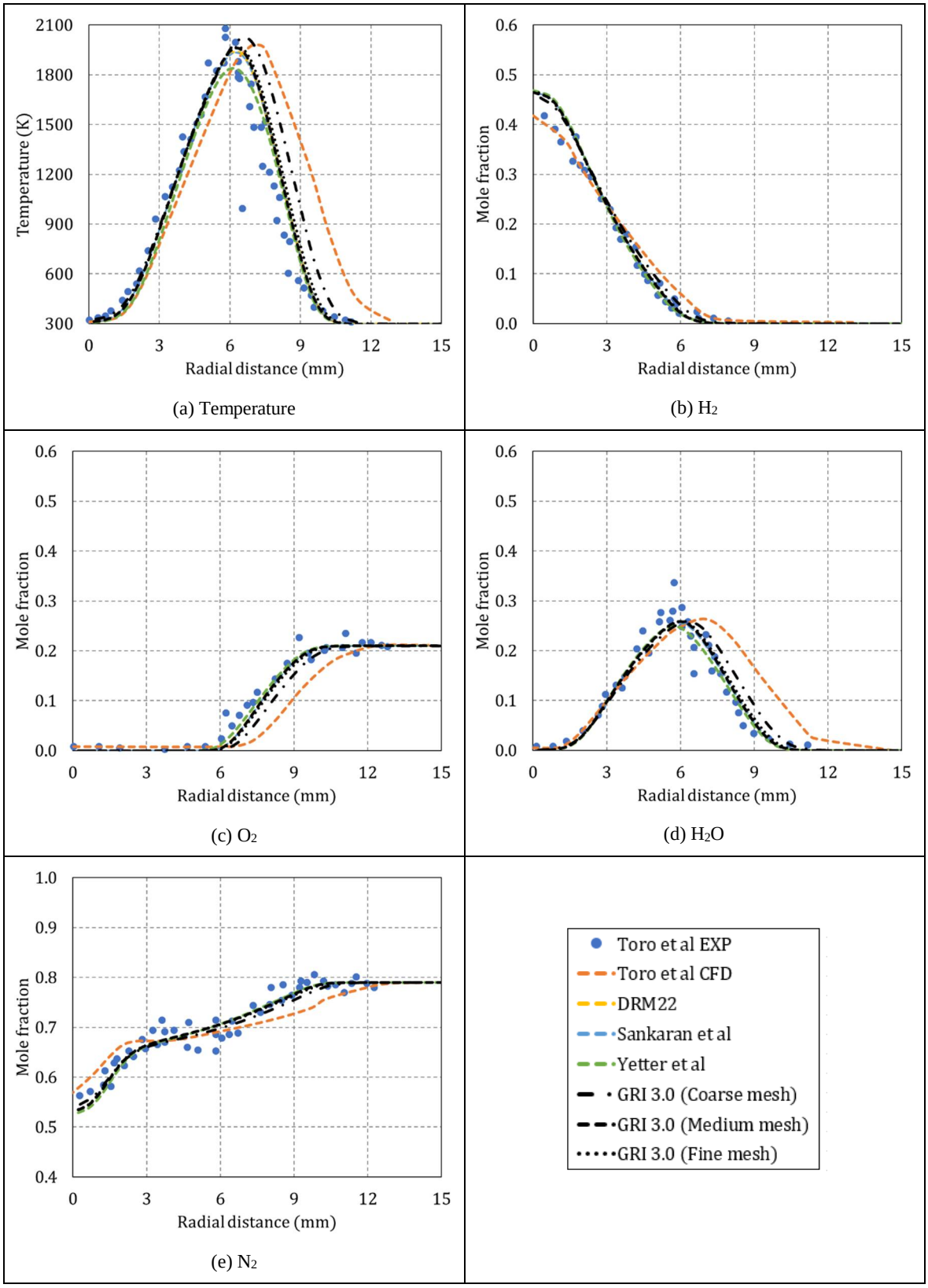

Figure 4-3 Radial temperature and species profile at 10 mm above the fuel exit

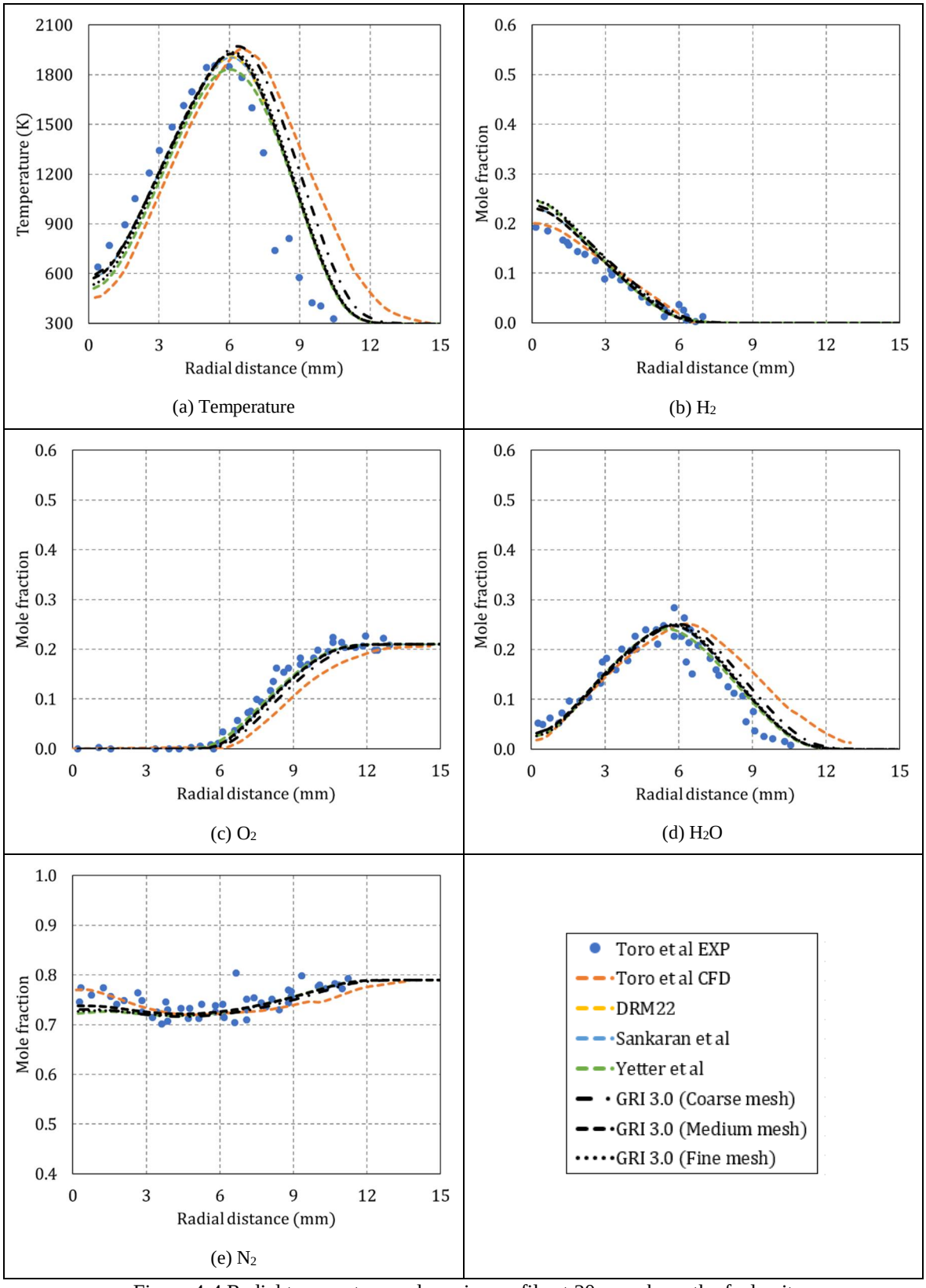

Figure 4-4 Radial temperature and species profile at 20 mm above the fuel exit

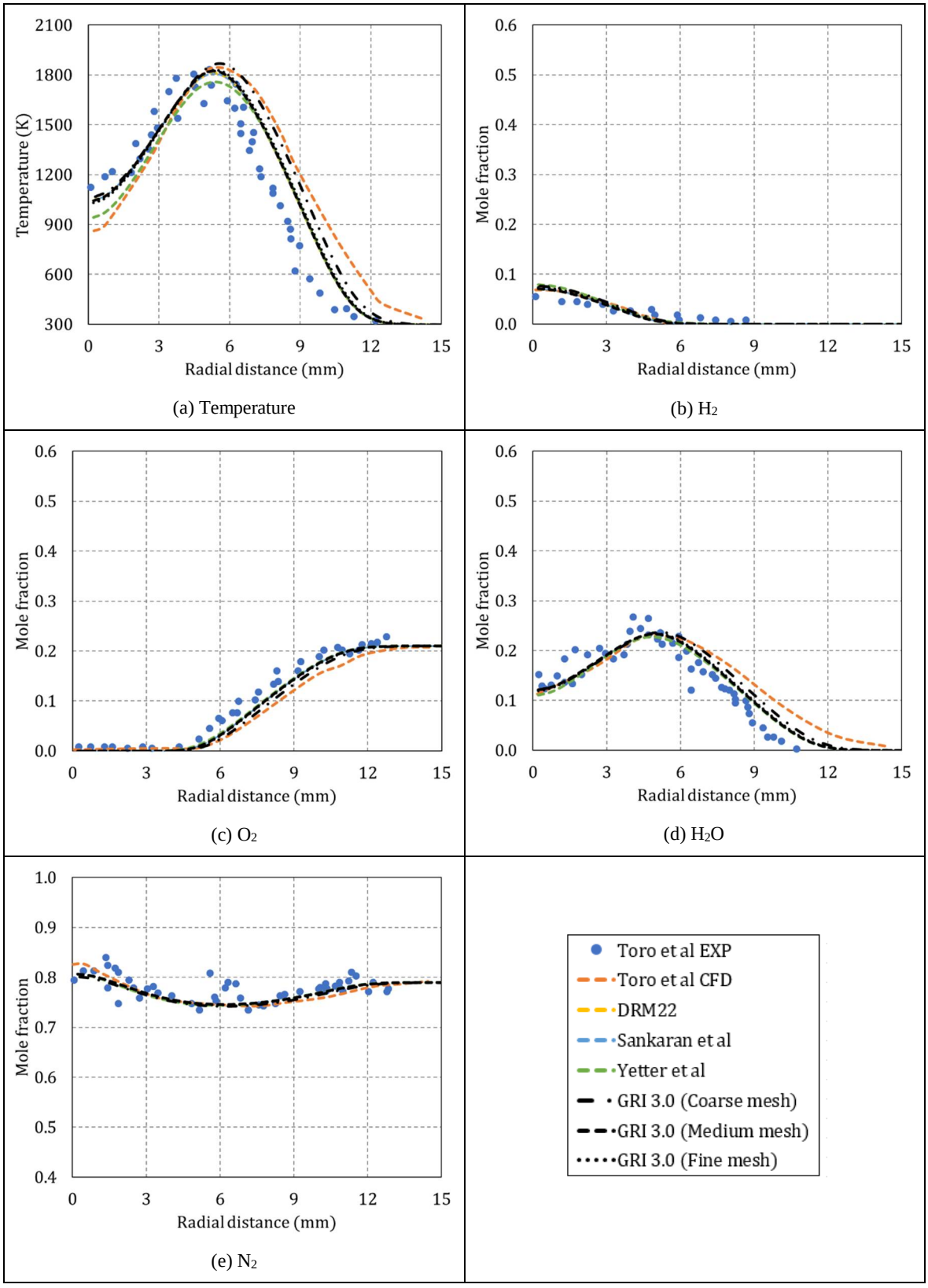

Figure 4-5 Radial temperature and species profile at 30 mm above the fuel exit

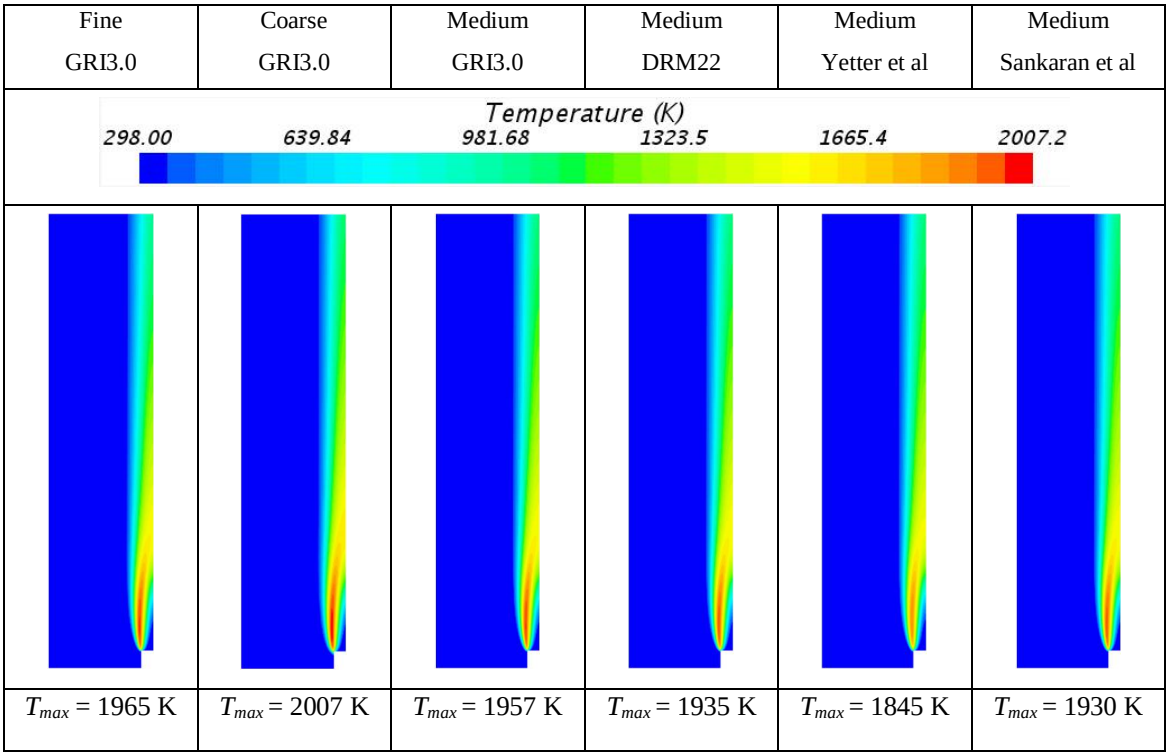

Figure 4-6 Flame structure generated by different CFD models

At 10 mm above the fuel exit, Figure 4-3, the CFD model with Yetter et al. [113] mechanism predicts the lower peak value of the temperature profile than the other models, whereas the CFD model with the coarse mesh overpredicts the temperature profile. The other models also predict a similar temperature profile and thus comparable to the experimental result. The profile of H_2 is computed similarly by all the CFD models at the radial distance more than 1.5 mm. The profile of this species predicted by all the CFD models is slightly higher than the experimental result at the radial distance less than 1.5 mm. All the CFD models and experimental methods provide the analogous radial profile of species O_2, N_2 and H_2O except one with the coarse mesh. The CFD model with the coarse mesh again underpredicts the profile of O_2 at the radial distance between 6 and 10 mm. Also, it overpredicts the radial profile of H_2O at the radial distance between 7 and 10 mm.

At 20 mm above the fuel inlet (Figure 4-4), all the CFD models compute the similar temperature profile to the experimental result at the radial distance less than 6 mm. The over-prediction of the result is seen from all the models at a distance greater than 6 mm. It can also be seen that the lower peak value is computed from the CFD model with Yetter et al. [113] mechanism than the other models. The temperature profile generated by the CFD with the coarse mesh is higher than the other cases at the radial distance above 6 mm. For the species profile, all the CFD models overpredict the profile of H_2 at the radial distance lower

than 2.5 mm but generate the comparable H_2 profile to the experimental result at a higher distance. The profiles of O_2, H_2O, and N_2 are well predicted by all the models at all the distances. Nevertheless, it is again found that the CFD model with the coarse mesh density formulates a slightly lower concentration of O_2 but a higher concentration of H_2O than the other mesh resolutions.

At 30 mm (Figure 4-5), the underprediction of the temperature profile at a radial distance lower than 6 mm and the over-prediction of the profile at above 6 mm are obtained from all the models. Among them, the higher temperature profile is predicted by the coarse mesh CFD model. Generally, a good agreement between the experimental and numerical results is found from all the CFD models for the profiles of H_2, O_2, and N_2. However, for the profile of H_2O, over-prediction is observed from all the models at the radial distance above 6 mm.

4.2.6.2 Flame structure

The flame structure is expressed by the temperature contour plot, as seen in Figure 4-6. The structure of flame generated by all the models is similar; however, the maximum temperature of each model is different. The highest flame temperature is found from the CFD model with the coarse mesh (2007 K) whereas the lowest flame temperature is obtained from the CFD model with the Yetter et al. [113] mechanism (1845 K). Considering the structure, the area on the domain having the highest temperature is above the fuel tube where the fuel and co-flow air stream initially interact, and the combustion is triggered. From the highest temperature area, the flame temperature reduces slightly along the flame front to the axis of the flame. The structure explained is observed from the flames formulated by all the compared models.

4.2.7 The validated model

Analysing the result, all the generated CFD models are capable of predicting the good agreement result comparing to the experimental data for the species distribution of H_2, O_2, H_2O and N_2. In other words, the reaction pathway provided by all the compared chemical reaction mechanism could be used for studying the generation/deconstruction of species due to the combustion of laminar diffusion H_2/N_2 flame. On the other hand, the prediction of temperature performs the good agreement result at the area close to the fuel exit. The difference between the numerical and experimental increases when the distance from the

fuel inlet is longer. As seen, the temperature profile was overpredicted by all the compared CFD models at the axial distance above 20 mm and the radial distance above 6 mm. This could be the impact of utilising the axisymmetric domain where the fluid interaction, thermal diffusion, and thermal radiation are considered in two directions, and there is no change of fluid variables (pressure, velocity etc.) in a circumferential direction. Further, the result is expected to be improved when the simulation is run on three-dimensional model where these parameters are considered

Overall, the results in the validation stage, when compared with the experimental results, show that all the generated CFD models are capable of formulating the laminar diffusion flame of H_2/N_2. However, the level of accuracy of each model is different depending on the chemical reaction mechanism and mesh density. Among them, the CFD model with the GRI3.0 mechanism and medium mesh density is selected for the study stage. The benefit of this mechanism is the detailed reaction pathway, which also includes the formation of NO_x emission; e.g. thermal and prompt NO_x formations. On the other hand, the medium mesh density level was sufficient to provide a reliable result with the lower computational cost. It is found that the temperature and species profiles computed by the CFD model with both the fine and medium mesh density were similar. They were also closer to the experimental results than the coarse mesh model.

4.3 Effect of H_2 content on flame characteristics

The selected CFD model from the validation stage (medium mesh with GRI3.0 mechanism) is utilised for simulating the flame of H_2/N_2 and pure H_2 (100% H_2). The study examines the effect of three parameters which are (i) H_2 content ($\dot{v}_{H_2}$), (ii) fuel and co-flow air velocity (V_{avg}), and (iii) concentration of H_2 in the fuel composition in terms of its mole fraction (X_{H_2}). Various aspects affected by these parameters are investigated, such as the flame structure, flame temperature, chemical heat release, species distribution, and NOx emission.

For the H_2/N_2 gas fuel, the value of $\dot{v}_{H_2}$ increases when the value of either V_{avg} or X_{H_2} is higher. Therefore, the effect of $\dot{v}_{H_2}$ could be illustrated by varying V_{avg} or X_{H_2} and observing the change of flame characteristics. This method results in the formulation of 12 flames with various values of X_{H_2}(0.25 - 1 in mole fraction) and V_{avg} (0.25 - 0.75 ms^{-1}). As seen, the flame of pure H_2 is also formulated at this range of fuel and co-flow air velocity. The details

regarding the fuel stream such as the flow velocity, fuel composition, and content of each species supplied into combustion are shown in Table 4-3.

Table 4-3 Composition, volume flow, and velocity of fuel and air of all simulated flames

Flame	X_{H_2}	X_{N_2}	V_{avg} (ms^{-1})	$\dot{v}_{H_2}$ (cm^{3}s^{-1})	$\dot{v}_{N_2}$ (cm^{3}s^{-1})	$\dot{v}_{total}$ (cm^{3}s^{-1})
Flame A	0.25	0.75	0.25	3.97	11.93	15.9
Flame B	0.5	0.5	0.25	7.95	7.95	15.9
Flame C	0.75	0.25	0.25	11.93	3.97	15.9
Flame D	1	0	0.25	15.9	0	15.9
Flame E	0.25	0.75	0.5	7.95	23.85	31.8
Flame F	0.5	0.5	0.5	15.9	15.9	31.8
Flame G	0.75	0.25	0.5	23.85	7.95	31.8
Flame H	1	0	0.5	31.8	0	31.8
Flame I	0.25	0.75	0.75	11.93	35.77	47.7
Flame J	0.5	0.5	0.75	23.85	23.85	47.7
Flame K	0.75	0.25	0.75	35.77	11.93	47.7
Flame L	1	0	0.75	47.7	0	47.7

Table 4-4 Category of flames

Resolution	**Enrich N_2**	**Equal H_2/N_2**	**Enrich H_2**	**Pure H_2**	V_{avg} (ms^{-1})
Flame set I	A	B	C	D	0.25
Flame set II	E	F	G	H	0.5
Flame set III	I	J	K	L	0.75
X_{H_2}	0.25	0.5	0.75	1	

The effect of $\dot{v}_{H_2}$ is projected by comparing the results of different flames. The impact of X_{H_2} is illustrated by studying the flames formulated by the same V_{avg} but with different fuel composition (different X_{H_2}). The role of V_{avg} is obtained from the comparison of flames generated from the same fuel composition (same X_{H_2}). The simulated flames are categorised based on X_{H_2} and V_{avg} to prevent any confusion and simplify the analysis as seen in Table 4-4. The flames generated based on the same fuel composition (same X_{H_2}) but with different V_{avg} are grouped for projecting the effect of V_{avg} as enrich N_2 flame (X_{H_2} = 0.25), equal H_2/N_2 flame (X_{H_2} = 0.5), enrich H_2 flame (X_{H_2} = 0.75), and a pure H_2 flame (X_{H_2} = 1). Conversely, the flames generated by fuel having the same V_{avg} are categorised into three

flame sets for studying the effect of X_{H_2}; flame set I (V_{avg} = 0.25 ms^{-1}), flame set II (V_{avg} = 0.5 ms^{-1}), and flame set III (V_{avg} = 0.75 ms^{-1}).

4.3.1 **Flame appearance**

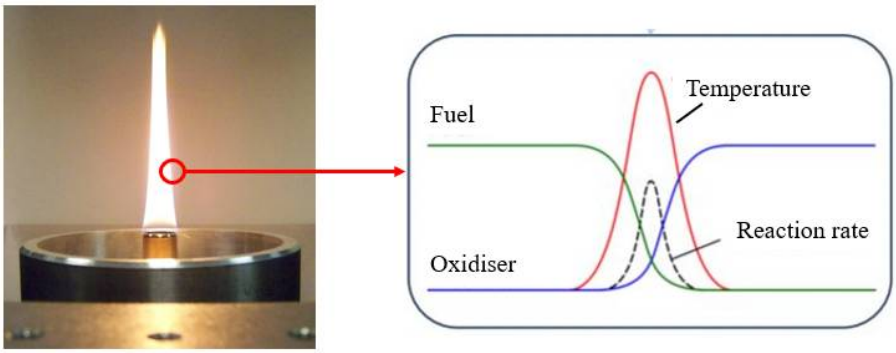

Figure 4-7 The profiles of fuel, oxidiser, flame temperature, and reaction rate at the flame front

According to the theory of diffusion flame, the flame front is a boundary of the flame where the stoichiometric combustion occurs (mixture fraction (z) = 1). The fuel and oxidiser concentration profile, reaction rate, and temperature at the flame front are illustrated in Figure 4-7. As seen, the reaction rate and the temperature are at the peak value at the flame front. For the single step global reaction, the flame front could be simply computed based on the value of mixture fraction. This method could be difficult when the simulation relates to several steps of reactions. In such a case, the flame front line could be drawn based on the peak temperature. The line is formulated by the zero-temperature gradient method; i.e. the grids on the domain having the zero-temperature gradient are connected to form a flame front line. These grids have the highest temperature at each vertical (y-direction) and horizontal (x-direction) levels of the created grid system, as presented in the mesh generation section. As these grids have the peak temperature, their positions are hence the location where the stoichiometric combustion of multi-steps chemical reaction occurs. Connecting them forms the flame front line or the stochiometric contour. The dimension and shape of the formulated flames are presented on the temperature contour plots, as shown in Figure 4-8.

The comparison of the dimension between flames in the same flame set is presented in Figure 4-9. As seen, the shape of all the simulated flames is almost downward parabolic. The flame front line covers the distance from the outer of the fuel exit tube, passes through the axis and finishes on the other side of the outer fuel exit tube. The flame dimension (length and width)

is obtained from the extraction of the flame front in Figure 4-9 and presented in Figure 4-10a. Furthermore, the flame size or volume is computed by integrating the area inside the flame front line around the flame axis. The comparison of the flame size as well as $\dot{v}_{H_2}$ of all the simulated flames are presented in Figure 4-10b.

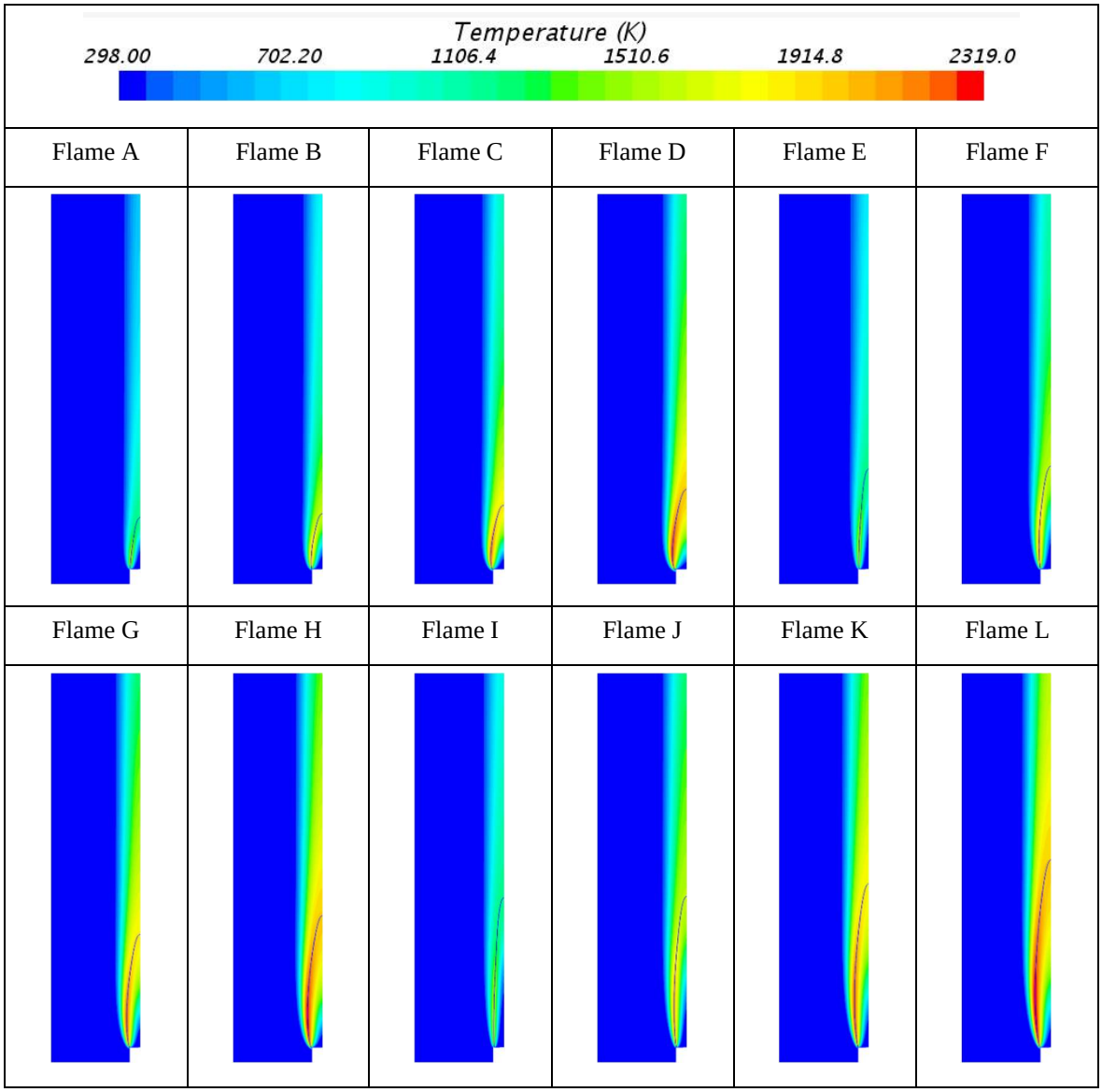

Figure 4-8 Temperature contour

Analysing Figure 4-10a-b reveals the effect of X_{H_2}, V_{avg}, and $\dot{v}_{H_2}$ on the flame appearance. The effect of X_{H_2} is projected by analysing flame set I, II, and III solely. In every flame set, the longest and widest flame is pure H_2 (flame D, H, and L) while the shortest and narrowest flame is the enrich N_2 flames (flame A, E, and I). The average increasing rate of the flame length for flame set I, II, and III is 0.46, 0.51, 0.58 cm per an increment of X_{H_2} = 0.25 respectively. On the other hand, flame width escalates at the rate of 0.160, 0.186, and 0.214

cm per increment of X_{H_2} = 0.25 for flame set I, II, and III, respectively. The result illustrates that the flame with the higher X_{H_2} is longer and wider. Consequently, the flame with the higher X_{H_2} has a larger flame size as seen in Figure 4-10b. An average increasing rate of flame size per an increment of X_{H_2} = 0.25 for flame set I, II, and III is 2.84, 6.09, and 9.31 cm^3, respectively.

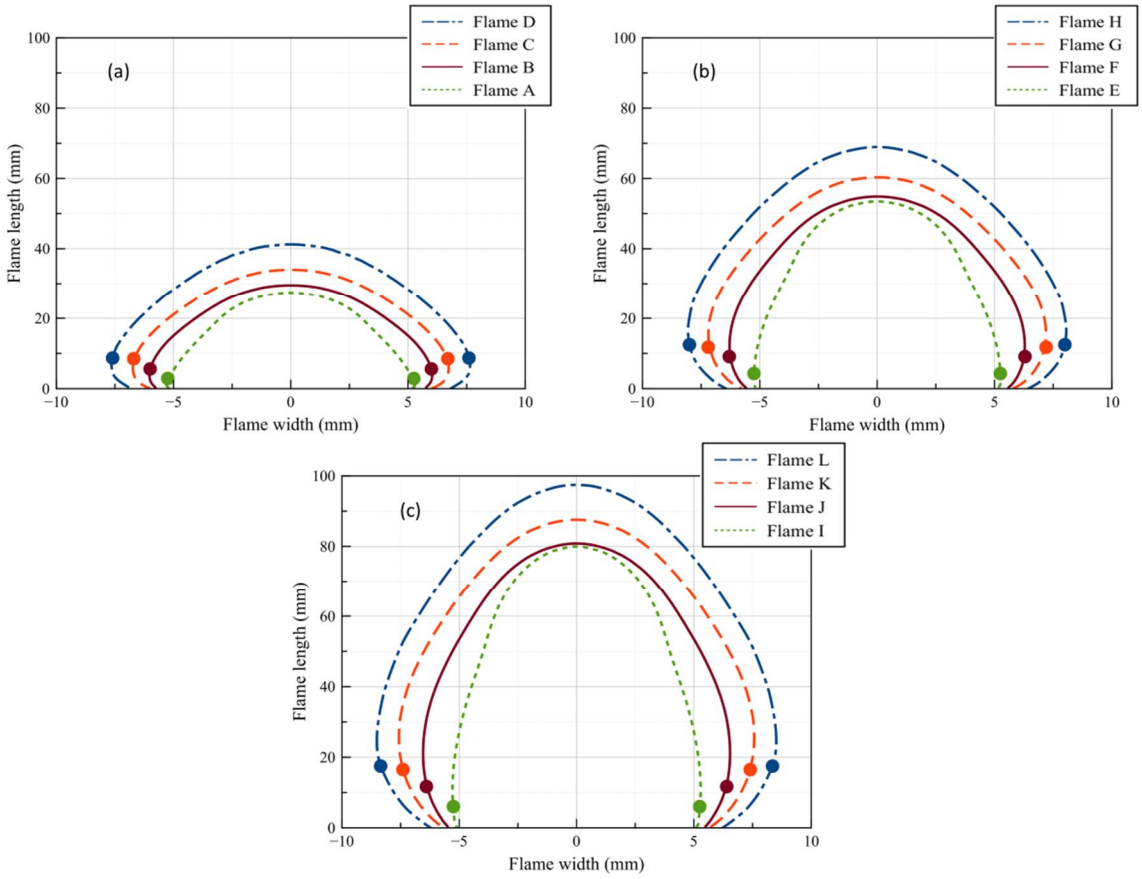

Figure 4-9 Flame dimension

The flames of the same fuel composition, formulated by different V_{avg}, are compared for identifying the impact of V_{avg}. The length and width of the flame are found to be strongly affected by V_{avg}. The flame formulated by the fuel stream with the higher V_{avg} is longer and wider. For an increment of V_{avg} = 0.25 ms^{-1}, the flame length escalates 2.62, 2.56, 2.69, and 2.81 cm for the enrich N_2, equal H_2/N_2, enrich H_2, and pure H_2 flames, respectively. An increasing rate of flame width is 0.004, 0.051, 0.064, and 0.085 cm per increment of V_{avg} = 0.25 ms^{-1} for enrich N_2, equal H_2/N_2, enrich H_2 and pure H_2 in order. As a result, the flame size is larger for the flame formulated by the higher V_{avg}. An average increasing rate for the flame size of the enrich N_2, equal H_2/N_2, enrich H_2, and pure H_2 flames are 1.7, 2.65, 3.64, and 4.95 cm^3 per increment of V_{avg} = 0.25 ms^{-1}, respectively.

(a)

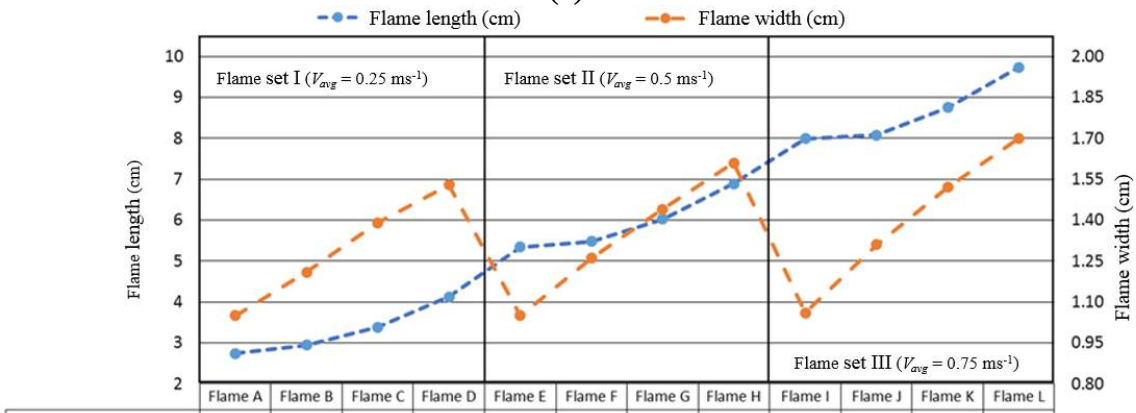

	Flame A	Flame B	Flame C	Flame D	Flame E	Flame F	Flame G	Flame H	Flame I	Flame J	Flame K	Flame L
Flame length (cm)	2.74	2.95	3.38	4.12	5.34	5.48	6.03	6.89	7.99	8.08	8.75	9.74
Flame width (cm)	1.05	1.21	1.39	1.53	1.05	1.26	1.44	1.61	1.06	1.31	1.52	1.70
X_{H_2}	0.25	0.5	0.75	1	0.25	0.5	0.75	1	0.25	0.5	0.75	1

(b)

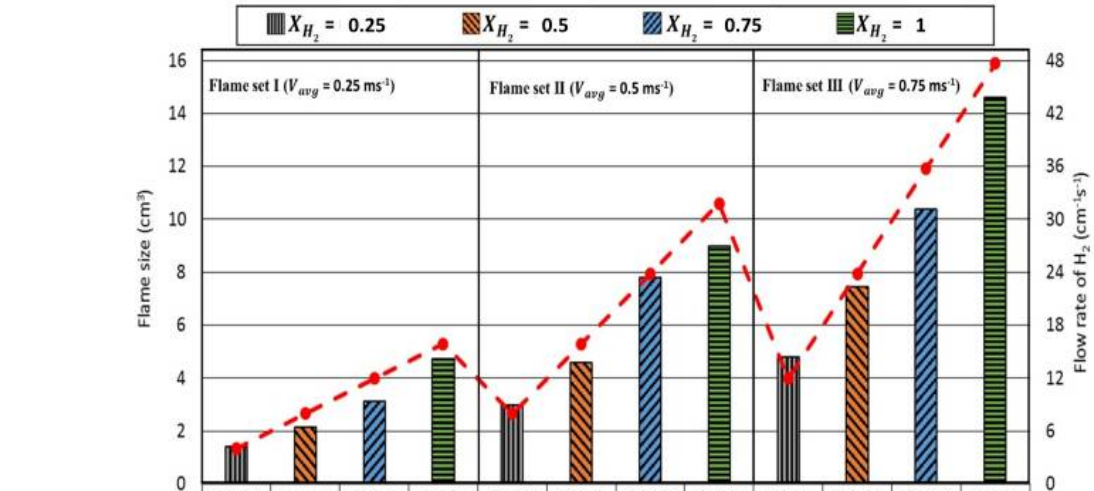

	Flame A	Flame B	Flame C	Flame D	Flame E	Flame F	Flame G	Flame H	Flame I	Flame J	Flame K	Flame L
Flame size (bar)	1.39	2.14	3.12	4.71	2.97	4.60	7.79	8.99	4.79	7.44	10.38	14.62
Flow rate of H_2 content (line)	3.97	7.95	11.93	15.9	7.95	15.9	23.85	31.8	11.93	23.85	35.77	47.7

Figure 4-10 (a) Flame length and maximum flame width, and (b) Flame size and volume flow rate of H_2

On the other hand, the effect of H_2 content ($\dot{v}_{H_2}$) is less significant than X_{H_2} and V_{avg}. The flame formulated by the lower $\dot{v}_{H_2}$ in the fuel stream could be longer and wider than the flame formulated by the higher value. For example, the length of flame E which $\dot{v}_{H_2}$ = 7.95 cm^{3}s^{-1} is longer than flame C which $\dot{v}_{H_2}$ = 11.93 cm^{3}s^{-1} and flame D which $\dot{v}_{H_2}$ = 15.9 cm^{3}s^{-1}. Also, the width of flame C is wider than flame F which $\dot{v}_{H_2}$ = 15.9 cm^{3}s^{-1} and flame J which $\dot{v}_{H_2}$ = 23.85 cm^{3}s^{-1}. Nevertheless, the relation between $\dot{v}_{H_2}$ and flame size is direct proportion; i.e. the flame supplied with the higher $\dot{v}_{H_2}$ has a larger flame size. As seen, the largest flame is flame L (14.6 cm^3) which has the highest $\dot{v}_{H_2}$ as 47.7 cm^{3}s^{-1}, and the smallest

flame is flame A (10.4 cm^3), which has the lowest $\dot{v}_{H_2}$ (3.97 cm^3s^{-1}) among all the formulated flames.

4.3.2 **Flame temperature**

In Figure 4-8 (the temperature contour plot), the position of the maximum flame temperature on the flame front line is slightly above the outer region of the fuel exit tube. The position of the maximum temperature is plotted as solid circles on the flame front line, as seen in Figure 4-9. The effect of X_{H_2}, V_{avg} and $\dot{v}_{H_2}$ on the position of the maximum temperature are in the same direction. The position is at a higher vertical distance from the fuel exit, and longer horizontal distance from the axis when the value of X_{H_2}, V_{avg} and $\dot{v}_{H_2}$ are higher.

The flame temperature of all the simulated flames is presented and compared with their adiabatic flame temperature in Figure 4-11a. Except the enrich N_2 flames, the flame temperature of all the other flames is lower than their adiabatic temperature. Flame L (pure H_2 flame with V_{avg} = 0.75 ms^{-1}) provides the highest flame temperature as 2319 K whereas the lowest flame temperature is computed from flame A (enrich N_2 flame with V_{avg} = 0.25 ms^{-1}) as 1552 K. The difference between the adiabatic flame temperature and flame temperature is computed as ~36 K for the enrich N_2 flame, ~68 K for the equal H_2/N_2 flame, ~96 K for the enrich H_2 flame, and ~91 K for the pure H_2 flame.

The effect of X_{H_2} on the flame temperature is pointed out in a similar direction for every flame set, i.e. the higher X_{H_2} leads to a higher flame temperature. The average increasing rate of flame temperature per increment of X_{H_2} = 0.25 for flame set I, II, and III is 231, 243, 249 K, respectively. The role of V_{avg} is identified when the flames of fuel having the same fuel composition are compared. The higher value of this parameter causes a higher flame temperature. The flame temperature escalates 10, 34, 39, and 37 K in average for enrich N_2 flame, equal H_2/N_2 flame, enrich H_2 flame, and pure H_2 flame respectively when V_{avg} escalates as 0.25 ms^{-1}. The result projects the weak role of $\dot{v}_{H_2}$ in the flame temperature. There are several cases that the flame formulated by the fuel stream with a lower $\dot{v}_{H_2}$ have a higher maximum flame temperature than one generated by fuel stream having a higher value of $\dot{v}_{H_2}$. For example, flame C ($\dot{v}_{H_2}$ = 11.93 cm^3s^{-1}) has a higher flame temperature than flame F with ($\dot{v}_{H_2}$ = 15.9 cm^3s^{-1}).

(a)

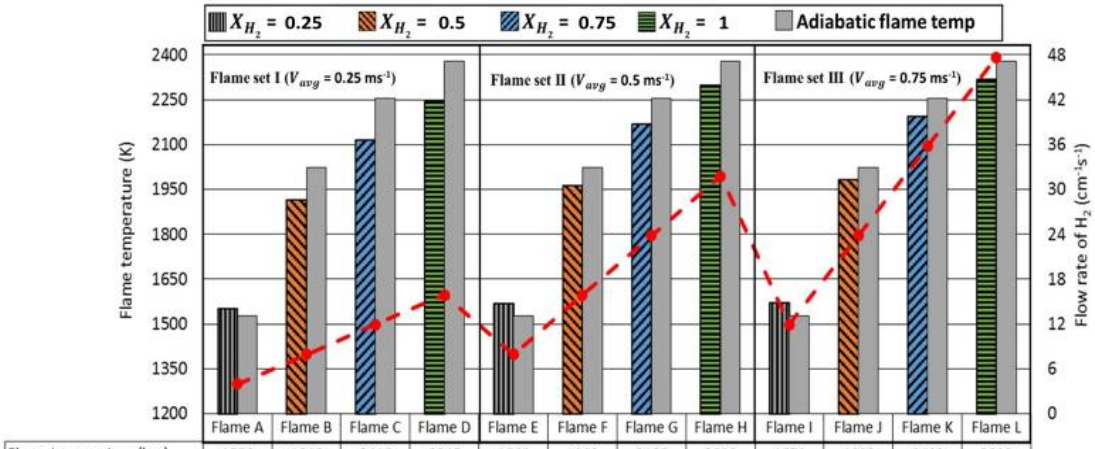

	Flame A	Flame B	Flame C	Flame D	Flame E	Flame F	Flame G	Flame H	Flame I	Flame J	Flame K	Flame L
Flame temperature (bar)	1552	1915	2115	2245	1568	1962	2169	2298	1572	1983	2193	2319
Adiabatic temp (bar)	1528	2022	2255	2379	1528	2022	2255	2379	1528	2022	2255	2379
Flow rate of H_2 content (line)	3.97	7.95	11.93	15.9	7.95	15.9	23.85	31.8	11.93	23.85	35.77	47.7

(b)

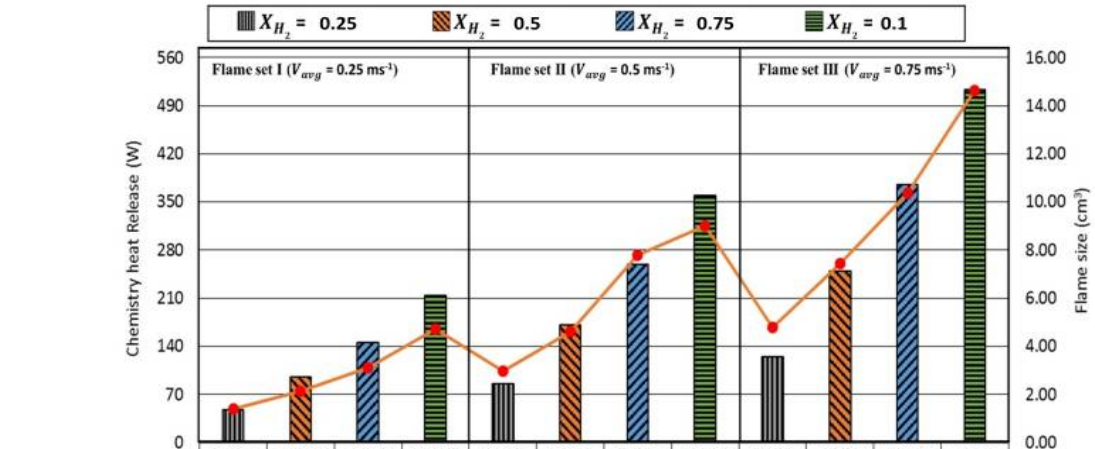

	Flame A	Flame B	Flame C	Flame D	Flame E	Flame F	Flame G	Flame H	Flame I	Flame J	Flame K	Flame L
Chemistry heat Release (bar)	48	95.4	146	214	85.86	171.35	259.32	360	124.5	249	375.64	514
Flame size (line)	1.39	2.14	3.12	4.71	2.97	4.60	7.79	8.99	4.79	7.44	10.38	14.62

Figure 4-11 (a) Flame temperature, adiabatic flame temperature, and flow rate of H2 content; (b) Chemical heat release of all flames and flame size

4.3.3 **Chemical heat release and heat flux generated by flames**

The total chemical heat release of the flame is computed by combining the heat released from the chemical reaction of every grid on the simulation domain. The comparison of the total chemical heat release of all flames is shown in Figure 4-11b. Among them, flame A (enrich N_2 flame with V_{avg} = 0.25 ms^{-1}) generates the lowest total chemical heat release as 48 W whereas the highest value (514 W) is obtained from flame L (pure H_2 with V_{avg} = 0.75 ms^{-1}). The analysis of flame chemical heat release establishes the relation between this

parameter and X_{H_2}, V_{avg} and $\dot{v}_{H_2}$. The higher value of these parameters causes the higher chemical heat released from flame. An average increasing rate of the chemical heat release is 56, 91, and 130 W per increment of X_{H_2} = 0.25 for flame set I, II, and III, respectively. The average increasing rate for every 0.25 ms^{-1} is 40, 75, 110, and 150 W for enrich N_2, equal H_2/N_2, enrich H_2, and pure H_2 flames, respectively. The higher $\dot{v}_{H_2}$ in fuel stream also leads to the total higher chemical heat release from flame. In case that the compared flames have equal $\dot{v}_{H_2}$, one with the higher X_{H_2} provides a higher total chemical heat release. For instance, flame G (enrich H_2) generates a higher total chemical heat release (259 W) than flame J (249 W), which is equal H_2/N_2, though both the flames are formulated at an equal $\dot{v}_{H_2}$ as 23.85 cm^3s^{-1}.

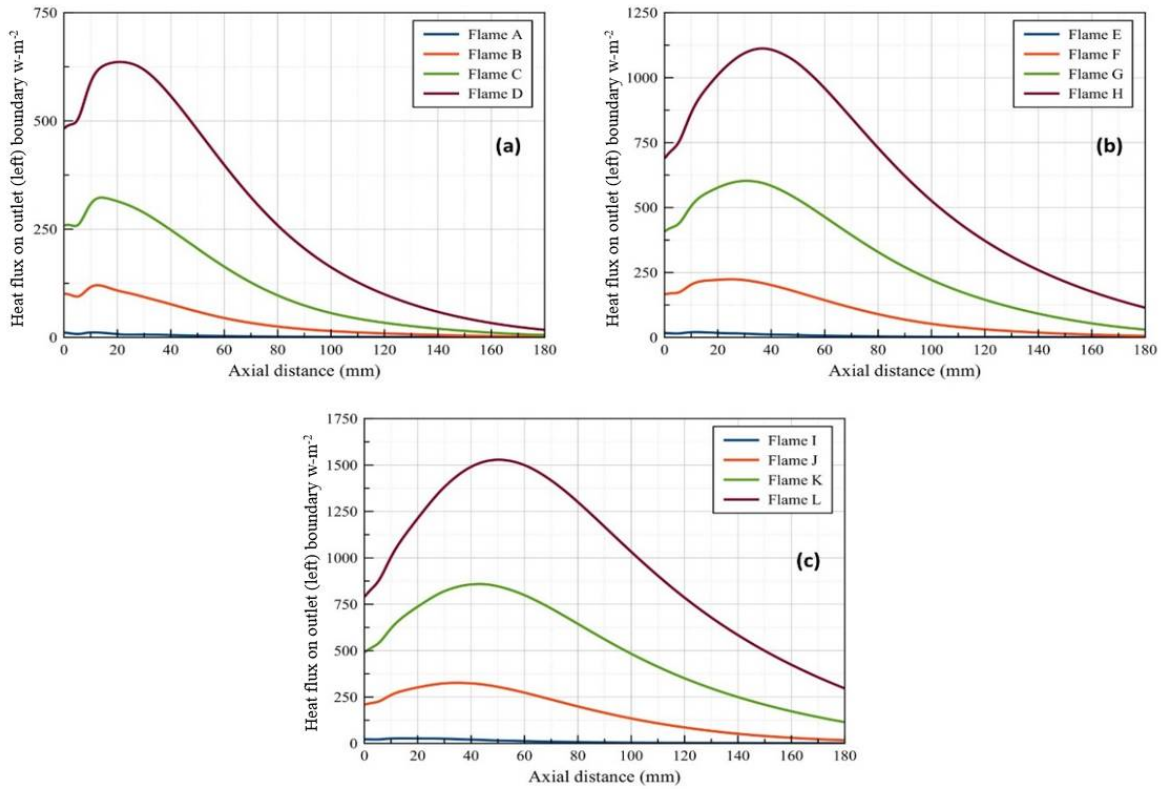

Figure 4-12 Heat flux profile on the outlet (left) boundary; (a) flames in flame set I, (b) flames in flame set II (c) flames in flame set III

The heat flux on the outlet boundary (left boundary) represents the heat generated and transferred from flame. The profile of this parameter of all the studied flames is compared, as seen in Figure 4-12. It is found that the radiative heat flux dominates the value of the heat flux on this boundary. The profile pattern of all the simulated flames is similar. It increases to the peak value then reduces along with the escalation of the vertical distance. The effect of X_{H_2}, V_{avg}, and $\dot{v}_{H_2}$ on the peak value are observed. The higher value of these parameters

leads to the higher peak value of the heat flux on the outlet boundary. However, the exception is found from the comparison between flame C and F. In such case, flame C ($\dot{v}_{H_2}$ = 11.93 cm^3s^{-1}) generates the higher heat flux profile and peak value than flame F ($\dot{v}_{H_2}$ = 15.9 cm^3s^{-1}). Among all the studied flames, the flame generating the highest peak of heat flux is flame L (1528 W/m^2) whereas one that produces the lowest value is flame A (11.42 W/m^2).

4.3.4 **Species distribution**

The distribution of species H_2, N_2, O_2, and H_2O along the axial and radial distance are studied. The axial plot of these species of all the H_2/N_2 flames at different V_{avg} is presented in Figure 4-13a-d while the radial plots of them at 9 mm above the fuel exit is shown in Figure 4-14a-d. H_2, which is a primary fuel species, is consumed significantly after the fuel is injected into combustion. As seen, H_2 concentration reduces dramatically at the higher axial distance. The chemical reactions related to H_2 convert this reactant to other product species. It is also noticed that the profile of H_2 approaches zero (fully consumed) slightly under the flame front. The position where the concentration of H_2 approaches zero is strongly affected by X_{H_2} and V_{avg}. The higher position is obtained when the value of these parameters is higher. The similar direction of the result is seen on the radial plot, i.e. the concentration of H_2 decreases along with the radial distance and becomes zero slightly before the flame front line.

The species N_2 is supplied to the combustion on both the fuel and oxidiser streams. The concentration of this species increases along with the axial and radial distances once it was injected into combustion. On the axis, Figure 4-13d, an increase in the concentration of N_2 is significant and tends to 0.79, which is equal to the concentration of N_2 in the air stream. The different profile pattern is seen in the enrich H_2 and equal H_2/N_2 flames. Concentration profile of N_2 of these fuel increases to the peak value and decreases to 0.79. The peak value is approximately 0.81 for the equal H_2/N_2 (flame B, F, and J), and 0.91 for enrich H_2 flame (flame C, G, and K). On the radial plot, the concentration of N_2 rises significantly along with an increase of the radial distance and tends to approach 0.79. The profile of flames in the flame set I (flame A, B, and C) is slightly different. The profile of these flames escalates to the peak value 0.86, 0.83, and 0.82 for flame A, B, and C, respectively. The value then reduces to 0.79. It is noticed that the level selected for monitoring the radial profile is higher than the position of the maximum temperature of the flames in flame set I. Additionally, the

role of species N_2 which is non-combustible species is confirmed from its axial and radial profiles. As seen, the concentration of this species increases and approaches the same concentration of N_2 in the air outside the reaction zone (mole fraction = 0.79). In addition, the fluctuation of the N_2 profile occurs when N_2 supplied in the co-flow air and fuel streams are encountered.

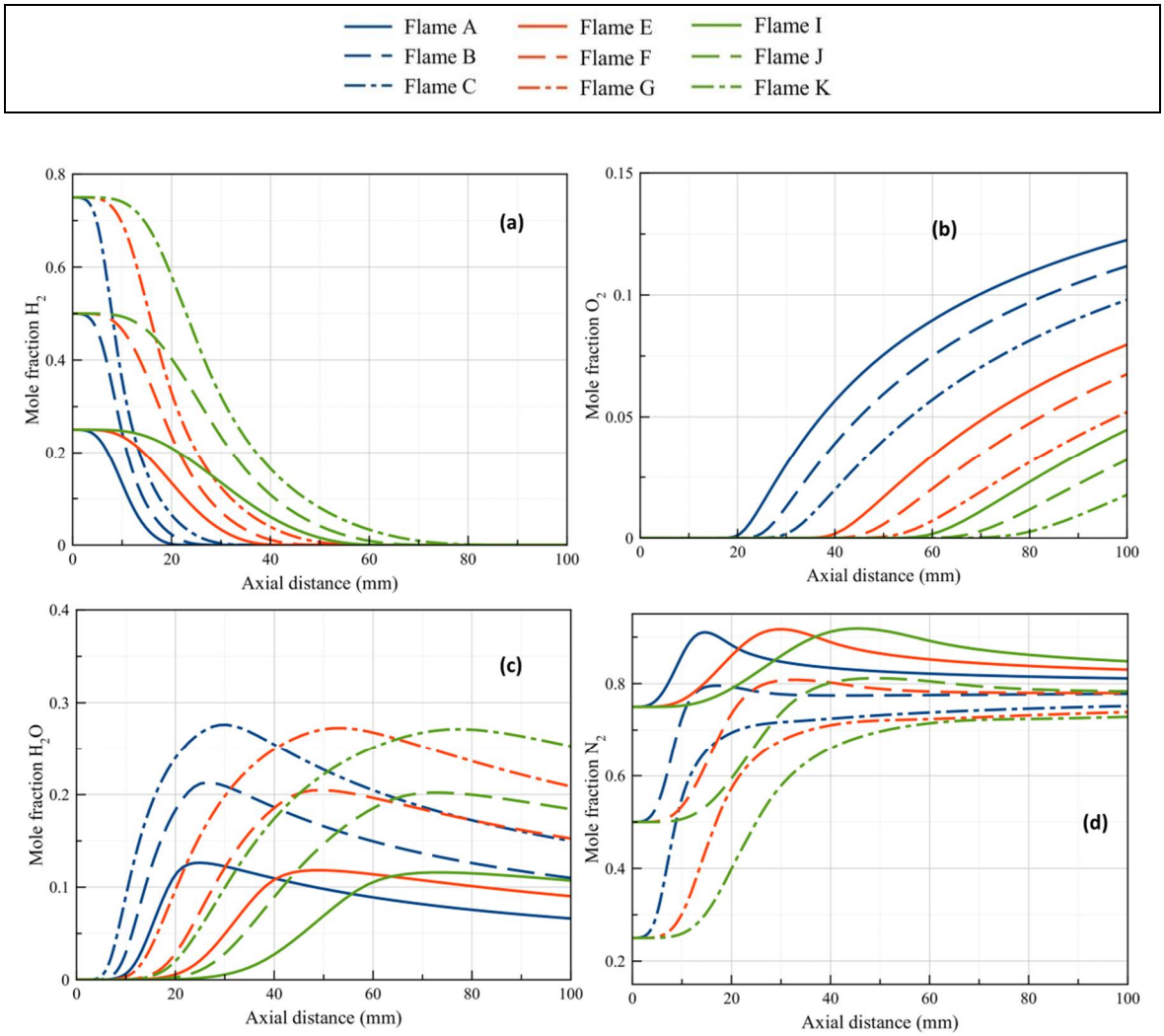

Figure 4-13 Species axial profiles of all the simulated flames (a) H_2; (b) O_2; (c) H_2O; (d) N_2

The co-flow air stream supplies O_2 into combustion, and this species is fully consumed at the area close to the flame front. Therefore, its axial and radial species profiles appear at the position close to and inside the flame front line, as shown in Figure 4-13c and Figure 4-14c. Hence, both X_{H_2} and V_{avg} play a significant role in the profile of O_2. From the position where the concentration of $O_2 > 0$, the profile of this species increases significantly until 0.21 of mole fraction, which is equal to the concentration of this species in the air stream.

In Figure 4-13b and Figure 4-14b, the profile of H_2O concentration increases from zero to the peak value then reduces to zero again. The position of the peak value is close to and inside the flame front line. This position is obtained differently from different flames. For example, flame C (enrich H_2) provides the highest peak value among all the simulated flames as 0.28 in terms of mole fraction on both the axial and radial plots. Conversely, the lowest peak value computed in flame A (enrich N_2) is 0.13 and 0.15 from the axial and radial plots, respectively. This result, therefore, projects the role of H_2 as a major reactant of H_2O. As also seen, the flame of enrich H_2 has a higher profile of H_2O than the flame of equal H_2/N_2 and enrich N_2, respectively.

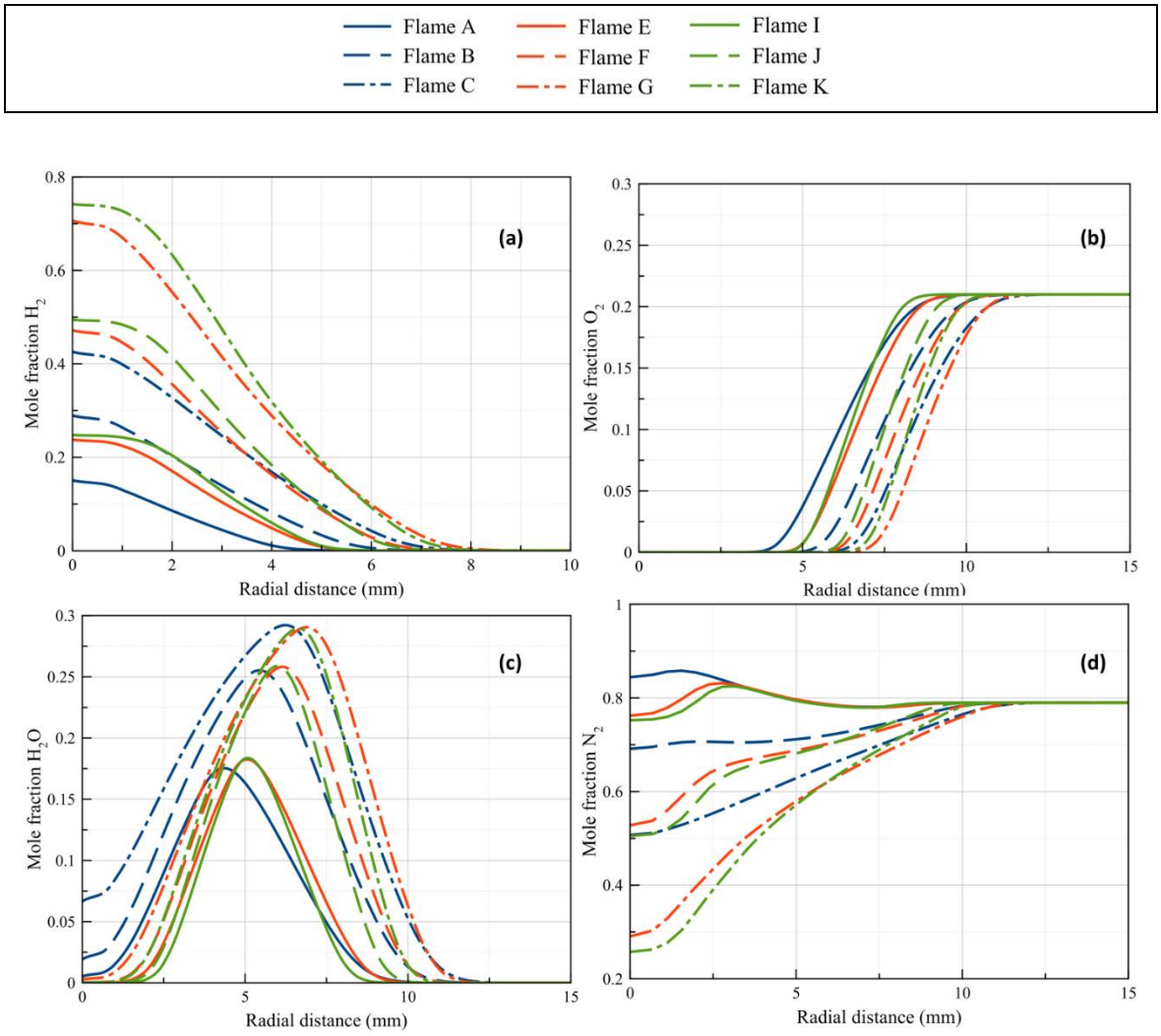

Figure 4-14 Species radial profiles at 9 mm above fuel exit of all the simulated flames (a) H_2; (b) O_2; (c) H_2O; (d) N_2

4.3.5 **NOx emission**

(a)

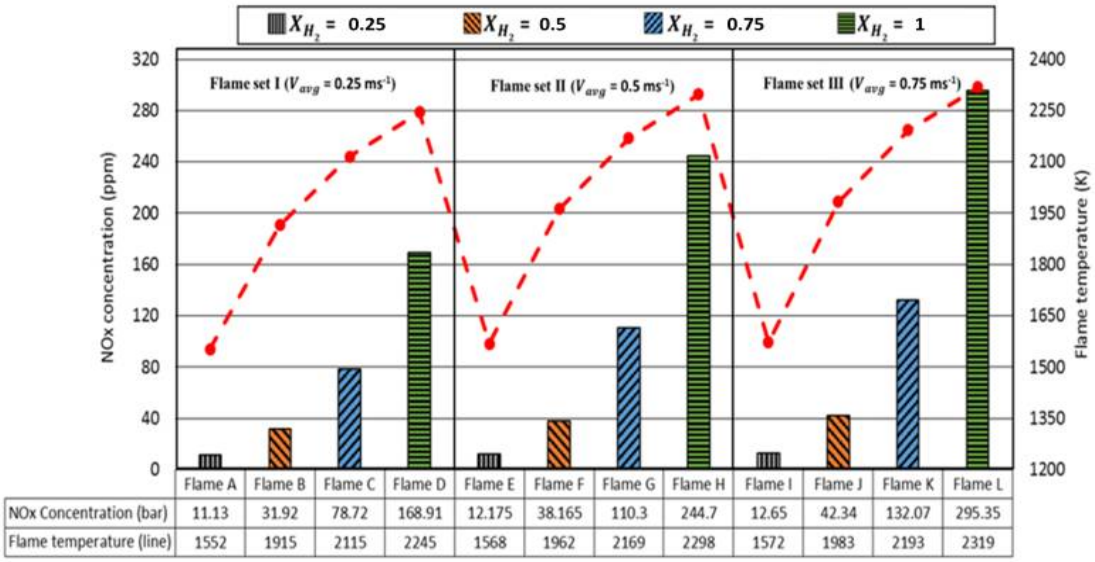

	Flame A	Flame B	Flame C	Flame D	Flame E	Flame F	Flame G	Flame H	Flame I	Flame J	Flame K	Flame L
NOx Concentration (bar)	11.13	31.92	78.72	168.91	12.175	38.165	110.3	244.7	12.65	42.34	132.07	295.35
Flame temperature (line)	1552	1915	2115	2245	1568	1962	2169	2298	1572	1983	2193	2319

(b)

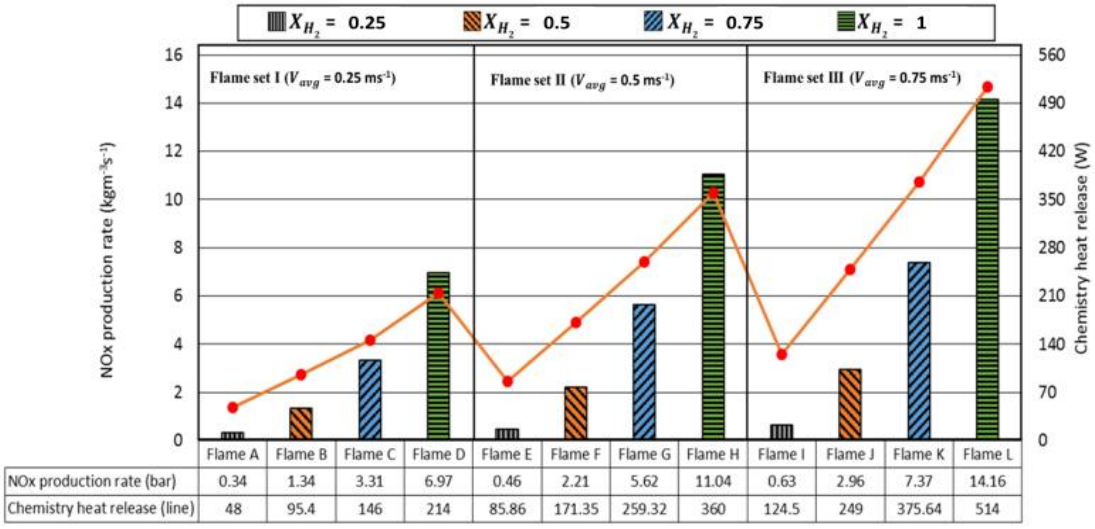

	Flame A	Flame B	Flame C	Flame D	Flame E	Flame F	Flame G	Flame H	Flame I	Flame J	Flame K	Flame L
NOx production rate (bar)	0.34	1.34	3.31	6.97	0.46	2.21	5.62	11.04	0.63	2.96	7.37	14.16
Chemistry heat release (line)	48	95.4	146	214	85.86	171.35	259.32	360	124.5	249	375.64	514

Figure 4-15 (a) Maximum concentration of NO_x and maximum temperature; (b) NO_x production rate and H_2 content

The benefit of utilising GRI3 reaction mechanisms is the prediction of NO_x emission formation based on the thermal and prompt NO_x formation mechanisms [143]. In this work, the terms NO_x refers to species NO and NO_2. The maximum concentration and flame temperature are plotted together to project the relationship between these parameters in Figure 4-15a. The significant role of flame temperature on the concentration of NO_x is observed; the flame that formulates a higher flame temperature also generates a higher

maximum NO_x concentration. According to this, the higher value of either X_{H_2} or V_{avg}, which causes a higher flame temperature also promotes the NO_x concentration. The effect of these parameters is analysed in detail. The result shows that an average per increment of X_{H_2} = 0.25 for flame set I, II, and III is 72.67, 100.33, and 120.60 ppm, respectively. On the other hand, it is 11.98, 37.48, 107.03, and 236.32 ppm per increment of V_{avg} as 0.25 ms^{-1} for the enrich N_2 flame, equal H_2/N_2 flame, enrich H_2 flame, and pure H_2 flame, respectively. Among all the simulated flames, Flame L has the highest maximum NO_x concentration (295.35 ppm) while flame K has the lowest maximum concentration (11.13 ppm).

As X_{H_2} and V_{avg} play a significant role in the concentration of NO_x, the effect of both parameters on the production rate of NO_x are studied in more detail. The calculation of NO_x production rate is processed by integrating the summation of the production rates of NO and NO_2 on all the grids around the domain and presented in Figure 4-15b. For flame set I, II, and III, an increment of X_{H_2} as 0.25 results in the average increasing rate of 2.99, 4.83, 6.28 $kg\text{-}m^{-3}s^{-1}$, respectively. For the flame of the same fuel composition, the average increasing rate is 0.47, 2.17, 5.43, and 10.72 $kg\text{-}m^{-3}s^{-1}$ per V_{avg} as 0.25 ms^{-1} for the enrich N_2, equal H_2/N_2, enrich H_2, and pure H_2 flames, respectively. In contrast, the analysis of H_2 content ($\dot{v}_{H_2}$) on NO_x concentration and production rate are not processed since the role of $\dot{v}_{H_2}$ on flame temperature is insignificant.

4.4 Discussion

The laminar co-flow diffusion flame of H_2/N_2 and H_2 are simulated for identifying the impact of H_2 content in fuel stream ($\dot{v}_{H_2}$) on the flame characteristics. The key finding is discussed as follows:

The difference in the CFD result of Ref [2] and the one generated in this work are observed. The maximum difference in flame temperature and mole fraction of focused species (H_2, N_2, H_2O, and O_2) are ~150 K and 0.15, respectively. This finding could be explained by several factors. Firstly, the properties of related species (such as the dynamic viscosity, molecular diffusivity, thermal conductivity, and thermal diffusion) are defined by different methods. Secondly, the fluid interaction between the fuel tube and the co-flow air is considered for the newly generated CFD model. Lastly, the chemical reaction mechanism supplied into the finite rate chemical model of these two works are also different; e.g. hydrogen-oxygen sub-

mechanism of GRI2.11 [144] containing nine species were utilised in Toro et al. [2] while a full GRI3.0 [111] reaction mechanism is utilised in this work. Consequently, the CFD newly formulated in this work provides a better prediction of the temperature and species profiles along with the axial and radial distances.

In theory, the temperature change due to the combustion is dominated by the heat released from the chemical reaction. The direction of the CFD result obtained is hence expected since the fuel composition is the key factor. Increasing the concentration of H_2 and reducing the concentration of N_2 have a strong impact on an escalation of flame temperature since the chemical heat release is affected directly. The higher velocity encourages the chance of the collision between particles resulting in the greater diffusion rate and finally the higher flame temperature. H_2 with a higher diffusive property than the other combustible species play a significant role in promoting this interaction resulting in a higher flame temperature. On the other hand, the higher velocity does not affect the chemical reaction and only the small increase in flame temperature is found. This finding also explains the weak impact of $\dot{v}_{H_2}$ on flame temperature. As seen, flame C ($\dot{v}_{H_2}$= 11.93 cm^3s^{-1}, X_{H_2} = 0.75, and V_{avg} = 0.25 ms^{-1}) has a higher X_{H_2} than flame F ($\dot{v}_{H_2}$= 15.9 cm^3s^{-1}, X_{H_2} = 0.5, and V_{avg} = 0.5 ms^{-1}). This results in the higher flame temperature although flame C is supplied by the lower content of H_2 ($\dot{v}_{H_2}$).

According to the theory of flame length presented in equation (1) - (4), the higher velocity of fuel increases the volume flow rate of fuel (Q_f) while the higher dilution percentage of N_2 reduces the stoichiometric ratio (S). The higher value of Q_f and S are expected to provide the longer flame length. The impact of H_2 content ($\dot{v}_{H_2}$) in fuel composition is not considered in the theory; thus, the impact of this parameter on flame height is insignificant. As seen in section 4.3.1, the numerical result obtained from the CFD model follows this expectation. Furthermore, the flame length is calculated from the theory and compared with the CFD and experimental result. It is found that the formula introduced by Roper [93], [94] (equation (1)) provides the significantly lower flame length of H_2 and H_2/N_2. For example, the length of flame E, F, G, and H are computed as 20, 22, 23, and 24 mm, respectively. These values are more than 2.5 times lower than the results computed from CFD and experimental result. This finding is anticipated since the flame length formula of Roper [93], [94] was developed based on the hydrocarbon fuels e.g. CH_4 and C_3H_8 which have significantly lower mas diffusion coefficient but higher stoichiometric coefficient than H_2. Therefore, the

modification of the flame length formula for the calculation of flame having H_2 as a major combustible species is required.

The role of H_2 content ($\dot{v}_{H_2}$) in the fuel stream is pointed out throughout the study. This parameter plays a significant role in the flame size (volume of the flame), chemical heat release and heat flux. Thus, escalating $\dot{v}_{H_2}$ in the fuel stream leads to the higher heat generation from the diffusion flame. However, the effect of $\dot{v}_{H_2}$ on the other aspects of the flame characteristics (e.g. the flame dimension, flame temperature, and NO_x formation) are unclear. These aspects of the flame characteristics are found to be dominated by the methods of increasing $\dot{v}_{H_2}$such as an escalation of either or both X_{H_2} and V_{avg}.

As mentioned, the study emphasised the crucial roles of X_{H_2} and V_{avg} on the flame characteristics. It is further found that the higher value of X_{H_2} and V_{avg} enlarges the flame dimension (both length and width), flame size, flame temperature, chemical heat release, and NO_x emission formation. Nevertheless, the level of effect of X_{H_2} and V_{avg} on flame characteristics are different. This difference could be projected from the comparison of the average increasing rate of these flame characteristics when the value of X_{H_2} and V_{avg} increase by 0.25 in the mole fraction and 0.25 ms^{-1} of velocity. The impact of V_{avg} is significantly stronger than X_{H_2} on the increase of the flame length, but weaker on the flame width extension. Regarding the flame size, both parameters (flame width and length) could compensate for the role of each other. In other words, the wider flame could have a larger flame size. As seen from Figure 4-10a for flame length and width and Figure 4-10b for flame size, there are many cases in which the flames have a longer flame length but the smaller flame size. For example, the length of flame E is longer than one of flame C and D, but its size is still smaller. The flame temperature is dominated by X_{H_2} while the effect of V_{avg} on this parameter is considered weak. The heat released due to the chemical reaction is significantly affected by both X_{H_2} and V_{avg}. The analysis of the simulation results in details shows that the flame size and flame temperature, which are directly affected by X_{H_2} and V_{avg}, could compensate each other and strongly affects the total chemical heat release rate from flame. Also, the effect of X_{H_2} on the increase of NO_x formation rate is significantly stronger than the effect of V_{avg} since the formation of NO_x depends on the flame temperature.

The flame generating a higher heat generation capability is preferable. The heat released and transferred are analysed in this work along with the NOx emission. In most cases, the flame

with a higher flame temperature has a higher heat generation capability; thus, the higher NO_x emission is an inevitable side effect. However, some flames formulate the lower NO_x production rate but are capable of generating a higher chemical heat release. This finding reveals the method for decreasing NO_x emission while maintaining the level of heat generation at the preferred level. This method is processed by reducing X_{H_2} while increasing V_{avg}. The expected result is the diffusion flame having the lower flame temperature but larger size. Nevertheless, this technique could also result in an unstable diffusion flame or the transition from the laminar to turbulent flow regime of the fuel stream.

The result obtained in this work extends the study of [78], in which the turbulent diffusion flame of H_2/N_2 was studied. The similar direction of the result in flame temperature and size are obtained for both laminar and turbulent co-flow diffusion flames; i.e. the flame temperature and width are affected strongly by X_{H_2}.

4.5 Conclusion

The flames of H_2 and H_2/N_2 are simulated with a variation in the concentration ratio of H_2:N_2, and the fuel and co-flow air velocity (V_{avg}). The role of H_2 content defined by the volume flow rate of H_2 ($\dot{v}_{H_2}$) supplied into combustion and the factors (X_{H_2} and V_{avg}) controlling the H_2 content ($\dot{v}_{H_2}$) in the fuel stream on various aspects of flame characteristics have been studied. The results show that the higher $\dot{v}_{H_2}$, X_{H_2} and V_{avg} in the fuel stream leads to the larger flame size and higher heat generation. The flame temperature and flame width are dominated by X_{H_2} whereas the flame length is affected strongly by V_{avg}. The flame has a higher flame temperature, also formulates NO_x at a higher rate. Thus, thermal NO_x formation is found to be significant. The heat released due to the chemical reaction is affected by flame size and temperature, which could compensate for the role of each other. According to this, increasing the flame size by rising V_{avg} is an interesting option for escalating the heat generation from flame without a significant increase in NO_x emission.

Chapter 5 Heat generation and emission from syngas/producer gas flames

The study in this chapter focuses on the heat generation and emission from syngas/producer gas flames considering the effects of variations in the fuel composition of this fuel. The flame of syngas/producer gas, hydrogen (H_2), and methane (CH_4) are simulated by the CFD model generated in Chapter 4. Some modifications in the simulation domain are applied to support the flames size of all the studied fuel compositions. The predicted results are analysed to understand the role of each species in the syngas/producer gas composition, e.g. H_2, CO, CH_4, CO_2 and N_2. The heat generation capability and emission formation of the syngas/producer gas flame are assessed by comparing with those of the conventional fuels, such as H_2 and CH_4. In this study, the emission is perceived as a price to pay for a certain amount of heat. Lastly, the discussion and conclusion are provided.

5.1 Introduction

In several applications, the heat generated from flame is the source of energy. Due to the flexibility in the production process and feedstock, the syngas/producer gas composition contains not only H_2 and CO but also Nitrogen (N_2), steam (H_2O), carbon dioxide (CO_2) and methane (CH_4) at different concentration ratio. This diversity in the fuel composition directly affects the flame characteristics. Thus, the flame of different fuel composition has different flame temperature, structure, dimension, and size. The heat generation and emission formation from the flame depend strongly on these aspects of flame characteristics. As a result, heat generation capability and emission formation also rely on fuel composition. Understanding this impact is significant and beneficial for (i) the design of a suitable combustion system specifically for syngas/producer gas, (ii) the replacement of the conventional gas fuel with this fuel on the same combustion system, and also (iii) the development in fuel composition of syngas/producer gas to have a higher concentration of the desirable species.

The laminar co-flow diffusion flame of syngas/producer gas is studied in this chapter. The study of this flame could clearly project the difference in flame characteristics (e.g. temperature and dimension) of different fuel compositions. The CFD model generated and presented in Chapter 4 (medium mesh density with GRI 3.0 reaction mechanism) is able to model this flame type. The numerical methods selected in this CFD model can compute the

heat release rate from the chemical reaction during the combustion as well as the radiation of heat from the flame. Nevertheless, the domain (dimension of the burner) requires some modification to support the flame of various fuel especially the flame of fuel containing CH_4 which could be longer and wider than the H_2/N_2 flame studied in Chapter 4.

The study investigates two major topics; heat generation and emission. The impact of fuel composition on the flame temperature and flame size is firstly examined since these parameters are found to affect the heat generation of the flame in the previous chapter. This also provides a basic understanding of flame behaviour of each fuel. The heat generation is then studied in two phases; the heat released from the chemical reaction and the heat flux radiated from flame. The finite rate chemical model and the supplied chemical reaction mechanism (GRI 3.0) provide the capability to compute the heat from each chemical reaction. The combination of the heat release from every grid on the simulation domain provides the total chemical heat release from the flame (Q_{total}). The heat flux radiated from flame is predicted through the thermal radiation model explained in Chapter 3 and measured on the outlet boundary. Analysing both aspects leads to a detailed understanding of how fuel composition affects the heat generation of the flame.

The emission formation due to the combustion reaction is inevitable in the heat generation process. This work interests the formation of species CO_2 and NO_x due to the combustion of syngas. The reaction pathway of both CO_2 and NO_x are explained through the GRI 3.0 reaction mechanism. The analysis of emission is carried out according to the perception that it is a price to pay for a certain amount of heat. The simulation of flames of various fuel compositions and the comparison of their predicted results reveal the impact of each species in syngas/producer gas composition on the heat generation and emission formation.

5.2 Flame modelling

A total number of 15 co-flow diffusion flames with a variation in the fuel composition of H_2, CO, CH_4, CO_2, and N_2 are formulated. The details regarding the fuel compositions and their transport properties are presented in Table 5-1 while the transport property of these fuels is shown in Table 5-2. The fuel composition investigated in this work could be categorised as follows:

(i) Single species fuel, i.e. H_2 and CH_4.

(ii) Syngas with a variation of H_2:CO concentration ratio of 1:3, 1:1, and 3:1.

(iii) Syngas (H_2:CO = 1) mixed with either CH_4, CO_2, or N_2.

(iv) Biomass producer gas which is produced from bamboo, rubberwood, wood pellet, and rice husk presented in [25], [36]–[39].

Table 5-1 Composition of the studied fuel in the percentage of volume

Flame	H_2	CO	CH_4	CO_2	N_2	Total fuel % (H_2, CO, and CH_4)	H_2:CO	Mass flow rate (x 10^{-5} kg-s^{-1})	Volume flow rate (x 10^{-5} m^3-s^{-1})	Lower heating value (MJ/kg)
H_2	100.0%	-	-	-	-	100.0%	-	0.26	3.21	141.58
CH_4	-	-	100.0%	-	-	100.0%	-	2.10	3.21	55.51
H_2-rich	75.0%	25.0%	-	-	-	100.0%	3	1.17	3.21	33.30
EQ	50.0%	50.0%	-	-	-	100.0%	1	1.97	3.21	18.86
CO-rich	25.0%	75.0%	-	-	-	100.0%	0.33	2.82	3.21	13.15
EQ+10% CH_4	45.0%	45.0%	10.0%	-	-	100.0%	1	1.98	3.21	22.74
EQ+20% CH_4	40.0%	40.0%	20.0%	-	-	100.0%	1	2.00	3.21	26.58
EQ+10% CO_2	45.0%	45.0%	-	10.0%	-	90.0%	1	2.35	3.21	14.22
EQ+20% CO_2	40.0%	40.0%	-	20.0%	-	80.0%	1	2.73	3.21	10.88
EQ+10% N_2	45.0%	45.0%	-	-	10.0%	90.0%	1	2.14	3.21	15.62
EQ+20% N_2	40.0%	40.0%	-	-	20.0%	80.0%	1	2.31	3.21	12.86
Bamboo	19.7%	21.0%	1.5%	11.9%	45.9%	42.2%	0.94	3.43	3.21	5.22
Rubberwood	17.6%	20.4%	1.4%	10.8%	49.8%	39.4%	0.86	3.27	3.21	4.80
Wood pellets	21.7%	20.8%	2.2%	12.6%	42.7%	44.7%	1.04	3.17	3.21	5.79
Rice husk	19.8%	22.6%	2.0%	13.1%	42.5%	44.4%	0.88	3.24	3.21	5.57

The result of flames in category (i), H_2 and CH_4 flames, which are conventional is used as a reference in the analysis. The effect of having H_2 and CH_4 in the fuel composition can be identified by comparing the results of H_2 and CH_4 flames with those of syngas/producer gas. The analysis of syngas with the variation in the H_2:CO concentration ratio in category (ii) expresses the role of H_2:CO ratio as well as solely H_2 and CO species. The ratio of H_2:CO in this category is 1:3, 1:1, and 3:1, which are represented by CO-rich, EQ, and H_2-rich, respectively. In category (iii), the effect of adding CH_4, CO_2, or N_2 into the syngas composition is projected from the comparison. To prevent any confusion, the flames in this category are represented by EQ+n%CH_4, EQ+n%CO, and EQ+n%N_2; where n gives the number of concentration percentage. The flames of various biomass producer gases chosen from different sources e.g. Ref [25], [36]–[39] are in category (iv). The formulation of flame in this category projects the heat generation capability of the flame of practical producer gas comparing to the ideal syngas (category (ii)) and conventional fuel (category (i)).

Table 5-2 Properties of the studied fuel compositions

Flame	Density (kg-m^{-3})	Dynamic viscosity (Pa-s)	Specific heat (kJ-kg^{-1}K^{-1})	Thermal conductivity (W-m^{-1}K^{-1})	Air-fuel ratio
H_2	0.082	0.89E-5	14.31	0.191	2.38
CH_4	0.656	1.88E-5	2.23	0.030	9.52
H_2-rich	0.348	1.07E-5	3.39	0.111	2.38
EQ	0.614	1.27E-5	1.93	0.076	2.38
CO-rich	0.878	1.50E-5	1.35	0.050	2.38
EQ+10% CH_4	0.618	1.26E-5	1.96	0.072	3.09
EQ+20% CH_4	0.622	1.24E-5	1.99	0.068	3.80
EQ+10% CO_2	0.733	1.29E-5	1.66	0.069	2.14
EQ+20% CO_2	0.851	1.31E-5	1.47	0.062	1.90
EQ+10% N_2	0.667	1.31E-5	1.78	0.071	2.14
EQ+20% N_2	0.720	1.36E-5	1.65	0.066	1.90
Bamboo	1.070	1.52E-5	1.22	0.044	1.11
Rubberwood	1.020	1.55E-5	1.20	0.042	1.00
Wood pellets	0.987	1.50E-5	1.25	0.045	1.22
Rice husk	1.01	1.51E-5	1.38	0.043	1.20

5.3 Modification of the CFD model

The detail regarding the burner configuration, numerical methods, and numerical technique of the selected CFD model are presented in Chapters 3 and 4. The boundary condition and combustion condition (298 K and 101325 Pa) is the same as defined in the study of laminar diffusion flame of H_2/N_2 in Chapter 4. However, it is found during the study stage that the domain dimension, which is 4.75 cm in width and 20.8 cm in length, is not suitable for the flame of CH_4. The length of the CH_4 flame is significantly longer than the length of the simulation domain. Therefore, the modification is processed on the simulation domain dimension and mesh generation. The domain length is extended from 20.8 to 50.8 mm, and the mesh is regenerated according to the new domain dimension. The number of levels from the fuel exit to the top boundary increases from 100 to 250 levels while the other factors remain the same. This modification causes the generation of mesh with the smallest cell size of 1.25 E-4 and the total number of cells as 17,950 cells. The validation process of the modified CFD model is carried out based on the experimental work of Toro et al. [2]. The flame of H_2/N_2 with V_{avg} = 0.5 ms^{-1} is formulated and compared with the experimental result of this paper. The result is almost the same as the CFD model without the modification used in Chapter 4 (before modification). Thus, the reliability and accuracy of the results generated by both CFD models are comparable. Additionally, the modified model is capable of

simulating the flame of CH_4, which is significantly longer than that of H_2/N_2 at V_{avg} = 0.5 ms^{-1}.

5.4 Results

The analysis of the simulation results focuses on three major aspects, which are the heat generation, heat transfer and emission. These results are presented below:

5.4.1 Heat generation

Characteristics of the flame are affected directly by the fuel composition of syngas/producer gas [78], [145]. The difference in flame temperature, dimension and chemical heat release rate are obtained from the flames of fuel containing different concentration ratio of species H_2, CO, CH_4, CO_2 and N_2. The heat generation capability of the flame depends directly on these aspects of flame characteristics. The study initially analyses the temperature contour plot of each flame, as presented in Figure 5-1. This set of contour plot illustrates the difference in temperature and dimension of different flames. The line representing the flame front is drawn to project the dimension, shape and the stoichiometric contour of the flame. The combustion reaction of fuel and oxidiser occurs at the stoichiometric condition on the flame front line. The line is plotted by the zero-temperature gradient method, as already discussed in the previous chapter. The grid with the highest temperature at each vertical and horizontal level is a position in which the combustion occurs at the stoichiometric condition. Connecting these grids forms the stoichiometric contour called 'flame front'.

The impact of fuel composition on flame temperature and size of all the simulated flames are identified by comparing the results of all the studied flames in Figure 5-2a-b. The maximum temperature on the contour plot is a flame temperature (T). The flame surface area (A_f) is computed by integrating the flame front line around the domain axis. The size of the flame is compared based on this parameter, and it also represents the size of stoichiometric contour or reaction zone of the diffusion flame. The flame front line of all the studied flames are compared together in Figure 5-3a-b, and this comparison projects the difference in flame dimension.

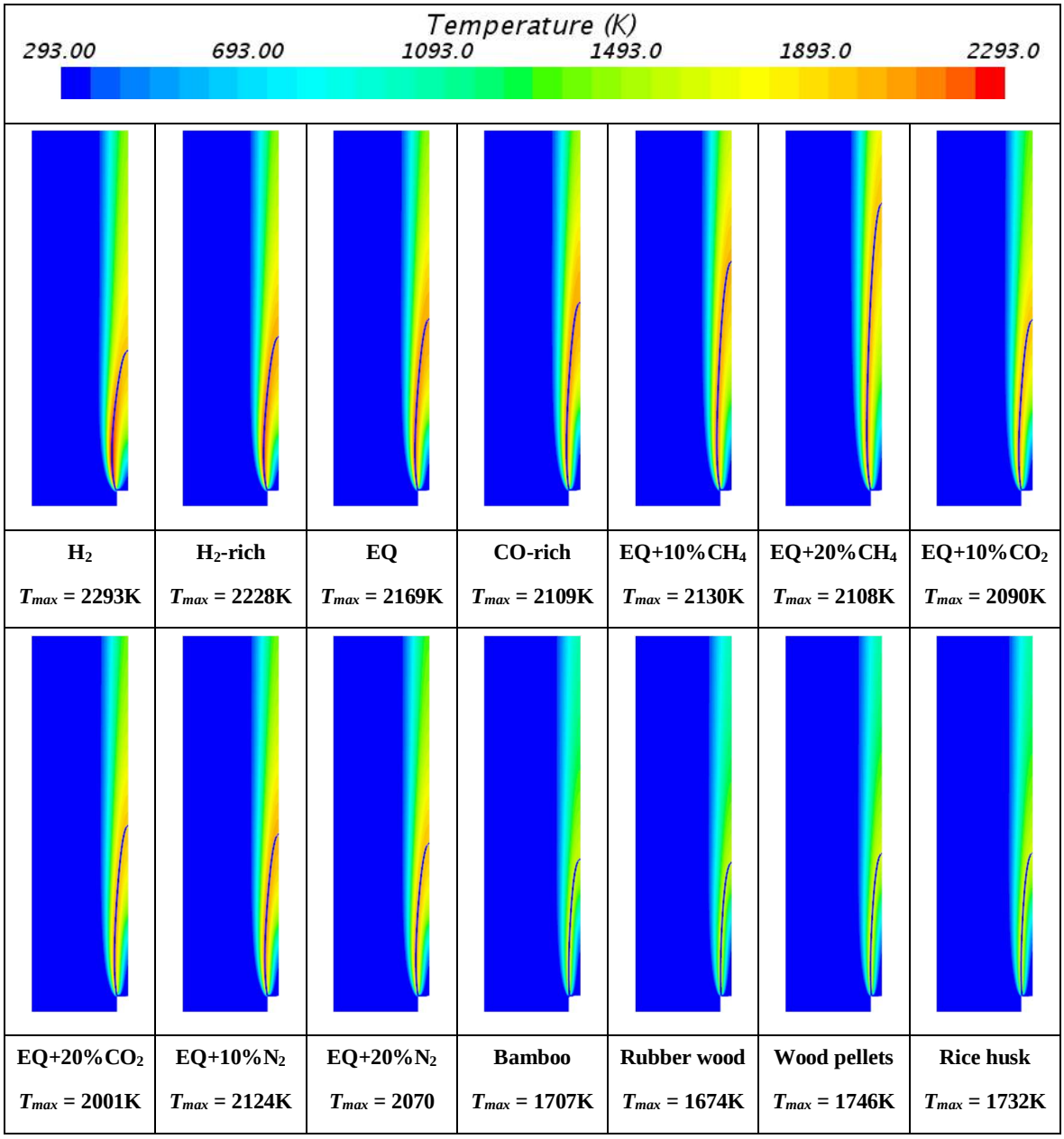

Figure 5-1 Temperature contour of the studied flame

The reaction pathway of each fuel composition is different due to their diversity in the fuel composition and subsequently results in the different amount of heat released from the related chemical reactions. The analysis of heat generation capability is processed in two layers in order to clearly express the property of fuel and flame. The first layer is the chemical heat release of fuel, where the parameter explaining this aspect is the maximum chemical heat release on the contour plot (Q_{max}). In other words, it is the highest possible chemical heat release property of the specific fuel composition. This parameter, therefore, provides the understanding of fuel combustion property which is typically computed and analysed based only on the concentration percentage of combustible species H_2, CH_4, and CO through parameters such as lower heating value (LHV) and higher heating value (HHV)). The second

layer of the analysis focuses on the total chemical heat released from the flame (Q_{total}). This parameter is computed by combining the chemical heat release rate at every grid on the simulation domain. To simplify and prevent any confusion, the chemical heat release property of fuel is expressed by Q_{max}, whereas the total chemical heat release from the flame is expressed by Q_{total}. The comparison of Q_{max} and Q_{total} of all the simulated flames are presented in Figure 5-4a-b.

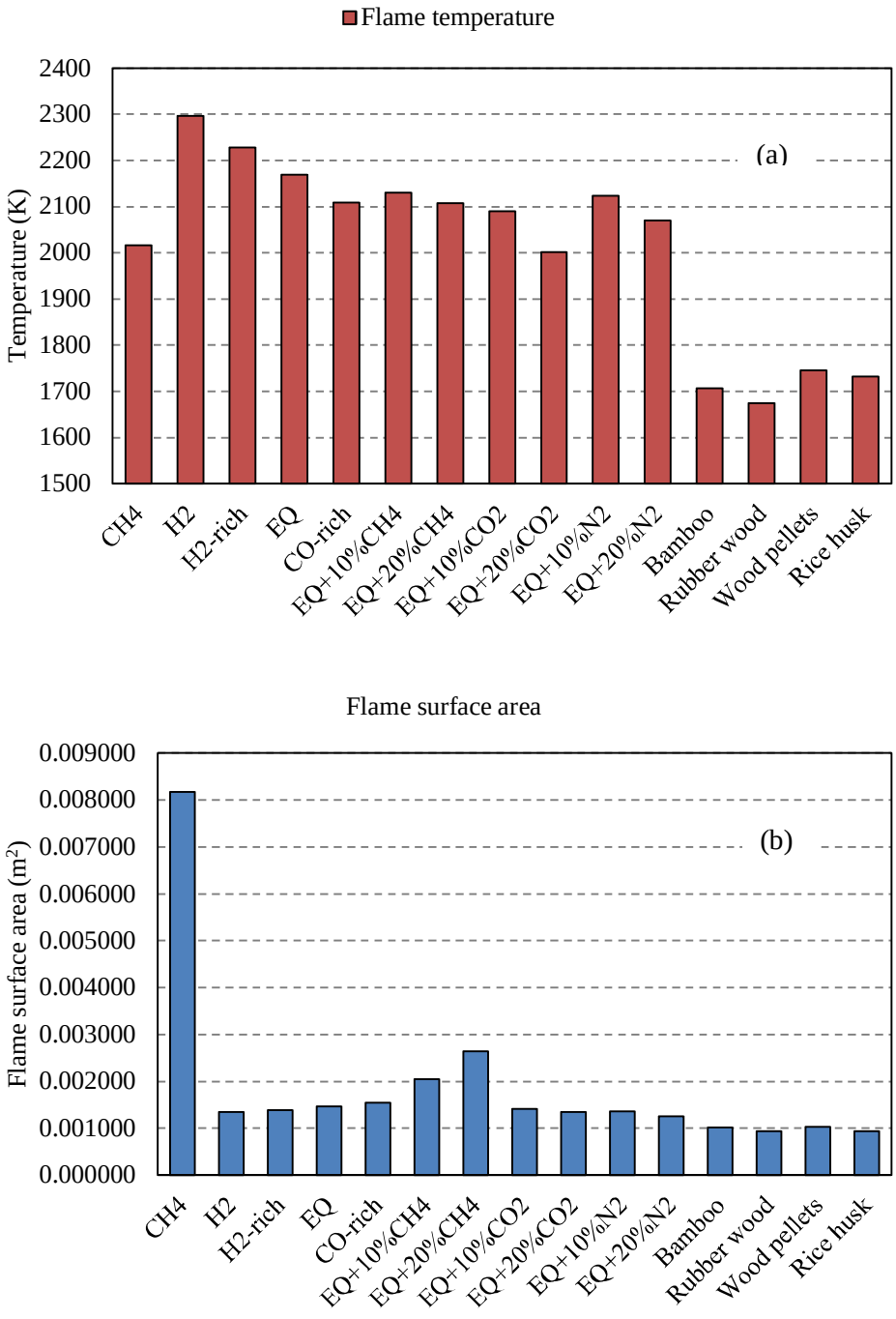

Figure 5-2 (a) Flame temperature (*T*) and (b) flame surface area (*Af*)

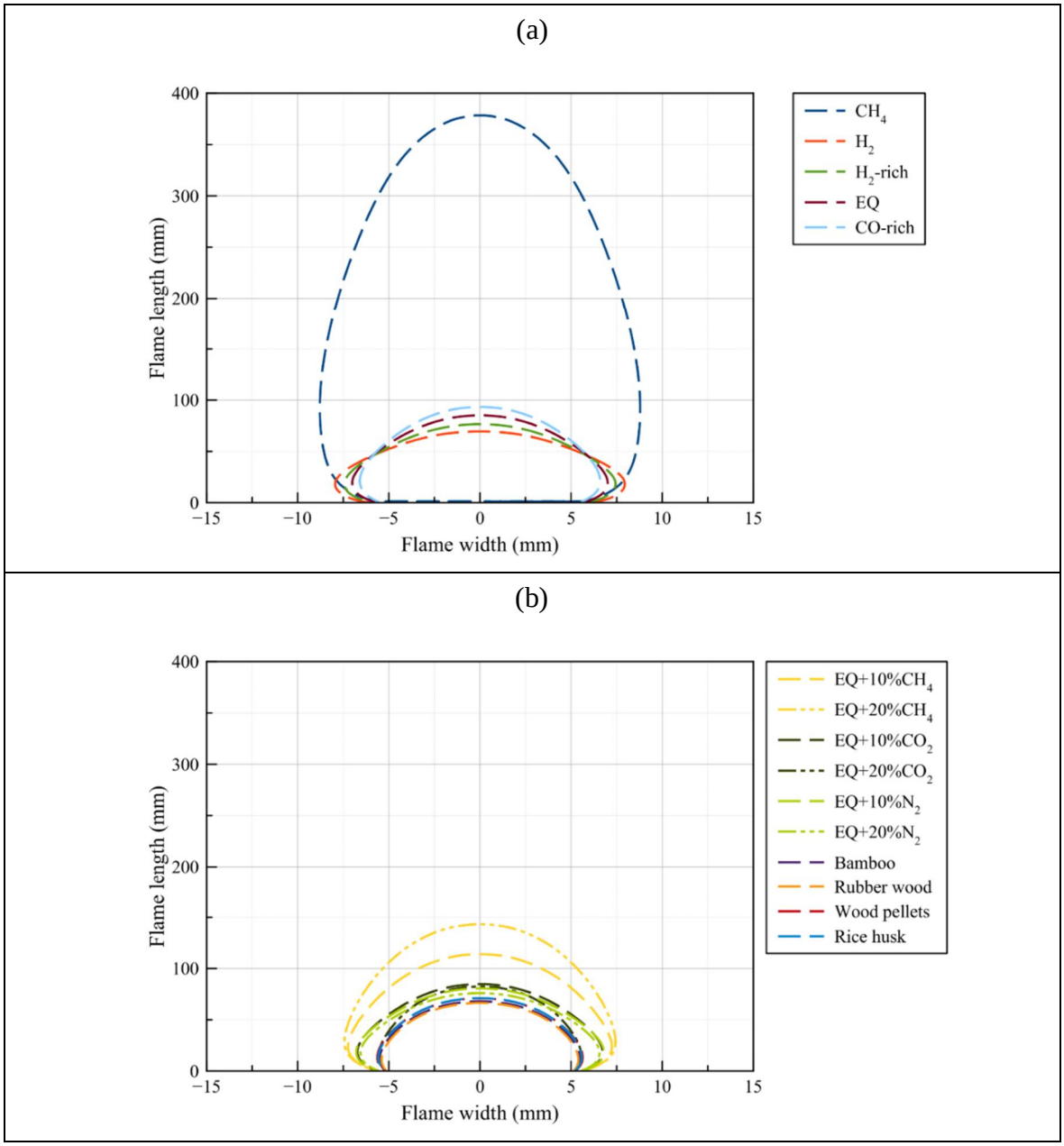

Figure 5-3 Flame front line of (a) H_2, CH_4, and syngas, and (b) syngas mixed with CH_4, CO_2, and N_2, and producer gas

Considering the fuel in category (i), H_2 gas fuel has a higher flame temperature and releases more heat from the chemical reaction than CH_4. The values of T and Q_{max} observed from H_2 flame are 2297 K and 0.25 W respectively, while the ones that obtained from CH_4 are 2016 K and 0.22 W. On the other hand, it is found that the flame of CH_4 has longer and wider dimension. The value of A_f of the CH_4 flame (8.35E-3 m^2) is, therefore, higher than that of the H_2 flame (1.35E-3 m^2). The result of the larger flame size is the larger area that generates heat for the flame of CH_4. Consequently, the CH_4 flame provides a higher value of total chemical heat release or flame heat release (1058 W) than that of H_2 flame (357 W). It could be noticed that the maximum chemical heat release (Q_{max}) of the CH_4 flame is lower than

one of the H_2 flame. This finding shows that the impact of flame size (A_f) on Q_{total} is stronger than the role of Q_{max}. In other words, the larger flame can provide a higher heat release than the smaller flame although the fuel of the larger one releases less heat from the chemical reaction. Further, the results of the single-species fuel in this category could be used as a guideline in the analysis of flames in the other categories.

The study of the flames in category (ii) reveals the effect of H_2:CO. The result of the flames in this category is supported by the result of H_2 flame (category (i)). For instance, the results show that the combustion of syngas with a higher concentration ratio of H_2:CO releases heat at a higher rate (i.e. higher Q_{max}). The same condition of H_2:CO also leads to the higher value of T. The flame having the highest values of T and Q_{max} in category (ii) is H_2-rich syngas (2228 K and 0.22) followed by EQ (2169 K and 0.19 W) and CO-rich syngas (2109 K and 0.15 W). In terms of the flame dimension, the shorter but wider flame is observed from syngas with the higher H_2:CO. The comparison of flame size between the flames in this category based only on the flame length is not suitable since the wider flame could have a larger size than the longer flame. Thus, the analysis of flame size is processed based on the value of A_f. The larger one is found from CO-rich syngas (1.55E-3 m^2) followed by EQ (1.47E-3 m^2) and H_2-rich syngas (1.39E-3 m^2). This result refers to the role of CO in an increase of flame size since the larger flame of fuel having a lower H_2:CO is observed. The larger flame size of syngas with a lower H_2:CO compensates its lower Q_{max} and generates the higher flame total heat release (higher Q_{total}). The highest Q_{total} is predicted from the CO-rich syngas (363 W) followed by EQ (355 W) and H_2-rich syngas (350 W), respectively.

The fuel composition of EQ syngas is added by either CH_4, CO_2, or N_2 at 10% and 20% in category (iii). The result of CH_4 flame analysed previously is used as a reference for the analysis of flames in this category. The comparison between CH_4 and EQ syngas shows that CH_4 flame has a lower T but higher A_f, Q_{max}, and Q_{total}. The same direction of the result is found when EQ syngas is mixed with CH_4. As seen, the flame temperature of EQ+20%CH_4 (2108 K) is lower than EQ+10%CH_4 (2130 K) and EQ syngas. On the other hand, the flame size (A_f) of EQ+20%CH_4 (2.64E-3 m^2) is larger than EQ+10%CH_4 (2.04E-3 m^2) and EQ syngas. The addition of CH_4 at 20% slightly rises the value of Q_{max} (0.195 W) comparing to one of EQ syngas. Due to an increase of A_f and Q_{max}, the addition of CH_4 to EQ syngas consequently leads to a higher value of Q_{total}. One of EQ+20%CH_4 is 495 W whereas one of EQ+10%CH_4 is 425 W.

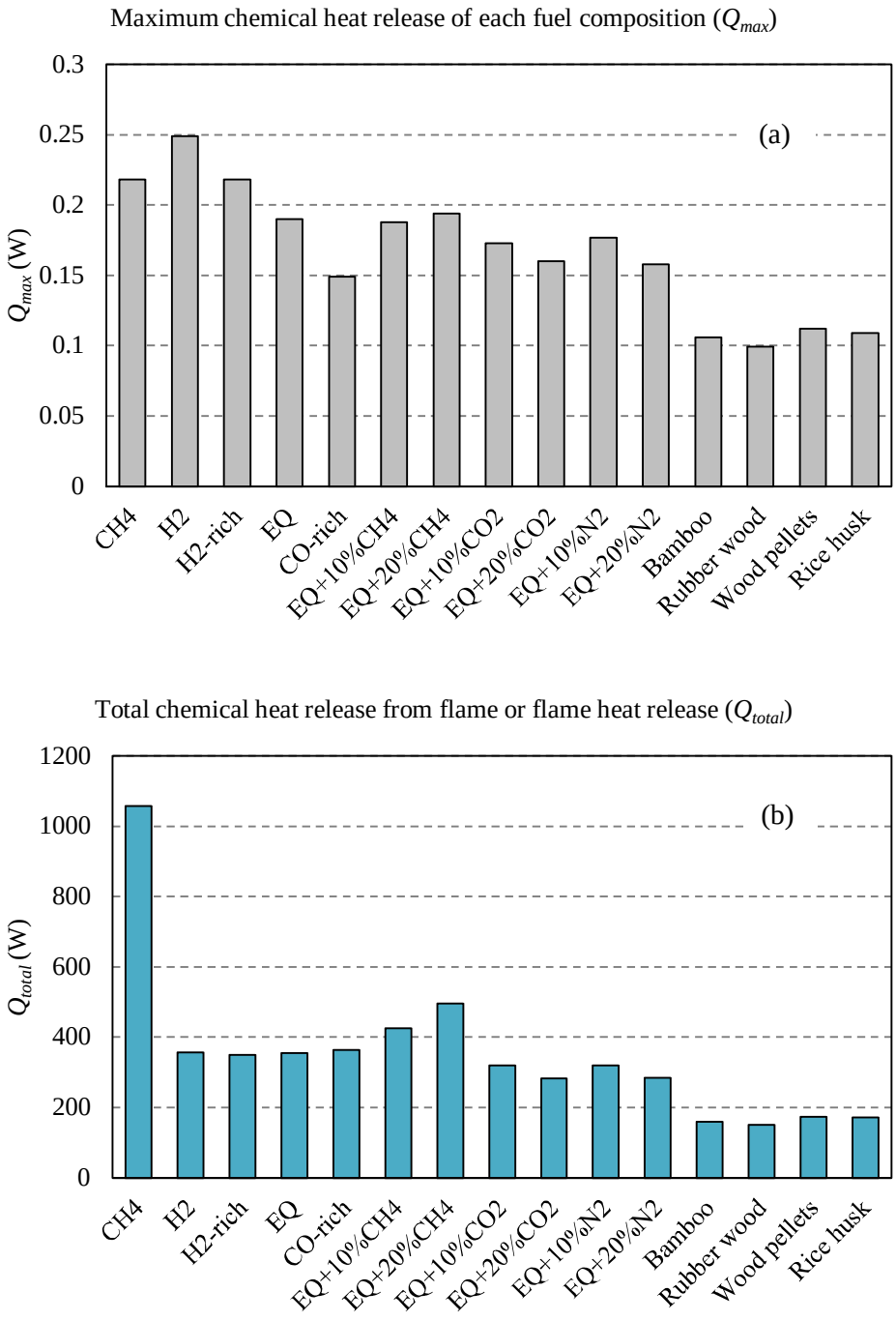

Figure 5-4 (a) Maximum chemical heat release (Q_{max}) of each fuel composition and (b) Flame chemical heat release (Q_{total})

Furthermore, the addition of CO_2 and N_2 to syngas/producer gas causes the reduction of the total concentration of combustible species in the composition. The lower value of T, A_f, Q_{max}, and Q_{total} are hence the result of this action. This result is observed from the flames in category (iii) where 10% and 20% of either CO_2 or N_2 is added to EQ syngas. The addition of 10% of CO_2 decreases the value of T and A_f to 2090 K and 1.41E-3 m^2, respectively. The same action but altering the additional species to N_2 reduces the value of T and A_f to 2124 K

and 1.36E-3 m^2 in order. The higher percentage of addition decreases the value of these parameters further. The flame temperature and size of EQ+20%CO_2 are 2001 K and 1.35E-3 m^2 while ones of EQ+20%N_2 are 2070 K and 1.25E-3 m^2. The effect of CO_2 is stronger than N_2 on the decrease of flame temperature. However, the opposite direction of the result is obtained from their impact on the reduction of flame size.

It could be seen that not only the fuel species (H_2, CO and CH_4) but also the diluted species (CO_2 and N_2) affect the characteristics of the flame. For the chemical heat release property of fuel (Q_{max}), having either CO_2 or N_2 in fuel composition of EQ syngas lowers the value of Q_{max}. As a result of the lower Q_{max} and A_f, the flame of EQ syngas mixed with CO_2 or N_2 generated the lower Q_{total} than EQ syngas without these species. The result also shows that the impact is stronger when the additional percentage is higher. Moreover, the level of the effect of both species is comparable since the value of Q_{max} and Q_{total} of EQ syngas mixed with CO_2 is almost equal to one mixed with N_2 at the same additional percentage. At 10%, Q_{max} of EQ+10%CO_2 and EQ+10%N_2 are similar as 0.17 W while Q_{total} of these fuels are 319 W. The values of them are lower at 20% of additional percentage. Q_{max} and Q_{total} of ~0.16 W and ~283 W are predicted from EQ+20%CO_2 and EQ+20%N_2 respectively.

The results of the flames in category (ii) and (iii) are utilised for explaining the characteristics and heat generation of the flames of producer gases in category (iv). The producer gas produced from wood pellets (1746 K) formulates the flame having the highest flame temperature in this category. This fuel contains the highest total percentage of fuel species (44.4%) with the highest H_2:CO ratio (1.04). Conversely, the flame of rubberwood producer gas has the lowest value of both H_2:CO ratio (0.86) and total combustible species percentage (39.4%). The flame of this fuel, therefore, has the lowest flame temperature (1674 K) amongst all the flames in this category. The flame size of all the flames in this category are comparable and between 9.5E-4 and 1.0E-3 m^2. Regarding the chemical heat release, the role of total fuel species concentration percentage is confirmed since the combustion reaction of wood pellets gas releases heat at the highest rate as Q_{max} = 0.11 W. The flame of this fuel also generates the highest heat as 174 W of Q_{total}. In opposite, the lowest Q_{max} and Q_{total} are predicted from the producer gas of rubberwood respectively as 0.099 W and 150 W.

5.4.2 **Heat transfer**

The selected thermal radiation model is capable of computing the heat radiated through a participating medium considering the high-temperature combustion product gases, such as H_2O and CO_2. These species play a crucial role in the emission and absorption of heat created by the flame. The composition and concentration of the combustion product depend directly on the reactant, such as the fuel composition of syngas/producer gas. Thus, the diversity in fuel composition directly affects the heat transfer capability of the flame. The heat flux profile on the left outlet boundary of the simulation domain (left-hand boundary in Figure 4-1) of all the studied flames is plotted and compared, as seen in Figure 5-5. The impact of each species is identified by analysing these data. It could be seen from the comparison of flames in category (i) that the profile of CH_4 is outstanding from the other fuels. The value of heat flux begins at 554 W-m^{-2} at zero vertical distance then increases dramatically to the peak value 1781 W-m^{-2} at 0.17 m. Then, the heat flux decreases significantly until passing the top boundary of the domain. The different pattern of the profile is observed from the heat flux profile of H_2 flame since the heat flux profile of this fuel has two peaks. The heat flux generated by H_2 flame is 672 W-m^{-2} at zero vertical distance, and it increases to the first peak value (948 W-m^{-2}) at 0.02 m. Above this vertical level, the profile decreases and increases again to the second peak (960 W-m^{-2}) at 0.05 m where the downtrend of the profile begins.

It is noticed that the profile pattern of the heat flux on the measured boundary depends strongly on the fuel species. Also, the position of the highest peak (the second peak for H_2 flame) relies on the flame length. The profile pattern of heat flux is affected by H_2 as seen from the comparison of flames in category (ii). The heat flux profile of the H_2-rich flame has a similar pattern as H_2 flame; their profiles have two peaks. Nevertheless, the heat flux profile of H_2-rich syngas has the lower first peak (895 W-m^{-2} at 0.015 m) than the second peak (1018 W-m^{-2} at 0.055 m). The first peak of the profile is affected by the concentration percentage of H_2 in fuel composition. As seen, the lower percentage of H_2 results in the lower peak value. Also, the profile of EQ syngas has the lower first peak value than H_2-rich, whereas the first peak of the heat flux profile of CO-rich syngas is disappeared. The second peak of the heat flux profile of flames in this category is thus the maximum heat flux of each flame. This maximum value is found to be related to the concentration of CO. Syngas having a higher CO concentration percentage formulates the flame that radiates the heat flux with the higher maximum value. The effect of flame length on the position of the maximum heat

flux (the second peak) is confirmed. The flame with the longer flame length has a higher vertical level of this position. Among the flames in category (ii), the flame of CO-rich syngas has the highest maximum heat flux (1518 W-m^{-2} at 0.065 m) followed by EQ syngas (1309 W-m^{-2} at 0.058 m) and H_2-rich syngas.

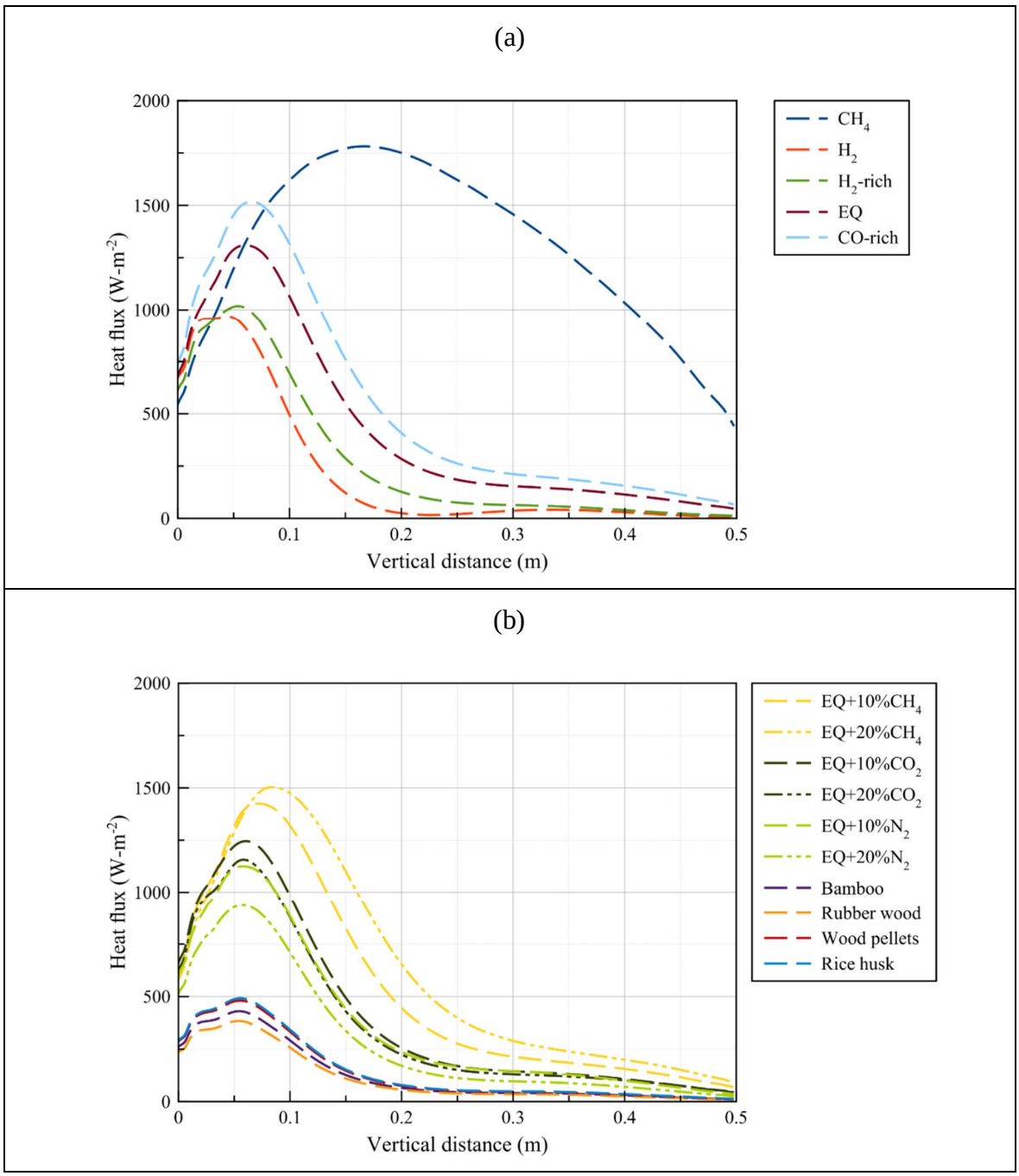

Figure 5-5 Heat flux profile on the outlet boundary (a) H_2, CH_4, and syngas (b) syngas mixed with CH_4, CO_2, and N_2 and producer gas of different feedstocks

The heat flux profile of flames in category (iii) is similar to EQ syngas (category (ii)) since their H_2:CO = 1. In details, the first peak is unclear as the concentration of H_2 and CO is 40-45%. The heat flux profiles of EQ+20%CH_4 and EQ+10%CH_4 are in the same direction as

the CH_4 flame. The maximum heat flux of these flames is significantly affected by the concentration percentage of CH_4, and the higher percentage causes a higher maximum heat flux value. The flame of EQ+20%CH_4 has a higher maximum heat flux (1503 W-m^{-2} at 0.085 m) than EQ+10%CH_4 (1404 W-m^{-2} at 0.07 m). Furthermore, the result could be used for comparing the level of effect of CO and CH_4 on the increase of maximum heat flux. The higher percentage of both species increase the maximum heat flux, and CH_4 is stronger than CO.

The heat flux profile of EQ syngas is utilised as a reference for studying the role of CO_2 and N_2. The lower maximum heat flux is obtained when EQ syngas is mixed with either CO_2 or N_2. This result could be explained by the lower total percentage of combustible species in fuel composition. The pattern of the profile is in the same direction for EQ syngas and EQ syngas mixed with either CO_2 or N_2 since the H_2:CO ratio of them are equally as 1. The level of the effect on the decrease of maximum heat flux is found to be stronger for EQ syngas mixed with N_2. At 10 % of additional percentage, EQ+10%CO_2 (1245 W-m^{-2} at 0.0593 m) is higher than EQ+10%N_2 (1125 W-m^{-2} at 0.0579 m). The maximum heat flux reduces further at 20 % of the additional percentage. As seen, EQ+20%CO_2 (1155 W-m^{-2} at 0.0603 m) is higher than EQ+20%N_2 (936 W-m^{-2} at 0.0568 m). The role of CO_2 on the thermal radiation could be used for explaining this finding. This species is considered to dominate the cloud emission and absorption of heat radiation in the selected thermal radiation model (WSGG model). It is also found that CO_2 decreases the flame temperature but encourages the heat radiation of the flame when both aspects are considered together.

Similar to categories (ii) and (iii), the flame length strongly affects the position of the maximum heat flux; the higher position is observed from the longer flame. The simulation result of flames in category (iv) confirms the finding of the analysis of flames in the previous categories. The profile pattern of heat flux of them depends on the fuel composition as well as the flame length. The fuel composition of flames in this category contains a lower concentration percentage of CO (20.4 – 22.6%) and CH_4 (1.4 - 2.2%) compared to the fuel of the other categories. Therefore, the first and the second peak of the profile are clearly seen. In the previous section, the length of flames in this category was also found to be comparable. The position of the maximum heat flux (the second peak of the profile) of flames in this category is, thus, similar as ~0.057 m. The H_2:CO ratio of these fuels is close to 1, and the flame of fuel containing the higher total percentage of fuel species has a higher maximum heat flux profile. Furthermore, the higher peak value is found from the flame of

fuel having a higher percentage of CO and CH_4 when the total percentage of fuel species of them is similar. Among them, the producer gas of rice husk has the highest maximum heat flux (492 W-m^{-2}) followed by wood pellets (480 W-m^{-2}), bamboo (430 W-m^{-2}), and rubberwood (384 W-m^{-2}).

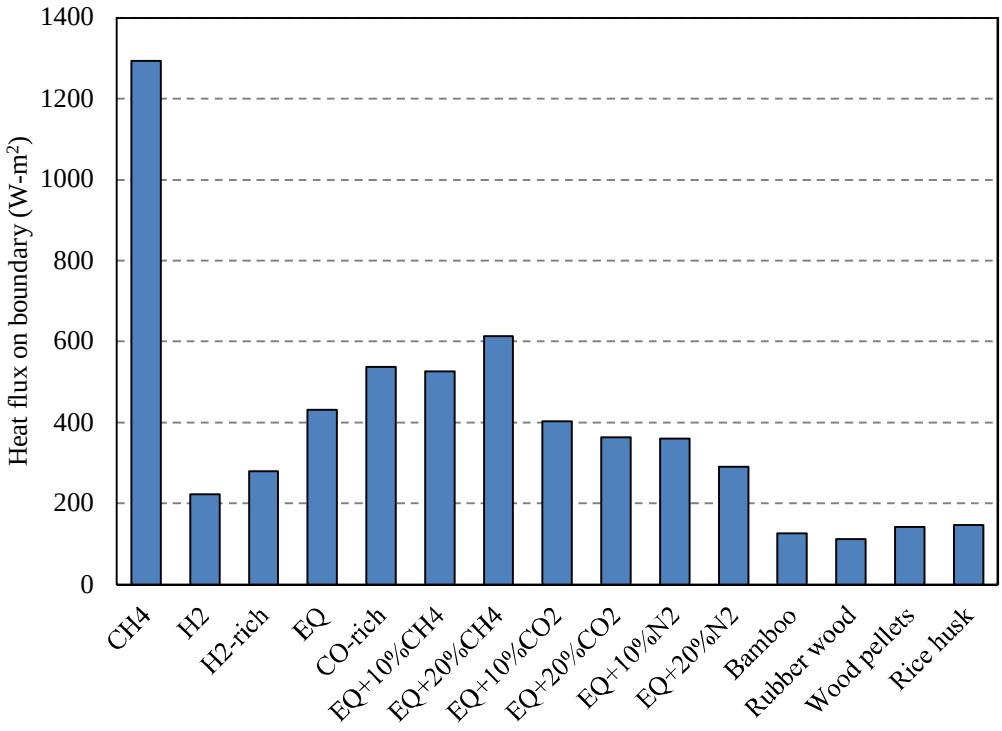

Figure 5-6 Average heat flux on a measured boundary

The study of heat flux profile provides the guideline for effectively utilising these flames as a source of energy since the heat at each vertical distance from the co-flow air exit is illustrated. Nevertheless, the complex pattern of heat flux profile could cause the difficulty in the comparison of heat flux of different flames. The average heat flux ($Q^{\prime}$) is introduced to address this issue. This parameter is calculated from the heat flux profile and the area of the measured boundary. The average heat flux ($Q^{\prime}$) is computed for all the studied flames and compared in Figure 5-6. This comparison projects a different level of heat flux generation capability. The outstanding one could be seen from $Q^{\prime}$ of CH_4 flame (1293 W-m^{-2}) which is the highest value among the studied flames. Within the same category, the impact of each species on $Q^{\prime}$ is the same as their impact on the maximum value of the heat flux profile. The comparison of $Q^{\prime}$ could also be processed across different flame categories. The interesting result is obtained since the flame of fuel with the lower total concentration percentage of combustible species (80-90%) generates the higher $Q^{\prime}$ than ones having 100% concentration percentage of total combustible species. For example, $Q^{\prime}$ generated by

EQ+10%N_2 (360 W-m^{-2}), EQ+10%CO_2 (403 W-m^{-2}), EQ+20%N_2 (290 W-m^{-2}), and EQ+20%CO_2 (364 W-m^{-2}) are higher than $Q´$ generated by H_2 (222 W-m^{-2}) and H_2-rich syngas (280 W-m^{-2}). The role of carbon fuel species (CO and CH_4) and CO_2 on the heat flux generation and heat transfer of flame are emphasised. As seen, the flame of H_2 and H_2-rich cannot provide a higher heat flux even though their total heat release from the chemical reaction (Q_{total}) is higher due to an absent and a lower concentration of CO.

5.4.3 **Emission formation of CO_2 and NOx**

Emissions, CO_2 and NO_x, are the unpreferable products of combustion. The perception of them in this study is a price to pay for a certain amount of heat generation. Therefore, the study focuses on the total production rate of them per a certain amount of heat generated from the flame. The total production rate of CO_2 and NO_x are computed firstly by combining the production rate of them on every grid of the simulation domain. The definition of NO_x in this study refers to NO and NO_2. The average heat flux ($Q´$) presented in the previous section is considered as the heat generated and transferred by flame. The total production rate of each emission species (CO_2 or NO_x) is therefore divided by $Q´$ for the production rate of them per heat generated and transferred by flame. In other words, the result of this method is the emission formation that must be paid for 1 W-m^{-2} of generated heat flux. The comparison of CO_2 and NO_x production rate of each flame are presented in Figure 5-7a and Figure 5-8a, respectively. The price to be paid or the rate of CO_2 and NO_x produced for 1 W-m^{-2} of $Q´$are shown in Figure 5-7b and Figure 5-8b, respectively.

Without considering the heat generation from the flame (Figure 5-7a), the flame of CH_4 formulates the NO_x emission at a higher rate than syngas mixed with CO_2 and the producer gas of bamboo, rubberwood, wood pellets, and rice husk. this is the result of a higher flame temperature of CH_4. Based only this information, CH_4 flame might not be preferable in case that the emission formation of NO_x is concerned. When the heat generation is considered (Figure 5-7b), the result expresses that the price to be paid or NO_x production rate for 1 W-m^{-2} is lower than all the studied fuel composition. CH_4 significantly promotes a higher heat generation capability of flame; thus, a lower NO_x is formulated at the same amount of heat generated. For CO_2 emission, the flame of CH_4, which is hydrocarbon fuel, produces the CO_2 emission at a lower rate than most fuel composition except the flame of H_2, H_2-rich, and EQ+20%CO_2. The significantly higher heat generation capability of this fuel, again, causes its flame produces lower CO_2 production rate for 1 W-m^{-2}. Having CH_4 in fuel

composition, hence, benefit not only the higher heat generation capability but also the lower emission formation as seen from the lower NO_x and CO_2 emission produced for 1 W-m^{-2} of EQ+20%CH_4 than EQ+10%CH_4 and EQ syngas in Figure 5-7b and Figure 5-8b.

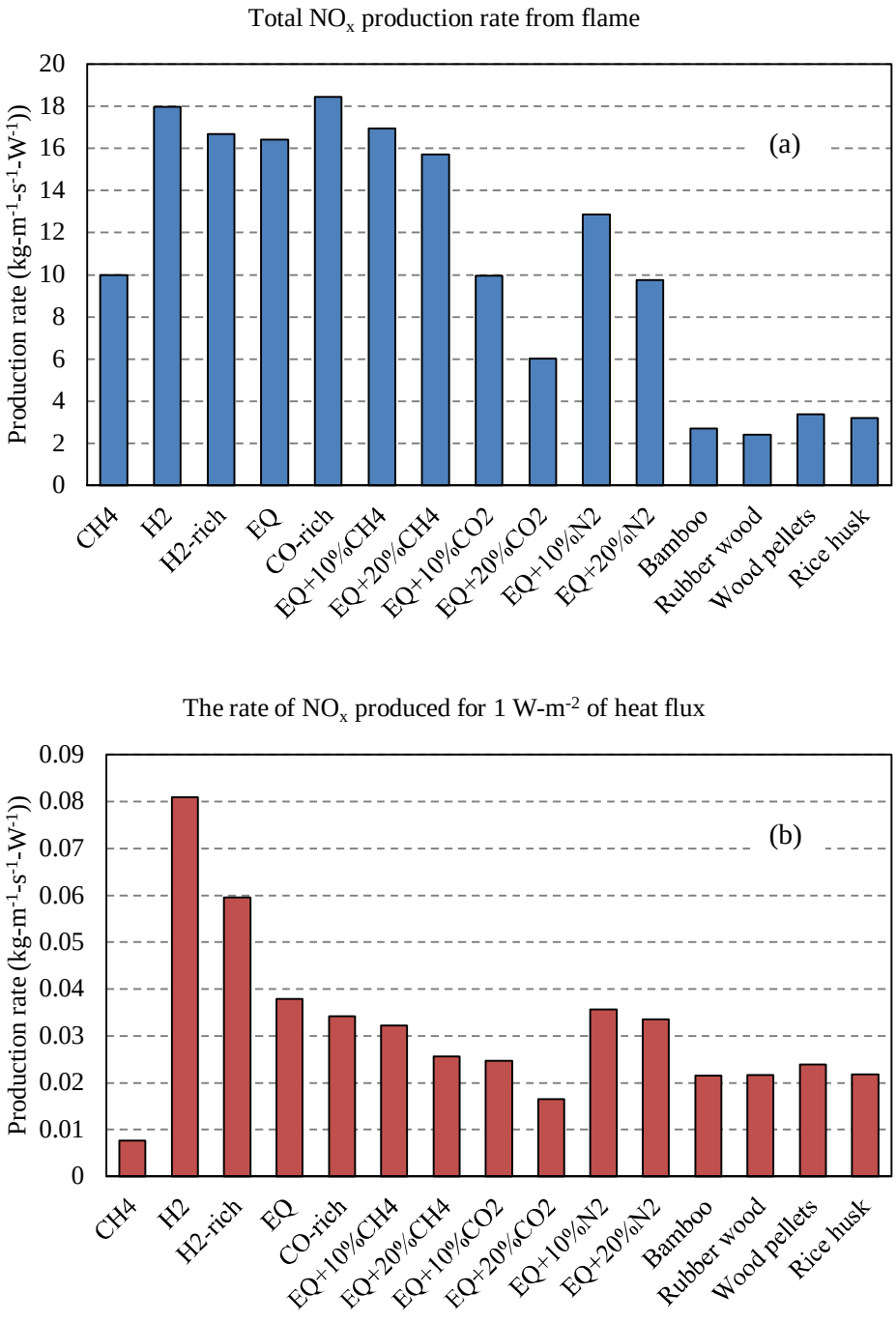

Figure 5-7 (a) Total NO_x production rate from each flame, and (b) The rate of NO_x produced for 1 W-m^{-2} of heat flux

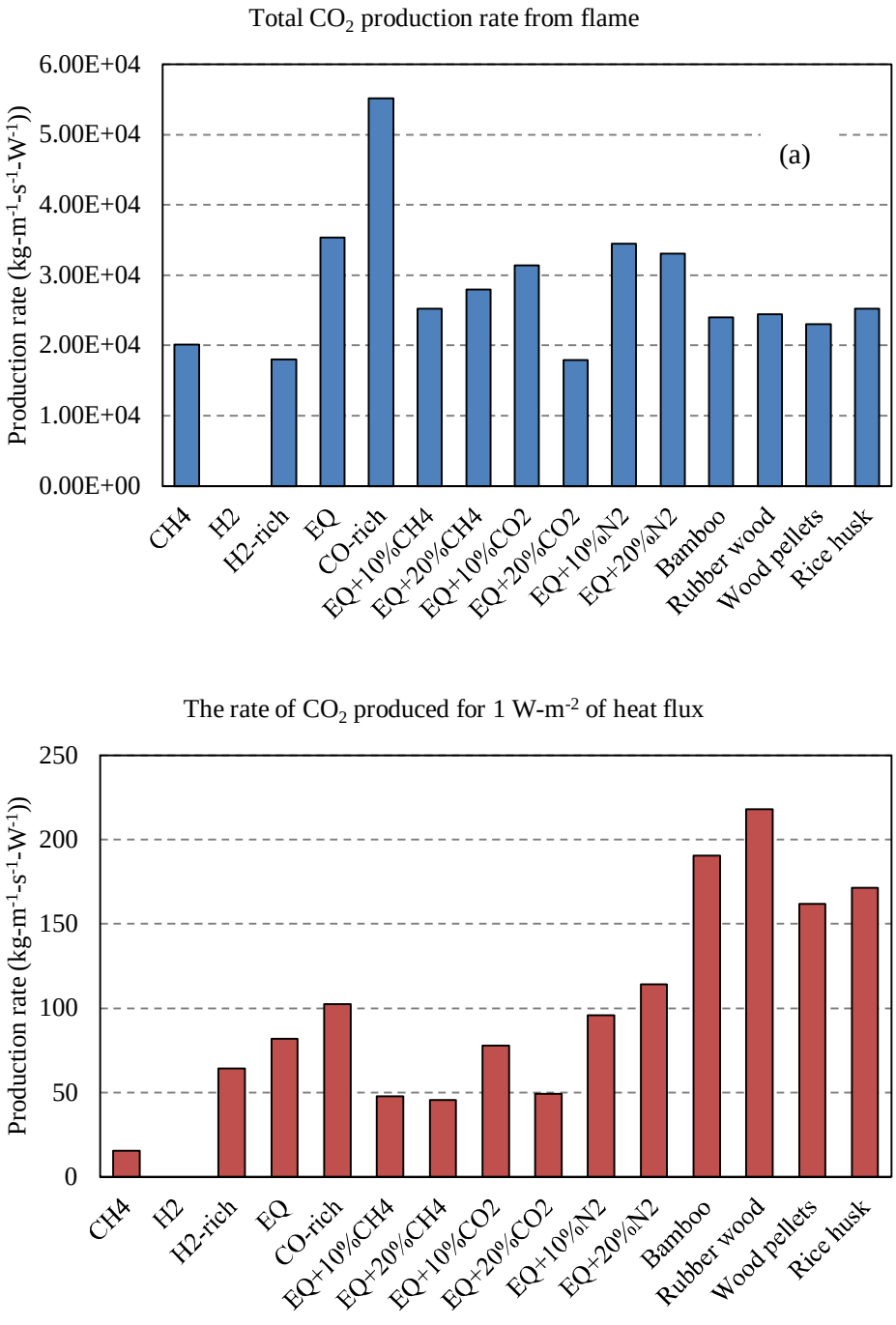

Figure 5-8 (a) Total CO_2 production rate from each flame, and (b) The rate of CO_2 produced for 1 W-m^{-2} of heat flux

In Figure 5-7a and Figure 5-8a, the role of H_2 on higher flame temperature leads to the higher production rate of NO_x. It is also noticed that the higher concentration of CO in fuel composition encourages the higher production rate of NO_x. The benefit of having H_2 in fuel composition is illustrated on CO_2 emission since there is no CO_2 related in the reaction pathway of H_2. In turn, CO plays a significant role in an increase of CO_2 emission, and this impact is also stronger than the impact of CH_4 on the same aspect. When the heat generation

capability of the flame is considered with the emission (Figure 5-7b and Figure 5-8b), NO_x is formulated at a higher rate for 1 W-m^{-2} of heat flux from the flame of fuel with higher H_2:CO concentration. This due to the lower heat generation capability of this fuel compared to the flame of fuel with the lower H_2:CO. The opposite direction is observed for the CO_2 produced for 1 W-m^{-2} of heat flux.

As seen in Figure 5-7a and Figure 5-8a, the lower CO_2 and NO_x production rate is computed from EQ syngas consisting of N_2 in fuel composition (EQ syngas mixed with N_2) comparing to EQ syngas without additional species. This finding is the result of having a lower concentration percentage of combustible species (H_2, CO, and CH_4) in fuel composition. However, the average heat generated from EQ+10%N_2 and EQ+20%N_2 is also lower than EQ syngas according to the same reason. The results obtained from the CO_2 and NO_x production rate per 1 W-m^{-2} of heat flux generated are different as shown in Figure 5-7b and Figure 5-8b. Firstly, the lower NO_x is produced for 1 W-m^{-2} of heat flux at the higher dilution percentage of N_2. Secondly, the higher dilution percentage of N_2 in syngas leads to a higher CO_2 emission rate per 1 W-m^{-2} of heat flux generated.

On the other hand, adding CO_2 into fuel composition of EQ syngas assists the thermal radiation of flame, as mentioned in the previous section. In Figure 5-7a and Figure 5-8a, the role of CO_2 in the reduction of flame temperature results in the lower NO_x production rate. The higher concentration of CO_2 as a reactant supplied into the combustion reduces the CO_2 as a product of the combustion. Combining the results mentioned above, the higher concentration ratio of CO_2 in the syngas is beneficial for the reduction of CO_2 and NO_x emission since the lower production rates of them are obtained when 1 W-m^{-2} of heat flux is generated.

Lastly, the significantly lower flame temperature and Q' is predicted from the flames of producer gas in category (iv). The major cause of this finding is the meaningfully lower total concentration of combustible species than flames in the other categories. The lower concentration percentage of CO and CH_4 also leads to the lower total production rate of CO_2 than the fuel in the other categories as seen in Figure 5-8a. The flames in category (iv) have a similar concentration percentage of CO and CH_4, and this leads to a comparable level of the total production rate of CO_2. For NO_x production rate, the lower flame temperature of producer gas in category (iv) provides the lower total NO_x production rate as shown in Figure 5-7a. Within category (iv), the higher NO_x production rate is found from the flame having a

higher flame temperature. When the heat generation is considered along with the emission, the higher CO_2 and NO_x production rate per 1 W-m^{-2} of heat flux than the flame in the other categories is observed as presented in Figure 5-7b and Figure 5-8b. The flame of wood pellets producer gas provides the lowest CO_2 production rate per 1 W-m^{-2} of generated heat flux while the opposite direction is obtained from the flame of rubberwood producer gas.

5.5 Discussion

The heat generation and emission of syngas/producer gas affected by the diversity in fuel composition of syngas are presented above. The analysis and discussion of the key finding are presented as follow:

The flame temperature is found to have a minor role in the heat generation capability since the flame having a higher temperature cannot provide a higher heat than the lower one. In opposite, flame dimension, surface area (A_f) and chemical heat release of fuel (Q_{max}) are pointed out as the key parameters affecting the total chemical heat release of the flame (Q_{total}) and the average heat flux ($Q´$) generated from flame. The analysis is processed further to find the relation between flame temperature and Q_{max}. It could be seen that the higher value of Q_{max} is computed from the flame with a higher flame temperature. Nevertheless, this condition is valid for only the comparison of flames within the same category. The fuel composition in each category is defined to project the effect of species H_2, CO, CH_4, CO_2, and N_2. The impact of these species on Q_{max} is hence in the same direction as their impact on flame temperature. However, this cannot imply that the higher flame temperature accordingly could generate higher Q_{max}. As seen, the flame of CO-rich syngas has a higher flame temperature than EQ-syngas+20%CO_2; however, the lower value of Q_{max} of CO-rich syngas is obtained.

The dimension of the flame plays a key role in the generation and transfer of heat. Firstly, the larger surface area (A_f) is computed from the flame having the longer and wider dimension and is capable of compensating for a lower chemical heat release of fuel (Q_{max}). The flame with the larger A_f thus could generate the higher Q_{total}. Secondly, the longer flame creates a larger area on the boundary that the heat flux is radiated by flame at a higher rate. This result consequently leads to a higher average heat flux ($Q´$) produced from a longer flame. Due to this, the development of the heat generation and heat transfer of flame could be done by extending the width and length of the flame. There are two options for this

method which are (i) developing fuel composition to have a higher concentration of species that provides the larger flame size, and (ii) increasing the fuel rate supplied into combustion. However, the latter method would raise the opportunity that the flame could become unstable and transforms the flow regime of the fuel stream from laminar to turbulent.

The impact of each species also provides the guideline for the improvement of syngas/producer gas composition. According to the result, the role of fuel species H_2, CO, and CH_4 on the generation and transfer of heat is obtained at a different level. Syngas/producer gas, which contains these species at different concentration percentage, has a different level of capability to generate and transfer heat. Utilising the same method as one applied for the study of emission would allow the estimation of fuel consumption in the form of fuel rate required for 1 $W\text{-}m^{-2}$ of generated heat flux. The fuel rate is firstly converted from the velocity of fuel stream then calculated per amount of average generated heat flux ($Q´$). In this case, the velocity of fuel is equal to 0.5 ms^{-1} for all the studied flames and consumption per generated heat flux could be defined from the indirect proportion to the value of $Q´$. Thus, the fuel that provides the lower $Q´$ has a higher fuel consumption per a certain amount of generated heat. Due to this analysis, the most desirable species is CH_4 since the higher concentration of this species provides the higher heat but lower emission rate and consumption than the other species. CO is preferable than H_2 in case that heat generation and fuel consumption is prioritised. Increasing the concentrating percentage of CO in fuel composition escalates the heat generation; nevertheless, the side effect of this method is the higher CO_2 emission production rate per generated heat.

The emission production rate of CO_2 could be reduced by increasing the higher concentration percentage of H_2. The cost of this action is the higher fuel consumption and NOx emission production rate. The benefit of having CO_2 in fuel composition is revealed since it surprisingly assists the generation and transfer of heat as seen from the analysis of $Q´$. Also, the addition of CO_2 to fuel composition (as a reactant) reduces the production rate of itself as a combustion product. The optimisation of proper CO_2 concentration in fuel composition is necessary. The excessive addition of this non-combustible species would reduce the level of heat generation capability since the total concentration of fuel species is lower.

In theory, the length of laminar diffusion flame relies on several factors as presented in equation (1) - (4). Based on the combustion condition in this work, the flame length is calculated through these equations. The significantly shorter flame length than the CFD

result is obtained from the theory. For instance, the length of CH_4, H_2-rich, EQ, and CO-rich calculated from the theory are 335, 30, 40, and 57 mm, respectively. This direction of the result is already discussed in Chapter 4. Further, the flame length formula provides a similar result compared to the CFD result when the fuel has a higher stoichiometric ratio and lower diffusion coefficient. This finding confirms that the formula, which was designed for hydrocarbon fuel, is not suitable for syngas/producer gas, and the modification is required for this purpose. However, the relationship between parameters in this formula could be used for roughly estimating the flame length. For example, the lower mass diffusivity and stoichiometric ratio of fuel will cause a lower flame length.

Lastly, the impact of each species in syngas/producer gas composition on the flame temperature is found to have the same trend as the direction of the result reported in [74], [76], [80]. The concentration percentage of H_2 in fuel composition has a stronger effect than CO on the escalation of flame temperature. On the other hand, the role of H_2 and CO on the increase of flame temperature is comparable, and the impact of H_2:CO seems to be minor on this aspect according to the study of [78]. The difference in flow regime of fuel stream could be used for explaining the different aspects of the result. The laminar flow regime is focused in this work while the turbulent one is studied in [78]. Additionally, the result of the analysis of flame dimension and NOx emission has the same trend as reported in [80], [81].

5.6 Conclusion

The CFD model is formulated for investigating the heat generation and emission of conventional fuel, and syngas/producer gas. The combustion is computed by the finite rate chemical model where the GRI3 chemical reaction mechanism is supplied for the reaction pathway. The key conclusions are presented in the bullet points as follow:

- Flame temperature is not the only factor controlling the total heat generation capability (Q_{total}) and heat flux ($Q´$) of the diffusion flame. The factors such as the fuel combustion heat release (Q_{max}) and flame dimension are also significant. Both parameters play a crucial role and have the ability to compensate for the role of each other. For example, the fuel having the lower value of Q_{max} could formulate the flame generating the higher value of Q_{total} and $Q´$ if the flame has a larger dimension or size.

- Among the combustible species in fuel composition of syngas/producer gas, CH_4 is the most desirable species since the addition of this species increases the heat generation but reduces the fuel consumption and emission formation rate per generated heat. The second desirable species is CO; however, this consideration is based on the higher heat generation and lower fuel consumption. The side effect of adding CO is a significantly higher production rate of CO_2 per generated heat. Lastly, an increasing percentage of H_2 in fuel composition could decrease CO_2 emission dramatically; nevertheless, the fuel will provide less heat generation and higher fuel consumption.
- CO_2 is found to play a significant role in the radiation of heat and the reduction of emission.

Overall, it is found that the heat generated from CH_4 flame is significantly higher than the one generated from syngas/producer gas. Two methods are suggested for improving heat generation. The first one is the development of syngas/producer gas composition to release and transfer heat at a higher rate. Increasing the fuel rate for the larger flame dimension and surface area is the second option. However, this option might increase the possibility that the flame will be unstable and also the transition of the laminar flow regime of the fuel stream to the turbulent one.

Chapter 6 An occurrence of the instability of syngas/producer gas flames

Combustion instability is one of the significant issues having a detrimental effect on the heat generation of flame. Williams [146] classified the combustion instability into three categories. The chamber instability refers to the combustion instability occur due to the chamber e.g. shock instability, fluid dynamics instability due to the chamber. The intrinsic instability is the combustion instability that arises whether inside or outside the chamber. The example of this type of instability is chemical kinetic instability and diffusive thermal instability. Lastly, the system instability is defined as the combustion instability caused by the interaction between combustion processes and the other parts of the system. This type of instability is, for example, feed-system interactions, exhaust-system interactions.

In this work, the intrinsic instability found in the laminar diffusion flame called 'flame oscillation' is focused. The phenomenon occurs due to the buoyancy force which causes the flame front regularly oscillates at the low frequency (10 – 20 Hz). According to ref [97]–[101], the result obtained from the numerical study shown that the shear layer of burnt gas had an inflexional profile of velocity resulting in the Kelvin-Helmholtz type of instability. The details and the onset condition of this phenomenon were presented in Chapter 2. An occurrence of the flame oscillation in syngas laminar co-flow diffusion flame is focused in this chapter. The phenomenon is created by increasing the fuel rate without the supply of co-flow air to the combustion. This results in an increase of the velocity difference at the shear layer (between burnt gas and ambient air). The stable flame at the low fuel rate will then transform to the unstable oscillating flame e.g. flickering and tip-cutting flame. The stable and unstable flames of syngas/producer gas with various fuel compositions are formulated in this work to project their impact on the transition from the stable to an unstable oscillating flame. The results obtained from the different fuel compositions are compared, resulting in the impact of each species in syngas composition. Finally, this result is discussed, and the conclusion is given.

6.1 Introduction

The instability of co-flow laminar diffusion flame in sense of K-H instability occurs when the fuel is injected into the combustion without a sufficient amount of oxidiser stream supplied. The velocity difference at the shear layer between the burnt gas and the co-flow or

ambient air leads to an occurrence of vortices and flame oscillation. Two types of oscillation are observed from the laminar diffusion co-flow flame, e.g. flickering and tip-cutting flames [3], [88]. For the flickering flame, the flame extends and reduces in the upward and downward directions. The movement of the tip-cutting flame is slightly different from the flickering flame. The flame extends upward causing an increase of the flame length until the flame stability cannot be maintained. The top part of the flame consequently lifts upward and results in a cut at the top part of the flame body. The movement of both flickering and tip-cutting flames occurs regularly, and one cycle of movement is called 'a limit cycle of oscillation'.

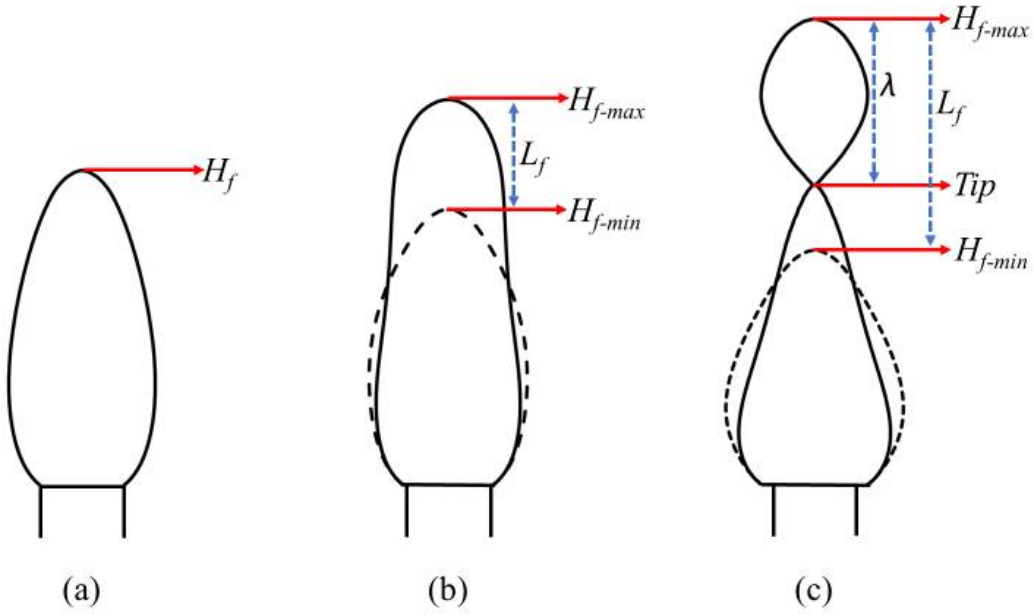

Figure 6-1 The explanation of the flame type and related parameters

The result of Chapter 5 expressed the significant role of flame length on the heat generation capability of the stable laminar diffusion syngas/producer gas flame. The change of flame length during the limit cycle of oscillation and its impact on heat generation are hence focused in this work. Several parameters are utilised for investigating the movement and behaviour of flickering and tip-cutting flames as presented in Figure 6-1. Flame length (H_f) is constant for a stable flame; however, the value of this parameter of the unstable flame changes during the limit cycle of oscillation. The average flame length ($H_{f\text{-}ave}$) is hence utilised rather than only H_f in the analysis. The value of H_f is equal to $H_{f\text{-}ave}$ for the stable flame. The value of $H_{f\text{-}ave}$ of an unstable flame is calculated from the maximum and minimum flame length as $(H_{f\text{-}min} + H_{f\text{-}max})/2$. The magnitude of oscillation (L_f) is defined as the difference between the maximum, and the minimum flame length ($H_{f\text{-}max} - H_{f\text{-}min}$) whereas

the oscillation wavelength (λ) is the difference between $H_{f\text{-}max}$ and tip-cutting position. The value of L_f, and λ represent the range of movement, and the higher value refers to the higher level. Also, L_f, and λ could be used for identifying the type of the oscillating flame. The flickering flame has $L_f > 0$ and $\lambda = 0$ while the value of both L_f and λ are greater than zero for a tip-cutting flame [88].

The study of the impact of the fuel composition on the value of L_f, and λ also reveals the transition from one fame type to another type (stable/flickering/tip-cutting). The oscillation of laminar diffusion flame could be created by increasing the fuel rate solely (without the supply of air rate). This action escalates the difference between the velocity of fuel and oxidizer (ambient air) which encourages an occurrence of K-H instability. The result is the transition from stable to flickering and tip-cutting flames, respectively.

The analysis of the profile of L_f, and λ changed by an increase of fuel rate of various fuel compositions projects the impact of diversity in fuel composition. Further, the heat generation and its fluctuation affected by the flame oscillation are included in this work. The total chemical heat released from the flame (Q_{total}) is computed and monitored during the limit cycle of oscillation. The average chemical heat release ($Q_{\text{-}ave}$) is computed by a similar approach as the average flame length ($H_{f\text{-}ave}$). Also, the flame temperature is computed for an average value ($T_{\text{-}ave}$) during the limit cycle and analysed along with $Q_{\text{-}ave}$. These data provide a comprehensive understanding regarding the heat generation capability and temperature of the flickering and tip-cutting syngas/producer gas flames. Also, the fluctuation of total chemical heat release (Q_{total}) and flame temperature (T) could be revealed by a similar method as the magnitude of oscillation (L_f). The syngas composition that provides a larger difference between the maximum and minimum values of Q_{total} and T also has a higher level of the fluctuation of each parameter. Thus, the fluctuation of flame temperature (dT) and total chemical heat release (dQ) are calculated to project the fluctuation level.

The co-flow burner of Darabkhani et al. [88] is selected and modelled by CFD. This burner is designed specifically for studying the oscillation of laminar co-flow flame and is capable of formulating stable, flickering, and tip-cutting flames. The assessment of reliability and accuracy of the newly generated CFD model is required. The experimental result presented in Ref [88] is hence used as a reference in the validation process. The generated model is ready for the study stage once it could produce a similar result comparing to the experimental

one. In this chapter, the CFD model formulation and validation are presented firstly. The CFD models are created with different chemical reaction mechanisms supplied and mesh resolutions. Among them, the model that provides the good agreement result compared to the experimental result is selected for utilising in the study stage. The selected CFD model from the validation stage will be used for formulating the stable, flickering, and tip-cutting flame of syngas/producer in the study stage. The study examines (i) the flame characteristics during the oscillation, (ii) the critical condition where the transition between flame types occurs, (iii) the level of oscillation and tip-cutting phenomenon, and finally (iv) the fluctuation in temperature and heat generation. Lastly, the discussion and conclusion according to the impact of each species on these aspects are provided.

6.2 Model formulation and validation

The burner geometry of Darabkhani et al. [88] is a reference for the model formulation. The simulation domain considers the area above the fuel and co-flow air inlet. The details regarding this process are described in this section.

6.2.1 Burner configuration and boundary condition

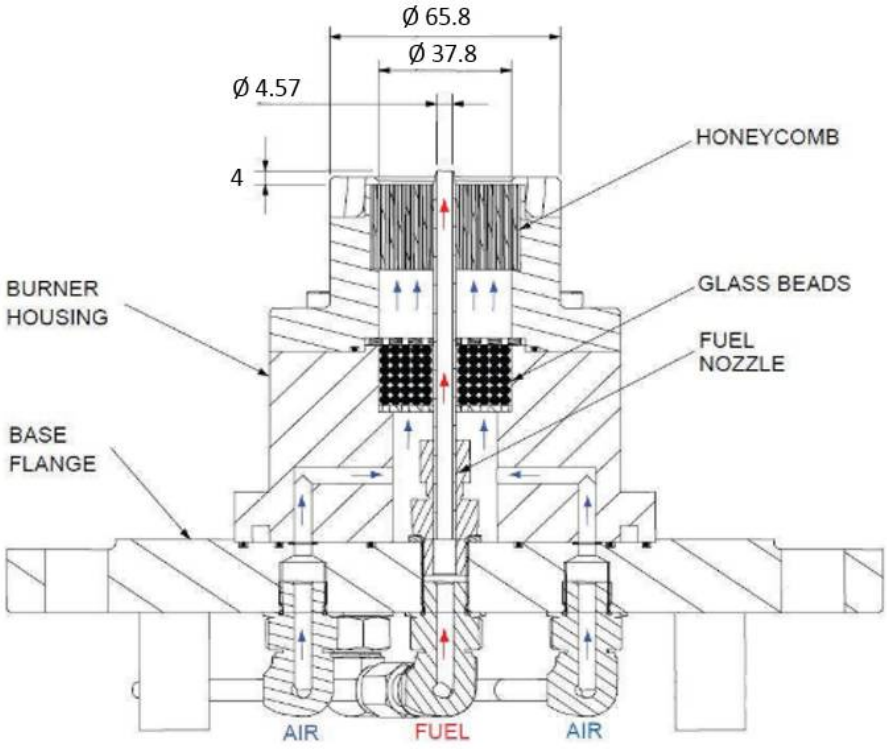

Figure 6-2 Cross-section of the selected burner [3]

The dimension and appearance of the selected co-flow burner are presented in Figure 6-2. The fuel inlet inner diameter is 4.57 mm, whereas the co-flow air inlet inner diameter is 37.8 mm. The exit of fuel is 4 mm above the co-flow air exit. The shape of the fuel inlet tube is a tapered nozzle which assists the stabilisation of the flame. This burner is modelled by considering the area above the fuel and air exit as the area of interest. The axisymmetric domain is created, and the axis of the simulation domain is the centreline of the fuel inlet. The height and width of the domain are 204 mm and 32.9 mm, respectively, as illustrated in Figure 6-3. The boundary conditions are defined based on the combustion condition of the reference paper. The top and left planes are a pressure boundary with the temperature and pressure respectively as 293 K and 101325 Pa. At the bottom of the domain, the fuel and co-flow air inlet are both set as a velocity inlet. The velocities of the fuel and air streams are converted from the volume flow rate, which is in the unit of SLPM (standard litre per minute). Lastly, the fuel and air tube are set as non-slip and non-adiabatic wall boundary.

6.2.2 **Overview of the numerical techniques**

The continuity, momentum, species, and energy equations are solved in a segregated manner with the boundary conditions described in the previous sections. The simulation is transient, so the time step is defined based on the value of convective courant number (CCN) which is expressed in equation (77). The maximum value of CCN is monitored every time-step, and this parameter is controlled at 1±0.05 by increasing or decreasing the time-step size. The cell having the smallest size (an area close to the fuel tube) is found to have the maximum value of CCN. The value is 30-50 % lower at the reaction zone of the flame. This setup causes the fluctuation of the time-step size when the simulation begins, and the size is stable once the maximum CCN value is in the preferable range.

The species transport equation is solved by an inbuilt algorithm called ‘operator splitting’ in STAR CCM+ CFD software. Various chemical reaction mechanisms are supplied into this combustion model to find the most suitable one. The details of this optimisation will be explained in the following sections. The dynamic viscosity of each species is defined by two different methods which are (i) interpolation of the gas property data of Ref [119], and (ii) constant value at the initial combustion condition (293 K and 1 atm). The dynamic viscosity of species H_2, CO, CH_4, N_2, CO_2, H_2O, and O_2 are computed by the previous method while one of the other species is defined by the latter method. Mass-weight mixture method is utilised for combining the dynamic viscosity of each species at the gas mixture level. The

molecular diffusivity coefficient of each species is considered based on the kinetic theory. The Discrete Ordinate Method (DOM) is selected for solving the thermal radiation transport equation where the absorption coefficient is provided by the Weighted Sum of Gray Gases Method (WSGGM).

The combustion is set to ignite at above the fuel tube. The cells at this area have a temperature of 1800 K for the first 0.5s to trigger the combustion. The simulation is run until (i) the flame and the focused parameters (e.g. the flame length, temperature, and total chemical heat release) are constant for the stable flame, or (ii) the profile of focused parameters (H_f, Q, and T) repeats its pattern 10 times with the difference in the maximum and minimum values between the limit cycles of oscillation less than 0.001 mm, 0.01 K, and 0.01 W for flame length, temperature, and total chemical heat release respectively.

6.2.3 **Mesh generation and optimisation**

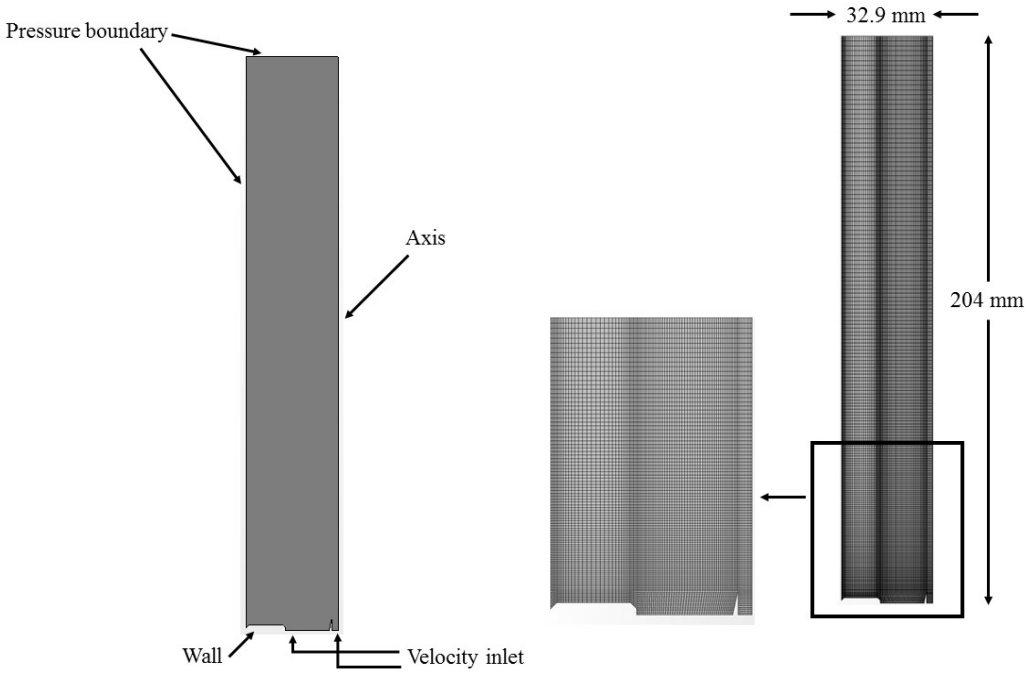

Figure 6-3 Simulation domain and mesh generation

The pattern of mesh generation is presented in Figure 6-3. The objective of the mesh design is to project the interaction between the fuel/air stream and the fuel/air tube, and chemical reactions between the fuel and co-flow air streams. The area close to the edge of the fuel and air tubes has a higher density mesh. From this location, the non-uniform mesh is stretched by a hyperbolic function from the smallest to largest cell size at the pressure boundary.

Similar to the formulation of the stable flame CFD model used in Chapter 3 and 4, the optimisation of the mesh resolution is processed for finding the level of mesh resolution that provides the sufficient detail of solution with an acceptable computational cost. Three CFD models with different levels of mesh resolution are created, and the results obtained from them are compared with the experimental result of Darabkhani et al. [88]. The fine mesh model has the highest resolution (39,560 cells and 1.25E-4 m of the smallest cell size) followed by the medium mesh model (19,720 cells and 2E-4 m) and coarse mesh model (6,720 cells and 3.33E-4 m). For the reasonable comparison, the same chemical reaction mechanism, which is DRM 22 [112], is supplied into these CFD models. This process provides the level of mesh resolution that is suitable for the study stage.

6.2.4 **Chemical reaction mechanism selection**

In the validation stage, the selection of the proper reaction mechanism is also carried out by comparing the simulation result generating from various chemical reaction mechanisms supplied into the CFD models. The GRI 3.0 reaction mechanism which is selected for studying the stable flame in the previous chapter consumed high computational cost due to its number of species and reactions (53 species and 325 reactions), especially in the unsteady simulation. The mechanisms selected in this work are smaller than GRI 3.0 to reduce the computational cost. These are DRM22 [112], Lu and Law [115], and Sankaran et al. [116]. Among them, the largest mechanism is Lu and Law [115] with 30 species and 184 reactions followed by DRM22 [112] (22 species and 104 reactions), and Sankaran et al. [116] (17 species and 73 reactions). The reaction pathways explained by these mechanisms are supplied into the complex chemical combustion model of the generated CFD model. The simulation is processed on the medium mesh resolution model for all the compared mechanisms. Similar to the mesh optimisation, the reaction mechanism that provides a good agreement to the experimental result under the acceptable compactional cost will be selected for the study stage.

6.2.5 **Data monitoring and extraction**

Regarding the unstable flame (flickering or tip-cutting), the parameters L_f and λ are the keys for the investigation of flame oscillation. The calculation of them requires H_f-*max*, H_f-*min*, and tip-cutting position. These parameters are extracted from the change of flame length during the limit cycle of oscillation as illustrated in Figure 6-4. The flame front line is firstly

drawn by the zero-temperature gradient method, and the position where the flame front line crosses the domain axis is the flame length, which is plotted and monitored every time step. This method forms the flame length profile changing over time, as seen in Figure 6-4. It could be noticed that the flame length profiles of flickering and tip-cutting flames are different. The cut at the flame body causes the immediate reduction of the flame length profile in tip-cutting flame, whereas the profile of flickering flame is the typical wave oscillation. The flame length profile is extracted for H_f-*max*, H_f-*min*, and tip-cutting position, which are used for calculating the value of L_f and λ. The analysis of the flame length profile also allows the calculation of flickering frequency (F), which represents the number of limit cycles of oscillation per second. This parameter could be computed from the inverse proportion of the period of the limit cycle. Nevertheless, the method has a limitation for a stable flame since its flame length profile has a constant value. Thus, the flickering frequency is only presented from the unstable flame (flickering and tip-cutting flame).

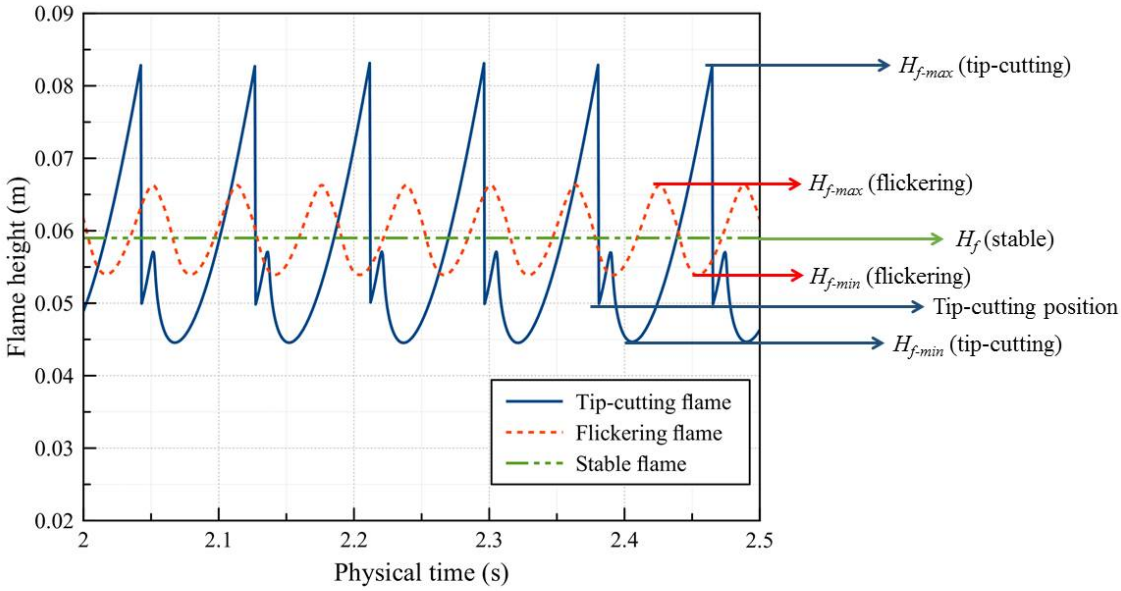

Figure 6-4 Flame length profile and data extraction

Flame length, flame temperature, and total chemical heat release are studied based on their average value throughout the limit cycle of oscillation. The parameters required for this purpose is the minimum and the maximum value of flame length, flame temperature, and total chemical heat release. The average flame length ($H_{f\text{-}ave}$) could be computed from (H_f-*max* + H_f-*min*)/2. The same method is applied for the flame temperature (T) and total chemical heat release (Q) resulting in the average value of these parameters. The profile of T and Q are monitored every time-step to form the profile of these parameters changing over

time. However, the tip-cutting phenomenon does not affect the profile of T and Q, and the profile of them are typical wave oscillation profile (similar to the flame length profile of flickering flame). Thus, only the maximum and minimum values are extracted from the profile of T and Q. These values are used for calculating the value of average flame temperature (T_{ave}) and total chemical heat release (Q_{ave}). Furthermore, the fluctuation level of temperature (T) and total chemical heat release (Q) could be computed from their extracted maximum and minimum value. The difference between the maximum and minimum value of T is computed for the fluctuation level of flame temperature (dT), and the same method is applied for the fluctuation of total chemical heat release (dQ).

6.2.6 **Validation and optimisation**

Total of five CFD models is created in the validation stage with the different mesh resolution and chemical reaction mechanisms, as stated in Section 6.2.3 and 6.2.4. Every model formulates the stable, flickering and tip-cutting flame at the same combustion condition as the reference literature (Ref [88]). The fuel is CH_4, and the volume flow rate of fuel stream is varied between 0.2 and 0.35 SLPM (standard litre per minute). At this range of fuel rate, the Reynolds number (Re_f) of fuel stream stays between 61.02 and 106.78, while the Froude number (Fr) is calculated between 1.249 and 3.845. The oxidiser is air ($79\%N_2+21\%O_2$), and the flow rate of the co-flow air stream is between 0 and 20 SLPM. The oxidiser is supplied from the co-flow air inlet when the co-flow air rate is above zero. Ambient air is an oxidiser when the co-flow air rate is 0 SLPM. Based on this setup, the flame is considered to be dominated by the buoyancy force rather than the momentum of the fuel stream for all the simulation cases according to ref [88], [147].

According to the experimental result provided, the validation process focuses on (i) the movement and behaviour of flames during a limit cycle of oscillation, (ii) the magnitude of oscillation (L_f), (iii) the oscillation wavelength (λ), and (iv) the average oscillating flame height (H_f-ave). The movement of the flames formulated by all the CFD models is in the same direction as the experimental result. The example of the movement of the simulated unstable flame could be seen in Figure 6-5. As seen, the complete cycle of the tip-cutting flames of CH_4 at a fuel rate of 0.3 SLPM and co-flow rate of 0 and 3 SLPM are presented as a series of temperature contour from left to right. The temperature contour presented in Figure 6-5 is predicted by the CFD model with the medium mesh resolution and DRM 22 reaction mechanism. The similar movement pattern is obtained when the simulation result

(Figure 6-5) is compared with the experimental result of [88] in Figure 6-6. The flame size and length increase from the minimum to the maximum value. The impact of buoyancy force leads to the K-H instability and the flame oscillation; thus, the top part of the flame body lifts upward and results in the tip-cutting phenomenon. After the tip-cutting, the fluctuation of flame size and length are observed; they increase slightly and reduce back to their minimum value at the end of the limit cycle. For the flame structure, the area having a high temperature (>1800 K) is at the top part of the flame at the beginning of the limit cycle. During the limit cycle, the temperature of this area decreases, and the new high-temperature area is formed on the flame front close to the fuel tube. This new high-temperature area moves along with the flame front line and reaches the axis when the tip-cutting occurs.

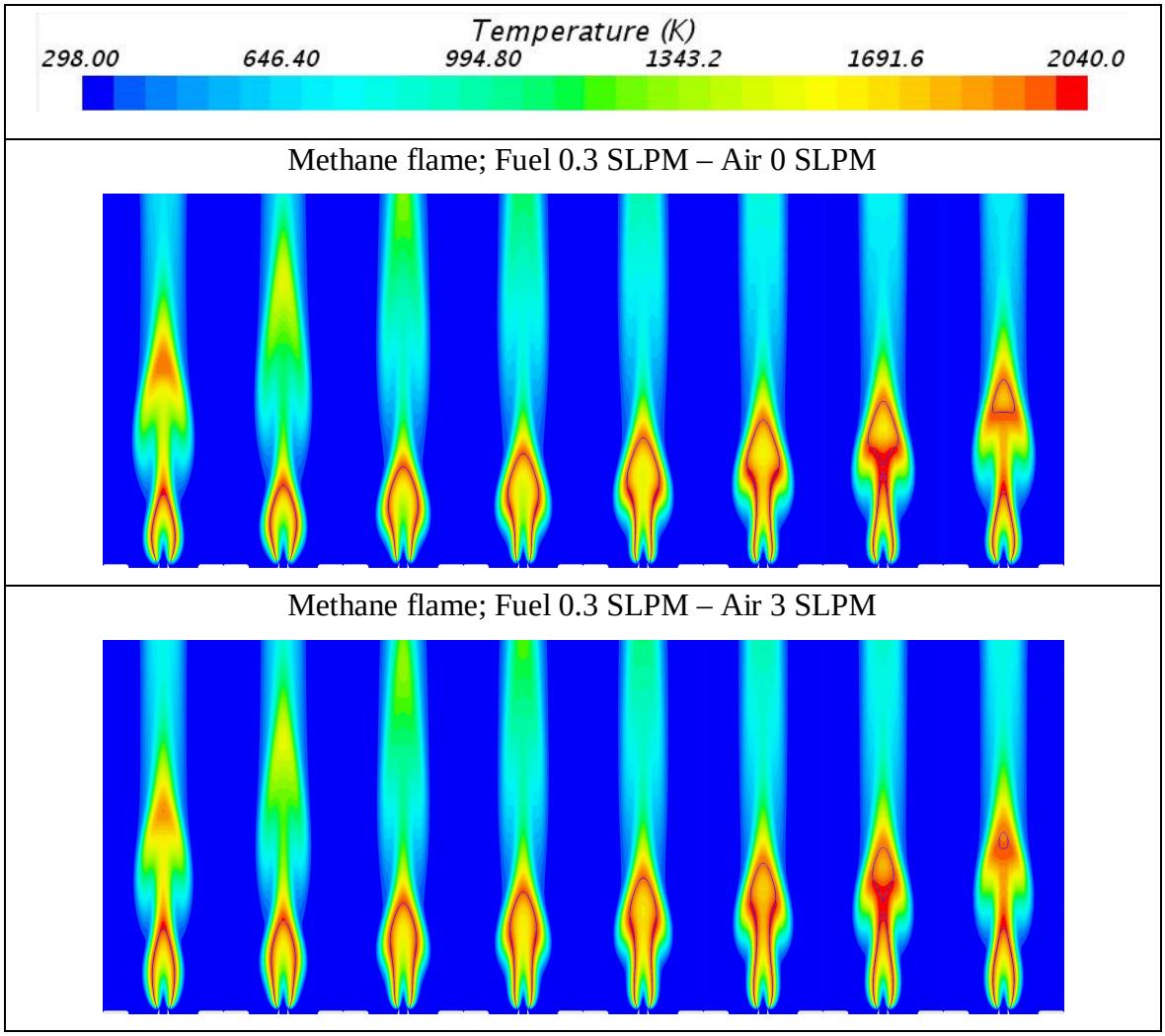

Figure 6-5 Temperature contours representing a limit cycle of oscillation of the tip-cutting flame of methane: (top) Fuel 0.3 SLPM – Air 0 SLPM, and (bottom) Fuel 0.3 SLPM – Air 3 SLPM

The analysis of temperature contour could project the movement of the unstable flame. Nevertheless, this method has a limitation when the flame moves in a small range (L_f < 3

mm). The temperature contour of the flickering flame of CH_4, which is found from the flame length profile to have the value of L_f lower than 3 mm, cannot clearly project the movement of the flame. This finding, therefore, points to the requirement for the detailed analysis of flame oscillation and tip-cutting phenomenon based on the other parameters such as the magnitude of oscillation (L_f), oscillation wavelength (λ) and average flame length ($H_{f\text{-}ave}$). The profile of parameters L_f, λ, and $H_{f\text{-}ave}$ formulated by different CFD models are compared with the experimental result of [88] in Figure 6-7 - Figure 6-9. The clear downtrend of L_f and λ are observed as their values reduce when the co-flow air rate is higher. This means that the level of oscillation and tip-cutting phenomenon of CH_4 flame reduces to the lower level and disappears when the co-flow air is supplied at a higher rate to the combustion. The pattern of the profile of both L_f and λ are similar; it decreases significantly and becomes zero. This pattern projects the behaviour of the unstable CH_4 flame when the supplied air rate is higher. It is also noticed that the relation between L_f and λ, and co-flow air rate are non-linear.

Methane flame; Fuel 0.3 SLPM – Air 0 SLPM

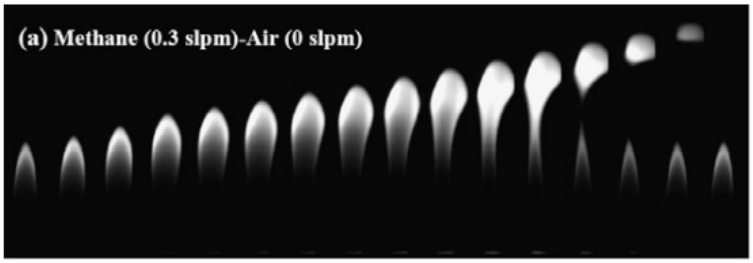

Methane flame; Fuel 0.3 SLPM – Air 3 SLPM

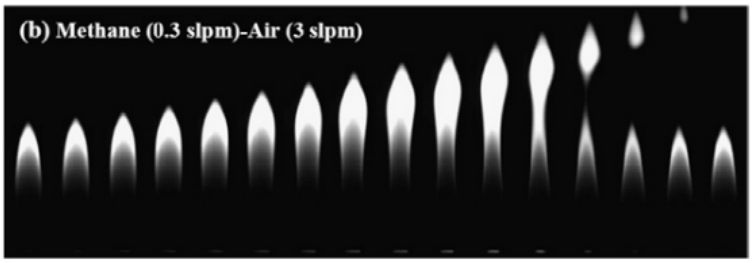

Figure 6-6 The movement of tip-cutting flame obtained from the experiment of [88]

The elimination of flame oscillation and tip-cutting phenomenon demands a different amount of co-flow air rate depending on the fuel rate supplied. This topic will be studied in detail in Chapter 7 for syngas diffusion flame. The higher fuel rate requires a higher amount of air rate to become stable. The pattern of average flame length ($H_{f\text{-}ave}$) of CH_4 depends on the flame type. The value of $H_{f\text{-}ave}$ rises when the co-flow air rate is higher for an unstable

flame ($L_f > 0$). Once the air rate is enough for the flame to become stable, the flame length decreases at the higher co-flow air rate.

The finding presented in this validation stage could be used as a guideline for the analysis in the study stage since CH_4 is one of the combustible species in syngas/producer gas composition, as seen in Figure 6-7 - Figure 6-10. All the mechanisms are capable of predicting the result in the same direction as the experiment result. The slightly over-prediction and under-prediction of the profile of L_f, λ, and $H_{f\text{-}ave}$ are obtained; nevertheless, the difference is insignificant. The same flame type (stable, flickering or tip-cutting) is predicted form all the compared reaction mechanisms at the same fuel and air rate, and it is the same as the experimental result. The profile of each focused parameter is also predicted similarly from these reaction mechanisms. As a result, they are capable of formulating the unstable flame that provides a reliable result. Among them, the DRM 22 reaction mechanism is selected. The CFD model with this mechanism is optimum when the computational cost is considered along with the reliability of the generated result. Furthermore, this mechanism considers the detailed reaction pathway of related species, which would benefit the prediction of chemical heat release from flame.

Further, regarding the mesh optimisation, the medium and fine mesh resolution models formulate the flame with a similar profile of L_f, λ, and $H_{f\text{-}ave}$. As a result, the same flame type is predicted by these models at a specific fuel and air rate. The difference in the profile of L_f and λ is computed from the coarse mesh model. The value of L_f and λ approach to zero at the lower co-flow air rate than ones obtained from the medium and fine mesh resolution models. The transition between flame type is hence predicted to occur at the lower air rate by the coarse mesh model. Comparing to the experiment result, the CFD model with the medium and fine mesh resolutions compute the values of L_f, λ, and $H_{f\text{-}ave}$ closer to the experimental result than the coarse mesh model. Consequently, the medium mesh model is selected for the study stage since it formulates the flame with the same value of the focused parameter as the experimental result with less computational cost than the fine mesh model. Consequently, the CFD model selected for the study stage is one with the medium mesh resolution and DRM22. This model provides a reliable result with a reasonable computational cost (~30 hours per simulation case on four processors parallel computing system).

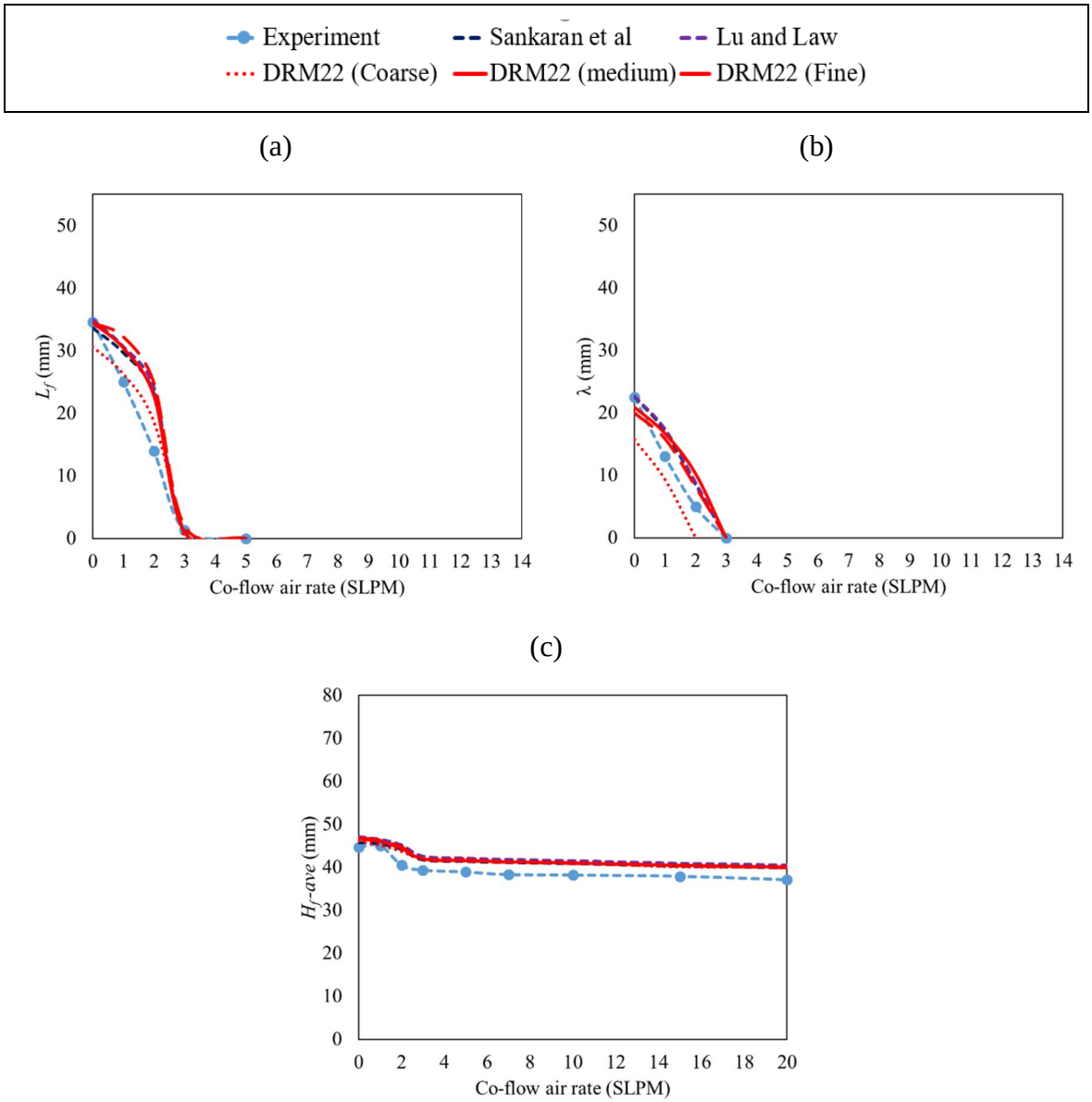

Figure 6-7 Results obtained from various CFD models in the validation stage compared with the experimental result at a fuel rate of 0.2 SLPM; (a) L_f, (b) λ, and (c) $H_{f\text{-}ave}$

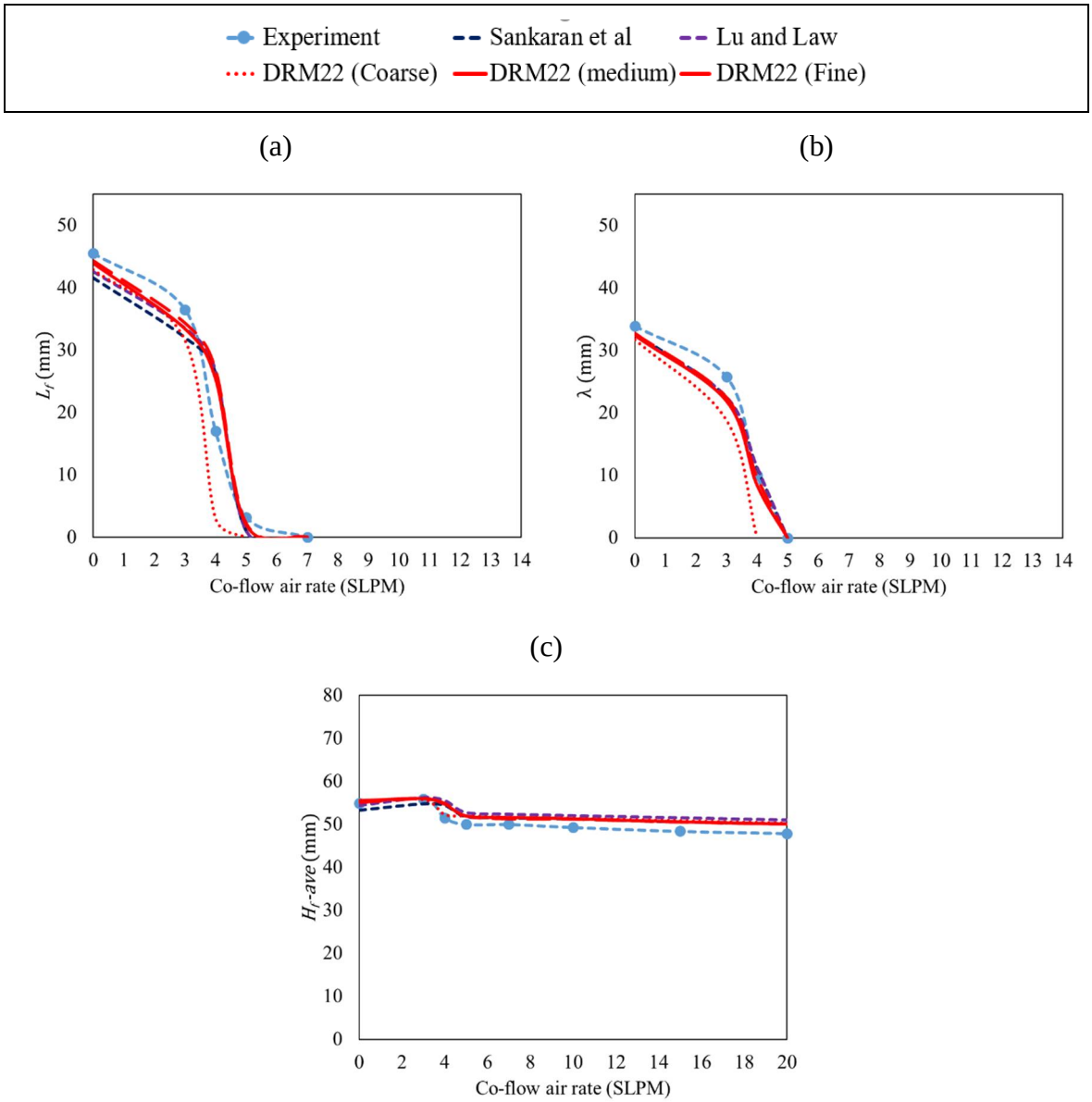

Figure 6-8 Results obtained from various CFD models in the validation stage compared with the experimental result at a fuel rate of 0.25 SLPM; (a) L_f, (b) λ, and (c) $H_{f\text{-}ave}$

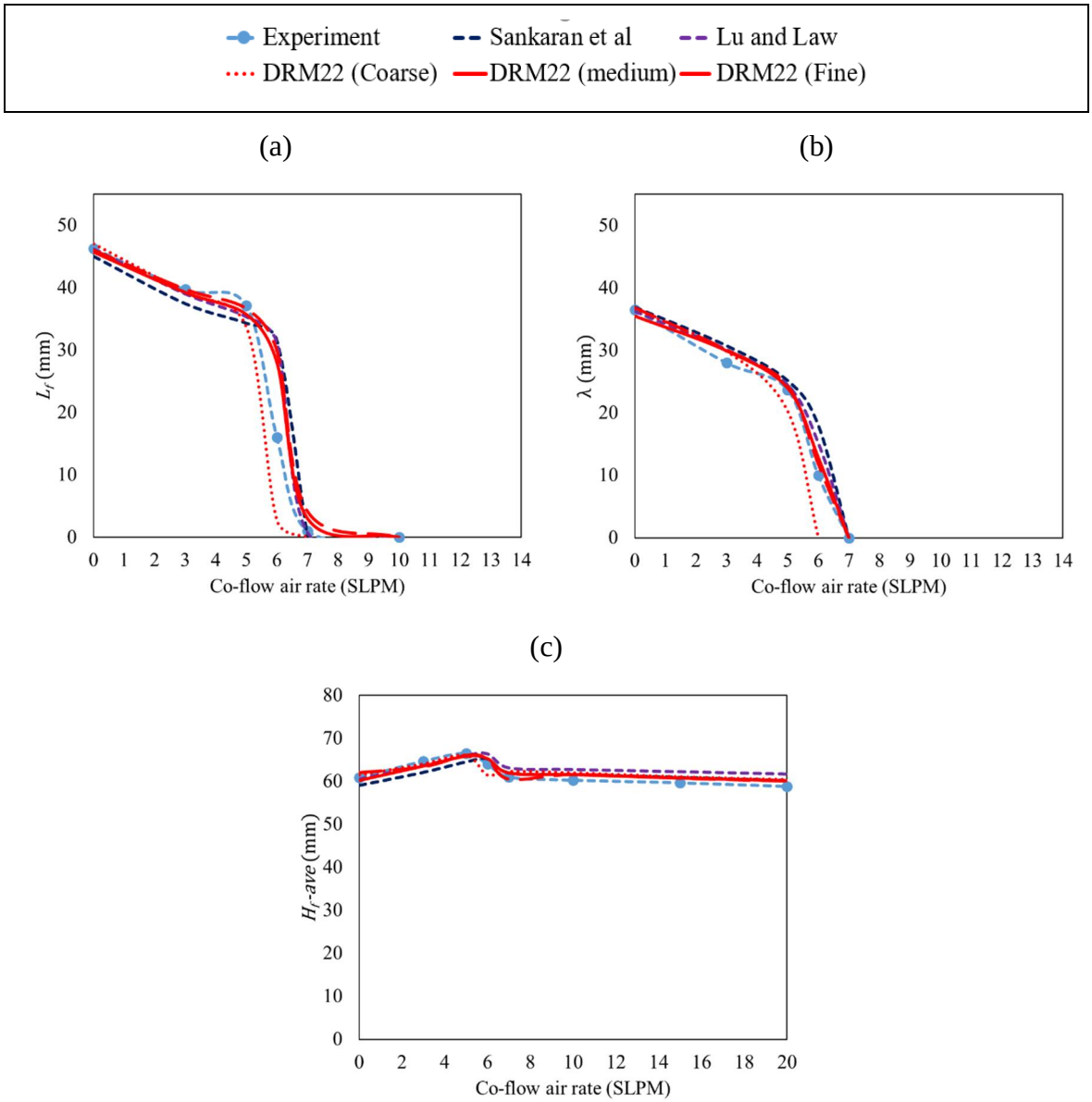

Figure 6-9 Results obtained from various CFD models in the validation stage compared with the experimental result at a fuel rate of 0.3 SLPM; (a) L_f, (b) λ, and (c) $H_{f\text{-}ave}$

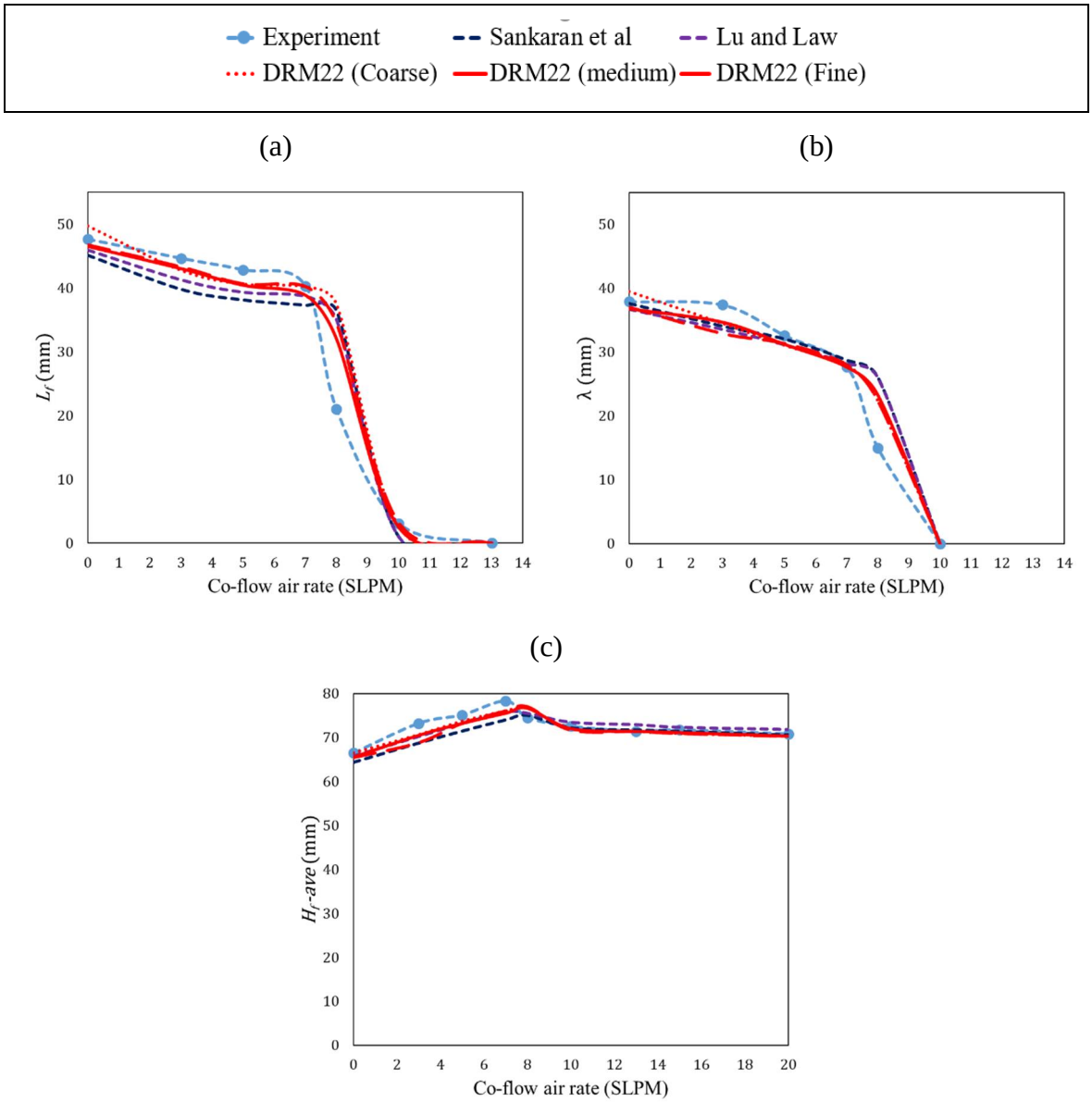

Figure 6-10 Results obtained from various CFD models in the validation stage compared with the experimental result at a fuel rate of 0.35 SLPM; (a) L_f, (b) λ, and (c) $H_{f\text{-}ave}$

6.3 Impacts of fuel composition

The CFD model, with the medium mesh resolution and DRM 22 [112] chemical reaction mechanism, is utilised for studying the oscillation of syngas/producer gas flame in this stage. The composition of syngas/producer gas in this study is the same as the composition in category (ii), and (iii) in the study of syngas /producer gas stable flame in Chapter 5. The details of composition along with the Reynolds number of fuel stream are shown in Table 6-1. The result of pure syngas with H_2:CO as 1:3, 1:1, and 3:1 (CO-rich, EQ, and H_2-rich) is analysed with one of H_2 to reveal the impact of H_2 and CO. The other fuel compositions are EQ syngas mixed with either CH_4, CO_2, or N_2 at the additional percentage of 10 and 20%. Examining the flame of these fuel compositions by utilising the flame of EQ syngas as a reference provides the impact of CH_4, CO_2, and N_2.

Table 6-1 Fuel composition

Fuel	Composition					Re_f	Fr_f
	H_2	CO	CH_4	CO_2	N_2		
CO-rich	25%	75%	-	-	-	52 - 367	1.88E-3 – 1.31E-2
EQ	50%	50%	-	-	-	37 - 261	1.10E-3 – 7.71E-3
H_2-rich	25%	75%	-	-	-	22 - 157	4.53E-4 – 3.17E-3
H_2	100%	-	-	-	-	9 - 66	4.00E-5 – 2.80E-4
EQ+10%CH_4	45%	45%	10%	-	-	26 - 180	8.08E-4 – 5.65E-3
EQ+20%CH_4	40%	40%	20%	-	-	29 - 205	6.27E-4 – 4.39E-3
EQ+10%CO_2	45%	45%	-	10%	-	33 - 228	1.65E-3 – 1.15E-2
EQ+20%CO_2	40%	40%	-	20%	-	43 - 299	2.36E-3 – 1.65E-2
EQ+10%N_2	45%	45%	-	-	10%	27 - 188	1.43E-3 – 1.00E-2
EQ+20%N_2	40%	40%	-	-	20%	31 - 219	1.85E-3 – 1.30E-2

The fuel rate is set between 0.2 and 1.4 SLPM, and the combustion occurs with ambient air as an oxidiser (i.e. the co-flow air rate is 0 SLPM). The transition between flame types (stable to flickering and tip-cutting flames) of all the studied fuels are observed at this range of fuel rate. The flame of all the fuels is stable at a fuel rate of 0.2 SLPM then transforms to flickering and tip-cutting flames at a higher fuel rate. The Reynolds number of fuel stream (Re_f) is calculated as 9 - 66 for hydrogen, and 22 - 367 for the other studied fuels.

The Froude number (Fr) is computed for all the studied cases to assess whether the flame is buoyancy or momentum dominated. The buoyancy force due to the gravity plays a significant role in the flow of fuel stream in the buoyancy dominated diffusion flame. The

flow of fuel stream is momentum dominated at a higher velocity or the condition that gravity impact is insignificant. Nevertheless, the value of Fr is computed between 2 and 103. This range is significantly higher than the value determined from the flame of CH_4 in the validation stage. According to this, another level of the analysis is required for assessing the flame type. The parameter called 'Flame Froude number (Fr_f)' which is introduced by [148], [149] and simplified by [150] is hence used for this purpose. This calculation of Fr_f relates to the several parameters, as presented in equation (75). The critical value is 5; the flame with Fr_f < 5 is a buoyancy-dominated diffusion flame, while one with Fr_f > 5 is a momentum-dominated flame. The Fr_f calculated from all the formulated flames are significantly lower than the critical value at every fuel rate as presented in Table 6-1. Therefore, all the studied flames are buoyancy dominated.

$$Fr_f = \frac{UY_s^{1.5}}{((T_{ad} - T_\infty)/T_\infty g D_f)^{0.5} \xi^{0.25}}, \tag{96}$$

where the parameters related to the stoichiometry mixture fraction (Y_s), air/fuel density ratio (ξ), the diameter of the fuel injector (D_f), adiabatic flame temperature (T_{ad}), the velocity of fuel (U), gravitational acceleration (g), and ambient temperature (T_∞).

6.3.1 **Flame characteristics**

Various aspects of the flame characteristics are focused such as (i) the flame movement and structure (the distribution of the temperature of the flame), (ii) average flame length, (iii) average flame temperature, and (iv) average chemical heat release. The study initially analyses the temperature contour plot, which projects the appearance and movement of the flame during the limit cycle of oscillation. As mentioned above, three types of flame are formulated; stable, flickering and tip-cutting flames. At 0.2 SLPM of fuel rate, the flames of all the studied fuel compositions are stable, and their structures are similar. As seen, the high-temperature area (>1800 K) is on the axis and top of the flame. The impact of the fuel composition on the structure is weak due to low fuel rate supplied. Their flame temperature is different since different fuel compositions are supplied into combustion. The stable flame of H_2, H_2-rich, EQ, CO-rich EQ+10%CH_4, EQ+10%CO_2, and EQ+10%N_2 are presented in Figure 6-11 - Figure 6-12. All of them are obtained at 0.2 SLPM of fuel rate.

The flickering flame appears once the higher fuel rate is injected, and the transition occurs at a different fuel rate depending on the fuel composition. The series of temperature contour

plot representing the movement and structure of the flickering flame of H_2, H_2-rich, EQ, CO-rich, EQ+10%CH_4, EQ+10%CO_2, and EQ+10%N_2 are illustrated in Figure 6-13 and Figure 6-14. These flames are formulated at 0.5 SLPM of fuel rate except the flame of EQ+10%CH_4, which is formulated at 0.4 SLPM. From left to right, the flame length and size rise from the minimum to the maximum values then decreases back to the minimum value. The same direction of the movement is observed from the flickering flame of all the fuel compositions. Nevertheless, the structure of them is different and relies on the concentration ratio of H_2:CO. As seen, the locations of the high-temperature area of H_2 and H_2-rich are different from one of EQ and CO-rich. This area is on the flame front and above the fuel tube for H_2 flame and H_2-rich syngas flames which has H_2:CO > 1. The high-temperature area is at the axis and on the top of the flame for EQ and CO-rich syngas where their H_2:CO ≤ 1. The structure of the flickering flame of EQ syngas mixed with CH_4, CO_2, or N_2 is similar to the structure of EQ syngas since their H_2:CO = 1. During the limit cycle of oscillation, the high-temperature area expands and reduces upward and downward when the flame length increases and decreases, respectively. This could be explained by the impact of K-H instability on the mix of the fuel and oxidizer. Also, the flame temperature oscillates throughout the limit cycle of movement.

The tip-cutting flame is observed at the higher fuel rate than the flickering flame. This phenomenon is affected by the fuel composition strongly since the transition is found at different fuel rate in the flames of different fuel compositions. However, the structure and movement of the tip-cutting flame of all the fuel compositions are similar. The movement and structure of the tip-cutting flame of H_2, H_2-rich, EQ, CO-rich, EQ+10%CH_4, EQ+10%CO_2, and EQ+10%N_2 at a fuel rate of 1.2 SLPM are presented in Figure 6-15 and Figure 6-16. As seen, the flame length and size develop from their minimum to maximum values before the tip-cutting occurs at the flame body. The flame height and size then fluctuate and decrease to their minimum value at the end of the limit cycle. The flame temperature is found to oscillate throughout the limit cycle in the same direction as the flame height. It increases to the maximum value when the flame length escalates and reduces after the tip-cutting occurs. For the structure, the high-temperature area locates on the flame front line above the fuel tube at the beginning of the limit cycle. The ratio of H_2:CO affects the position of the high-temperature area, and this area is closer to the fuel tube for the flame of syngas with a higher ratio. Once the limit cycle begins, the high-temperature area moves along with the flame front line and approaches the axis at the same position where the tip-

cutting occurs. The new high-temperature area is then formed at its original position after the tip-cutting. The movement during the limit cycle described above repeats its pattern over time.

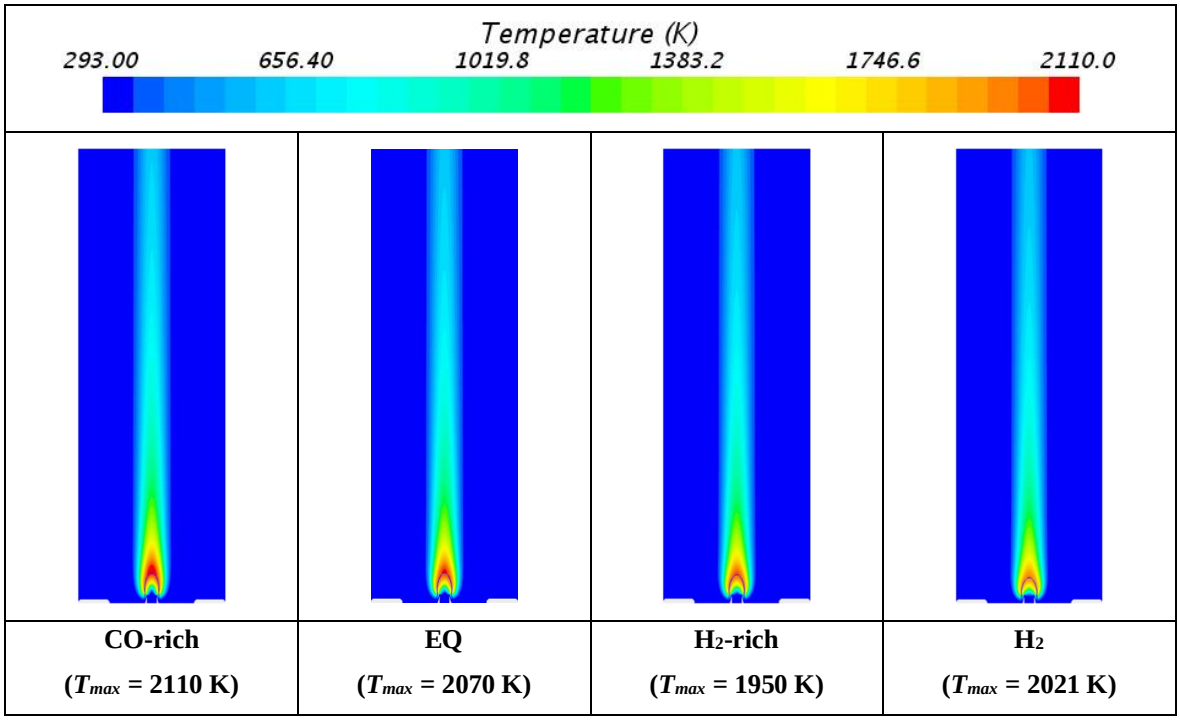

CO-rich (T_{max} = 2110 K)	**EQ** (T_{max} = 2070 K)	**H_2-rich** (T_{max} = 1950 K)	**H_2** (T_{max} = 2021 K)

Figure 6-11 Stable flames of pure syngas and H_2 at fuel rate = 0.2 SLPM

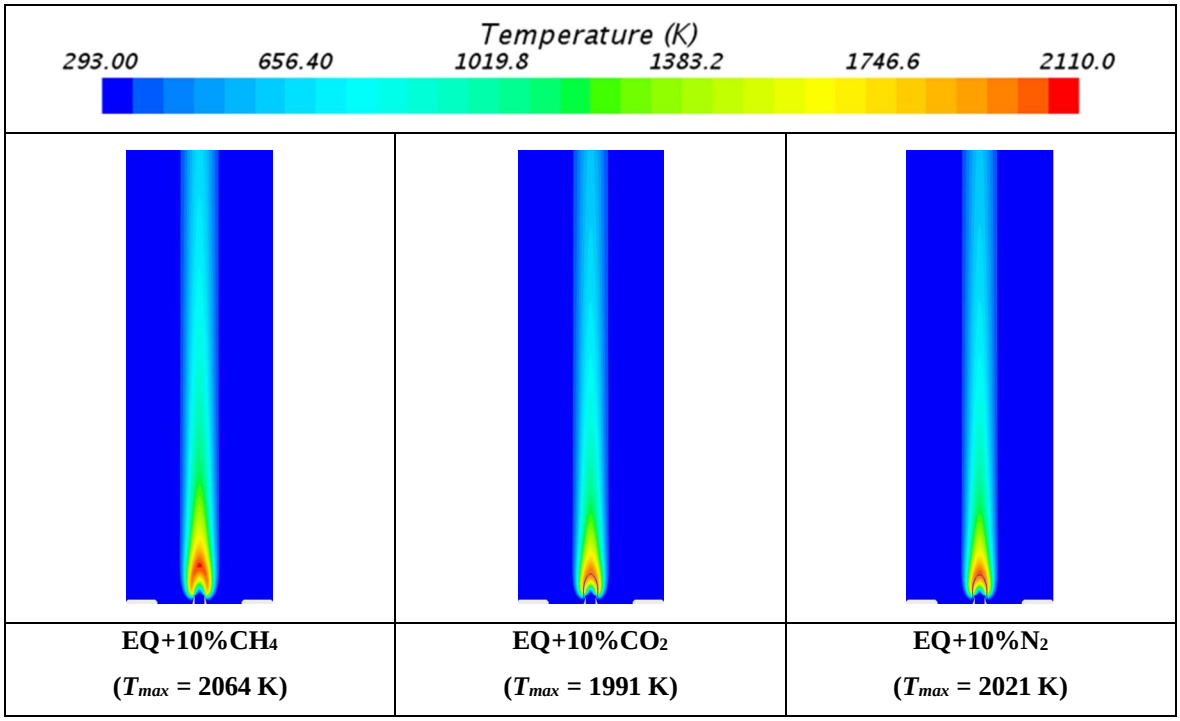

EQ+10%CH_4 (T_{max} = 2064 K)	**EQ+10%CO_2** (T_{max} = 1991 K)	**EQ+10%N_2** (T_{max} = 2021 K)

Figure 6-12 Stable flame of syngas mixed with either CH_4, CO_2, or N_2 at fuel rate = 0.2 SLPM

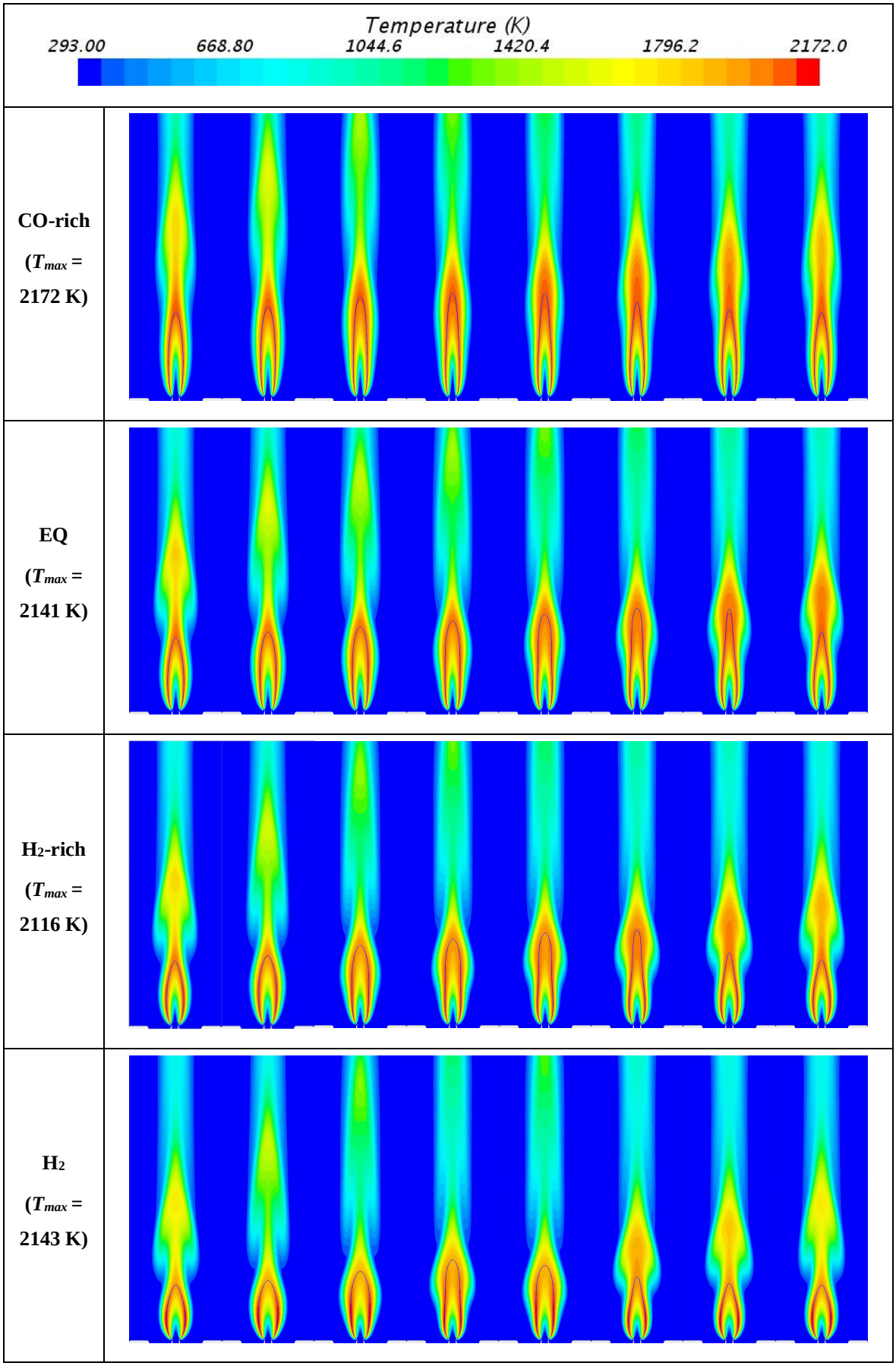

Figure 6-13 Appearance of flickering flame of pure syngas and H_2 at a fuel rate of 0.5 SLPM

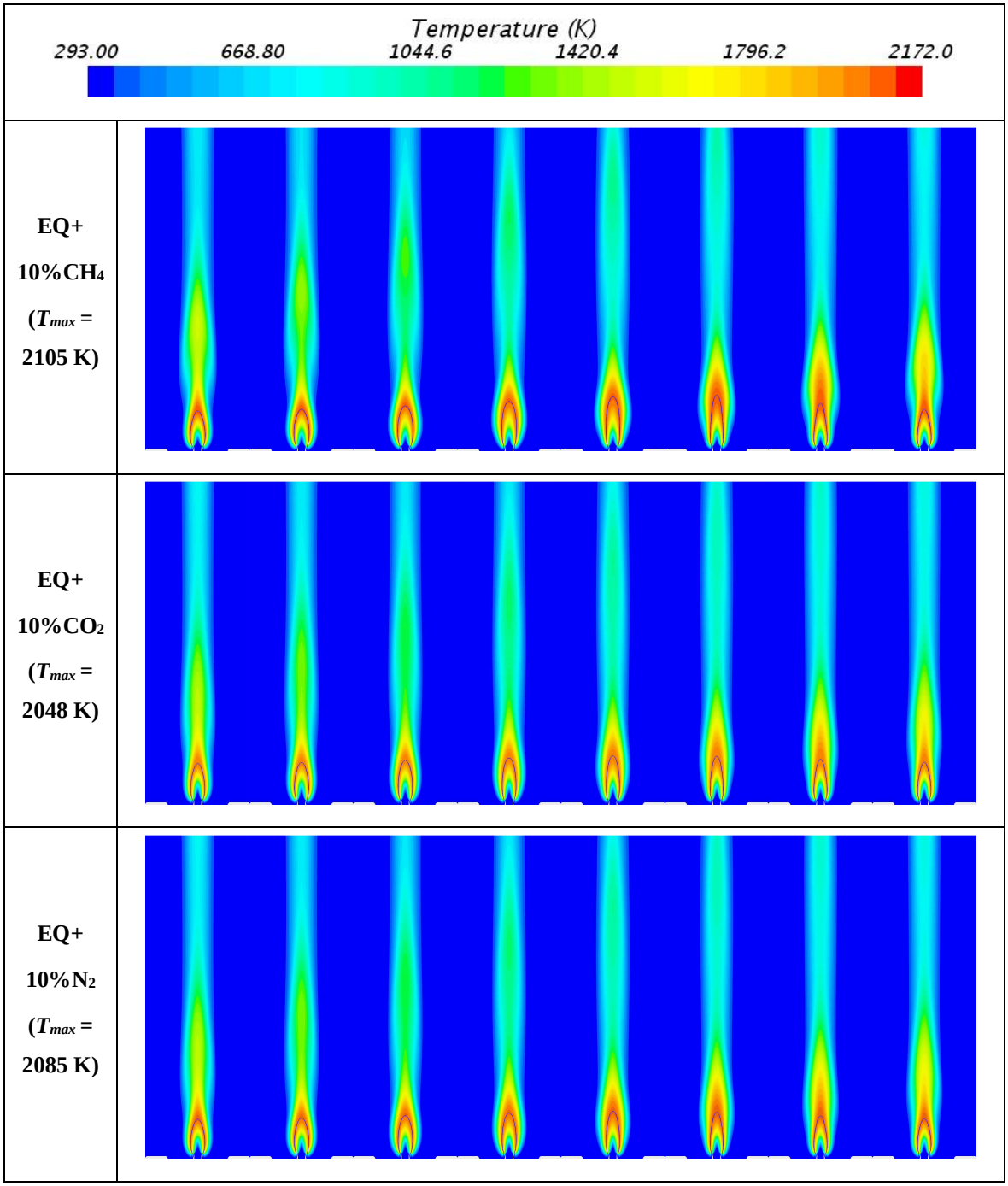

Figure 6-14 Appearance of flickering flame of syngas mixed with either CH_4, CO_2, or N_2 at a fuel rate of 0.4 SLPM for EQ+10%CH_4, and 0.5 SLPM for EQ+10CO_2 and EQ+10%N_2

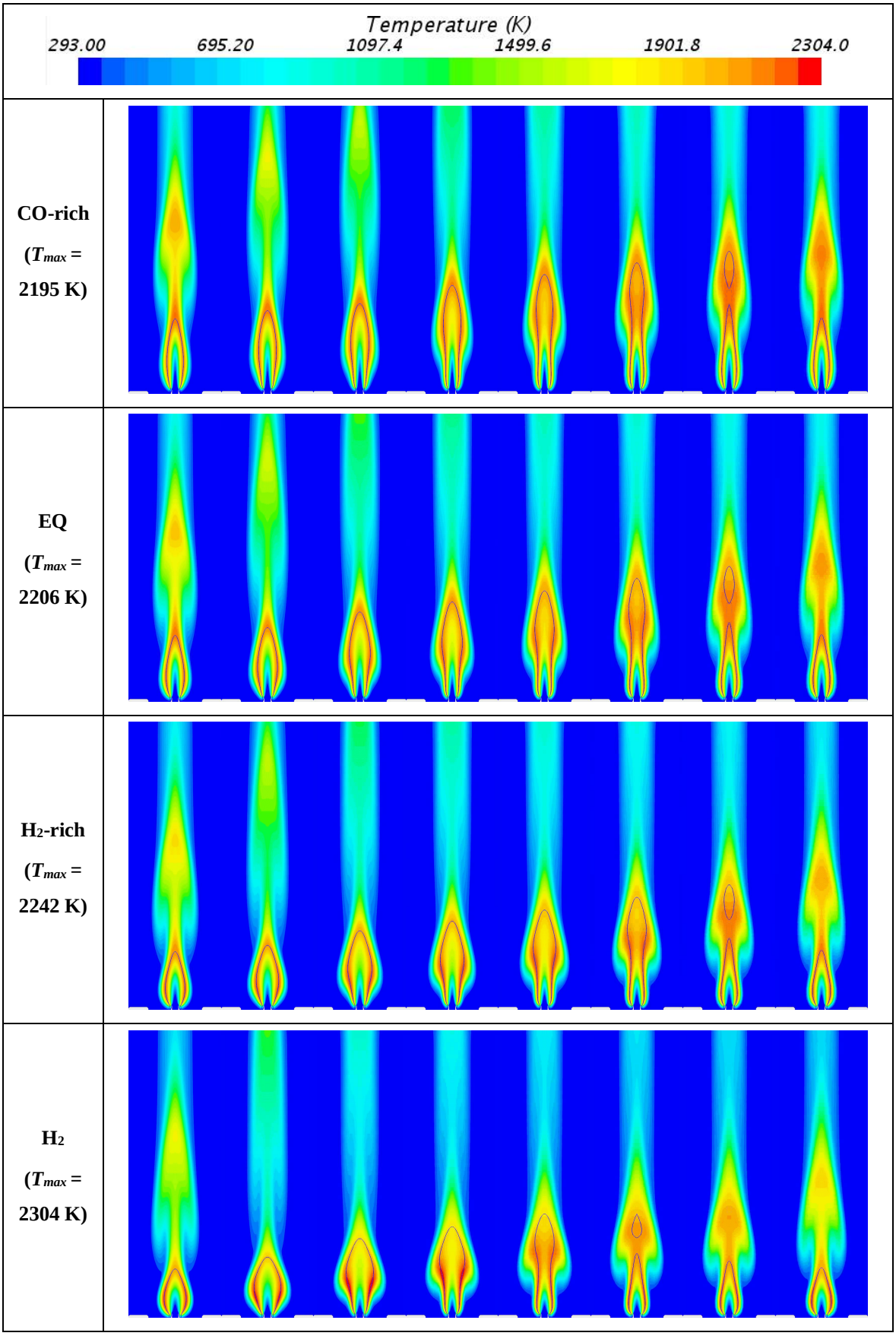

Figure 6-15 Appearance of tip-cutting flame of pure syngas and H_2 at fuel rate of 1.2 SLPM

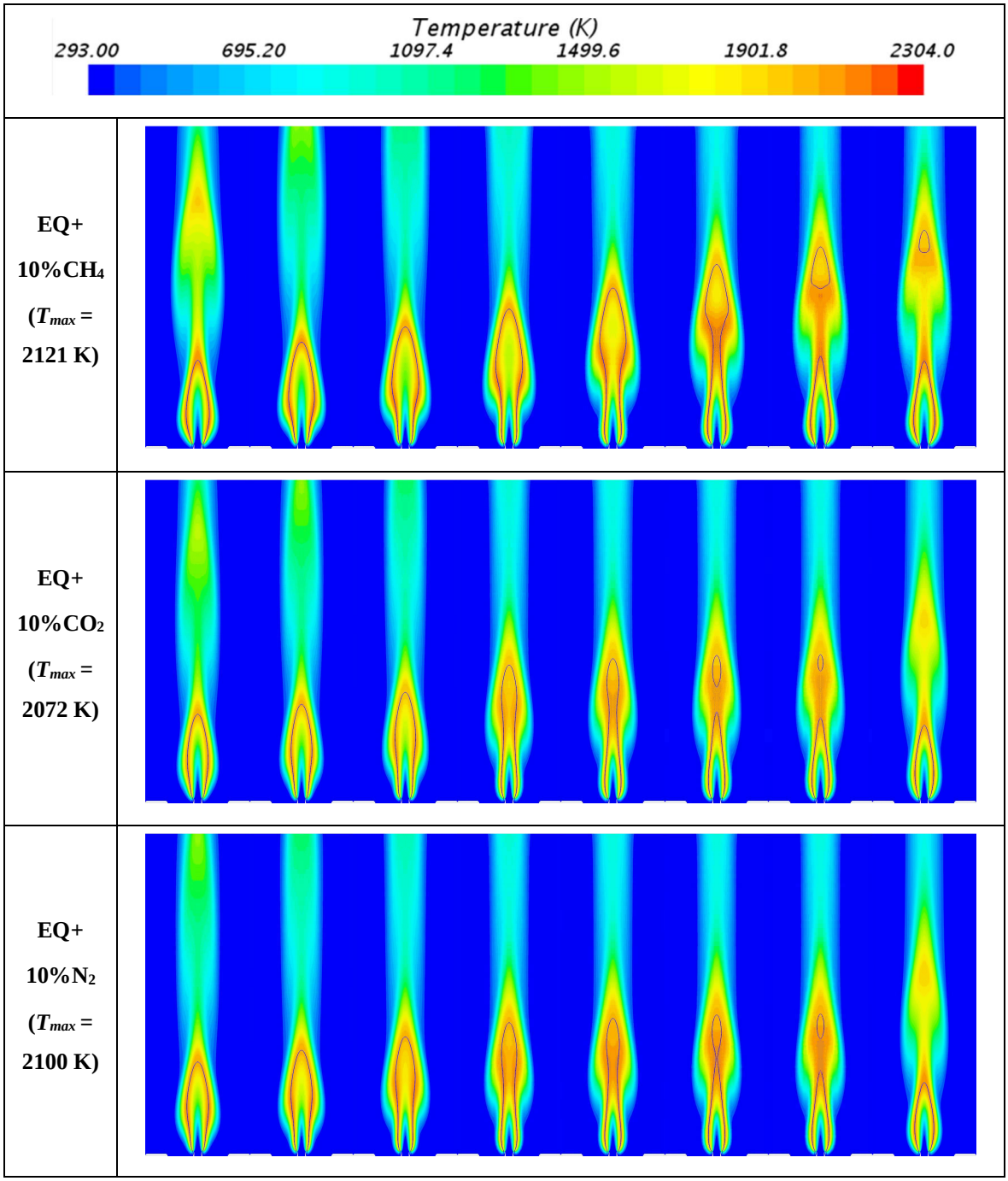

Figure 6-16 Appearance of tip-cutting flame of EQ syngas mixed with either CH_4, CO_2, or N_2 at fuel rate of 1.2 SLPM

The average flame length ($H_{f\text{-}ave}$) during the limit cycle of oscillation of all the fuel compositions are computed and compared in Figure 6-17. The $H_{f\text{-}ave}$ profile of all the fuel compositions is almost linear, and the relation between this parameter and the fuel rate is a direct proportion. In other words, the flame is longer when the higher fuel rate is supplied. CH_4, and CO play a strong role in an increase of $H_{f\text{-}ave}$, and the higher concentration percentage of these species leads to the higher value. The stronger role in this aspect is found from CH_4 over CO as seen from the profile of EQ+10%CH_4 and EQ+20%CH_4 which have

the higher value of $H_{f\text{-}ave}$ at the same fuel rate and also a higher increasing gradient than the $H_{f\text{-}ave}$ profile of CO-rich syngas. The higher H_2:CO ratio and the higher percentage of N_2 in the fuel composition leads to the lower value of $H_{f\text{-}ave}$. For instance, at the same fuel rate, H_2-rich has a lower $H_{f\text{-}ave}$ than EQ and CO-rich, whereas EQ+20%N_2 has a lower $H_{f\text{-}ave}$ than EQ+10%N_2 and EQ, respectively. Having CO_2 in the fuel composition surprisingly increases the value of $H_{f\text{-}ave}$ for the unstable flame.

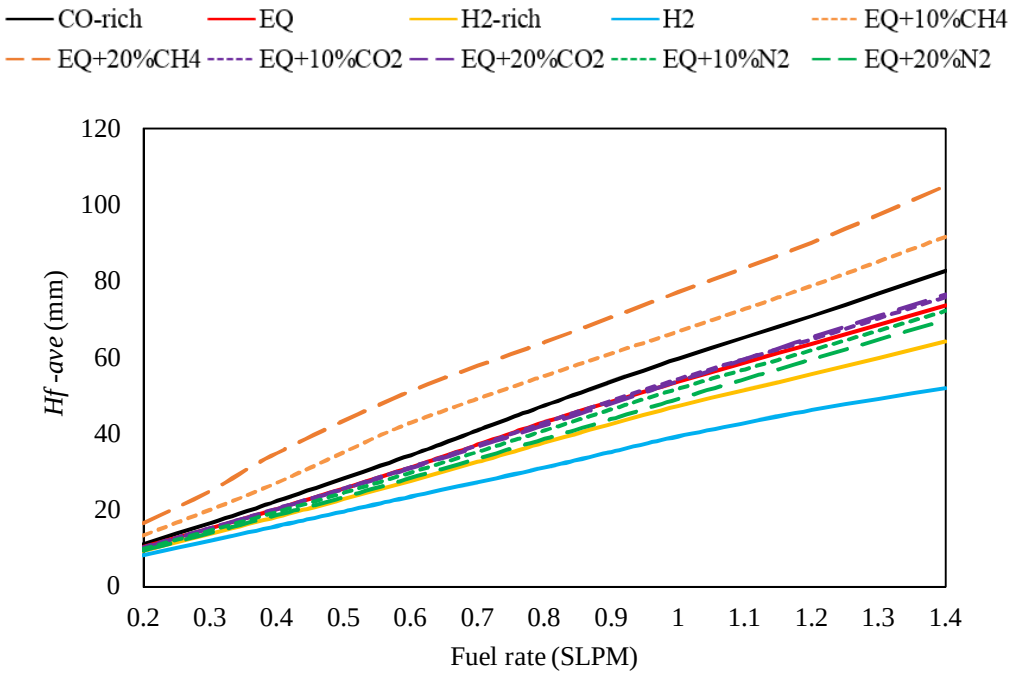

Figure 6-17 Average flame length

The average flame temperature is calculated and presented in Figure 6-18. The value of T_{ave}, increases along with an escalation of fuel rate. The higher difference in velocity at the shear layer between fuel and oxidiser stream encourages the mix of fuel and oxidiser resulting in the higher flame temperature. The profile pattern of T_{ave} depends strongly on H_2:CO ratio. H_2-rich syngas (H_2:CO > 1) and H_2 have a non-linear profile, and their increasing rate is higher at the lower fuel rate. The different pattern is seen from the profile of T_{ave} of syngas having H_2:CO ≤ 1 since they are non-linear at the fuel rate lower than 0.5 SLPM and linear at the fuel rate above. According to this, the average increasing rate is computed to analyse the impact of each species further. It is found that syngas/producer gas with a higher H_2:CO has a higher average increasing rate. As a result, CO-rich syngas (2110 K) has a higher T_{ave} than EQ (2064 K), H_2-rich (2017 K), and H_2 (1951 K) at 0.2 SLPM of fuel rate. The opposite direction is obtained at 1.4 SLPM of fuel rate where T_{ave} of CO-rich (2177 K) is lower than EQ (2180 K), H_2-rich (2214 K), and H_2 (2270 K). Having CH_4, CO_2,

and N_2 in the fuel composition further causes the reduction of $T_{-ave,}$ and the impact of CO_2 is stronger than N_2 and CH_4 at the same additional percentage. As seen, the value of T_{-ave} of EQ mixed with CO_2 is lower than one mixed with either N_2 or CH_4 respectively at the same fuel rate. The impact is also stronger when the additional percentage of these species is higher.

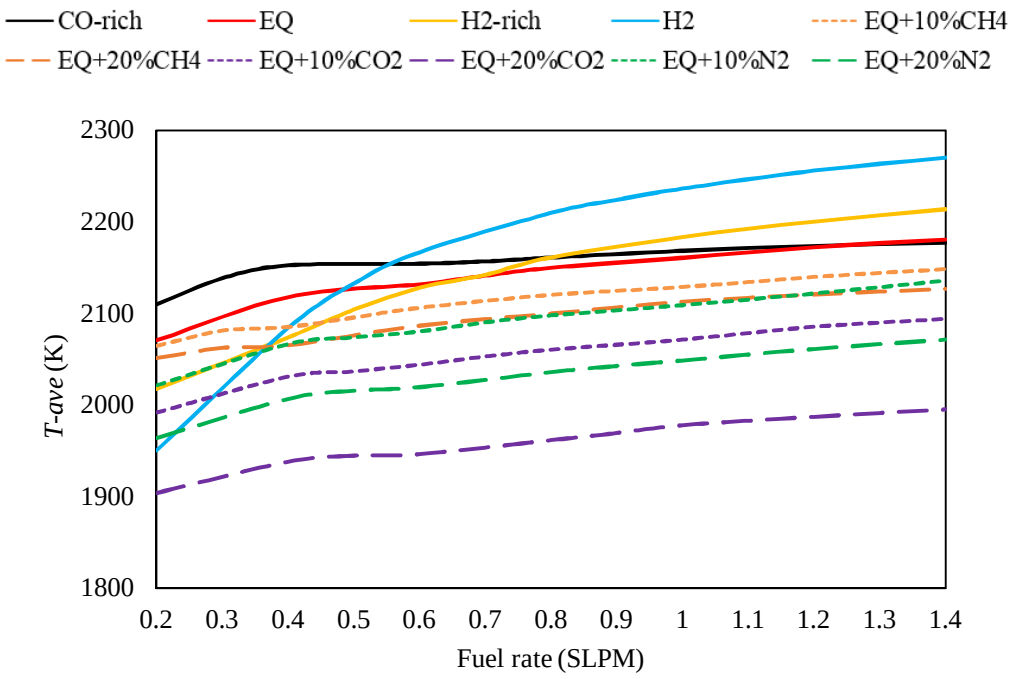

Figure 6-18 Average flame temperature

The total heat release from the chemical reaction of the flame is represented by Q_{-total}. This parameter is computed by combining the chemical heat release of every grid on the simulation domain. The average total chemical heat release (Q_{-ave}) is the average value of Q_{total} during the limit cycle. Thus, it is the average rate of the total heat generated from the chemical reaction during the limit cycle. The comparison of Q_{-ave} of all the studied flames is presented in Figure 6-19. The profile of Q_{-ave} of all the fuel compositions is almost linear, and this refers to a higher average heat generated at the higher fuel rate. The impact of species H_2, CO, CH_4, CO_2, and N_2 are in the same direction as the study of their effect on Q_{total} of the stable flame in Chapter 5. That is, CH_4 and CO play a significant role in the increase of heat generation capability of the stable flame, and this impact is also valid for the unstable flame. Similarly, the higher CO_2 and N_2, which are non-combustible, decrease the heat generation capability of both stable and unstable flames.

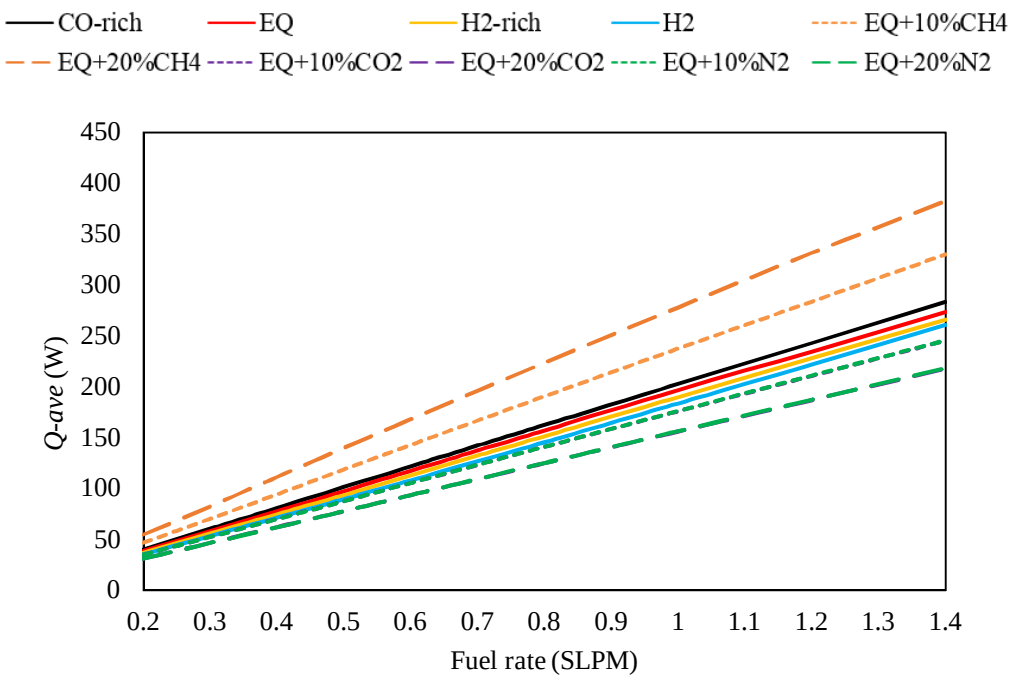

Figure 6-19 Average chemical heat release

As also seen from the profile of $Q_{\text{-}ave}$, an increasing rate of $Q_{\text{-}ave}$ profile of EQ mixed with CH_4 (236 and 273 W-SLPM^{-1} at 10 and 20% of addition) is significantly higher than the other flames. CO maintains its second place as a preferable species in terms of heat generation capability in both the stable and unstable flames. The higher concentration percentage of CO or the lower H_2:CO ratio in the syngas composition rises the value of $Q_{\text{-}ave}$. For instance, the increasing rate of $Q_{\text{-}ave}$ profile of CO-rich (202 W-SLPM^{-1}) is higher than EQ (196 W-SLPM^{-1}), H_2-rich (191 W-SLPM^{-1}) and H_2 (188 W-SLPM^{-1}). Also, the comparable role of CO_2 and N_2 are observed in both the stable and unstable flame, since both species affects the reduction of $Q_{\text{-}ave}$ at an equal level, and the higher percentage of them in the fuel composition causes a stronger impact.

6.3.2 **Critical condition**

The parameters L_f and λ are computed and used for identifying the flame type as presented in Table 6-2. The study of the critical condition focuses on the transformation between the flame type, e.g. (i) stable/flickering and (ii) flickering/tip-cutting. The maximum possible fuel rate that the flame can maintain its stability is a stable/flickering critical fuel rate. With a similar approach, the flickering/tip-cutting critical fuel rate is the maximum possible fuel rate that the flame is flickering. The transition between flame types occurs once the fuel rate supplied is above these critical fuel rates. The value of the critical fuel rate reveals the

sensitivity of the flame to transform into another flame type when the fuel rate increases or decreases. The flame is considered to be more sensitive when the critical fuel rate is lower since the smaller increase in the fuel rate could affect the transition between the flame types.

As an occurrence of K-H instability relies on the Richardson number (Ri) which is computed from two dimensionless parameters (Gr and Re) as explained in equation (9). In this work, the oscillating flame is created by escalating the fuel velocity. This action directly affects the higher value of Re resulting in the lower value of Ri where the onset of K-H instability occurs at the value lower than 0.25. Also, the diversity in fuel composition has an impact on the value of Re since the density and viscosity rely on the concentration of species in fuel composition. The Reynolds number is hence selected for representing the flow condition where the transition between flame types (stable/flickering/tip-cutting) is likely to occur. The value of Reynolds number of fuel stream (Re_f) at the critical fuel rate is the critical Re_f. The comparison of critical Re_f and critical fuel rate of all the studied fuels is presented in Figure 6-20 and Figure 6-21.

Table 6-2 Flame type at each fuel and air rate (S = stable, F = flickering, and T = tip-cutting)

Fuel composition	Fuel rate (SLPM)												
	0.2	0.3	0.4	0.5	0.6	0.7	0.8	0.9	1	1.1	1.2	1.3	1.4
CH_4	T	T	T	T	T	T	T	T	T	T	T	T	T
H_2	S	S	S	F	F	F	F	T	T	T	T	T	T
H_2-rich	S	S	S	F	F	F	T	T	T	T	T	T	T
EQ	S	S	S	F	F	T	T	T	T	T	T	T	T
CO-rich	S	S	S	F	F	T	T	T	T	T	T	T	T
EQ+10%CH_4	S	S	F	T	T	T	T	T	T	T	T	T	T
EQ+20%CH_4	S	F	T	T	T	T	T	T	T	T	T	T	T
EQ+10%CO_2	S	S	S	F	F	F	T	T	T	T	T	T	T
EQ+20%CO_2	S	S	S	S	F	F	F	F	T	T	T	T	T
EQ+10%N_2	S	S	S	F	F	F	T	T	T	T	T	T	T
EQ+20%N_2	S	S	S	S	F	F	F	F	T	T	T	T	T

At the stable/flickering transition (Figure 6-20), the critical fuel rate of CO-rich, EQ, H_2-rich, and H_2 are equal to 0.4 SLPM. The H_2:CO ratio, hence, does not affect the critical fuel rate at this transition condition. When the CH_4 is added into EQ syngas, the critical fuel rate reduces to 0.3 and 0.2 SLPM at 10% and 20% of addition, respectively. This result refers to the higher sensitivity level to the fuel rate of syngas mixed with CH_4 since it becomes a flickering flame at the lower fuel rate. The critical fuel rate is unchanged when the species CO_2 or N_2 is mixed with EQ syngas at 10%. As seen, the critical fuel rate of EQ+10%CO_2 and EQ+10%N_2 are equal to EQ syngas (0.4 SLPM). However, both species (CO_2 and N_2)

reduce the sensitivity level when they are added to the syngas composition at 20%. The critical fuel rate of EQ+20%CO_2 and EQ+20%N_2 are 0.5 SLPM. This result also projects the comparable level of the effect of CO_2 and N_2 on the critical fuel rate.

The critical Reynolds number at stable/flickering transition ($Re_{s\to f}$) of all the studied fuel compositions are computed at the critical fuel rate as presented in Figure 6-20. The impact of H_2:CO is clearly seen as the syngas with the lower ratio has a higher value of $Re_{s\to f}$. The value of $Re_{s\to f}$ of CO-rich (105) is higher than EQ (75), H_2-rich (45) and H_2 (19), respectively. The impact of adding CH_4, CO_2, or N_2, on $Re_{s\to f}$ is in the same direction as their effect on stable/flickering critical fuel rate. The addition of CH_4 at 10% and 20% reduces the value of $Re_{s\to f}$ of EQ syngas to 59 and 41, respectively. By the same action, but altering the species to CO_2 or N_2, the value of $Re_{s\to f}$ increases to 92 and 81 at 10% of the additional percentage, and to 136 and 108 at 20%. The level of impact of CO_2 on $Re_{s\to f}$ is hence stronger than N_2 according to this result. It is also noticed that the fluid property dominates the value of $Re_{s\to f}$ of pure syngas, e.g. H_2-rich, EQ, and CO-rich. These flames are formulated from the same fuel rate (same velocity) and diameter of fuel injector; thus, the value of $Re_{s\to f}$ relies strongly on the dynamic viscosity and density of the fuel mixture.

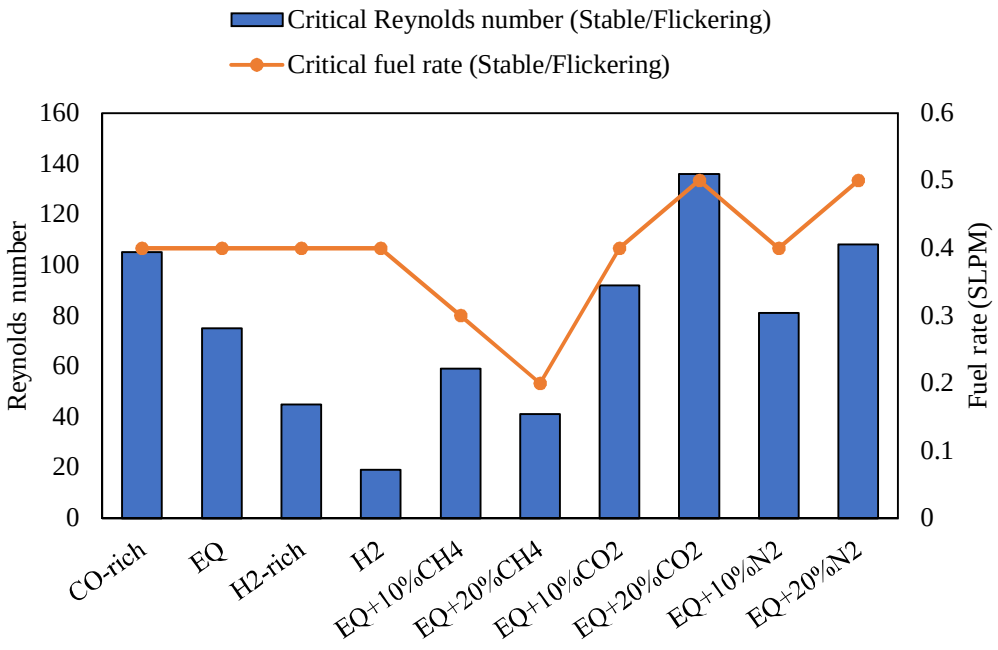

Figure 6-20 Critical fuel rate and Reynolds number at stable/flickering transition

In Figure 6-21, at the flickering/tip-cutting condition, the higher H_2:CO ratio escalates the critical fuel rate. As seen, the flame of H_2 has a higher critical rate (0.8 SLPM) than H_2-rich

(0.7 SLPM), EQ (0.6 SLPM), and CO-rich (0.6 SLPM). Thus, the flame is more sensitive to the change of fuel rate when the concentration of CO is higher, and the converse direction of the result is obtained from the higher concentration of H_2. The effects of CH_4, CO_2, and N_2 on the flickering/tip-cutting critical fuel rate are almost the same as their effect on the stable/flickering critical fuel rate. Adding CH_4 to syngas reduces the critical fuel rate (0.4 and 0.3 SLPM at 10% and 20%) and increases the sensitivity level. Conversely, the addition of CO_2 or N_2 increases the critical fuel rate and decreases the sensitivity level. Also, the comparable role of CO_2 and N_2 is observed at the flickering/tip-cutting transition. Unlike the stable/flickering transition, the additional percentage of 10% of either of CO_2 or N_2 in syngas composition is sufficient to raise the critical fuel rate at the flickering/tip-cutting condition. In detail, the critical fuel rate of EQ escalates to 0.7 and 0.8 SLPM when either of CO_2 or N_2 is diluted at 10 and 20%.

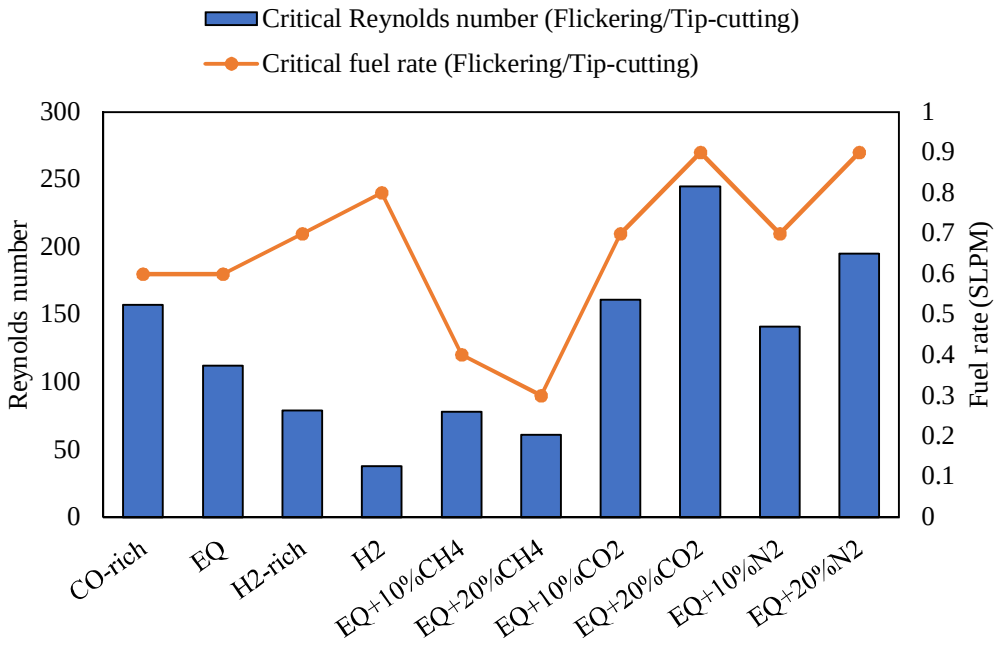

Figure 6-21 Critical fuel rate and Reynolds number at flickering/tip-cutting transition

The impact of H_2:CO on the critical Reynolds number at flickering/tip-cutting transition ($Re_{f\to t}$) is in the same direction as its impact on $Re_{s\to f}$, as presented in Figure 6-21. The fuel having the lower H_2:CO ratio has a higher value of $Re_{f\to t}$; one of CO-rich (157) is higher than EQ (112), H_2-rich (79), and H_2 (38). The impact of CH_4, CO_2, or N_2 on $Re_{f\to t}$ are also the same as their impact on $Re_{s\to f}$. Adding CH_4 to syngas composition decreases $Re_{f\to t}$ of EQ flame to 78 and 61 at 10% and 20%, respectively. Adding CO_2 and N_2 to syngas composition at 10% raise the value of $Re_{f\to t}$ to 161 and 141, respectively. The value of

$Re_{f\to t}$ increases to 245 and 195 at 20% of CO_2 and N_2. Hence, the stronger role of CO_2 over N_2 on the critical Reynolds number is confirmed at both types of transition. The result at the flickering/tip-cutting transition also supports the significant role of fluid property on the value of the critical Reynolds number. As seen, the flame H_2-rich has higher flickering/tip-cutting critical fuel rate but the significantly lower value of $Re_{f\to t}$ due to its low density.

6.3.3 **Flame instability**

The movement of the oscillating flame is analysed based on the value of L_f and λ. The higher value of L_f refers to the larger range of flame movement between the minimum and maximum flame length; thus, the higher level of impact of flame oscillation. Similarly, a higher value of λ expresses the longer distance between the maximum flame length and tip position, which implies the higher level of tip-cutting phenomenon. Besides, the flickering frequency (F), which is the number of the limit cycles per second is calculated from the flame length profile to project the behaviour of the flame.

The profiles of L_f and λ of all the studied fuel compositions are compared in Figure 6-22a-b, where their profile pattern is found to be similar. The values of L_f and λ are higher when the fuel rate is higher, and this relation is non-linear. This finding refers to the higher level of impact from flame oscillation and tip-cutting phenomenon when the fuel rate is supplied at a higher rate since the K-H instability is promoted. The value of L_f of all the studied fuels is above zero at the fuel rate above the stable/flickering critical fuel rate. Similarly, the value of λ is above zero at the fuel rate that is higher than the flickering/tip-cutting critical fuel rate. Once the values of L_f and λ are above zero, their profiles rise along with an increase of the fuel rate, and the highest value of them is at 1.4 SLPM; which is the maximum studied fuel rate. The strong increasing rate of the profile of both the parameters reflects that this trend will continue at the fuel rate higher than 1.4 SLPM.

The value of L_f of H_2, H_2-rich, EQ, and CO-rich are above zero at the same fuel rate due to their similar stable/flickering critical fuel rate. The comparison of is hence processed based on an increasing rate of L_f profile. The comparable increasing rate is seen from the flame of CO-rich and EQ where their H_2:CO ≤ 1. Both flames have a similar value of L_f at the same fuel rate, and their values are higher than the one of H_2-rich and H_2. The same direction of the result is obtained from the comparison of λ profile of different fuel compositions, where CO-rich and EQ syngas have a similar value of λ at the same fuel rate. Their values are also

higher than one of H_2-rich and H_2. As a result, the syngas with a lower ratio of H_2:CO promotes the flame oscillation and tip-cutting phenomenon at a stronger level. However, its impact has the upper limit when the fuel composition has H_2:CO = 1. The level of impact will not rise further even the fuel has H_2:CO ratio lower than this value.

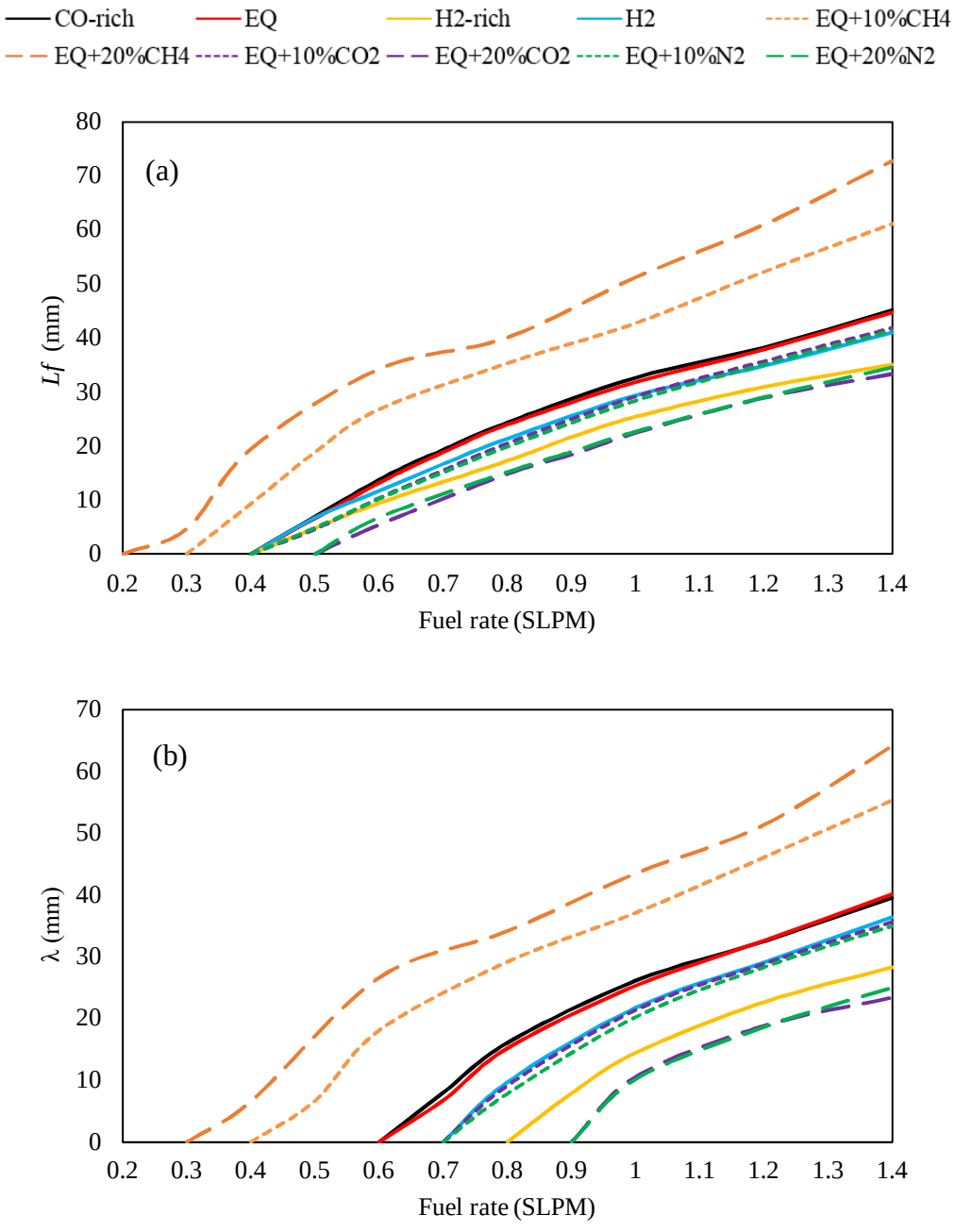

Figure 6-22 (a) Magnitude of oscillation (L_f) and (b) oscillation wavelength (λ)

The profile of L_f and λ of EQ+10%CH_4 and EQ+20%CH_4 are clearly above the profiles of the same parameters of the other fuel compositions. The larger range of movement and tip-cutting phenomenon are encouraged significantly once CH_4 is added into the fuel

composition of syngas/producer gas. Also, the stronger effect is obtained when the additional percentage of this species is higher. The opposite direction of the result is found from the addition of CO_2 and N_2. As seen, the profile of L_f and λ of EQ+10%CO_2, EQ+20%CO_2, EQ+10%N_2 and EQ+20%N_2 are lower than the profile of EQ. Thus, flame oscillation and tip-cutting phenomenon are discouraged by the higher concentration of CO_2 or N_2 in syngas composition. Also, the value of both L_f and λ of EQ mixed with CO_2 and one mixed with N_2 are similar at the same fuel rate. Therefore, the roles of these species on flame oscillation are comparable.

For the oscillating flame, the number of limit cycles per second is represented by the flickering frequency (F). It could be computed from all the fuel compositions and compared in Figure 6-23a-b. The profile pattern of F tends to be dominated by the H_2:CO ratio in fuel composition. As seen, the profile of F of syngas having the H_2:CO > 1 (H_2-rich) is in a downtrend, and the higher fuel rate causes the lower value of F. This finding is supported by the profile of F of H_2 flame which reduces at the higher rate than one of H_2-rich. This downtrend is expected at the fuel rate higher than 1.4 SLPM according to the direction of this result. The different pattern is found when the syngas has H_2:CO ≤ 1, where the profile of F decreases to the minimum value then rises again. The minimum frequency of CO-rich (12.5 Hz at 0.8 SLPM) is higher but occurs at the lower fuel rate than one of EQ syngas (11.8 Hz at 1.0 SLPM). Beyond the minimum frequency, the uptrend of F of CO-rich syngas has a higher increasing gradient than EQ syngas. The impact of H_2:CO on the profile pattern of F is supported by the profile of EQ syngas mixed with CH_4, CO_2, and N_2, as shown in Figure 6-23b. These flames have H_2:CO = 1, and their profiles pattern of F are similar to EQ, which also has the same H_2:CO ratio.

In addition, the profile of F syngas with H_2:CO ≤ 1 presented in Figure 6-23a-b could be divided into two parts depending on the flame type. It is found that the profile of F of the most fuel compositions has the downtrend when the flame is flickering. A reverse direction of the profile appears when the flame is tip-cutting. However, this finding is not valid for EQ+20%CO_2 and EQ+20%N_2. The reverse direction of the profile of F of these flames is found when they are the flickering flame.

On the other hand, the range of frequency depends not only on the H_2:CO ratio but also on the concentration of each species. It could be seen that the syngas with the higher H_2:CO ratio has a lower frequency at the same fuel rate. The range of frequency of CO-rich is 12.5-

13.2 Hz, and this is higher than the frequency range obtained from the flame of EQ (11.8-12.3 Hz), H_2-rich syngas (10.8-12 Hz), and H_2 (9.6-11.8 Hz). The impact of adding CH_4, CO_2, and N_2 to the syngas composition on the value of *F* is observed from the analysis of Figure 6-23b. The flame of EQ mixed with CO_2 has a higher value of *F* than one mixed with N_2 and CH_4 at the same additional percentage and the same fuel rate. Comparing to the flame of EQ (reference flame), adding CO_2 and N_2 rises the value of *F* of syngas flame, and the opposite direction is found from the addition of CH_4. Besides, the higher percentage of them in syngas results in a stronger effect.

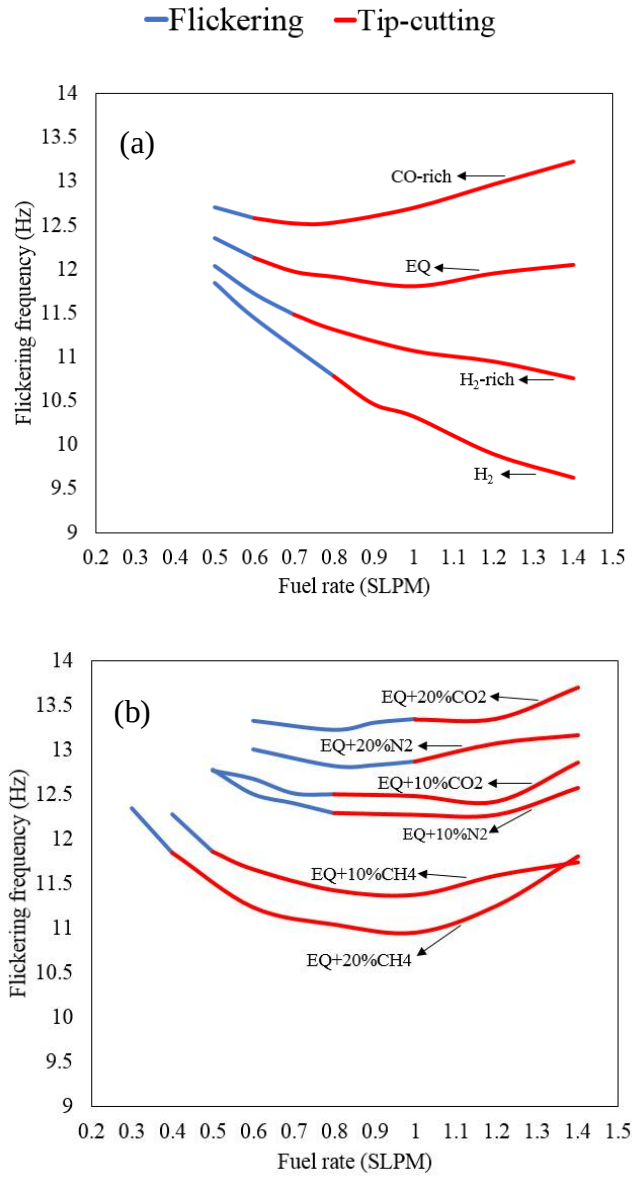

Figure 6-23 Comparison of flickering frequency (*F*) of (a) pure syngas and H_2, and (b) syngas mixed with either CH_4, CO_2, and N_2

6.3.4 **The fluctuation of flame temperature and heat release**

The impact of K-H instability on the mix between fuel and oxidiser causes the fluctuation of flame temperature (*dT*) and total chemical heat release (*dQ*). The higher value of *dT* and *dQ* projects the higher level of fluctuation. These parameters are analysed to reveal the role of each species in syngas composition. The profile of *dT* of all the studied fuel compositions is compared, as presented in Figure 6-24. The pattern of *dT* profile relies on the H_2:CO ratio as well as the average flame temperature (T_{-ave}). The flame of H_2 and H_2-rich have an uptrend profile of *dT*, and this result implies a higher level of temperature fluctuation at the higher fuel rate. The value of *dT* of H_2 flame is comparable to that of H_2-rich at a fuel rate ≤ 0.8 SLPM, and one of H_2 flame is higher at fuel rate above. On the other hand, the syngas/producer gas containing H_2:CO ≤ 1 has an unclear trend of *dT* profile. For instance, the profile of *dT* increases to the peak value then reduces for the flame of CO-rich (H_2:CO < 1), while the profile increases to the peak value then reduces and fluctuates for the flame of syngas having H_2:CO = 1 (e.g. EQ and EQ mixed with either CH_4, CO_2, or N_2). The peak value of *dT* profile of CO-rich syngas is higher than syngas having H_2:CO = 1. At the maximum studied fuel rate (1.4 SLPM), the flames of syngas having H_2:CO = 1 has a lower level of temperature fluctuation than CO-rich, H_2-rich, and H_2, respectively. Therefore, the conclusion could be drawn for only the role of H_2, which encourages the fluctuation level of flame temperature. This finding could be explained by the higher diffusive property of H_2 combines with the impact of K-H instability. Additionally, the larger range of the studied fuel rate is required for investigating the impact of the other species on *dT*.

Similarly, the K-H instability directly affects the fluctuation of heat generation from flame. The level of fluctuation of Q_{total} is higher when the fuel rate is higher for all the fuel compositions as seen from the profile of *dQ* in Figure 6-25. Adding CH_4 to syngas/producer gas provides a higher value of Q_{-ave}; nevertheless, this method escalates the fluctuation level of total heat release significantly. As seen, the *dQ* profile of EQ mixed with CH_4 is clearly above the profile of the other fuels, and the higher additional percentage causes the higher value of *dQ* at the same fuel rate. The interesting result is obtained from pure syngas since the flame of CO-rich that provides the higher value of Q_{-ave} has a lower level of fluctuation in heat generation than the flame of EQ and H_2-rich. The higher concentration of CO in fuel composition would benefit the heat generation capability following this finding. Lastly, the roles of CO_2 and N_2 in the fluctuation level of total heat release are comparable. At the same

fuel rate, the similar value of *dQ* is found for EQ mixed with either CO_2 or N_2 at the same additional percentage except at 20% of addition and fuel rate < 0.9 SLPM.

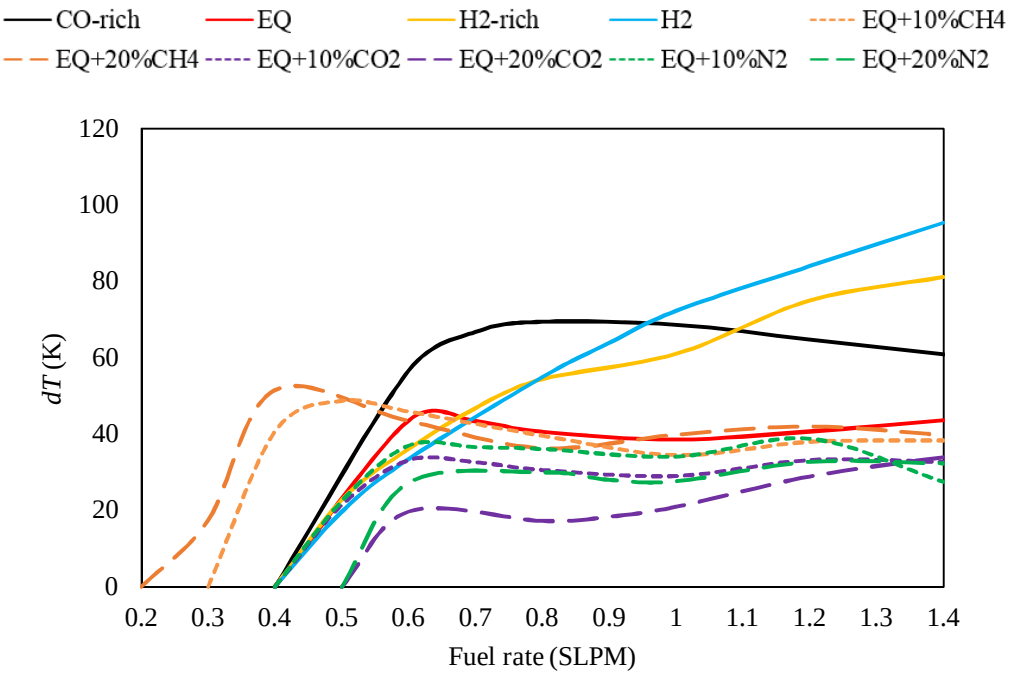

Figure 6-24 Fluctuation of flame temperature

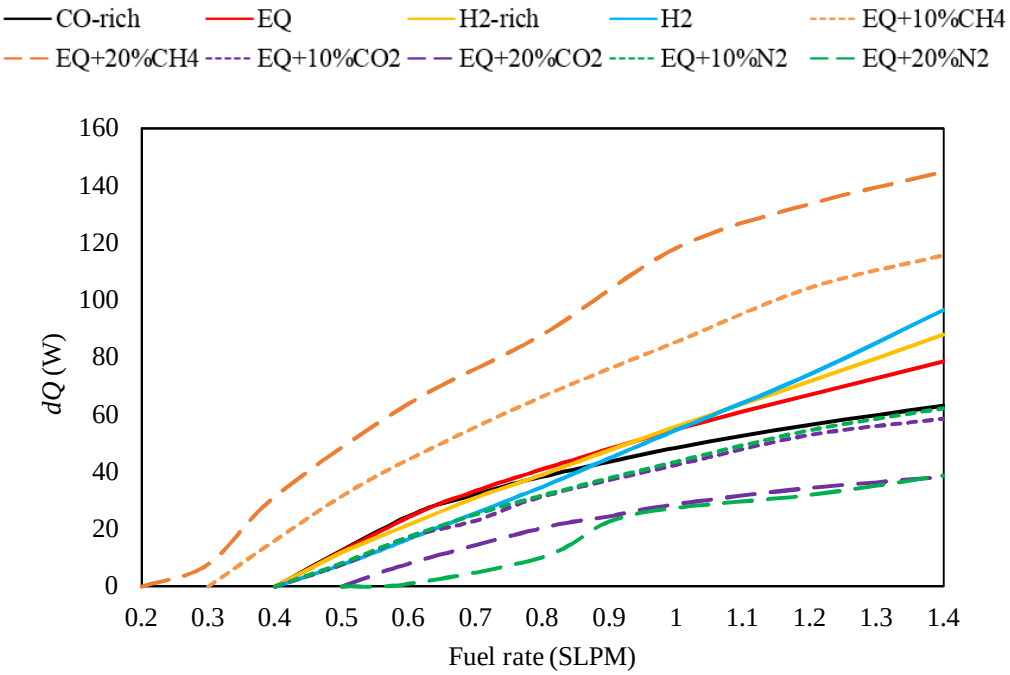

Figure 6-25 Fluctuation of total chemical heat release

6.3.5 **Stable heat generation**

Unlike the stable flame, flame temperature and total chemical heat release of oscillating flame fluctuate due to the impact of K-H instability. The value of Q_{-ave} and T_{-ave} are the average value without the consideration of its fluctuation. Therefore, it is unreasonable to conclude that the higher value of these parameters represents the higher heat generation capability. The fluctuation of total chemical heat release (dQ) and one of flame temperature (dT) are found to rely on the magnitude of oscillation (L_f). The fluctuation of flame temperature and total chemical heat release appears when the flame begins to oscillate. As seen, dQ, dT, and L_f are above zero at the same fuel rate for every fuel composition. Considering that the stable chemical total chemical heat release is preferable, the value of Q_{-ave} at the stable/flickering critical fuel rate (where L_f, dQ and dT are equal to 0) is the maximum stable value. The comparison of Q_{-ave} at this condition of all studied fuel compositions is presented in Figure 6-26. Besides, the flame temperature at this condition is plotted along with Q_{-ave} on the same figure.

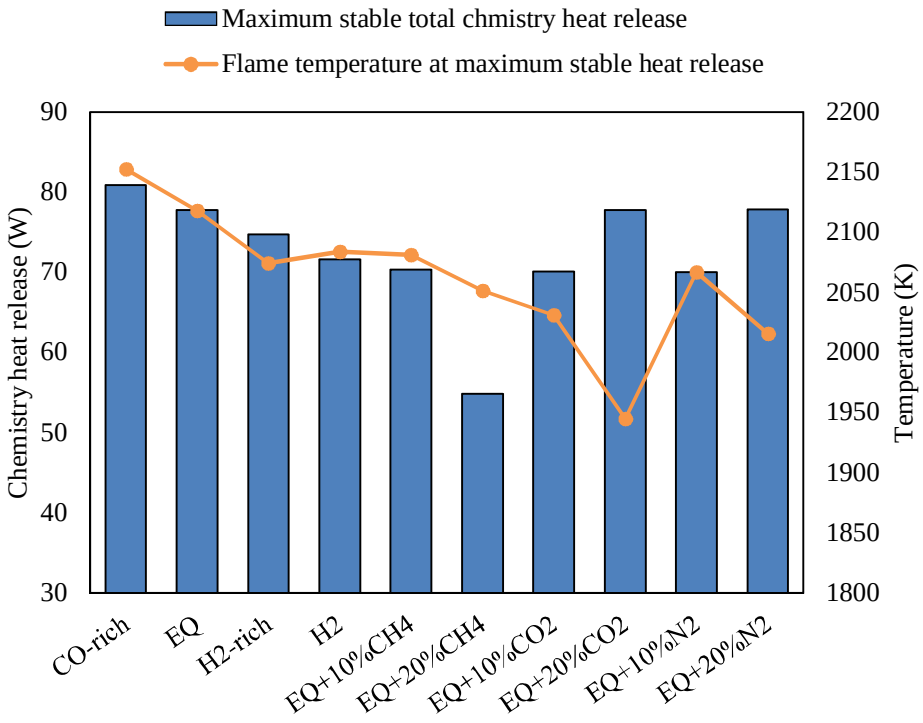

Figure 6-26 Maximum stable total chemical heat release and flame temperature at that condition

Among all the studied compositions, the flame of CO-rich generates the highest maximum stable heat rate at 0.4 SLPM as 81 W and 2153 K. This is followed by the flame of EQ, EQ+20%CO_2, and EQ+20%N_2 which provide the maximum stable heat release at a

comparable rate as ~78 W. The temperature of these flames is 2118 K at 0.4 SLPM for EQ syngas, 1945 K at 0.5 SLPM for EQ20%CO_2, and 2016 K at 0.5 SLPM for EQ+20%N_2 at this amount of generated heat. This result expresses the role of CO, CO_2, and N_2, which encourages the stable heat generation of syngas/producer gas flame.

The analysis also projects the fuel consumption at the maximum stable total chemical heat release. The consumption of CO-rich and EQ are lower than one of EQ+20%CO_2, and EQ+20%N_2. Hence, the higher concentration of CO in syngas composition benefits not only the heat generation capability but also fuel consumption. Conversely, the addition of CH_4 increases the value of Q_{-ave} as discussed above. However, this action reduces the maximum stable heat release significantly, especially when the additional percentage is 20%. Consequently, the flame of EQ+20%CH_4 generates the lowest maximum stable heat release (55 W at 2052 K) among the studied fuel compositions.

6.4 Discussion

The stable and unstable oscillating flames (flickering and tip-cutting flames) of syngas/producer gas with variety in fuel compositions are formulated in this chapter to project the impact of each species in fuel composition on the occurrence of flame oscillation and heat generation capability. The finding obtained from the oscillating flame is also compared with the result of the previous chapter, which focused on the stable flame of the same fuel composition. The role of each species is discussed as follows:

Two major species in syngas composition (H_2 and CO) play a significant role in different aspects according to the results presented. The advantage of having a higher concentration of CO over H_2 in syngas composition is pointed out. Syngas with the lower H_2:CO encourages the oscillation of the flame; however, the magnitude of oscillation (L_f) has an upper limit when H_2:CO = 1 and will not increase further. Additionally, the flame of syngas with the lower H_2:CO provides a higher average total chemical heat release (higher *Q-ave*) with a lower fluctuation level in heat generation (lower *dQ*). As a result, CO is the most desirable among the combustible and non-combustible species in syngas composition. However, this result is obtained by taking into account only the heat generation capability and the oscillation of the flame. The consideration of emission formation from the flame is excluded. In opposite, an increase in average flame temperature (higher *T-ave*) and the

fluctuation of this parameter are strongly encouraged by the concentration of H_2 in syngas composition.

Regarding the stable diffusion flame, having a higher concentration of CH_4 in syngas composition is suggested since it encourages heat generation capability and reduces emission formation. For an unstable diffusion flame, however, CH_4 promotes the magnitude of oscillation also the fluctuation in heat generation. Further, the concentration of CH_4 in syngas composition raises the sensitivity level to become an unstable flame when the fuel rate increases. Therefore, this species is less desirable than other combustible species in syngas composition under the combustion condition in which oxidiser supplied is limited and the flame is likely to oscillate.

The higher concentration of CO_2 and N_2, which are non-combustible, in syngas composition reduces the heat generation capability. Diluting either of these species into syngas composition has an advantage in the reduction of the magnitude of flame oscillation and fluctuation in heat generation. The result also points to the comparable role of CO_2 and N_2 in various aspects such as the magnitude of oscillation (L_f), average total chemical heat release (*Q-ave*), and the fluctuation in heat generation (*dQ*). Nevertheless, this method demands further study for the suitable additional percentage that balances between the reduced heat generation capability and the escalated stability level.

Analysing the CFD result with theory, the direction of the result obtained from CFD is expected for the flame length. According to Sato et al. [91], the higher Re leads to the longer average flame length. However, the average flame length computed from the theory is almost double compared to the CFD result for all fuel composition. Also, the formula presented by Sato et al. [91] did not consider the stoichiometric ratio of fuel and oxidiser, and diffusivity. Therefore, the diversity in fuel composition only affects the value of Reynolds number (Re); the higher value of Re leads to the higher average flame length. The formula of Sato et al. [91] may provide a good estimation for the oscillating flame of CH_4 and C_3H_8 but not for the flame of syngas. As seen, the flame of syngas mixed with CH_4 has lower Re than CO-rich but longer flame length.

The result obtained is mostly in the same direction as the study in Chapter 5 where the stable flame of these fuel compositions is studied extensively. The impact of each species on flame length is almost in the same direction for stable and unstable flames. Only the impact of CO_2

that is different since the addition of this species into the fuel composition of syngas/producer gas decreases the length of stable flame but increases the average length during the limit cycle of oscillation of an unstable flame. As a result, the relationship between the parameters in the flame length formula of the stable diffusion flame proposed by Roper [93], [94] is also valid for the average flame length of the unstable oscillating flame. The detail of this theory is explained in Chapter 2 while its limitation and accuracy are assessed and discussed in Chapter 4 and 5.

The K-H instability and molecular diffusivity of syngas play a significant role in the flame movement and temperature. The mix of fuel and oxidiser at the flame front is affected directly by the mentioned factors resulting in the flame oscillation. This impact also leads to the lower flame temperature than the adiabatic flame temperature as well as the fluctuation of this parameter.

The value of Richardson number (Ri) is computed at the stable/flickering transition for all fuel compositions. It is found that the stable/flickering transition occurs at the value of Ri as ~0.2. The exception is found from the EQ mixed with CH_4 where the transition happens at the value of Ri of 0.35 and 0.8 for the additional percentage of CH_4 as 10% and 20%, respectively. Thus, utilising the condition of $Ri \leq 0.25$ for identifying the impact of K-H instability might not be effective for all the fuel composition. This finding is expected since the parameter Ri is typically used for computing the flow of single species without the consideration of combustion. The study for the critical value of Ri for specific fuel composition is hence suggested. Additionally, the prediction of the transition from the stable flame to the unstable oscillating flame for each burner would be more effective if both critical Re and Ri are analysed together. Nevertheless, it is necessary to take into account that the value of Ri and Re at the transition condition in this work is obtained from the flame without the co-flow air. The value of them could be different when the co-flow air is supplied since the difference of velocity at the shear layer is lower, and the impact of K-H instability is weaker. In this case, the flame is anticipated to oscillate at the higher Re and lower Ri.

According to the study of Sato et al. [104], the flickering frequency depends on two dimensionless parameters, St and Fr, as presented in equation (11) and (12). Analysing these equations, there is no consideration of fuel composition, and the flickering frequency relies on fuel nozzle diameter, fuel velocity, and gravity. The result obtained in this work does not follow the theory of Sato et al. [104] since the higher velocity does not provide the higher

flickering frequency in several cases. Also, the ranges of the flickering frequency of different fuel composition are different as presented in the previous section. Consequently, the finding emphasises the impact of diversity in fuel composition on the flickering frequency which should not be neglected. Further study may be required for this purpose.

6.5 Conclusion

The stable and unstable flames of syngas/producer gas with different fuel composition are formulated for studying the impact of H_2, CO, CH_4, CO_2 and N_2 on the occurrence of flame oscillation, and the fluctuation in flame heat generation capability and temperature. The key conclusion is drawn and presented as bullet points as follows:

- The flame of syngas with the lower ratio of H_2:CO ratio has a higher magnitude of oscillation; however, the value will not increase when the ratio is lower than 1. Having CH_4 in fuel composition of syngas significantly increase the magnitude of oscillation and promote the oscillation of the flame since the flame is more sensitive to the increase of fuel rate to become unstable. The opposite direction is found when CO_2 and N_2 are mixed with syngas.

- CH_4 and CO play a significant role in the increase in heat generation capability. CH_4 has a stronger role than CO on this aspect. Nevertheless, the higher concentration of CH_4 in fuel composition promotes the fluctuation in heat generation strongly. CO is hence the most desirable species among the combustible species in syngas composition since it could provide a lower level of fluctuation.

- The role of the higher diffusive property of H_2 on an increase of flame temperature is significant. This impact combines with the K-H instability resulting in the higher fluctuation level of flame temperature.

- The impact of H_2, CO, CH_4, CO_2 and N_2 are mostly in the same direction for the stable and unstable oscillating flames of syngas/producer gas. An exception is seen from the effect of CO_2 on the flame length; the dilution of this species causes the reduction of flame length (H_f) in stable flame but rises average flame length ($H_{f\text{-}ave}$) of unstable flame

Chapter 7 Elimination of flame instability

The oscillation phenomenon in the buoyancy dominated laminar co-flow diffusion flame could be reduced and eliminated by increasing the flow rate of oxidiser supplied into combustion. The co-flow air supplied decreases the difference velocity at the shear layer where the K-H instability occurs; thus, the impact of K-H instability is lower and the flame is more stable. The diversity in fuel composition of syngas/producer gas causes a different level of flame instability, as reported in Chapter 6. The flame of syngas/producer gas hence demands the control of oxidiser for combustion so that the stability of the flame is maintained.

The study in this chapter particularly focuses on this topic along with an impact of the fuel composition on the reduction and disappearance of flame oscillation. The specific objective is to project the role of each species in this phenomenon and identify the species that encourage the impact of co-flow air on the reduction and disappearance of flame oscillation. The species that promote the impact of co-flow air is more desirable. Besides, how the reduction and elimination of flame oscillation affect the level of fluctuations of flame temperature and total chemical heat release are included in this investigation. Lastly, the study result is discussed, and the conclusion is provided.

7.1 Introduction

An impact of diversity in fuel composition on an occurrence of flame oscillation in syngas laminar diffusion flame was studied in the previous chapter. The K-H instability due to the impact of the buoyancy force of the fluid is the major cause. The difference velocity at the shear layer results in the vortices in which affects the mix of fuel and oxidizer. Thus, the flame oscillates at the flickering frequency between 10 and 13 Hz. The study in Chapter 6 considers the laminar diffusion flame without the co-flow air rate. Hence, the onset of K-H instability is encouraged with the aim of studying the impact of variations in syngas composition on this phenomenon. In this chapter, the co-flow air rate is supplied into the combustion. The difference of the velocity at the shear layer is lower and the K-H instability level is reduced and finally disappeared. The impact of diversity in syngas composition on this phenomenon is projected by comparing the result obtained from different syngas composition.

The vortex dynamic and structure of the oscillating flame of diffusion flame with co-flow air was studied by Wang et al. [90]. The result expressed the impact of co-flow air which escalates the initiation point of toroidal vortices from the nozzle exit to downstream. The oscillation of the flame disappears, and the flame becomes stable when the position of the vortices is pushed beyond the visible flame height. This finding is supported by the study of Darabkhani et al. [88] as the higher co-flow air velocity reduce the flame oscillation and increases the flickering frequency. Based on these results, the difference in the velocity at the shear layer is not the only factor affecting an occurrence of flame oscillation. The visible flame height is also significant as the longer average flame length would demand the higher air rate to push the initiation point of toroidal vortices outside the visible flame and become stable.

The results reported in Chapter 5 and 6 points to the role of each species in syngas composition on the flame length and average flame length. Therefore, each species affects the minimum demand of air rate to become stable differently. In opposite, an excessive amount of air rate could affect the flame extinction called 'blow out' [151]. Also, the higher co-flow air rate supplied into combustion requires the higher power input, which could be immoderate to drive the higher velocity of the air stream. The estimation for the proper amount of co-flow air supplied is hence significant.

The CFD model formulated in Chapter 6 remains the same for this work. The burner configuration is designed for projecting and examining the oscillation of buoyancy dominated laminar diffusion flame [88]. The validation and formulation of this CFD model were already presented in that chapter. The model was capable of predicting the stable and unstable oscillating flames with a similar result compared to the experimental method. In this chapter, a tip-cutting flame is initially formulated at the maximum value of the magnitude of oscillation without any co-flow air supplied for combustion (i.e. air rate = 0 SLPM), and the ambient air is an oxidiser of the combustion. From this condition, the fuel rate is fixed while the co-flow air rate is escalated. This action results in the transformation from tip-cutting to flickering and stable flames, respectively. In other words, the magnitude of oscillation reduces, and the flame oscillation is eliminated once the air rate is sufficient. The reduction profiles of the magnitude of oscillation (L_f) and oscillation wavelength (λ) of various syngas composition are analysed for the role of each species in syngas composition. The tip-cutting flame becomes flickering flame when $\lambda = 0$ while the flicker transforms to a stable flame when $L_f = 0$. Along with the reduction and disappearance of flame oscillation,

the fluctuation of flame temperature and total chemical heat release decreases and disappears once the flame is stable. The impact of the variation in syngas/producer gas composition on these aspects is also included in the analysis.

7.2 Numerical approach

The co-flow burner of Darabkhani et al. [88] is modelled by CFD and utilised in this work. Details of the formulation and validation of this CFD model were presented in Chapter 6 and will not be repeatedly presented. This CFD model could formulate the stable, flickering, and tip-cutting flame with a similar result compared to the experimental method. The model supports the diffusion flame modelling of gas fuel consisting of combustible species H_2, CO, and CH_4 and allows the variation in fuel composition and flow rate of fuel and co-flow air.

The fuel compositions of syngas/producer gas in this study are also the same as the fuel composition defined in Chapter 6. These are H_2, CO-rich, EQ, H_2-rich, EQ+10%CH_4, EQ+20%CH_4, EQ+10%CO_2, EQ+20%CO_2, EQ+10%N_2, and EQ+20%N_2. The details regarding the concentration percentage of each species in fuel compositions are shown in that chapter. Briefly, CO-rich, EQ and H_2-rich are pure syngas with H_2:CO ratio as 1:3, 1:1, and 3:1. The other fuel compositions are EQ mixed with either CH_4, CO_2, or N_2 at 10 and 20%. The analysis of the results obtained from the flames of these fuel compositions provides the impact of each species. For instance, comparing the result of pure syngas (CO-rich, EQ and H_2-rich) and H_2 flames reveals the impact of H_2 and CO. The analysis of the result of the other fuel compositions by using the result of EQ syngas as a reference expresses the impact of CH_4, CO_2 and N_2.

The flame is formulated at the fixed fuel rate of 1.2 SLPM for all the simulation cases while the co-flow air rate is varied between 0 and 20 SLPM. At this fuel rate, the flame is buoyancy dominated according to the flame Froude number (Fr_f). The ambient air is an oxidiser at 0 SLPM of co-flow air rate. Without the co-flow air supplied (0 SLPM of air rate), the flame formulated at 1.2 SLPM of fuel rate is a tip-cutting flame with the maximum magnitude of oscillation (maximum L_f) and oscillation wavelength (λ). Once the co-flow air rate increases, the tip-cutting flame transforms to flickering and stable flames at a different air rate depending on the fuel composition. The reduction of the magnitude of oscillation (L_f) and the oscillation wavelength (λ) and the disappearance of flame oscillation are hence illustrated at this range of fuel and air rate.

7.3 Impact of fuel composition

The study examines the impact of fuel composition on the flame oscillation, characteristics, and heat generation capability with an effect of co-flow air rate. Firstly, the flame structure, movement, and the average value of flame temperature and total chemical heat release are analysed. Secondly, the demand for air rate to transform the flame from one flame type to another type is presented in the form of transition air flow rate. Thirdly, decreasing profiles of the magnitude of oscillation (L_f) and oscillation wavelength (λ) are studied for understanding the reduction and disappearance of flame oscillation and tip-cutting phenomenon. Lastly, the reduction and disappearance of the fluctuation of flame temperature and the total chemical heat release are examined. Besides, the result obtained in Chapter 6, which focused on an occurrence of flame oscillation of various syngas composition, is the guideline and reference in the analysis.

7.3.1 Flame characteristics and heat generation

Flame movement and structure are initially analysed through a set of temperature contour plots. The series of contour plots projecting these aspects of the tip-cutting flame of CO-rich, EQ, H_2-rich, H_2, EQ+10%CH_4, EQ+10%CO_2, and EQ+10%N_2 at 1.2 SLPM of fuel rate and 0 SLPM of air rate were presented in Figure 6-15 and Figure 6-16. This fuel and air rate formulate the oscillating flame with the highest magnitude of oscillation (L_f) and oscillation wavelength (λ). To project the impact of co-flow air, the tip-cutting flame of these fuel compositions at 1.2 SLPM of fuel rate and 3 SLPM of air rate are shown in Figure 7-1 and 7-2. The movement and structure (the distribution of the temperature of the visible flame) of the tip-cutting flame of all the fuel compositions presented in these figures are similar. So, the impact of the co-flow air rate as well as the impact of the fuel composition on the movement and structure of the tip-cutting flame could be neglected.

For the movement of the tip-cutting flame, the flame size and length increase to the maximum value then the tip-cutting at the flame body occurs, causing a reduction in the flame length significantly. Then, the flame length and size increase slightly and decrease to the minimum value. The structure of the tip-cutting flame changes during the limit cycle of oscillation. The high-temperature area (> 1900 K) is above the fuel tube at the beginning of the limit cycle. This high-temperature area moves upward following the flame front line to

the axis. During the movement, the temperature decreases, and the new high-temperature area is formed at the original location after the occurrence of tip-cutting.

Once the higher co-flow air rate is supplied, the tip-cutting flame transforms into the flickering flame. The co-flow air flow rate in which the transition occurs is found to be different for each the fuel composition. The temperature contours illustrating the movement and structure of flickering flame of CO-rich, EQ, H_2-rich, H_2, EQ+10%CH_4, EQ+10%CO_2, and EQ+10%N_2 are presented in Figure 7-3 and Figure 7-4. The movement of the flickering flame is in the same direction for all the fuel composition. However, the structure is different depending on the H_2:CO in fuel composition. The flame length and size increase from the minimum to the maximum and reduces back to a minimum during the limit cycle of oscillation. The high-temperature area (> 1900 K) is on the top of the flame for syngas with H_2:CO $\leq$ 1 whereas this area is above the fuel tube for syngas with H_2:CO > 1 and H_2. The small change in flame structure is observed during the limit cycle of oscillation. This high-temperature area only extends and reduces upward and downward; the area does not move to the axis like a tip-cutting flame. The finding is the same for the flickering flame formulated without a co-flow air supplied in Chapter 6. Thus, the co-flow air does not affect the movement and structure of this flame type.

The flame becomes stable once the co-flow air rate is sufficient, and this transition is again observed at the different air rate depending on the fuel composition. The stable flames of CO-rich, EQ, H_2-rich, H_2, EQ+10%CH_4, EQ+10%CO_2, and EQ+10%N_2 are presented in Figure 7-5 and Figure 7-6. The structure of the stable flame is similar to the flickering flame. The high-temperature area is at the top of the flame for syngas with H_2:CO $\leq$ 1, and it is over the fuel tube for syngas with H_2:CO > 1 and H_2. There no change in flame structure over time. Also, the structure of the stable flame of each composition is in the same direction as found in Chapter 5 and 6 where the stable flames with and without co-flow air supplied were studied.

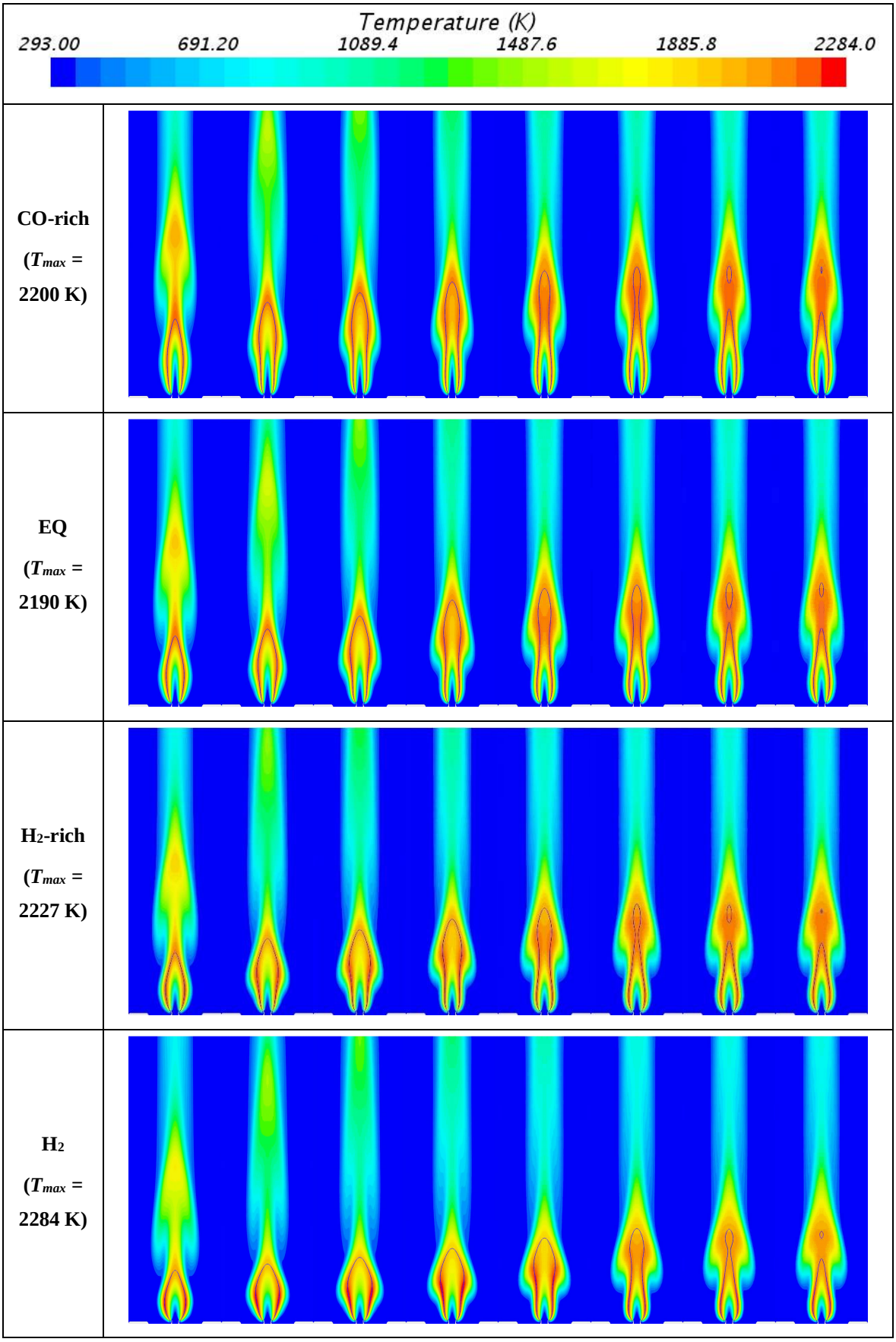

Figure 7-1 Tip-cutting flame of pure syngas (CO-rich, EQ, and H_2-rich) and H_2 at fuel rate = 1.2 SLPM and air rate = 3 SLPM

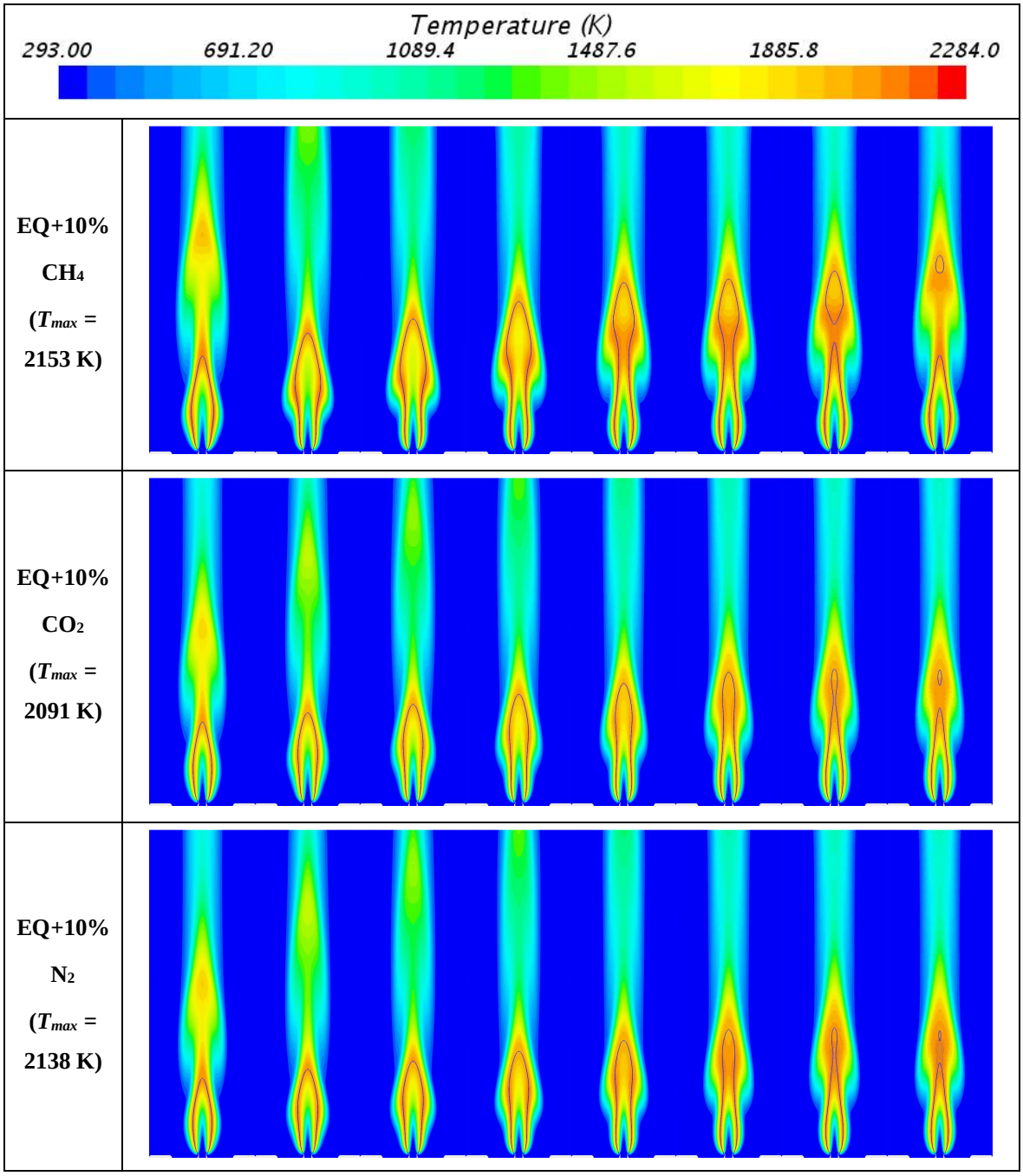

Figure 7-2 Tip-cutting flame of EQ syngas mixed with either CH_4, CO_2, and N_2 at fuel rate = 1.2 SLPM, air rate = 3 SLPM

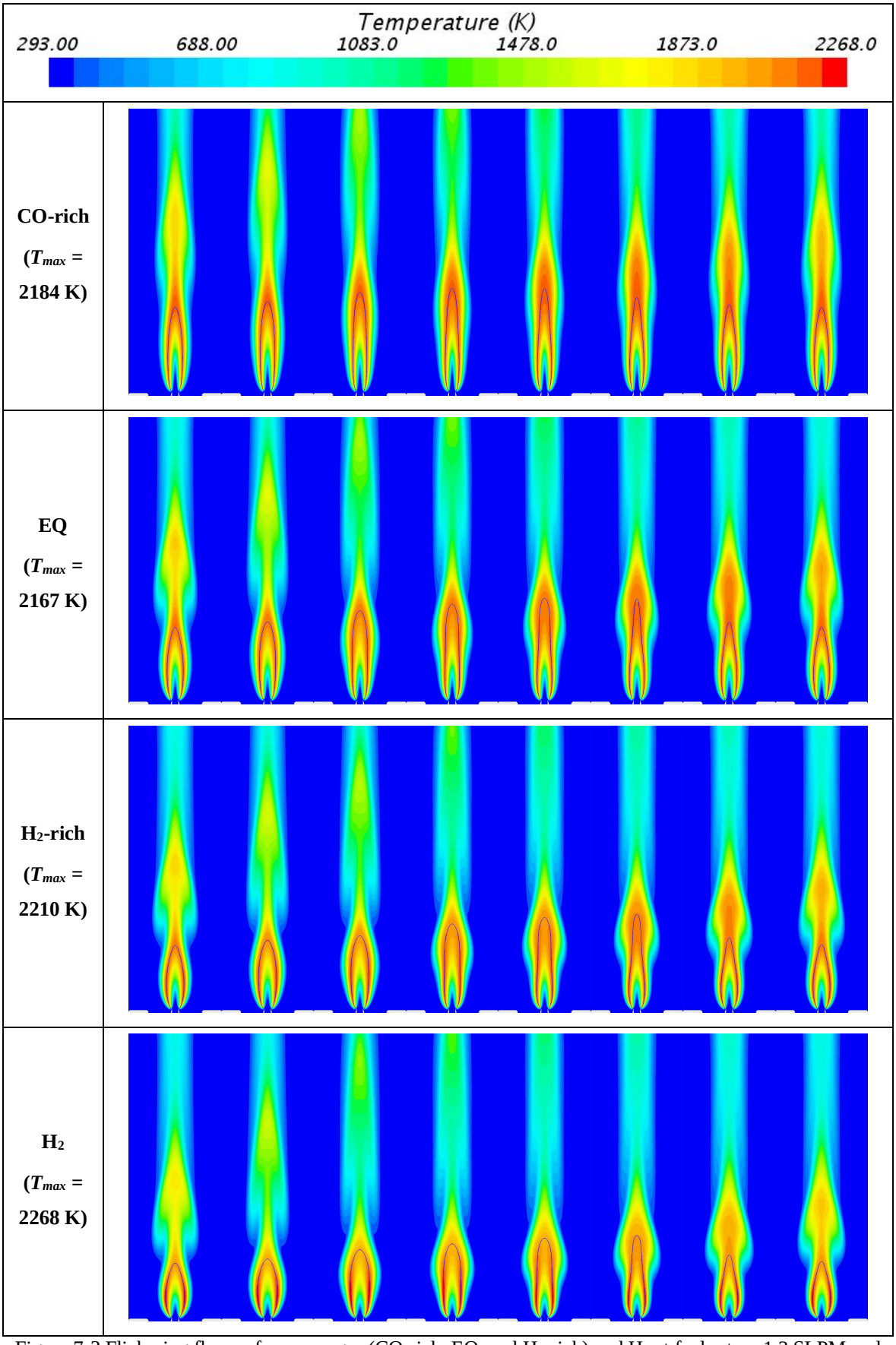

Figure 7-3 Flickering flame of pure syngas (CO-rich, EQ, and H_2-rich) and H_2 at fuel rate = 1.2 SLPM and air rate = 9 SLPM

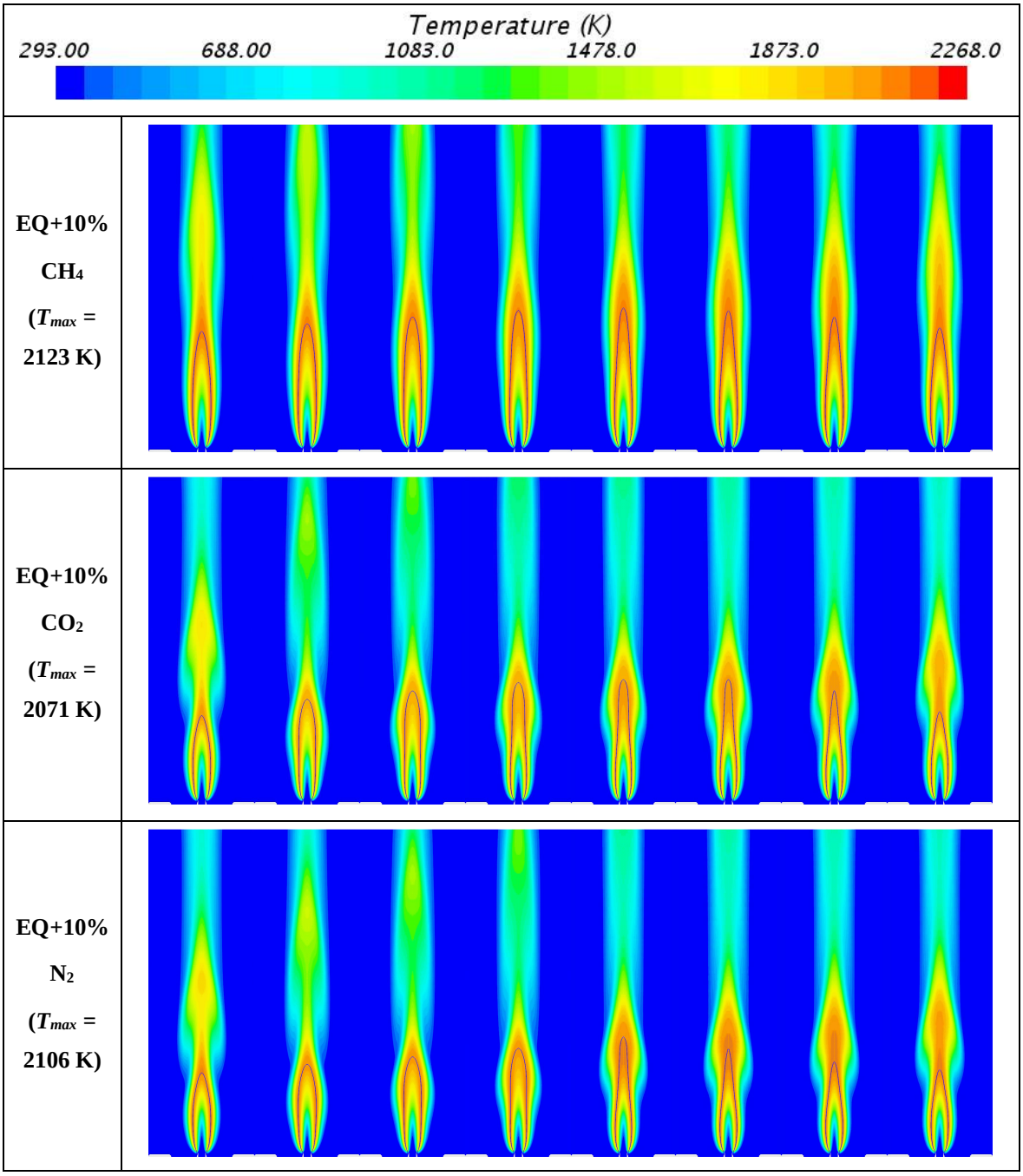

Figure 7-4 Flickering flame of EQ syngas mixed with either CH_4, CO_2, or N_2; fuel rate = 1.2 SLPM and air rate = 15 SLPM for EQ+10%CH_4, and fuel rate = 1.2 SLPM and air rate = 6 SLPM for EQ+10%CO_2 and EQ+10%N_2

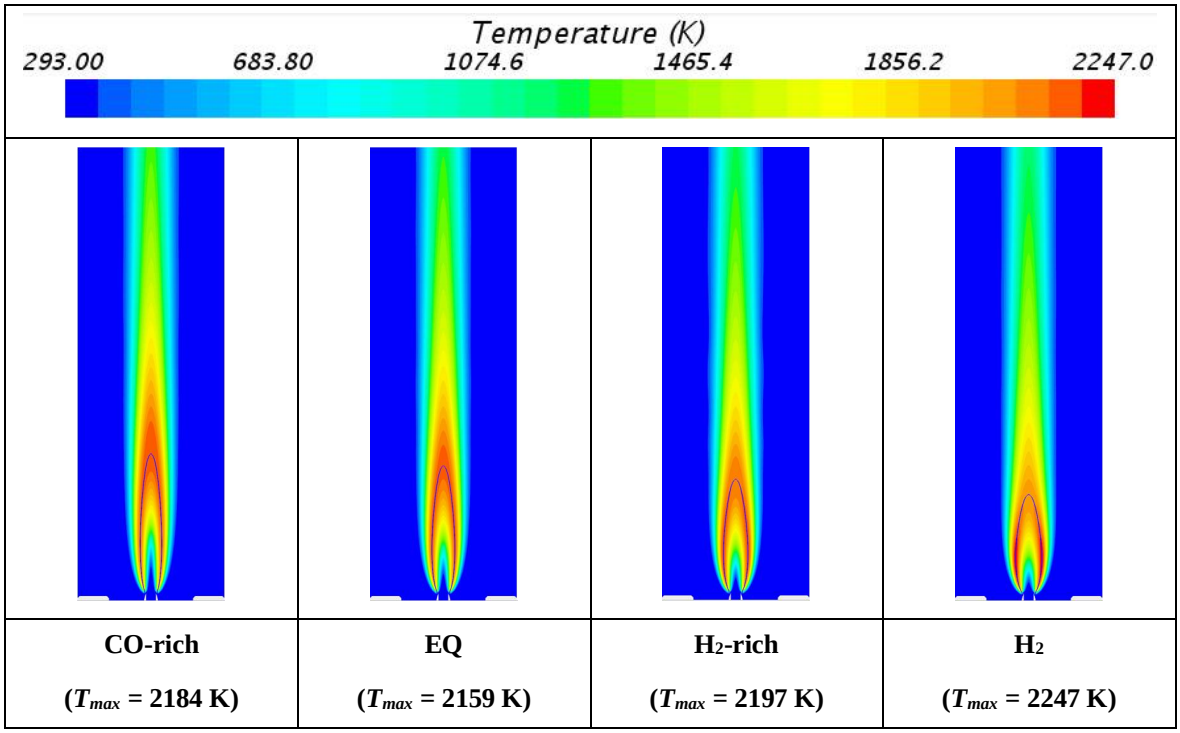

Figure 7-5 Stable flame of pure syngas (CO-rich, EQ, and H_2-rich) and H_2 at fuel rate = 1.2 SLPM and air rate = 20 SLPM

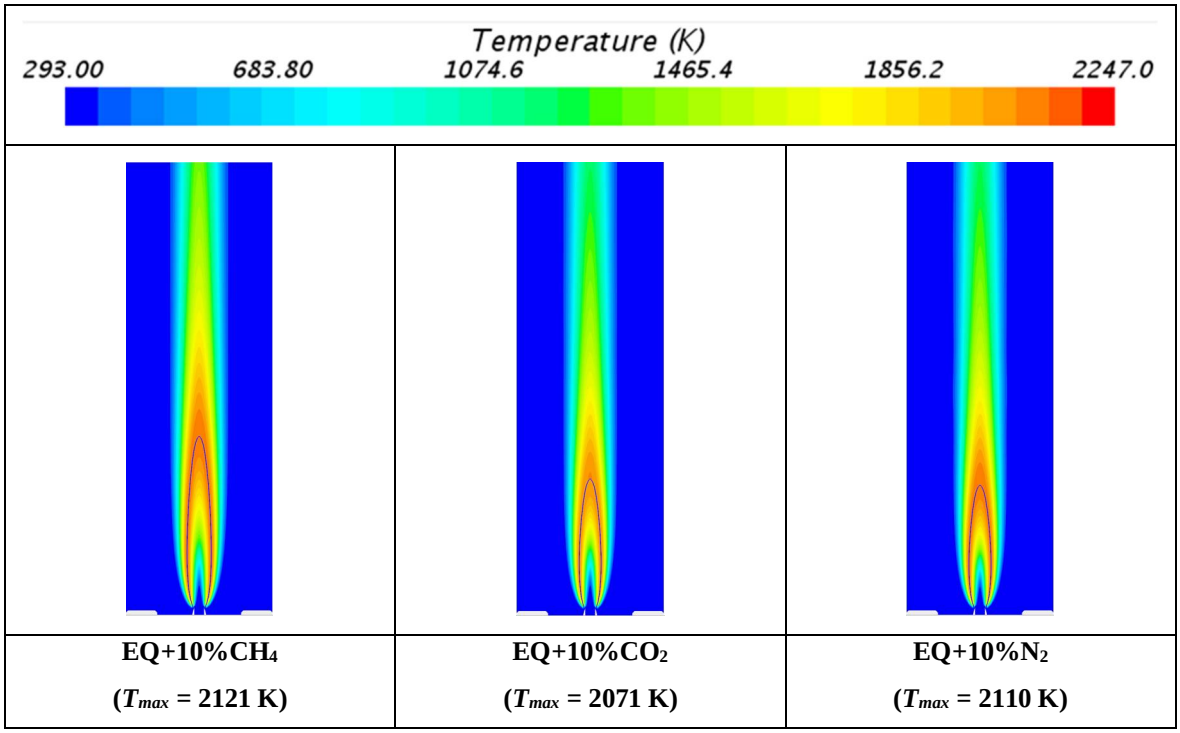

Figure 7-6 Stable flame of EQ syngas mixed with either CH_4, CO_2, and N_2 at fuel rate = 1.2 SLPM and air rate = 20 SLPM

According to the results obtained from the temperature contours, the movement and structure of the syngas/producer gas flames rely strongly on the H_2:CO and flame type (stable/flickering/tip-cutting). The co-flow air rate affects the transition between the flame

types but does not influence the structure of the flame. Following the transition, the movement and structure of stable and flickering flame rely on H_2:CO. Both the movement and structure of tip-cutting flame are not influenced by the fuel composition. The average flame length ($H_{f\text{-}ave}$), temperature ($T_{\text{-}ave}$), and chemical heat release ($Q_{\text{-}ave}$) are computed for further projecting the impact of the fuel composition and co-flow air on the flame characteristics at a deeper level. The flame length, temperature, and total chemical heat release changing over the limit cycle of oscillation are monitored and extracted for their minimum and maximum values, and the tip-cutting position. The method used for extracting and calculating $H_{f\text{-}ave}$, $T_{\text{-}ave}$, and $Q_{\text{-}ave}$ were already explained in Section 6.2.5 of Chapter 6.

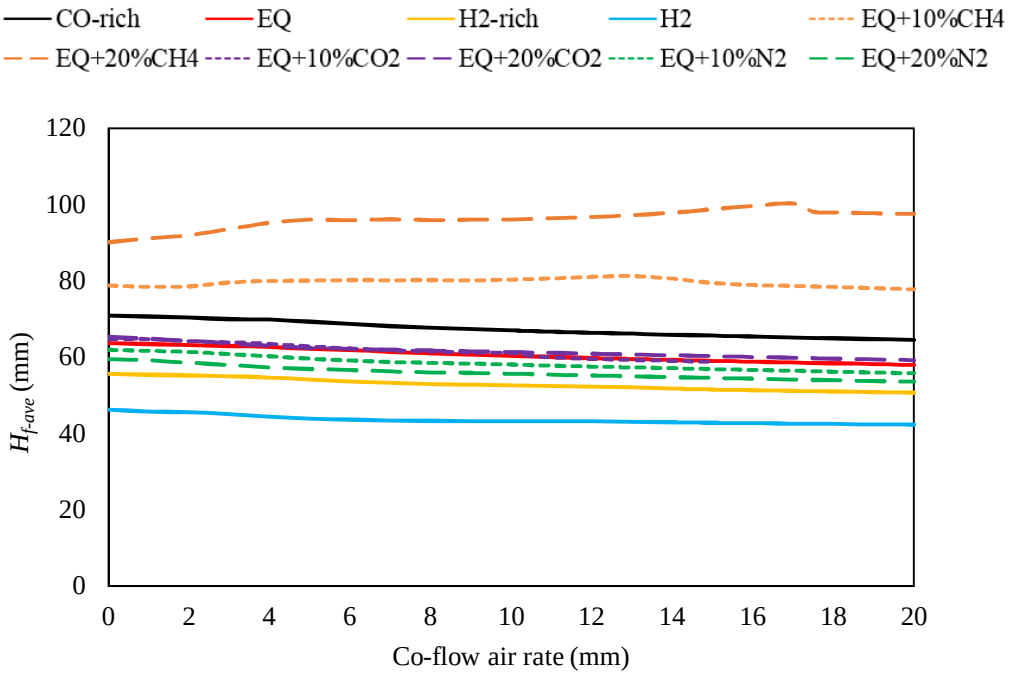

Figure 7-7 Average flame length ($H_{f\text{-}ave}$)

The profiles of $H_{f\text{-}ave}$ of all the studied fuel compositions are compared in Figure 7-7. The impact of H_2, CO, CH_4, CO_2 and N_2 on this parameter are in the same direction as the finding in Chapter 5 and 6. That is, at the same air rate, the longer $H_{f\text{-}ave}$ is obtained from syngas with a lower H_2:CO ratio and from producer gas with a higher concentration of CH_4. The impact of co-flow air is observed as the value of $H_{f\text{-}ave}$ is lower when the air rate supplied into combustion is larger for most of the fuel compositions. The result, therefore, implies that the average flame length of an unstable flame is longer when the magnitude of oscillation (L_f) is higher. Nevertheless, this finding is not valid for EQ+20%CH_4, since its profile of $H_{f\text{-}ave}$ escalates along with an increase of the air rate, and the fluctuation of this parameter is seen when the flame is unstable (air rate < 17 SLPM).

The reduction or increasing rate of $H_{f\text{-}ave}$ is also computed to examine the level of the impact of each species. The species causing the higher reduction gradient encourages the impact of co-flow air at a stronger level. Syngas/producer gas with a lower ratio of H_2:CO has a higher reduction rate of the $H_{f\text{-}ave}$ profile. The reduction rate of CO-rich (H_2:CO = 1:3) is 0.32 mm-SLPM^{-1}, which is higher than that of EQ (0.3 mm-SLPM^{-1}), and H_2-rich (0.25 mm-SLPM^{-1}). This direction of the result is supported by the lower reduction rate computed from the flame of H_2 (0.2 mm-SLPM^{-1}). Also, all the fuel compositions with H_2:CO = 1, e.g. EQ mixed with either CO_2 or N_2 have a similar reduction rate as EQ syngas (~0.3 mm-SLPM^{-1}). For EQ+20%CH_4 and EQ+10%CH_4, the previous composition has an increasing rate of 0.37 mm-SLPM^{-1} whereas the latter one has a significantly low reduction rate of 0.05 mm-SLPM^{-1}. As a result, CO and CH_4 affect the average flame length at a slightly stronger level than the other species but in the opposite direction as they cause a higher reduction and increasing rate, respectively.

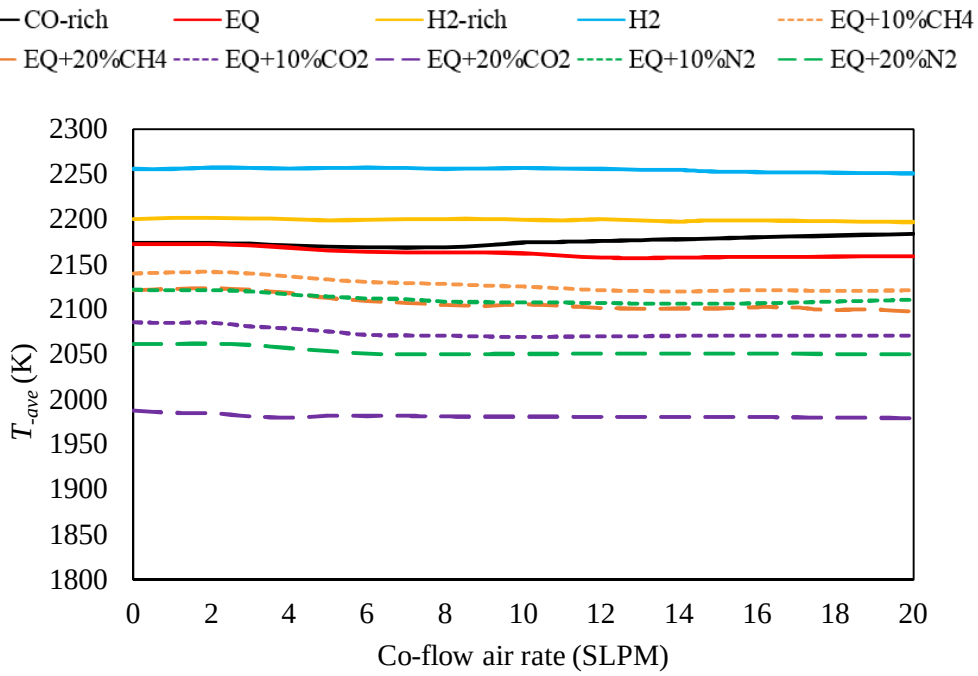

Figure 7-8 Average flame temperature ($T_{\text{-}ave}$)

A similar approach as the analysis of flame length is processed for the study of flame temperature. The average flame temperature during the limit cycle of oscillation ($T_{\text{-}ave}$) is computed and compared in Figure 7-8. In this figure, the profile of $T_{\text{-}ave}$ is plotted against the co-flow air rate supplied into combustion. When the amount of air rate is equal, the higher H_2:CO ratio leads to the higher value of $T_{\text{-}ave}$ while the higher concentration

percentage of CH_4, CO_2, and N_2 result in the lower value of T_{-ave}. The result also projects the stronger impact of CO_2 than N_2 and CH_4 respectively since the value of T_{-ave} of EQ mixed with CO_2 is lower than EQ mixed with either N_2 or CH_4 at the same additional percentage. This finding confirms the role of each species on flame temperature reported in Chapter 5 and 6. Considering the profile of T_{-ave}, the value of this parameter slightly reduces when the air rate is higher for most of the studied fuel compositions. The average temperature of the stable flame is hence lower than that of the unstable flickering flame for the same fuel composition. The different direction of the result is observed from the T_{-ave} profile of CO-rich syngas since its value of T_{-ave} rises along with an increase of air rate. It is also noticed that the value of T_{-ave} of EQ syngas and CO-rich syngas are equal at the air rate below 4 SLPM where their flame types are tip-cutting.

The reduction or increasing profile of T_{-ave} is further analysed for understanding the level of impact of each species through the reduction or increasing rate of this parameter. It is noticed that the ratio of H_2:CO plays a significant role in the average flame temperature. The uptrend is found from syngas with H_2:CO < 1, while the downtrend is seen from one with H_2:CO≥ 1. An increasing rate for an uptrend profile of CO-rich syngas is 1.25 K-SLPM^{-1}. The reduction rate of EQ syngas (0.65 K-SLPM^{-1}) is higher than that of H_2 rich syngas (0.25 K-SLPM^{-1}), and this direction of the result is supported by the lower rate of H_2 flame (0.2 K-SLPM^{-1}). A higher reduction rate is found when the percentage of CH_4 in fuel composition is higher. EQ+10%CH_4 has a reduced rate of T_{-ave} as 0.95 K-SLPM^{-1}, which is lower than the rate computed from EQ+20%CH_4 (1.2 K-SLPM^{-1}). Conversely, the reduction rate of T_{-ave} of EQ mixed with CO_2 is lower when the additional percentage is higher. EQ+10%CO_2 and EQ+20%CO_2 have a decreasing rate of T_{-ave} as 0.7 and 0.4 K-SLPM^{-1}, respectively. The addition of N_2 also affects a lower reduction rate of T_{-ave}; nevertheless, the level is weaker than the addition of CO_2. The comparable rate of ~0.5 K-SLPM^{-1} is computed from the downtrend profile of EQ+10%N_2 and EQ+20%N_2. According to this finding, CH_4 and CO again encourage the impact of co-flow air on the flame temperature at a stronger level than the other species. CH_4 assists the reduction of T_{-ave} when the air rate is higher while the opposite direction is obtained from the role of CO.

The average total chemical heat release (Q_{-ave}) of all the studied fuel compositions during the limit cycle of oscillation is presented in Figure 7-9. At the same air rate, the lower H_2:CO and the higher CH_4 concentration cause the higher value of Q_{-ave}, whereas the higher CO_2 and N_2 concentration play an equal role in the reduction of this parameter. This finding is

also in the same direction as the result of Chapter 5 and 6. The pattern of $Q_{\text{-}ave}$ profile is similar for most fuel composition. The value of $Q_{\text{-}ave}$ is almost stable, although the higher air rate is supplied into combustion. The result is, however, slightly different for H_2 and H_2-rich syngas, where their values of $Q_{\text{-}ave}$ decrease along with an increase of the air rate. The decreasing rate of the profile of $Q_{\text{-}ave}$ is hence computed for only H_2 and H_2-rich as 0.25 and 0.2 W-SLPM^{-1}, respectively. According to this, H_2 encourages the impact of co-flow air on the total chemical heat release at a stronger level than the other species.

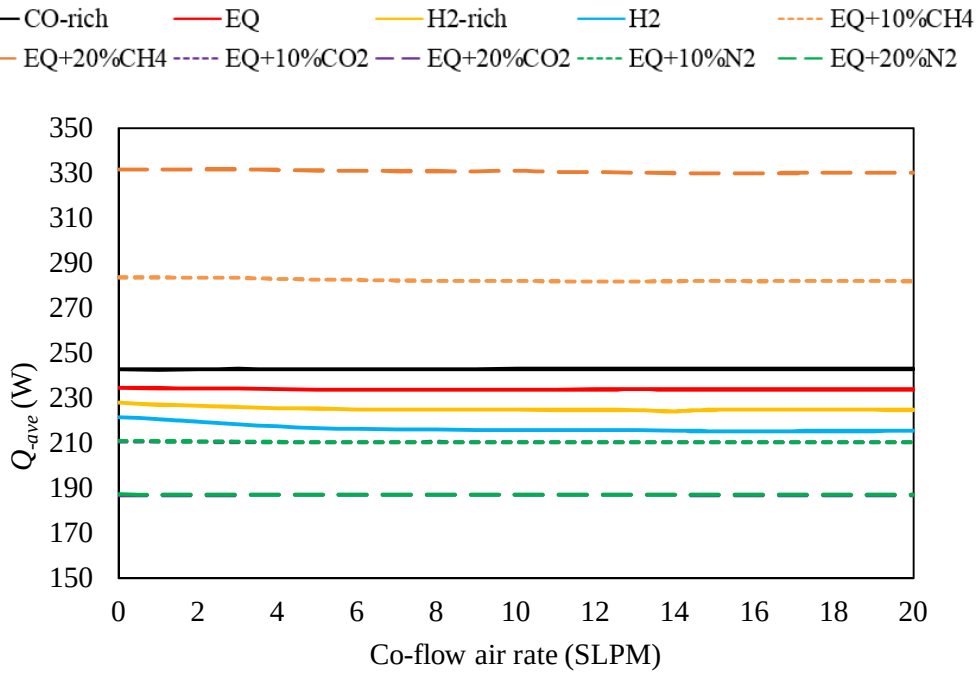

Figure 7-9 Average total chemical heat release ($Q_{\text{-}ave}$)

7.3.2 **Transition air flow rate**

The profile of the flame length changing over time are extracted for the magnitude of oscillation (L_f), and the oscillation wavelength (λ). The definition of these parameters and the calculation method were already presented in Chapter 6. The type of flame is identified based on the value of these parameters. The stable flame has L_f and λ equal to zero, the flickering flame has $L_f > 0$ and $\lambda = 0$, and the tip-cutting flame has both L_f and λ above zero. By applying this criterion, the types of flame at each fuel and air rate of all the studied fuel composition are presented in Table 7-1. The table reveals the critical air rate, in which the transition between the flame types occurs. The transition air rate is defined as the minimum air rate required for the flame to transform from one flame type to another type. Hence, there

are two types of transition air flow rate depending on the flame type: (i) tip-cutting/flickering ($Air_{t\to f}$) and (ii) flickering/stable ($Air_{f\to s}$).

Table 7-1 Flame type at each fuel and air rate

Fuel composition	Co-flow air rate (SLPM)																				
	0	1	2	3	4	5	6	7	8	9	10	11	12	13	14	15	16	17	18	19	20
CO-rich	T	T	T	T	T	T	T	F	F	F	F	S	S	S	S	S	S	S	S	S	S
EQ	T	T	T	T	T	T	T	T	F	F	F	F	F	S	S	S	S	S	S	S	S
H_2-rich	T	T	T	T	T	T	T	T	F	F	F	F	F	F	F	S	S	S	S	S	S
H_2	T	T	T	T	T	F	F	F	F	F	F	F	F	F	F	S	S	S	S	S	S
EQ+10%CH_4	T	T	T	T	T	T	T	T	T	T	T	T	T	T	T	F	F	S	S	S	S
EQ+20%CH_4	T	T	T	T	T	T	T	T	T	T	T	T	T	T	T	T	T	T	F	S	S
EQ+10%CO_2	T	T	T	T	T	T	F	F	F	F	S	S	S	S	S	S	S	S	S	S	S
EQ+20%CO_2	T	T	T	T	F	F	S	S	S	S	S	S	S	S	S	S	S	S	S	S	S
EQ+10%N_2	T	T	T	T	T	T	F	F	F	F	F	S	S	S	S	S	S	S	S	S	S
EQ+20%N_2	T	T	T	T	F	F	F	F	S	S	S	S	S	S	S	S	S	S	S	S	S

Pure syngas (CO-rich, EQ, and H_2-rich) with a higher H_2:CO ratio requires a larger amount of air rate for both types of transition. As seen, CO-rich syngas has a lower $Air_{t\to f}$ and $Air_{f\to s}$ (7 and 11 SLPM respectively) than EQ and H_2-rich. EQ and H_2-rich has an equal $Air_{t\to f}$ at 8 SLPM but different $Air_{f\to s}$. The value of $Air_{f\to s}$ of EQ (13 SLPM) is lower than that of H_2-rich (15 SLPM). The result obtained from H_2 is in the same direction for $Air_{f\to s}$ but not for $Air_{t\to f}$. The value of $Air_{t\to f}$ of H_2 (5 SLPM) is lower than that of the pure syngas but $Air_{f\to s}$ of this fuel is higher. The flame of EQ mixed with CH_4 demands the higher rate for both types of the transition than the other fuel compositions. As seen, the higher concentration percentage of CH_4 in fuel composition increases the value of $Air_{t\to f}$ and $Air_{f\to s}$ compared to ones of EQ syngas. At the tip-cutting/flickering transition, $Air_{t\to f}$ of EQ+10%CH_4 (15 SLPM) and EQ+20%CH_4 (18 SLPM) are significantly higher than that of the reference flame EQ (8 SLPM). The same direction of the result is found at the flickering/stable transition. E.g. EQ+10%CH_4 and EQ+20%CH_4 have $Air_{f\to s}$ at 17 SLPM and 19 SLPM, respectively. According to this, the impact of CH_4 on $Air_{t\to f}$ and $Air_{f\to s}$ is stronger when the additional percentage is higher.

In opposite, adding CO_2 or N_2 to syngas reduces the value of $Air_{t\to f}$ and $Air_{f\to s}$, and the higher additional percentage of them causes the lower value of these parameters. The comparable role of both species is found at the tip-cutting/flickering transition since $Air_{t\to f}$ of EQ mixed with CO_2 and EQ mixed with N_2 are equal as 6 SLPM at 10% of addition

and 4 SLPM at 20%. The different level of the impact of these species is observed at the flickering/stable transition. The value of $Air_{f\rightarrow s}$ of EQ mixed with CO_2 is lower than EQ mixed with N_2 when the additional percentage is equal. For example, the value of $Air_{f\rightarrow s}$ of EQ+10%CO_2 (10 SLPM) is lower than EQ+10%N_2 (11 SLPM). Also, EQ+20%CO_2 has the lower $Air_{f\rightarrow s}$ (6 SLPM) than EQ+20%N_2 (9 SLPM).

In addition, the value of $Air_{t\rightarrow f}$ projects the range of air rate that the flame is tip-cutting. The difference between the value of $Air_{t\rightarrow f}$ and $Air_{f\rightarrow s}$ reveals the range of air rate that the flame is flickering. The flame of EQ+20%CH_4 is found to be a tip-cutting flame in the largest range of air rate (0 - 17 SLPM) followed by EQ+10%CH_4 (0 - 14 SLPM). On the other hand, the flame of H_2 is flickering in the largest range of air rate (5 – 14 SLPM) followed by H_2-rich syngas (8 – 14 SLPM). This information provides the possibility of flame type when the higher air rate is supplied into combustion but insufficient to eliminate the instability. For instance, an increase of air rate in syngas with the higher H_2:CO ratio has a higher possibility that the flame is flickering. Also, processing the same action on EQ+20%CH_4 has a higher chance that the flame is tip-cutting.

7.3.3 **The disappearance of flame oscillation**

The analysis of the transition air rate shows that the different amount of air rate is required for different fuel composition for the transition between flame types. The profile of magnitude of oscillation (L_f), and the oscillation wavelength (λ) is analysed in this section. The profiles of these parameters are plotted against the co-flow air rate, as presented in Figure 7-10a-b. The different profiles of L_f and λ of each fuel composition are observed. The maximum value of these parameters is at 0 SLPM of air rate for all the studied fuel composition. Due to this, the combustion at fuel rate = 1.2 SLPM and air rate = 0 SLPM formulates the tip-cutting flame with the highest value of L_f and λ. The profiles pattern of L_f and λ are in the same direction; the values of them are lower when the co-flow air rate increases. The profile of L_f approaches zero at the air rate equal to $Air_{f\rightarrow t}$, while one of λ is zero at the air rate equal to $Air_{t\rightarrow f}$. Furthermore, it is noticed from the profile of L_f of each fuel composition that the reduction rate is lower when the flame is a tip-cutting.

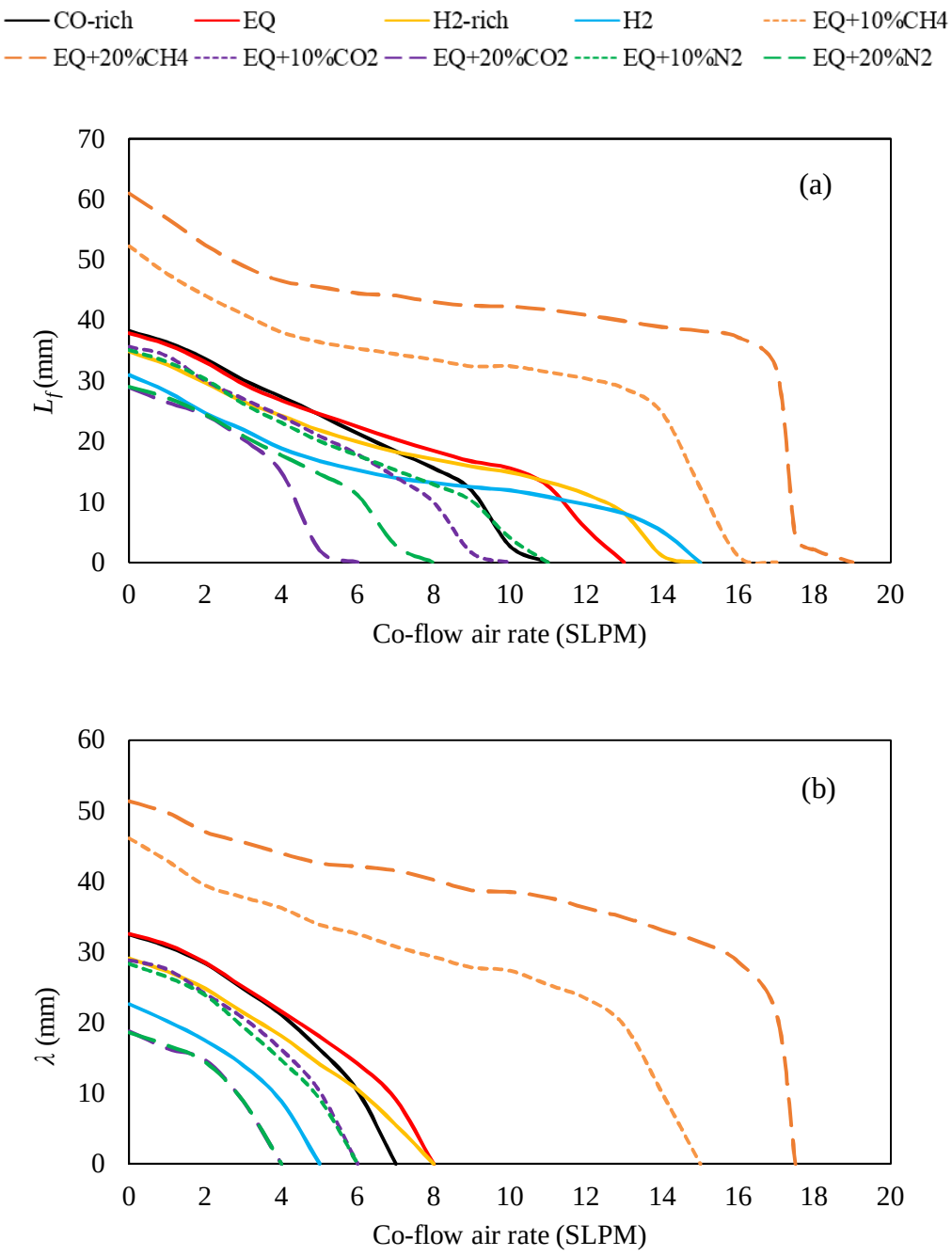

Figure 7-10 (a) the magnitude of oscillation (L_f), and (b) Oscillation wavelength (λ)

As the maximum values of L_f and λ of different fuel compositions (at 0 SLPM of air rate) are different, the analysis of the impact of fuel composition is processed based on the average reduction rate of L_f and λ profile. This method reveals the impact of each species on the reduction of the degree of flame oscillation and tip-cutting phenomenon. One affecting the higher reduction rate is considered to assist the co-flow air in the reduction of the magnitude of oscillation and level of tip-cutting phenomenon at a stronger level. For pure syngas, the highest reduction rate of L_f is computed from CO-rich syngas (3.45 mm-SLPM^{-1}) followed

by EQ syngas (2.93 mm-SLPM^{-1}), and H_2-rich syngas (2.33 mm-SLPM^{-1}). The similar result is found from the reduction rate of λ. CO-rich syngas has a higher reduction rate (4.71 mm-SLPM^{-1}) than EQ syngas (4.13 mm-SLPM^{-1}), and H_2-rich syngas (3.5 mm-SLPM^{-1}). This result projects the role of CO, which is stronger than H_2 on a reduction of the degree of flame oscillation as well as the tip-cutting phenomenon. The reduction rate of H_2 flame of L_f supports this direction of the result; nevertheless, the reduction rate of λ of this fuel is in a different direction. The reduction rate of L_f of H_2 flame (1.93 mm-SLPM^{-1}) is lower than all the pure syngas, but the reduction rate of λ (4.6 mm-SLPM^{-1}) of this fuel is higher than that of EQ and H_2-rich syngas.

In Figure 7-10a-b, the flame of EQ mixed with CH_4 has the highest and the second-highest maximum L_f and λ among the studied fuel compositions. The maximum value of L_f at 0 SLPM of air rate of EQ+20%CH_4 and EQ+10%CH_4 are 61 and 52 mm, respectively, while one of λ at this air rate is 51 and 46 mm in order. The reduction rates of the profile of L_f and λ are computed for these fuel compositions. The higher CH_4 concentration increases the reduction rate of L_f but decreases the reduction rate of λ. The reduction rate of L_f of EQ+20%CH_4 is 3.21 mm-SLPM^{-1}, and it is higher than one of EQ+10%CH_4 (3.05 mm-SLPM^{-1}). On the other hand, EQ+20%CH_4 has a lower reduction rate of λ (2.9 mm-SLPM^{-1}) than EQ+10%CH_4 (3 mm-SLPM^{-1}). The addition of CH_4 to syngas composition is considered to assist the reduction of flame oscillation level (decrease of L_f) since the reduction rate of L_f of EQ mixed with CH_4 is higher than one of EQ syngas. However, the addition of CH_4 results in the opposite direction for the tip-cutting phenomenon. The lower reduction rate of λ of EQ mixed with CH_4 than EQ syngas expresses that this species does not encourage the impact of co-flow air on the reduction of the level of tip-cutting phenomenon.

Comparable role of CO_2 and N_2 is observed on the reduction of tip-cutting level (reduction of λ). The profiles and reduction rates of λ of EQ with CO_2 and EQ mixed with N_2 are comparable at the same additional percentage as seen in Figure 7-10b. EQ+10%CO_2 and EQ+10%N_2 have the reduction rate of λ as 4.6 mm-SLPM^{-1}, and the rate is slightly higher for EQ+20%CO_2 and EQ+20%N_2 (4.7 mm-SLPM^{-1}). On the other hand, the stronger role of CO_2 over N_2 is found in the reduction of flame oscillation level (reduction of L_f) in Figure 7-10a. The reduction rate of L_f of EQ mixed with CO_2 is 3.5 and 4.83 mm-SLPM^{-1} at 10% and 20% of the additional percentage. The rate is lower for EQ mixed with N_2; 3.18 and 3.63 mm-SLPM^{-1} at 10% and 20%, respectively. Therefore, adding CO_2 or N_2 into the

composition of EQ syngas assists the reduction and disappearance of flame oscillation also tip-cutting phenomenon. The reduction gradient of L_f and λ are higher when either CO_2 or N_2 is mixed with EQ syngas compared to that of EQ syngas without additional species. Further, the higher additional percentage of CO_2 or N_2 leads to a stronger level of impact.

The flickering frequency (*F*) is another parameter representing the behaviour of the unstable laminar diffusion flame. It is defined as the number of limit cycles of oscillation per second. The value of *F* could be computed from the flame length profile changing over time. It is the inverse proportion of the period per the limit cycle. However, this method has a limitation for stable flame since the flame length profile of this flame type is constant over time. The relation between *F* and co-flow air rate is direct proportion, and the profile is almost linear, as seen in Figure 7-11. This result refers to the higher flickering frequency when the flame has a lower level of oscillation (more stable). For pure syngas, the value of *F* is higher for the syngas with the lower H_2:CO ratio at the same air rate. The value of *F* of CO-rich is higher than that of EQ, H_2-rich, and H_2, respectively. The addition of CH_4 to syngas composition decreases the value of *F* while diluting the syngas composition with either CO_2 or N_2 results in the higher value of *F*. The impact of CO_2 is stronger than N_2 on this aspect. The result emphasises the role of CO, CO_2, and N_2 on an assist of the reduction and elimination of flame oscillation since a higher *F* is obtained from the fuel composition having the higher concentration of these species.

An increasing rate of the profile of *F* of all the studied fuel composition is calculated. The higher rate is found from syngas with the higher H_2:CO ratio. The rate computed from H_2-rich (0.39 Hz-SLPM^{-1}) is higher than EQ (0.38 Hz-SLPM^{-1}), and CO-rich (0.36 Hz-SLPM^{-1}), respectively. This finding is supported by the higher increasing rate of H_2 flame (0.43 Hz-SLPM^{-1}) than all the pure syngas. It is also noticed that the syngas with a higher H_2:CO ratio has a higher increasing rate of *F* profile, although its value of *F* is lower than the syngas with the lower H_2:CO ratio. Thus, it is possible that *F* of H_2 flame and syngas with the higher H_2:CO will be higher than syngas with the lower ratio at the higher co-flow air rate where the flame is stable. For the additional species, the addition of CH_4 decreases the increasing rate of the profile of *F* of EQ to 0.33 and 0.34 Hz-SLPM^{-1} at 10% and 20 %. The opposite direction is observed from the addition of either CO_2 or N_2. EQ+10%CO_2 and EQ+10%N_2 have an equal rate as 0.42 Hz-SLPM^{-1}, and the rate increases to 0.52 Hz-SLPM^{-1}for EQ+20%CO_2 and EQ+20%N_2. According to this, the higher concentration of H_2, CO_2 and N_2 assist the impact of co-flow air on the increase of flickering frequency.

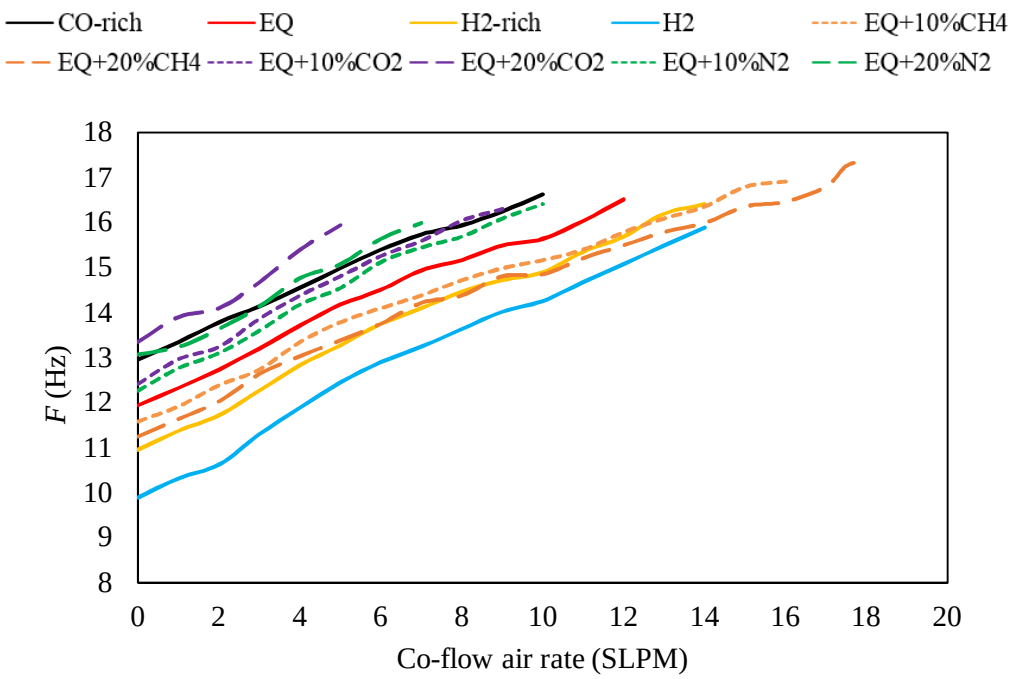

Figure 7-11 Flickering frequency (*F*)

7.3.4 **The fluctuation of temperature and heat generation**

The K-H instability due to the buoyancy force is the primary cause of the flame oscillation and the fluctuation in the heat generation (*dQ*) and flame temperature (*dT*). These parameters of the flame of different compositions are compared, as seen in Figure 7-12 and Figure 7-13, respectively. The method of calculation of these parameters was also presented in Chapter 6. The larger difference between the maximum and minimum values of the total chemical heat release and flame temperature leads to the higher value of *dQ*, and *dT*, respectively. By this definition, the higher value of them implies to the higher level of fluctuation.

In Figure 7-12, the profile pattern of *dQ* is similar to the profile pattern of L_f for the flame of the same fuel composition. The value of *dQ* reduces from the maximum value at 0 SLPM and approaches zero at the same air rate as the profile of L_f. Therefore, the disappearance of the fluctuation in chemical heat release occurs when the flame is stable. The species that encourages the reduction and elimination of magnitude of oscillation also decrease the fluctuation of chemical heat release. However, the flame having a higher L_f is not necessary to provide a higher value of *dQ* at the same air rate. For instance, at 0 SLPM of air rate, the flame of H_2 has a higher value of *dQ* but a lower value of L_f than the flame of pure syngas (CO-rich, EQ, and H_2-rich). The reduction rate of *dQ* profile is computed and compared for further details. However, it is necessary to take into account that the rate only represents the

profile pattern of *dQ*, and the profile of L_f dominates the disappearance of this parameter. The decreasing rate is found between 5 and 7.1 W-SLPM^{-1}, and the highest rate is computed from EQ+20%CH_4 (7.1 W-SLPM^{-1}) followed by EQ+10%CH_4 and EQ+20%CO_2 at 5.9 W-SLPM^{-1}. The reduction rate of the other fuel compositions is similar at ~5 W-SLPM^{-1}.

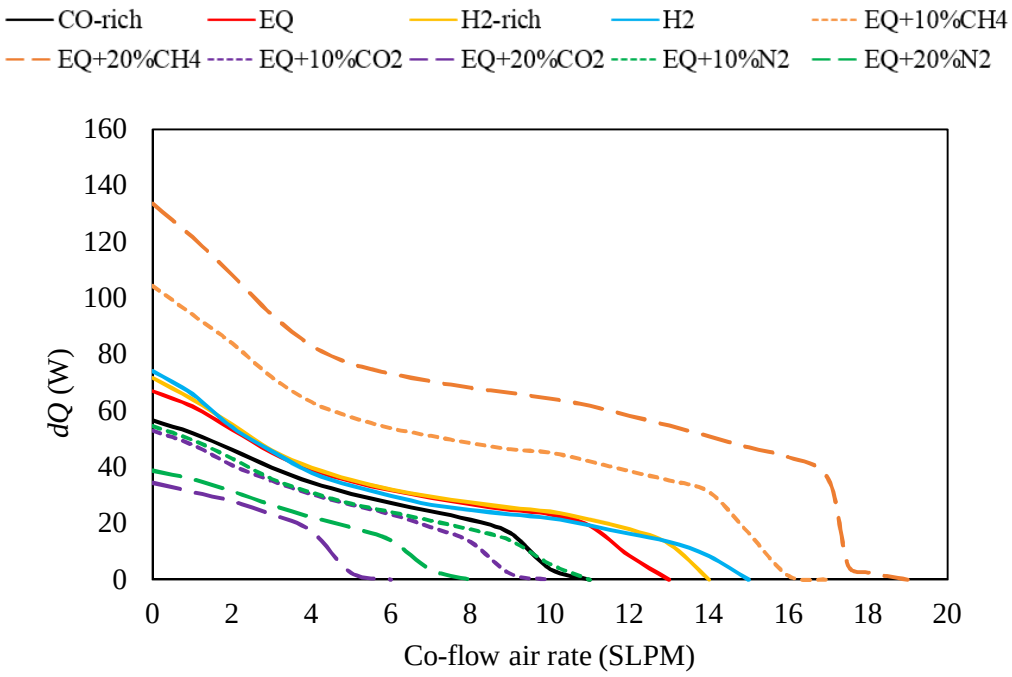

Figure 7-12 Fluctuation of total chemical heat release (*dQ*)

Similar to the profile of *dQ*, the profile of *dT* has the maximum value at 0 SLPM of air rate and approaches zero at the same air rate as the profile of L_f. However, the profile of *dQ* and *dT* have a different pattern. Along with an increase in air rate, the value of *dT* reduces then increases slightly and decreases again to zero, as seen in Figure 7-13. This pattern is obtained from most of the fuel compositions except for CO-rich and EQ+20%CO_2 as their profiles decrease directly and significantly to zero. At 0 SLPM, the highest level of fluctuation is computed from the flame of H_2 followed by H_2-rich and CO-rich. Similar to the analysis of *dQ*, the decreasing rate of *dT* only projects the profile pattern. The average reduction rate of *dT* profile of pure syngas (CO-rich, EQ, and H_2-rich) are similar as ~5.5 K-SLPM^{-1}. EQ mixed with CH_4 at 10% and 20 % have a comparable reduction rate of *dT* (2.3 K-SLPM^{-1}). The reduction rate of EQ mixed with CO_2 or N_2 is lower than the rate of EQ. The rate is 3.5 and 4.2 K-SLPM^{-1} for the addition of CO_2 at 10% and 20%, respectively. The similar rate is computed as 3.3 and 4.8 K-SLPM^{-1} for EQ+20%N_2 and EQ+10%N_2.

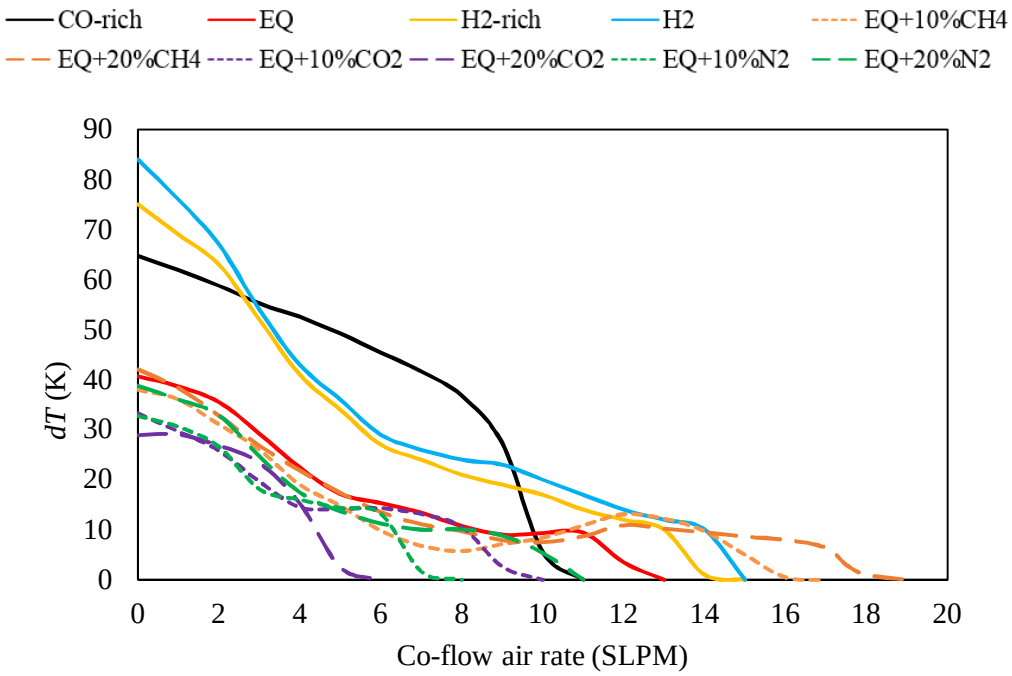

Figure 7-13 Fluctuation of flame temperature (*dT*)

7.4 Discussion

The CFD model is used for studying the impact of fuel composition of syngas/producer gas on the reduction and disappearance of flame oscillation. The key findings are discussed as follow:

At the higher co-flow air rate, the impact of K-H instability and flame oscillation is weaker. The profile of $T_{\text{-ave}}$, $H_{\text{-ave}}$ and $Q_{\text{-ave}}$ obtained from different fuel composition also expresses the role of K-H instability and flame oscillation on flame characteristics. The higher impact of K-H instability at the lower air rate leads to the larger range of movement of the flame (larger magnitude of oscillation) and hence the longer average flame length ($H_{\text{-ave}}$). Similarly, the mix between fuel and oxidiser is encouraged by the K-H instability resulting in the higher average temperature at the lower co-flow air rate. For the total chemical heat release, the impact of K-H instability and flame oscillation is weak as the average total chemical heat release only change slightly at the higher air rate. On the other hand, the result also expresses that the impact of each species on $T_{\text{-ave}}$, $H_{\text{-ave}}$ and $Q_{\text{-ave}}$ are stronger than the impact of K-H instability and flame oscillation. The details regarding the role of each species on these parameters are presented in Chapter 5.

Utilising the Richardson number (equation (9)) for explaining the oscillating flame might not be effective as discussed in the previous chapter. According to the result reported in Ref [88], [90], the longer flame is expected to demand the larger air flow rate to push the vortices outside the visible flame so the flame becomes stable. In this work, the condition is valid for CH_4 flame and syngas with H_2:CO = 1. Apart from this, the flame of CO-rich syngas demands less air rate to become stable although it is longer than H_2-rich and H_2 flame. According to this, the assumption could be made as the high diffusive property of H_2 might encourage the K-H instability causing more difficulty for the co-flow air to push the vortices outside the visible flame. This assumption could also be used for explaining the role of H_2 as its higher diffusive property encourages the K-H instability causing the larger demand of air rate than CO to eliminate the flame oscillation.

Diversity in fuel composition has an impact on a different level of magnitude of oscillation in unstable oscillating flame. The demand for air rate for transforming the oscillating flame to the stable flame is hence different depending on the fuel composition. Among the combustible species (H_2, CO, and CH_4) in syngas composition, CO is considered to be the most desirable one as it assists the reduction of the magnitude of oscillation at the strongest level comparing to the others. The flame of syngas consisting of the higher concentration of this species demand less air rate to become stable. Combining this finding with the result obtained in Chapters 5 and 6, the role of this species is emphasised as it provides the lower magnitude of oscillation but the higher heat generation capability. Thus, syngas with the lower H_2:CO ratio is preferable. However, it is necessary to take into account that this study does not consider the flammability limit also emission formation.

On the other hand, adding CH_4 into syngas composition escalates the average flame length significantly causing the larger demand for the amount of air supplied into combustion to push the vortices outside the visible flame, so the flame is stable. Increasing the concentration of this species in fuel composition is an effective method for escalating the heat generation and heat transfer performance of the flame according to the result of Chapter 5. In this chapter, the mentioned method is found to be beneficial only when the flame is stable. Thus, it is necessary to provide a sufficient amount of air rate when this method is applied. Without a sufficient amount of air rate, the flame with a higher percentage of CH_4 has a higher magnitude of oscillation and the possibility to be a tip-cutting flame. Hence, a significantly higher level of fluctuation of heat generation is expected.

A contradictive result is found when CH_4 is added into syngas composition. This species assists the reduction of the magnitude of oscillation but causes a higher demand for air rate to become a stable flame. Further study on the larger range of fuel and air rate is required in order to understand this finding and confirm the role of this species on the reduction and elimination of the flame oscillation.

Apart from the disappearance of flame oscillation, the impact of co-flow air on the flame characteristics (e.g. the flame movement and structure, flame temperature, total chemical heat release, and flame length) is considered as insignificant. The higher air rate supplied into the combustion could reduce the average flame length ($H_{f\text{-}ave}$) and flame temperature ($T_{\text{-}ave}$). Nevertheless, the reduction rate of the profile of these parameters per increasing co-flow air rate is significantly low compared to the value of the average flame length and flame temperature. For instance, the value of $H_{f\text{-}ave}$ and $T_{\text{-}ave}$ change ~0.5% and ~0.05% respectively when 20 SLPM of air rate is supplied. For the average total chemical heat release $Q_{\text{-}ave}$, the co-flow air rate does not affect the value as seen from the profile of this parameter of most fuel composition which is constant at the range of air rate studied. For the flame of H_2 and H_2-rich, the reduction rate of $Q_{\text{-}ave}$ profile is significantly low compared to the value of $Q_{\text{-}ave}$; the value of this parameter change ~0.07% after 20 SLPM of air rate is supplied. As a result, the impact of co-flow air on these parameters is considered as weak.

The significant role of CO_2 and N_2 is seen from a study of the disappearance of flame oscillation. Adding either of these species into the syngas composition is an effective method for increasing the flame stability. This finding is in the same as reported in Chapter 6. However, both CO_2 and N_2 are non-combustible species, and the dilution of them to syngas composition decreases the percentage of combustible species resulting in the lower heat generation capability. The additional percentage of them in fuel composition should be optimised for a suitable value.

7.5 Conclusion

The CFD model formulated in Chapter 6 initially simulates the unstable flame with the highest magnitude of oscillation and oscillating wavelength. An increase of co-flow air results in the reduction of the magnitude of oscillation and disappearance of flame oscillation. It also causes the lower level of fluctuation in the flame temperature and total

chemical heat release. The impact of fuel composition on this phenomenon is investigated, and the conclusion could be drawn as follows:

- At the same fuel rate, syngas with the lower ratio of H_2:CO ratio requires less air rate to become stable. The assumption is proposed as the high diffusive property of H_2 might encourage the Kelvin–Helmholtz (K-H) instability. The additional species CH_4 increases the demand of air rate to become stable significantly. The addition of CH_4 increases the flame length; thus, the higher air rate is demanded to push the vortices outside the visible flame. Conversely, the species CO_2 and N_2 reduce the demand of air rate for the same purpose.

- The impact of co-flow air on the average flame length ($H_{f\text{-}ave}$), flame temperature ($T_{\text{-}ave}$), and chemical heat release ($Q_{\text{-}ave}$) are insignificant. The higher air rate supplied into combustion affects the lower value of these parameters. However, the reduction rate of them with respect to an increased air rate is significantly low compared to the values of $H_{f\text{-}ave}$, $T_{\text{-}ave}$, and $Q_{\text{-}ave}$. The values of these parameters change less than 0.5% after 20 SLPM of air rate is supplied into combustion.

- The result emphasises the role of CO as the most desirable species among combustible species in the syngas/producer gas composition. Less air demand for maintaining the stability of the flame refers to the lower power input to drive the co-flow air stream.

- Adding CO_2 and N_2 to the fuel composition is an effective method for assisting the reduction magnitude of oscillation and disappearance of flame oscillation. Both species are non-combustible species; hence, the optimisation for the proper additional percentage that balances between the flame stability and heat generation capability of the flame is required.

Chapter 8 Final conclusions and further study

In this work, the impact of each species in fuel composition of syngas/producer gas on the flame characteristics, heat generation capability, emission, and stability were focused. The stable and unstable flame of H_2, H_2/N_2, and syngas/producer gas were formulated using Computational fluid dynamics (CFD). The results obtained were compared and analysed for projecting the impact of each species in syngas/producer gas composition. The finding is summarised in this chapter, then the recommendation for further study is provided.

8.1 Conclusions

Two CFD models (stable and unstable flame models) were formulated and validated based on the experimental result. The burner of Toro et al. [2] was the reference for the first model, which was used for studying the stable H_2/N_2, H_2, CH_4, syngas/producer gas laminar diffusion flame. The second CFD model was generated based on the burner of Gohari et al. [88], and this model was specifically designed for investigating the laminar diffusion unstable flame of the same fuel. The key findings in Chapter 4-7 were concluded as follow:

In Chapter 4, the study focused on the impact of H_2 content defined as the volume flow rate of H_2 ($\dot{v}_{H_2}$) on flame characteristics (e.g. flame appearance, temperature, dimension and chemical heat release), and emission of a stable laminar diffusion flame. The fuel composition was H_2 and H_2/N_2 with a variation in the concentration ratio of H_2:N_2 as 1:3, 1:1, and 3:1. The fuel and co-flow air velocity (V_{avg}) were equal for each case, and the value was between 0.25 and 0.75 ms^{-1}. Two methods causing the higher content of H_2 in fuel composition were (i) increasing concentration of H_2 (X_{H_2}) in fuel composition, and (ii) escalating velocity of the fuel stream. The effect of these methods on flame characteristics was also examined in this work.

The result showed that the higher H_2 content (higher $\dot{v}_{H_2}$) in fuel composition led to the larger flame size and higher heat generation. The impact of both methods used for increasing H_2 content was more significant than the effect of H_2 content. The flame temperature and flame width were dominated by the concentration of H_2 in fuel composition (X_{H_2}), whereas the velocity of fuel stream (V_{avg}) played a significant role in flame length. The NO_x emission formation due to combustion was analysed along with the study of flame characteristics. The production rate of NO_x was dominated by the thermal NO_x formation mechanism (Zel'dovich

mechanism [152]) since the flame having a higher flame temperature formulated NO_x at a higher rate. Also, it was noticed that the larger (longer and wider) and higher temperature flame provided the higher total chemical heat release rate (*Q*). The result obtained from the study supports the flame length theory of Roper [93] in terms of the relationship between parameters (e.g. the higher fuel rate and stoichiometric ratio causes the longer flame). However, this theory which was designed for the flame of hydrocarbon fuel predicted a significantly lower flame length than the experimental result. Therefore, the modification of the theory is required as H_2 and syngas have a significantly higher diffusive property and lower stoichiometric ratio than the hydrocarbon fuel.

In Chapter 5, the CFD model formulated and used for the study in Chapter 4 was modified in terms of dimension for supporting the formulation of the flame of syngas/producer gas and CH_4. The study focused on the impact of syngas composition on heat generation capability and emission formation. The stable co-flow flame of various syngas composition was formulated. The composition was set to projects the effect of H_2, CO, CH_4, CO_2, and N_2. The comparison and analysis of the result projected the role of each species on the focused topics. Additionally, the flames of producer gas produced from various feedstocks (e.g. rice husk, rubberwood, wood pellets and bamboo) were simulated. The results of these flames were examined to confirm the impact of each species.

The result showed that species CH_4 was preferable than other species. The heat generation capability was significantly higher when this species was added into syngas/producer gas fuel composition. Also, the same action caused the lower emission production rate of NO_x and CO_2 per amount of heat generated. CO was the second preferable species in case that the heat generation capability was prioritised. Nevertheless, a significantly higher production rate of CO_2 per generated heat was an inevitable effect of having a higher concentration of CO in fuel composition. The impact of H_2 obtained from the syngas/producer was in the same direction as the result of Chapter 4. The higher H_2:CO reduced the CO_2 production rate but escalated the NO_x production rate as the flame temperature increased. Apart from fuel species mentioned, the concentration of CO_2 in fuel composition was found to reduce the emission production rate of NO_x and CO_2 per amount of generated heat and assist the radiative heat flux transferred from flame. The result again confirms the requirement for modifying the theory since significantly lower flame length is computed from the theory compared to the CFD result for all the fuel composition.

Not only the impact of each species in fuel composition but also the relation between flame characteristics and heat generation capability were observed throughout the study. The flame temperature was not the major factor controlling the total heat generation capability of the diffusion flame (Q_{total}). Fuel combustion heat release (Q_{max}) and flame dimension also played a significant role in the heat generation capability of the flame. The higher value of these parameters led to the higher Q_{total}, and they were capable of compensating the role of each other. For instance, the fuel composition having the lower value of Q_{max} was able to formulate the flame having a higher value of Q_{total} in case that this flame had a larger dimension.

In Chapter 6, the CFD model was created based on the burner of Gohari et al. [88]. The experimental result of this model was utilised as a reference in the validation process. An occurrence of flame oscillation due to the Kelvin-Helmholtz type of instability was investigated as well as the impact of this phenomenon on heat generation. The fuel composition in this study was (i) H_2, (ii) syngas with H_2:CO as 1:3, 1:1, and 3:1, (iii) syngas with H_2:CO = 1 mixed with either CH_4, CO_2, or N_2. Comparing the result obtained from these compositions projected the impact of each species in the fuel composition of syngas/producer gas. The volume flow rate of fuel stream was between 0.2 and 1.4 SLPM while the oxidiser of the combustion was ambient air. The flames of all the studied fuel compositions were stable at 0.2 SLPM and transformed to oscillating flame called 'flickering and tip-cutting flame' respectively at different fuel rate depending on fuel composition.

The study results expressed that syngas with a lower ratio of H_2:CO caused a higher magnitude of oscillation. Nevertheless, the value of this parameter will not rise further when the H_2:CO is lower than 1. For instance, the flame of syngas having H_2:CO = 1 had a similar magnitude of oscillation to the flame of syngas with H_2:CO < 1. Adding CH_4 into fuel composition increased the magnitude of oscillation significantly, and the stable flame was more sensitive to the fuel rate in order to become unstable. The opposite direction of the result was observed when either CO_2 or N_2 was added into fuel composition.

The unstable flame was undesirable as the heat generated from this flame was inconsistent. The higher concentration of CH_4 was preferable for a stable flame since it encourages heat generation capability significantly. The impact of this species on an unstable flame was in the same direction, and syngas mixed with CH_4 generated the average heat release at a higher rate than other fuel composition. However, the side effect of this result was the higher

fluctuation level of heat release. Thus, the stability of the flame was a crucial factor in order to effectively use the fuel consisting of CH_4. The sufficient co-flow air rate was required to maintain the stability of the flame when this species was added into syngas/producer gas composition. This finding, on the other hand, pointed to the benefit of having CO in fuel composition. Syngas with the lower ratio of H_2:CO generated a higher heat than one with a higher ratio and also had a lower fluctuation level in heat generation capability. Syngas with the lower ratio of H_2:CO was hence recommended when flame stability and heat generation capability were prioritised. Nonetheless, the higher CO_2 emission is again the side impact. CO_2 and N_2 were non-combustible species and the addition of them to fuel composition decreased the heat generation capability and the fluctuation level of heat release.

The role of each species on characteristics of a stable and unstable flame of syngas/producer was mostly in the same direction. The impact was already mentioned above on the conclusion of Chapter 5. The only exceptional case was seen from the effect of CO_2 on the flame length. Diluting this species to syngas composition decreased the flame length for the stable flame but increased the value of this parameter in the unstable oscillating flame. The method for computing the average flame length presented in [91] predicts significantly lower flame length than the result obtained from the experiment and CFD. In opposite, the flame length formula of Roper [93] could provide the flame length closer to the experimental result though it was developed for the stable flame.

In Chapter 7, the same CFD model as Chapter 6 was utilised for studying the impact of fuel composition on the reduction and disappearance of flame oscillation. The fuel composition was also the same as defined in Chapter 6 as it could project the role of each species on the focused topic. The fuel rate was fixed at 1.2 SLPM, while the air rate was varied between 0 and 20 SLPM. The flame with the maximum magnitude of oscillation was firstly formulated at 0 SLPM of air rate where the ambient air was an oxidiser of the combustion. The co-flow air rate was then escalated, and this action reduces the impact of K-H instability and pushes the vortices outside the visible flame, so the flame oscillation disappears. It was found that the unstable flame of different fuel composition became stable at the different air rate. The concentration of CO, CO_2, and N_2 assisted this phenomenon since the flame of fuel consisting of the higher concentration of these species required the lower air rate to become stable. The opposite direction of the result was observed from the flame of fuel with a higher concentration of H_2 and CH_4. Apart from the reduction of flame stability, the impact of co-

flow air on the flame characteristics and heat generation capability was considered as insignificant compared to the impact of fuel rate and fuel composition.

8.2 Recommendations for future research

The fuel composition of syngas/producer gas contains not only single species but also several fuel species, e.g. H_2, CO, and CH_4, and this diversity affected the various aspects of the flame property. In this work, the stable and unstable laminar diffusion flame of syngas/producer gas was the main focus. Gas turbine and external combustion application are suitable for syngas as presented in Chapter 2. However, further study on several topics is required for utilising syngas in those applications effectively. The suggested tasks could be divided into three aspects.

Firstly, the knowledge regarding the impact of syngas composition of combustion should be extended. In this work, the understanding of this impact was extended. However, the result also points to the requirement of further works on the following topics

- The results projected the benefit of having CO_2 in the fuel composition as this species assists the heat transfer and the reduction of emission formation. The detailed understanding of the role of this species in various combustion applications and conditions is recommended. This aspect will further confirm the role of CO_2 for this advantage/disadvantage and provide the method of utilising the benefit of this species.

- The syngas having a lower H_2:CO has a higher capability in terms of heat generation according to the study result. However, the investigation did not consider the aspect of extinction, which could occur due to the significantly lower H_2:CO. The research for optimising the proper ratio of H_2:CO that balances between the heat generation capability and the risk of extinction is hence suggested.

- Adding either CO_2 or N_2 to fuel composition was one among the effective methods for reducing the flame instability. The side effect of this action was the reduction of the chemical heat release since the higher concentration percentage of them also refers to a lower concentration percentage of combustible species (H_2, CO, and CH_4). Hence, further optimisation for the suitable percentage of CO_2 and N_2 in syngas composition is required.

- Apart from the flame oscillation, there are several aspects of the combustion instability (e.g. lift-off, blowout, and extinction limit) of syngas/producer gases, remain unanswered. The diversity of fuel composition of syngas/producer gas would affect the behaviour of the flame under these situations differently. The study of these topics would provide a full understanding of the impact of each species on the flame instability.

Secondly, the combustion is operated under the turbulent flow regime in many applications. The study of turbulent diffusion flame of syngas is significant. The turbulent diffusion flame of syngas/producer gas was researched as per the survey of various works of literature. However, most of them focused on the flame characteristics, e.g. flame appearance, temperature, and dimension but not on the heat generation and heat transfer. Thus, the study of heat generation capability of the turbulent flame is suggested. Understanding of this aspect would provide the method of developing the performance of those applications when syngas/producer gas is used as fuel.

Thirdly, the study of Chanphavong [41] suggested the redesign of the combustion chamber for syngas. Based on the result obtained in this thesis, this suggestion is supported since the behaviour and characteristics of syngas are different from the conventional gas fuel. In other words, the combustion of syngas at the same condition as the conventional gas fuel results in different flame temperature, size, the amount of heat generated, and emission formation. The redesign of the combustion chamber for a gas turbine engine and the furnace for external combustion application is a significant step. The innovative design would lead to the effective combustion system which promotes the use of syngas.

Bibliography

[1] A. Molino, V. Larocca, S. Chianese, and D. Musmarra, 'Biofuels production by biomass gasification: A review', *Energies*, vol. 11, no. 4, pp. 1–31, 2018.

[2] V. V. Toro, A. V. Mokhov, H. B. Levinsky, and M. D. Smooke, 'Combined experimental and computational study of laminar, axisymmetric hydrogen–air diffusion flames', *Proc. Combust. Inst.*, vol. 30, no. 1, pp. 485–492, 2005.

[3] H. G. Darabkhani and Y. Zhang, 'Stabilisation mechanism of a flickering methane diffusion flame with co-flow of air', *Eng. Lett.*, vol. 18, no. 4, pp. 2–8, 2010.

[4] International Monetary Fund (IMF), 'World Economic Outlook', 2019. [Online]. Available: https://www.imf.org/en/Publications/WEO. [Accessed: 12-Aug-2019].

[5] International Energy Agency (IEA), 'Global Energy and CO2 Status Report 2018', 2019.

[6] The British Petroleum Company plc, 'BP Statistical Review of World Energy June 2016', 2016.

[7] A. Pradhan, P. Baredar, Kumar, and Anil, 'Syngas as An Alternative Fuel Used in Internal Combustion Engines: A Review', *J. Pure Appl. Sci. Technol.*, vol. 5, no. 2, pp. 51–66, 2015.

[8] The National Aeronautics and Space Administration (NASA), 'Climate Change: Vital Signs of the Planet', 2019. [Online]. Available: https://climate.nasa.gov/. [Accessed: 12-Aug-2019].

[9] O. Ellabban, H. Abu-Rub, and F. Blaabjerg, 'Renewable energy resources: Current status, future prospects and their enabling technology', *Renew. Sustain. Energy Rev.*, vol. 39, pp. 748–764, 2014.

[10] D. Klass, *Biomass for Renewable Energy, Fuels, and Chemicals*, 1st ed. San Diego: Academic Press, 1998.

[11] The World Bank, 'Solid Waste Management', 2019. [Online]. Available: https://www.worldbank.org/en/topic/urbandevelopment/brief/solid-waste-management. [Accessed: 12-Aug-2019].

[12] R. Koppmann, K. von Czapiewski, and J. S. Reid, 'A review of biomass burning emissions, part I: gaseous emissions of carbon monoxide, methane, volatile organic compounds, and nitrogen containing compounds', *Atmos. Chem. Phys. Discuss.*, vol. 5, no. 5, pp. 10455–10516, 2005.

[13] J. S. Reid, R. Koppmann, T. F. Eck, and D. P. Eleuterio, 'A review of biomass burning emissions, part II: Intensive physical properties of biomass burning particles', *Atmos. Chem. Phys.*, vol. 5, no. 3, pp. 799–825, 2015.

[14] J. S. Reid *et al.*, 'A review of biomass burning emissions part III: intensive optical properties of biomass burning particles', *Atmos. Chem. Phys. Discuss.*, vol. 4, no. 5, pp. 5201–5260, 2004.

[15] L. Yu *et al.*, 'Characterization and source apportionment of PM2.5 in an urban environment in Beijing', *Aerosol Air Qual. Res.*, vol. 13, no. 2, pp. 574–583, 2013.

[16] X. Zhang, A. Hecobian, M. Zheng, N. H. Frank, and R. J. Weber, 'Biomass burning impact on PM 2.5 over the southeastern US during 2007: Integrating chemically speciated FRM filter measurements, MODIS fire counts and PMF analysis', *Atmos. Chem. Phys.*, vol. 10, no. 14, pp. 6839–6853, 2010.

[17] O. W. Awe, Y. Zhao, A. Nzihou, D. P. Minh, and N. Lyczko, ‘A Review of Biogas Utilisation, Purification and Upgrading Technologies’, *Waste and Biomass Valorization*, vol. 8, no. 2, pp. 267–283, 2017.

[18] J. A. Ruiz, M. C. Juárez, M. P. Morales, P. Muñoz, and M. A. Mendívil, ‘Biomass gasification for electricity generation: Review of current technology barriers’, *Renew. Sustain. Energy Rev.*, vol. 18, pp. 174–183, 2013.

[19] D. O. Hall and J. I. Scrase, ‘Will biomass be the environmentally friendly fuel of the future?’, *Biomass and Bioenergy*, vol. 15, no. 4–5, pp. 357–367, 1998.

[20] K. Azizi, M. Keshavarz Moraveji, and H. Abedini Najafabadi, ‘A review on bio-fuel production from microalgal biomass by using pyrolysis method’, *Renew. Sustain. Energy Rev.*, vol. 82, no. October 2017, pp. 3046–3059, 2018.

[21] A. Hlavsová, A. Corsaro, H. Raclavská, D. Juchelková, H. Škrobánková, and J. Frydrych, ‘Syngas production from pyrolysis of nine composts obtained from nonhybrid and hybrid perennial grasses’, *Sci. World J.*, vol. 2014, 2014.

[22] A. Frassoldati, T. Faravelli, and E. Ranzi, ‘The ignition, combustion and flame structure of carbon monoxide/hydrogen mixtures. Note 1: Detailed kinetic modeling of syngas combustion also in presence of nitrogen compounds’, *Int. J. Hydrogen Energy*, vol. 32, no. 15, pp. 3471–3485, 2007.

[23] A. Cuoci, A. Frassoldati, G. Buzzi Ferraris, T. Faravelli, and E. Ranzi, ‘The ignition, combustion and flame structure of carbon monoxide/hydrogen mixtures. Note 2: Fluid dynamics and kinetic aspects of syngas combustion’, *Int. J. Hydrogen Energy*, vol. 32, no. 15 SPEC. ISS., pp. 3486–3500, 2007.

[24] International Energy Agency (IEA), ‘IEA BioEnergy Agreement Task 33: Thermal Gasification of Biomass’, 2019. [Online]. Available: http://task33.ieabioenergy.com/. [Accessed: 12-Aug-2019].

[25] G. M. Vincent, *Key Combustion Issues Associated with Syngas and High-Hydrogen Fuels*. University of California Irvine, 2006.

[26] J. W. Kim, T. Y. Mun, J. O. Kim, and J. S. Kim, ‘Air gasification of mixed plastic wastes using a two-stage gasifier for the production of producer gas with low tar and a high caloric value’, *Fuel*, vol. 90, no. 6, pp. 2266–2272, 2011.

[27] C. Gai and Y. Dong, ‘Experimental study on non-woody biomass gasification in a downdraft gasifier’, *Int. J. Hydrogen Energy*, vol. 37, no. 6, pp. 4935–4944, 2012.

[28] M. Ouadi, J. G. Brammer, M. Kay, and A. Hornung, ‘Fixed bed downdraft gasification of paper industry wastes’, *Appl. Energy*, vol. 103, pp. 692–699, 2013.

[29] V. Skoulou, G. Koufodimos, Z. Samaras, and A. Zabaniotou, ‘Low temperature gasification of olive kernels in a 5-kW fluidized bed reactor for H2-rich producer gas’, *Int. J. Hydrogen Energy*, vol. 33, no. 22, pp. 6515–6524, 2008.

[30] M. Dogru, C. R. Howarth, G. Akay, B. Keskinler, and A. A. Malik, ‘Gasification of hazelnut shells in a downdraft gasifier’, *Energy*, vol. 27, no. 5, pp. 415–427, 2002.

[31] J. Rafidah *et al.*, ‘Effects of different gasifying agents on syngas production from oil palm trunk’, *J. Trop. For. Sci.*, vol. 23, no. 3, pp. 282–288, 2011.

[32] Z. Wang *et al.*, ‘Gasification of biomass with oxygen-enriched air in a pilot scale two-stage gasifier’, *Fuel*, vol. 150, pp. 386–393, 2015.

[33] S. Rapagnà, N. Jand, A. Kiennemann, and P. U. Foscolo, ‘Steam-gasification of biomass in a fluidised-bed of olivine particles’, *Biomass and Bioenergy*, vol. 19, no.

3, pp. 187–197, 2000.

[34] D. Barisano *et al.*, ‘Steam/oxygen biomass gasification at pilot scale in an internally circulating bubbling fluidized bed reactor’, *Fuel Process. Technol.*, vol. 141, pp. 74–81, 2016.

[35] Y. K. Choi, M. H. Cho, and J. S. Kim, ‘Steam/oxygen gasification of dried sewage sludge in a two-stage gasifier: Effects of the steam to fuel ratio and ash of the activated carbon on the production of hydrogen and tar removal’, *Energy*, vol. 91, pp. 160–167, 2015.

[36] A. M. Salem and M. C. Paul, ‘An integrated kinetic model for downdraft gasifier based on a novel approach that optimises the reduction zone of gasifier’, *Biomass and Bioenergy*, vol. 109, no. January, pp. 172–181, 2018.

[37] A. M. Sepe, J. Li, and M. C. Paul, ‘Assessing biomass steam gasification technologies using a multi-purpose model’, *Energy Convers. Manag.*, vol. 129, pp. 216–226, 2016.

[38] T. Sutardi, M. C. Paul, and N. Karimi, ‘Investigation of coal particle gasification processes with application leading to underground coal gasification’, *Fuel*, vol. 237, no. October 2018, pp. 1186–1202, 2019.

[39] U. Kumar and M. C. Paul, ‘CFD modelling of biomass gasification with a volatile break-up approach’, *Chem. Eng. Sci.*, vol. 195, pp. 413–422, 2019.

[40] P. De Filippis, M. Scarsella, B. De Caprariis, and R. Uccellari, ‘Biomass Gasification Plant and Syngas Clean-up System’, *Energy Procedia*, vol. 75, pp. 240–245, 2015.

[41] L. Chanphavong and Z. A. Zainal, ‘Characterization and challenge of development of producer gas fuel combustor: A review’, *J. Energy Inst.*, 2018.

[42] S. C. Bhattacharya, S. Shwe Hla, and H. L. Pham, ‘A study on a multi-stage hybrid gasifier-engine system’, *Biomass and Bioenergy*, vol. 21, no. 6, pp. 445–460, 2001.

[43] U. Henriksen *et al.*, ‘The design, construction and operation of a 75 kW two-stage gasifier’, *Energy*, vol. 31, no. 10–11, pp. 1542–1553, 2006.

[44] G. Sridhar, P. J. Paul, and H. S. Mukunda, ‘Biomass derived producer gas as a reciprocating engine fuel - An experimental analysis’, *Biomass and Bioenergy*, vol. 21, no. 1, pp. 61–72, 2001.

[45] A. S. Ramadhas, S. Jayaraj, and C. Muraleedharan, ‘Dual fuel mode operation in diesel engines using renewable fuels: Rubber seed oil and coir-pith producer gas’, *Renew. Energy*, vol. 33, no. 9, pp. 2077–2083, 2008.

[46] N. R. Banapurmath and P. G. Tewari, ‘Comparative performance studies of a 4-stroke CI engine operated on dual fuel mode with producer gas and Honge oil and its methyl ester (HOME) with and without carburetor’, *Renew. Energy*, vol. 34, no. 4, pp. 1009–1015, 2009.

[47] L. P. L. M. Rabou, J. M. Grift, R. E. Conradie, and S. Fransen, ‘Micro gas turbine operation with biomass producer gas and mixtures of biomass producer gas and natural gas’, *Energy and Fuels*, vol. 22, no. 3, pp. 1944–1948, 2008.

[48] F. Baina, A. Malmquist, L. Alejo, and T. H. Fransson, ‘Effect of the fuel type on the performance of an externally fired micro gas turbine cycle’, *Appl. Therm. Eng.*, vol. 87, pp. 150–160, 2015.

[49] A. Saliamonas, R. Navakas, N. Striūgas, A. Džiugys, and K. Zakarauskas, ‘Effect of

producer gas addition on spectral characteristics of the natural gas flame', *Energetika*, vol. 60, no. 4, pp. 210–219, 2014.

[50] J. J. Hernández, M. Lapuerta, and J. Barba, 'Flame stability and OH and CH radical emissions from mixtures of natural gas with biomass gasification gas', *Appl. Therm. Eng.*, vol. 55, no. 1–2, pp. 133–139, 2013.

[51] M. Renzi, F. Patuzzi, and M. Baratieri, 'Syngas feed of micro gas turbines with steam injection: Effects on performance, combustion and pollutants formation', *Appl. Energy*, vol. 206, no. May, pp. 697–707, 2017.

[52] H. Nikpey Somehsaraei, M. Mansouri Majoumerd, P. Breuhaus, and M. Assadi, 'Performance analysis of a biogas-fueled micro gas turbine using a validated thermodynamic model', *Appl. Therm. Eng.*, vol. 66, no. 1–2, pp. 181–190, 2014.

[53] F. Delattin, G. Di Lorenzo, S. Rizzo, S. Bram, and J. De Ruyck, 'Combustion of syngas in a pressurized microturbine-like combustor: Experimental results', *Appl. Energy*, vol. 87, no. 4, pp. 1441–1452, 2010.

[54] K. A. Al-attab and Z. A. Zainal, 'Externally fired gas turbine technology: A review', *Appl. Energy*, vol. 138, pp. 474–487, 2015.

[55] A. Rentizelas, S. Karellas, E. Kakaras, and I. Tatsiopoulos, 'Comparative techno-economic analysis of ORC and gasification for bioenergy applications', *Energy Convers. Manag.*, vol. 50, no. 3, pp. 674–681, 2009.

[56] M. Moran and H. Shapiro, 'Thermodynamic Properties Tables'. 2011.

[57] J. M. Kuchta, *Investigation of fire and explosion accidents in the chemical, mining and fuel related industries: A manual*. Washington DC, USA: United states: Department of the Interior, Bureau of Mines, 1986.

[58] M. Fossum and R. V. Beyer, *Co-combustion: Biomass fuel gas and natural gas*. Trondheim: SINTEF Energy Research, 1998.

[59] J. Chomiak, J. P. Longwell, and A. F. Sarofim, 'Combustion of low calorific value gases; Problems and prospects', *Prog. Energy Combust. Sci.*, vol. 15, no. 2, pp. 109–129, 1989.

[60] H. F. Coward and G. W. Jones, *Limits of flammability of gases and vapors*. Washington, D.C.: United States Government Printing Office (U.S. G.P.O.), 1952.

[61] M. J. Moran, *Fundamentals of engineering thermodynamics*. Sixth edition. Hoboken, N.J. : Wiley, 2008.

[62] T. S. Cheng, Y. C. Chang, Y. C. Chao, G. B. Chen, Y. H. Li, and C. Y. Wu, 'An experimental and numerical study on characteristics of laminar premixed H2/CO/CH4/air flames', *Int. J. Hydrogen Energy*, vol. 36, no. 20, pp. 13207–13217, 2011.

[63] W. Uchman and S. Werlr, 'The use of low-calorific value gases in environmental protection engineering', *Archit. Civ. Eng. Environ.*, vol. 9, pp. 127–132, 2016.

[64] J. J. Hernandez, M. Lapuerta, C. Serrano, and A. Melgar, 'Estimation of the laminar flame speed of producer gas from biomass gasification', *Energy and Fuels*, vol. 19, no. 5, pp. 2172–2178, 2005.

[65] P. Ouimette and P. Seers, 'Numerical comparison of premixed laminar flame velocity of methane and wood syngas', *Fuel*, vol. 88, no. 3, pp. 528–533, 2009.

[66] E. Monteiro, M. Bellenoue, J. Sotton, N. A. Moreira, and S. Malheiro, 'Laminar burning velocities and Markstein numbers of syngas-air mixtures', *Fuel*, vol. 89, no.

8, pp. 1985–1991, 2010.

[67] B. Yan *et al.*, ‘Experimental and modeling study of laminar burning velocity of biomass derived gases/air mixtures’, *Int. J. Hydrogen Energy*, vol. 36, no. 5, pp. 3769–3777, 2011.

[68] I. Glassman and R. A. Yetter, *Combustion*. Burlington: Elsevier Science, 2014.

[69] S. Khosid and J. B. Greenberg, ‘The Burke-Schumann spray diffusion flame in a nonuniform flow field’, *Combust. Flame*, vol. 118, no. 1, pp. 13–24, 1999.

[70] T S E research group the State University of New Jersey, ‘Combustion, Nanomaterials Synthesis, and Laser-Diagnostics Laboratories’, 2019. [Online]. Available: http://coewww.rutgers.edu/~sdytse/research.html. [Accessed: 12-Aug-2019].

[71] H. Ghaziaskar and A. Naseri, ‘Coflow Diffusion Burner – Thomson Lab’, *Combustion Research Laboratory*, 2019. [Online]. Available: https://combustion.mie.utoronto.ca/?page_id=502. [Accessed: 12-Aug-2019].

[72] H. Tsuji, ‘Counterflow diffusion flames’, *Prog. Energy Combust. Sci.*, vol. 8, no. 2, pp. 93–119, 1982.

[73] S. L. Chung and J. L. Katz, ‘The counterflow diffusion flame burner: A new tool for the study of the nucleation of refractory compounds’, *Combust. Flame*, vol. 61, no. 3, pp. 271–284, 1985.

[74] J. Park *et al.*, ‘Flame characteristics in H2/CO synthetic gas diffusion flames diluted with CO_2: Effects of radiative heat loss and mixture composition’, *Int. J. Hydrogen Energy*, vol. 33, no. 23, pp. 7256–7264, 2008.

[75] R. Barlow and A. Dreizler, ‘International work shop; measurement and computation of turbulent non-premixed flame’, *Sandia.gov*, 2019. [Online]. Available: http://www.sandia.gov/TNF/DataArch/FlameD/SandiaPilotDoc21.pdf. [Accessed: 12-Aug-2019].

[76] J. Park, O. B. Kwon, J. H. Yun, S. I. Keel, H. Chang Cho, and S. Kim, ‘Preferential diffusion effects on flame characteristics in H2/CO syngas diffusion flames diluted with CO2’, *Int. J. Hydrogen Energy*, vol. 33, no. 23, pp. 7286–7294, 2008.

[77] H. Y. Shih, J. R. Hsu, and Y. H. Lin, ‘Computed flammability limits of opposed-jet H_2/CO syngas diffusion flames’, *Int. J. Hydrogen Energy*, vol. 39, no. 7, pp. 3459–3468, 2014.

[78] K. K. J. Ranga Dinesh, X. Jiang, M. P. Kirkpatrick, and W. Malalasekera, ‘Combustion characteristics of H2/N2 and H2/CO syngas nonpremixed flames’, *Int. J. Hydrogen Energy*, vol. 37, no. 21, pp. 16186–16200, 2012.

[79] P. Swarnkar, A. K. Sahu, and T. Sundararajan, ‘Numerical study of effect of hydrogen content on the structure of syngas diffusion flame’, in *10th International Conference on Heat Transfer, Fluid Mechanics and Thermodynamics (HEFAT2014)*, 2014, no. July, pp. 704–713.

[80] J. Xi, Y. Yuan, Z. Gu, W. Yang, X. Zhang, and S. Wang, ‘Effect of CO2/N2/CH4 dilution on NO formation in laminar coflow syngas diffusion flames’, *Energy Sources, Part A Recover. Util. Environ. Eff.*, vol. 40, no. 7, pp. 821–829, Apr. 2018.

[81] H. Xu, F. Liu, S. Sun, Y. Zhao, S. Meng, and W. Tang, ‘Effects of H_2O and CO_2 diluted oxidizer on the structure and shape of laminar coflow syngas diffusion flames’, *Combust. Flame*, vol. 177, no. x, pp. 67–78, 2017.

[82] K. K. J. Ranga Dinesh, X. Jiang, and J. A. Van Oijen, 'Direct numerical simulation of non-premixed syngas burning with detailed chemistry', *Fuel*, vol. 107, pp. 343–355, 2013.

[83] J. Lee, S. Park, and Y. Kim, 'Effects of Fuel-Side Nitrogen Dilution on Structure and NOx Formation of Turbulent Syngas Non-premixed Jet Flames', *Energy & Fuels*, vol. 26, pp. 3304–3315, May 2012.

[84] K. H. Yang and H. Y. Shih, 'NO formation of opposed-jet syngas diffusion flames: Strain rate and dilution effects', *Int. J. Hydrogen Energy*, vol. 42, no. 38, pp. 24517–24531, 2017.

[85] J. Park, J. S. Kim, J. O. Chung, J. H. Yun, and S. I. Keel, 'Chemical effects of added CO2 on the extinction characteristics of H_2/CO/CO_2 syngas diffusion flames', *Int. J. Hydrogen Energy*, vol. 34, no. 20, pp. 8756–8762, 2009.

[86] S. Quattrocchi, S. K. Aggarwal, and V. R. Katta, 'Liftoff and blowout characteristics of laminar syngas nonpremixed flames', *Int. J. Hydrogen Energy*, vol. 43, no. 12, pp. 6421–6433, 2018.

[87] K. Mu, Y. Zhang, Z. Zhang, Y. Wang, Y. Xiao, and X. Hui, 'Effect of fuel dilution on the stability characteristics of syngas diffusion flames', *Proc. ASME Turbo Expo*, vol. 3, no. PART A, pp. 221–228, 2008.

[88] H. Gohari Darabkhani, Q. Wang, L. Chen, and Y. Zhang, 'Impact of co-flow air on buoyant diffusion flames flicker', *Energy Convers. Manag.*, vol. 52, no. 8–9, pp. 2996–3003, 2011.

[89] N. Fujisawa, Y. Matsumoto, and T. Yamagata, 'Influence of Co-flow on Flickering Diffusion Flame', *Flow, Turbul. Combust.*, vol. 97, no. 3, pp. 931–950, 2016.

[90] Q. Wang, H. Gohari Darabkhani, L. Chen, and Y. Zhang, 'Vortex dynamics and structures of methane/air jet diffusion flames with air coflow', *Exp. Therm. Fluid Sci.*, vol. 37, no. January, pp. 84–90, 2012.

[91] H. Sato, K. Amagai, and M. Arai, 'Diffusion flames and their flickering motions related with Froude numbers under various gravity levels', *Combust. Flame*, vol. 123, no. 1–2, pp. 107–118, 2000.

[92] S. P. Burke and T. E. W. Schumann, 'Diffusion Flames', *Ind. Eng. Chem.*, vol. 20, no. 10, pp. 998–1004, 1928.

[93] F. G. Roper, 'The prediction of laminar jet diffusion flame sizes: Part I. Theoretical model', *Combust. Flame*, vol. 29, pp. 219–226, 1977.

[94] F. G. Roper, C. Smith, and A. C. Cunningham, 'The prediction of laminar jet diffusion flame sizes: Part II. Experimental verification', *Combust. Flame*, vol. 29, no. C, pp. 227–234, 1977.

[95] J. A. Miller and R. J. Kee, 'Chemical nonequilibrium effects in hydrogen-air laminar jet diffusion flames', *J. Phys. Chem.*, vol. 81, no. 25, pp. 2534–2542, Dec. 1977.

[96] J. Fay, 'The Distributions of Concentration and Temperature in a Laminar Jet Diffusion Flame', *J. Aeronaut. Sci.*, vol. 21, no. 10, pp. 681–689, Oct. 1954.

[97] J. Buckmaster and N. Peters, 'The infinite candle and its stability-A paradigm for flickering diffusion flames', *Symp. Combust.*, vol. 21, no. 1, pp. 1829–1836, 1988.

[98] A. Lingens, K. Neemann, J. Meyer, and M. Schreiber, 'Instability of diffusion flames', *Symp. Combust.*, vol. 26, no. 1, pp. 1053–1061, 1996.

[99] A. Lingens, M. Reeker, and M. Schreiber, ‘Instability of buoyant diffusion flames’, *Exp. Fluids*, vol. 20, no. 4, pp. 241–248, 1996.

[100] L. D. Chen, J. P. Seaba, W. M. Roquemore, and L. P. Goss, ‘Buoyant diffusion flames’, *Symp. Combust.*, vol. 22, no. 1, pp. 677–684, 1989.

[101] H. Gotoda, T. Ueda, I. G. Shepherd, and R. K. Cheng, ‘Flame flickering frequency on a rotating Bunsen burner’, *Chem. Eng. Sci.*, vol. 62, no. 6, pp. 1753–1759, 2007.

[102] J. Li and Y. Zhang, ‘Fuel variability effect on flickering frequency of diffusion flames’, *Front. Energy Power Eng. China*, vol. 3, no. 2, pp. 134–140, 2009.

[103] D. Durox, T. Yuan, and E. Villermaux, ‘The Effect of Buoyancy on Flickering in Diffusion Flames’, *Combust. Sci. Technol.*, vol. 124, no. 1–6, pp. 277–294, Mar. 1997.

[104] M. Arai, H. Sato, and K. Amagai, ‘Gravity effects on stability and flickering motion of diffusion flames’, *Combust. Flame*, vol. 118, no. 1–2, pp. 293–300, 1999.

[105] J. Piehl, L. Bravo, W. Acosta, G. Kumar, S. Drennan, and O. Samimi-Abianeh, ‘On predictions of fuel effects on lean blow off limits in a realistic gas turbine combustor using finite rate chemistry’, *Proc. ASME Turbo Expo*, vol. 4B-2018, pp. 1–10, 2018.

[106] P. Gobbato, M. Masi, A. Lazzaretto, and A. Toffolo, ‘Analysis of the natural acoustic modes of a gas turbine combustor using isothermal CFD simulations’, *Appl. Therm. Eng.*, vol. 126, pp. 489–499, 2017.

[107] J. Liu and C. E. Dumitrescu, ‘3D CFD simulation of a CI engine converted to SI natural gas operation using the G-equation’, *Fuel*, vol. 232, no. May, pp. 833–844, 2018.

[108] G. Maragkos, P. Rauwoens, and B. Merci, ‘Assessment of a methodology to include differential diffusion in numerical simulations of a turbulent flame’, *Int. J. Hydrogen Energy*, vol. 39, no. 25, pp. 13285–13291, 2014.

[109] M. Fischer and X. Jiang, ‘An assessment of chemical kinetics for bio-syngas combustion’, *Fuel*, vol. 137, pp. 293–305, 2014.

[110] C. Olm, I. G. Zsély, T. Varga, H. J. Curran, and T. Turányi, ‘Comparison of the performance of several recent syngas combustion mechanisms’, *Combust. Flame*, vol. 162, no. 5, pp. 1793–1812, 2015.

[111] G. P. Smith *et al.*, ‘GRI-Mech 3.0’, *University of California at Berkeley*. [Online]. Available: http://www.me.berkeley.edu/gri_mech/. [Accessed: 12-Aug-2019].

[112] A. Kazakov and F. Michael, ‘Reduced Reaction Sets based on GRI-Mech 1.2’, *University of California at Berkeley*. [Online]. Available: http://combustion.berkeley.edu/drm/. [Accessed: 12-Aug-2019].

[113] R. A. Yetter, F. L. Dryer, and H. Rabitz, ‘A comprehensive reaction mechanism for carbon monoxide/hydrogen/oxygen kinetics’, *Combust. Sci. Technol.*, vol. 79, no. 1–3, pp. 97–128, 1991.

[114] S. G. Davis, A. V. Joshi, H. Wang, and F. Egolfopoulos, ‘An optimized kinetic model of H2/CO combustion’, *Proc. Combust. Inst.*, vol. 30, no. 1, pp. 1283–1292, 2005.

[115] T. Lu and C. K. Law, ‘A criterion based on computational singular perturbation for the identification of quasi steady state species: A reduced mechanism for methane oxidation with NO chemistry’, *Combust. Flame*, vol. 154, no. 4, pp. 761–774, 2008.

[116] R. Sankaran, E. R. Hawkes, J. H. Chen, T. Lu, and C. K. Law, ‘Structure of a

spatially developing turbulent lean methane-air Bunsen flame', *Proc. Combust. Inst.*, vol. 31 I, no. 1, pp. 1291–1298, 2007.

[117] M. Frenklach *et al.*, 'GRI-Mech—An Optimized Detailed Chemical Reaction Mechanism for Methane Combustion', Jan. 2000.

[118] S. Chapman, T. G. Cowling, and D. Burnett, *The Mathematical Theory of Non-Uniform Gases*. Cambridge: University Press, 1970.

[119] S. A. Klein and F. L. Alvarado, *Engineering Equation Solver (EES) User Manual*. 4406 Fox Bluff Rd, Middleton, WI 53562: F-Chart Software, 1999.

[120] Cd-adapco, *cd-adapco, "STAR CCM+ version 12 User guide*. 2018.

[121] S. Mathur and S. C. Saxena, 'Methods of calculating thermal conductivity of binary mixtures involving polyatomic gases', *Appl. Sci. Res.*, vol. 17, no. 2, pp. 155–168, 1967.

[122] J. C. Maxwell, 'On the Dynamical Theory of Gases', *Philos. Trans. R. Soc. London*, vol. 157, pp. 49–88, 1867.

[123] J. Warnatz, U. Mass, and R. W. Dibble, *Combustion: Physical and Chemical Fundamentals, Modeling and Simulations, Experiments, Pollutant Formation 3rd edition*. Berlin: Springer-Verlag, 2001.

[124] R. Kee, G. Dixon-lewis, J. Warnatz, M. Coltrin, and J. Miller, 'A Fortran Computer Code Package For The Evaluation Of Gas-Phase, Multicomponent Transport Properties', Aug. 1996.

[125] B. J. McBride, S. Gordon, and M. A. Reno, 'Coefficients for Calculating Thermodynamic and Transport Properties of Individual Species', 1993.

[126] J. R. Howell and R. O. Buckius, *Fundamentals of engineering thermodynamics*. McGraw-Hill, Inc., 1992.

[127] J. Howell, R. Siegel, and M. P. Mengüç, *Thermal Radiation Heat Transfer*. 2010.

[128] M. G. Carvalho and T. L. Farias, 'Modelling of Heat Transfer in Radiating and Combusting Systems', *Chem. Eng. Res. Des.*, vol. 76, no. 2, pp. 175–184, 1998.

[129] E. ~H. Chui and G. ~D. Raithby, 'Computation of Radiant Heat Transfer on a Nonorthogonal Mesh Using the Finite-Volume Method', *Numer. Heat Transf. Part B - Fundam.*, vol. 23, pp. 269–288, Apr. 1993.

[130] G. D. Raithby and E. H. Chui, 'A finite-volume method for predicting a radiant heat transfer in enclosures with participating media', *J. Heat Transf. (Transactions ASME (American Soc. Mech. Eng. Ser. C); (United States)*.

[131] M. Modest, *Radiative Heat Transfer 3rd Edition*. Academic Press, 2013.

[132] S. C. Paul and M. C. Paul, 'Radiative heat transfer during turbulent combustion process', *Int. Commun. Heat Mass Transf.*, vol. 37, no. 1, pp. 1–6, 2010.

[133] M. C. Paul, 'Performance of the Various Sn Approximations of DOM in a 3D Combustion Chamber', *J. Heat Transfer*, vol. 130, no. 7, May 2008.

[134] W. P. Jones and M. C. Paul, 'Combination of DOM with LES in a gas turbine combustor', *Int. J. Eng. Sci.*, vol. 43, no. 5–6, pp. 379–397, 2005.

[135] H. C. Hottel, *Radiant-Heat Transmission*, vol. 3rd Ed., no. W. H. McAdams (Ed.). New York: McGraw-Hill, 1954.

[136] W. Gander and W. Gautschi, 'Adaptive Quadrature - Revisited', *Bit Numer. Math.*,

vol. 40, no. 1, pp. 84–101, 2000.

[137] S. Turns, *An Introduction to Combustion; Concepts and Applications*. Singapore: McGraw-Hill, 1996.

[138] H.-O. Kreiss and O. E. Ortiz, 'Introduction to numerical methods for time dependent differential equations', 2014.

[139] C. F. Curtiss and J. O. Hirschfelder, 'Integration of Stiff Equations', *Proc. Natl. Acad. Sci. U. S. A.*, vol. 38, no. 3, pp. 235–243, Mar. 1952.

[140] S.-E. Kim, 'A Multi-Dimensional Linear Reconstruction Scheme for Arbitrary Unstructured Mesh', in *16th AIAA Computational Fluid Dynamics Conference*, American Institute of Aeronautics and Astronautics, 2003.

[141] C. X. Xu, 'Hybrid method for nonlinear least-square problems without calculating derivatives', *J. Optim. Theory Appl.*, vol. 65, no. 3, pp. 555–574, 1990.

[142] V. Venkatakrishnan, 'On the accuracy of limiters and convergence to steady state solutions', in *31st Aerospace Sciences Meeting*, American Institute of Aeronautics and Astronautics, 1993.

[143] E. S. Cho and S. H. Chung, 'Numerical evaluation of NOx mechanisms in methane-air counterflow premixed flames', *J. Mech. Sci. Technol.*, vol. 23, no. 3, pp. 659–666, 2009.

[144] C. T. Bowman *et al.*, 'GRI-Mech 2.11', 2008. [Online]. Available: http://combustion.berkeley.edu/gri-mech/new21/version21/text21.html. [Accessed: 12-Aug-2019].

[145] T. Piemsinlapakunchon and M. Paul, 'Characterisation of Syngas Laminar Diffusion Flame with an Effect of its Varying Composition', *World Congress on Engineering 2017 (WCE 2017)*. pp. 1008–1012, Jul-2017.

[146] F. A. Williams, *Combustion theory: The fundamental theory of chemically reacting flow systems, second edition*. 2018.

[147] D. Drysdale, *An Introduction to Fire Dynamics*. Wiley, 2011.

[148] M. A. Delichatsios, 'Transition from momentum to buoyancy-controlled turbulent jet diffusion flames and flame height relationships', *Combust. Flame*, vol. 92, no. 4, pp. 349–364, 1993.

[149] M. Y. Bahadori, D. P. Stocker, D. F. Vaughan, L. Zhou, and R. B. Edelman, 'CHAPTER 4 - Effects of Buoyancy on Laminar, Transitional, and Turbulent Gas Jet Diffusion Flames', *Combustion and Spectroscopy, Eds*. Oxford: Pergamon, 1993, pp. 49–66.

[150] A. R. Choudhuri and S. R. Gollahalli, 'Characteristics of hydrogen-hydrocarbon composite fuel turbulent jet flames', *Int. J. Hydrogen Energy*, vol. 28, no. 4, pp. 445–454, 2003.

[151] D. Feikema, R. H. Chen, and J. F. Driscoll, 'Blowout of nonpremixed flames: Maximum coaxial air velocities achievable, with and without swirl', *Combust. Flame*, vol. 86, no. 4, pp. 347–358, 1991.

[152] J. Zeldovich, 'The Oxidation of Nitrogen in Combustion Explosions', *Eur. Phys. J. A. Hadron. Nucl.*, vol. 21, pp. 577–628, 1946.